OPTIMISATION OF COMPOSITE MARINE PROPELLER BLADES AND HYDROFOILS

Manudha T. Herath

A Thesis presented for the degree of Doctor of Philosophy

School of Mechanical and Manufacturing Engineering

University of New South Wales Australia

February 2016

Abstract

Traditional marine propellers that are manufactured using alloys have a fixed shape. These propellers are designed to achieve the highest propulsion efficiency at the cruise condition of the vessel. However, if the flow conditions change from the vessel's cruise condition, the propulsion efficiency reduces significantly. The objective of this thesis is to develop flexible shape-adaptive (self-morphing) blades using high performance composite materials, with particular focus on Carbon Fibre Reinforced Polymer (CFRP). By careful tailoring of fibre angle of composite layers, composite laminates can be catered to optimally change its twist under various lateral loading conditions. This special characteristic is proposed to be used for optimal change of pitch of the propeller blade based on incoming flow conditions.

An in-house optimisation algorithm has been developed to search for the optimum fibre angle of each carbon fibre layer that can enable the required shape change. The optimisation algorithm uses the Genetic Algorithm (GA) coupled with the state-of-the-art Finite Element techniques such as Cell-Based Smoothed Finite Element Method (CS-FEM) and Iso-Geometric FEM. The CS-FEM uses a stable triangular element scheme, while the NURBS based iso-geometric FEM has the capability of representing the complex geometry without any mesh based approximations. The finite element techniques also take into account ply terminations of the blade and hygrothermal effects that may be present in the composite. An iterative procedure to search for the initial shape of the blades was also developed.

The developed techniques were used to optimise a hydrofoil using experimental data from cavitation tunnel tests of a non-optimised hydrofoil. The optimised hydrofoil was then manufactured and was subjected to rigorous structural testing in order to ensure the strength and safety of the hydrofoil and to validate the reliability of the manufacturing technique. Additionally, hydrodynamic tests were conducted at the cavitation tunnel facility to characterise the performance of the optimised hydrofoil and compare against previously tested identical non-optimised hydrofoils. The optimised hydrofoil indeed showed more favourable results in terms of lift to drag (L/D) ratio of the hydrofoil and hydrodynamic fluctuations and uncertainties due to turbulence. The cavitation tunnel results were then validated against Fluid-Structure Interaction (FSI) simulations and were found to be in good agreement with the predictions

Originality Statement

"I hereby declare that this submission is my own work and to the best of my knowledge it contains no materials previously published or written by another person, or substantial proportions of material which have been accepted for the award of any other degree or diploma at UNSW or any other educational institution, except where due acknowledgement is made in the thesis. Any contribution made to the research by others, with whom I have worked at UNSW or elsewhere, is explicitly acknowledged in the thesis. I also declare that the intellectual content of this thesis is the product of my own work, except to the extent that assistance from others in the project's design and conception or in style, presentation and linguistic expression is acknowledged."

.

Signed ………………………………………………

Date ………………………………………………

Copyright Statement

Authenticity Statement

'I certify that the Library deposit digital copy is a direct equivalent of the final officially approved version of my thesis. No emendation of content has occurred and if there are any minor variations in formatting, they are the result of the conversion to digital format.'

Signed ………………………………………………

Date ………………………………………………

Acknowledgements

- To my primary supervisor Prof. Gangadhara Prusty and Co-Supervisors A/Prof. Guan H. Yeoh and Dr Mac Chowdhury from UNSW for their guidance and encouragement continuously throughout my PhD
- To Dr Sundararajan Natarajan (IIT, Madras, formerly UNSW) for his guidance and support in Finite Element coding and general structural mechanics support
- To Defence Science and Technology (DSTO) of Australia for providing me financial support and allowing me to use their state-of-the-art facilities and knowledge for experimental work
- To my Co-supervisor Dr Nigel St John (DSTO) for his amazing support, encouragement, hosting my visits to DSTO many times and paving the way to a truly unique research experience
- To Dr Andrew Phillips (DSTO) for his continuous support and willingness to help me anytime regardless of how busy he was.
- To Mr Russell Cairns (DSTO) and Dr Asintha Nanayakkara (DSTO) for their help and guidance in manufacturing and experimentation tasks
- To Mr Matthew Ibrahim and Dr Robert Ditchburn for their guidance in damage detection efforts in composites
- To Dr Ulf Gabre of Australian Nuclear Science and Technology Organisation (ANSTO) for taking time to perform Neutron Tomography imaging
- To A/Prof. Paul Brandner, Mr Bryce Pearce and Mr Daniel Butler of Australian Maritime College (AMC) for providing all the help and guidance to conduct cavitation tunnel experiments
- To my girlfriend Jendi and my family for their constant encouragement and support to constantly keep doing the best I could

Table of Contents

List of Figures

List of Tables

Nomenclature

C_D	Drag coefficient
C_L	Lift coefficient
K_T	Thrust coefficient
K_q	Torque coefficient
V_a	Advance speed (m/s)
D	Drag (N)
J	Advance ratio
L	Lift (N)
M	Moment per unit plate width (Nm/m)
N	Force per unit plate width (N/m)
Q	Torque (Nm)
T	Thrust (N)
d	Diameter (m)
n	Rotational frequency (rev/s)
p	Pitch (m)
α	Angle of Attach, AoA (°)
η	Efficiency
κ	Curvature (1/m)
ρ	Density (kg/m^3)
ϵ	Strain (m/m)

CFRP	Carbon Fibre Reinforced Polymer
CLPT	Classical Laminate Plate Theory
FBG	Fibre Bragg Grating Sensor
FSDT	First-order Shear Deformation Theory
GFRP	Glass Fibre Reinforced Polymer
LDA	Laser Doppler Anemometry
LVDT	Linear Variable Differential Transformer
PIV	Particle Imaging Velocimetry
PTV	Particle Tracking Velocimetry

AMC	Australian Maritime College
DSTO	Defence Science and technology Organization of Australia
UNSW	University of New South Wales, Australia

List of Relevant Publications

Elements and contents of this thesis have been published in the following manuscripts:

- HERATH, M. T., NATARAJAN, S., PRUSTY, B. G. & ST JOHN, N. 2014. Smoothed finite element and genetic algorithm based optimization for shape adaptive composite marine propellers. *Composite Structures*, 109, 189-197.
- HERATH, M. T., NATARAJAN, S., PRUSTY, B. G. & ST JOHN, N. 2015. Iso-geometric analysis and Genetic Algorithm for shape-adaptive composite marine propellers. *Computer Methods in Applied Mechanics and Engineering*, 284, 835-860.
- HERATH, M. T., LEE, A. K. L. & PRUSTY, B. G. 2015. Design of shape-adaptive wind turbine blades using Differential Stiffness Bend-Twist coupling. *Ocean Engineering*, 95, 157-165.
- HERATH, M. T. & PRUSTY, B. G. 2012. Performance analysis and optimization of bend-twist coupled composite hydrofoils using fluid-structure interaction. *7th Australasian Congress on Applied Mechanics*, Adelaide, Australia.
- HERATH, M. T., PRUSTY, B. G., YEOH, G. H., CHOWDHURY, M. & ST JOHN, N. 2013. Development of a shape-adaptive composite marine propeller using bend-twist coupling characteristics of composites. *3rd International Symposium of Marine Propulsors*, Tasmania, Australia.
- HERATH, M. T., NATARAJAN, S., PRUSTY, B. G. & ST JOHN, N. 2013. Shape-Adaptive Composite Marine Propellers – Analysis and Optimization. *19th International Conference on Composite Materials*, Montreal, Canada.

1. Introduction

1.1. Background

The art and engineering behind designing traditional marine propellers has been in existence for several centuries. Such traditional marine propellers are generally constructed out of alloys such as Nickel-Aluminium-Bronze (NAB) or Manganese-Aluminium-Bronze (MAB). However, traditional fixed pitch metallic propellers have inherent limitations such as having a fixed shape (disregarding controllable pitch propellers that have mechanical means of controlling the pitch), magnetically active and prone to corrosion after prolonged periods of exposure to minerals in water. Recent developments in advanced materials such as fibre reinforced composites can potentially overcome these limitations. A particularly attractive capability of composites that has been widely researched is their ability to deform, in a controlled fashion, under different loading conditions. This can potentially be used to alleviate a fundamental shortcoming of fixed shape alloy propellers,

Fixed shape alloy propellers are designed with the intention of providing maximum propulsive efficiency at the cruise speed – the speed which the vessel travels over a majority of its lifetime. However, if the speed, more precisely the advance ratio (J), deviates from its designed value, the propulsive efficiency reduces by a significant amount. Such changes in conditions can occur due to various reasons such as changes in currents, manoeuvring operations, during acceleration and decelerations, etc. Composite propellers can potentially be used in such a way that the pitch of the propeller changes due to changes in flow conditions, i.e. – changes in lateral loads on propeller blades.

1.2. Advantages of Composites

Fibre reinforced Composites inherently possess a number of advantages over alloys. Some of these advantages can be listed as,

1. Flexibility
2. Light Weight
3. Corrosion resistance
4. The large number of materials and layup combinations
5. Capability of optimal design to cater many different design goals
6. Easier to achieve smoother surface finishes with higher manufacturing tolerances

These general advantages of composites over alloys apply directly in the context of marine propellers. However, they can be further elaborated in the context of propellers, as follows (Marine, 1993, Mouritz et al., 2001, Chen et al., 2006, Young, 2007a, Mulcahy et al., 2011):

1. Shape Adaptability to improve performance at off-design conditions
2. Potential weight and inertia reduction of up to 75%
3. Corrosion resistance, especially useful in saline water applications
4. Enhanced stealth capabilities due to composite materials typically are non-magnetic
5. Low sound generation and turbulence due to flexibility
6. Low manufacturing and repair costs under mass production
7. Large choice of high performance composite materials and layup combinations that can be optimised to achieve maximum performance
8. Lower risk of cavitation

Shape adaptability can be considered as the main focus of this research. It refers to the capability of composite propellers to deform, without the involvement of external mechanisms (such as in controllable pitch propellers), based on the flow conditions and rotational speed in order to achieve a higher efficiency, compared to alloy propellers, throughout its operating domain. Several researchers in the past (Lee and Lin, 2004, Lin et al., 2009, Liu and Young, 2009, Motley and Young, 2011b, Mulcahy et al., 2011, Young, 2008) have attempted to design shape adaptive propellers and optimise the performance based on the selection of optimum layup configurations and layup material combinations. However, the results thus far have been mixed. These will be discussed in detail in a later section.

Composite materials are inherently more flexible compared to alloys. However, the basis of shape-adaptability extends beyond just flexibility of composites. It is the unique bend-twist coupling characteristic of composites that can be used to enhance shape adaptability (Liu and Young, 2009). Bend-twist coupling is referred to the capability of composites to twist under an applied lateral loading. This characteristic has the potential to be used to change the pitch of the propeller based on the velocity of the incoming flow in order to maintain the optimal pitch for different incoming velocities. This has potential of increasing the efficiency of the propeller at off-design conditions compared to an alloy propeller. It must be noted that, even a small efficiency gain of 2 to 3% translates into a large fuel savings in the context of commercial ships that are continuously in operation. Based on the worldwide fuel consumption statistics given by Corbett and Koehler (2003), even 1% of fuel savings results in a fuel saving of 2.89 million tonnes. In addition, shape adaptability can be utilized to delay cavitation of the propeller (Motley and Young, 2011b), provide a higher acceleration and reduce the power and RPM requirements to achieve the top speed of the vessel (Volante, 2005).

Additionally, a major advantage of fibre reinforced composites over metals is their low density; thus, the light weight. Typically carbon fibre reinforced epoxy composites with a fibre volume fraction of 60% has a density of 1500 kgm^{-3} (Department of Defense, 2002); whereas, Nickel Aluminium Bronze (NAB) alloys have a density of approximately 7600 kgm^{-3}. Thus, the weight reduction of a composite propeller built with the same dimensions as an alloy propeller is roughly 81%. If glass-fibre reinforced epoxy is used a weight reduction of roughly 75% can be expected. This translates into a considerable weight savings in the context of most modern alloys propellers that weigh well over 20 tonnes (Carlton, 2007).

Reduction of weight results in many direct and indirect advantages. One of the direct advantages is the reduction of fuel consumption of the vessel. Reduced weight results reduced inertia and forces required to produce accelerations. These accelerations can be linear or curvilinear depending on the manoeuvre and they are constantly changing throughout the cruise of a ship. Thus, a large fuel saving can be expected by a considerable weight reduction. An indirect advantage of weight reduction is the increase of lifetime of other components of the engine that facilitate the rotational motion. This is due to the lower stresses and fatigue (Grabovac et al., 2006) applied on those components during rotations. In fact, weight reduction is an important factor in marine vessels to the extent where some commercial companies, such as QinetiQ, have manufactured composite propellers solely for the purpose of weight reduction of the ships without exploiting their potential efficiency gains (Marsh, 2004).

Enhanced stealth capability is another potential advantage of composite propellers. Composite propellers have the potential to have an enhanced stealth compared to alloy propellers due to two major reasons (Marsh, 2004):

1. Lower noise signature resulting from lower turbulence and cavitation (as a result of optimisation efforts)
2. Composites are magnetically inactive; thus, reduces the magnetic signature

In terms of noise generation, composite propellers can be designed to be superior to NAB propellers at off-design conditions. Noise generation in propellers is mainly caused by separation of flow from the propeller and turbulence during its rotation (Bertram, 2000). Cavitation is referred to the process which the pressure around the blade hydrofoil falls below the vapour pressure of water at that temperature causing water to vaporise and form bubbles. In addition to a significant noise generation, cavitation is also responsible for erosion of the propeller blades. With proper optimisation flexible composite can be capable of reducing cavitation by reducing the pitch (twist) according to the speed of the rotation of the propeller; whereby, increasing the smoothness of the flow to provide better cavitation performance (Motley and Young, 2011b). The end result is a low noise propeller. Commercially produced Contur-F Series propellers are claimed to have a noise reduction of the order of 5 dB compared to NAB propellers (Figure 1-1) (Voith, 2004).

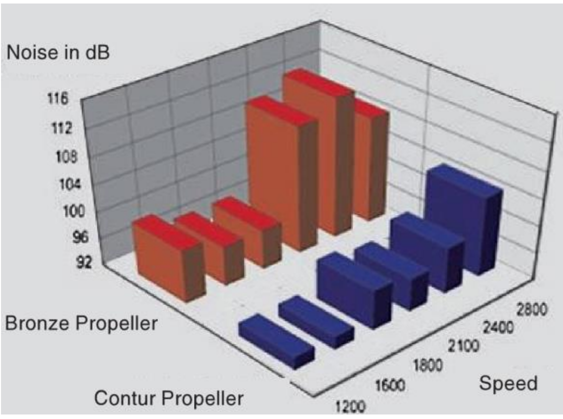

Figure 1-1: Noise reduction of Contur Propellers (Voith, 2004)

Composites are magnetically inactive; thus, are not detectable using magnetic detectors such as Magnetometers. However, this advantage may apply if it was decided to use metal-composite hybrid composites. Thus, it is more advantageous to be focussed on designing purely non-metallic composite propellers.

Polymers and carbon/glass fibres are naturally less prone to corrosion compared to most alloys due to their lower oxidization risk and reactance. Composites are also known to have better chemical stability and abrasion resistance (Marsh, 2004). These factors are especially important in sea water applications. Thus, the life expectancy of composite propellers is higher compared to alloy counterparts.

1.3. Propeller terminology and hydrofoil analogy

Propeller design is governed by a number of important design parameters. These parameters are mostly hydrodynamic entities that indicate the performance of a propeller. It is pertinent to provide a basic description of these entities as it helps the proceeding discussions.

In general, propeller design is governed by four non-dimensional entities; namely, advance ratio (non-dimensional speed), thrust coefficient (non-dimensional thrust), torque coefficient (non-dimensional torque) and propulsive efficiency (Carlton, 2007). In addition, the cavitation coefficient is important to understand the cavitation phenomenon of the propeller.

The advance ratio (J) of a propeller is the non-dimensional speed measurement of a propeller. This is essentially a ratio between the forward advancing speed of the propeller and the radial speed (Eq. 1-1). Consequently, the advance ratio is related to the resultant angle, which the flow enters the blade.

$$J = \frac{V_a}{nd} \quad \textbf{Eq. 1-1}$$

Where, V_a is the speed forward speed of the propeller relative to the fluid medium, n is the rotational frequency of the propeller in rev/s and d is the diameter of the propeller.

The thrust coefficient provides a non-dimensional measurement for the thrust produced by the propeller (Eq. 1-2). The thrust coefficient is related to the ratio between the thrust produced by the propeller and the product of dynamic pressure (ρV^2, related to $\rho n^2 d^2$) and area (πr^2, related to d^2) of the propeller. The torque coefficient is similar to the thrust coefficient, but with the addition of an extra dimensional term (diameter of the propeller, d) to normalise against the moment arm.

$$K_T = \frac{T}{\rho n^2 d^4} \qquad \textbf{Eq. 1-2}$$

$$K_Q = \frac{Q}{\rho n^2 d^5} \qquad \textbf{Eq. 1-3}$$

Where, T is the thrust produced, Q is the torque required, ρ is the density of the fluid and n, d as in Eq. 1-1.

The propulsive efficiency is defined as the ratio between the power harnessed by propulsion and the power input as torque (Eq. 1-4). Terms in η_{prop} can be rearranged to be represented using K_T, K_Q and J (Eq. 1-4).

$$\eta_{prop} = \frac{TV_a}{Q.(2\pi n)} = \frac{K_T}{K_Q}.\frac{J}{2\pi} \qquad \textbf{Eq. 1-4}$$

The performance of a marine propeller is typically characterised using K_T, K_Q and η by presenting their variation against J. Typically, a curve series for various pitch angles of the same propeller class is generated based on open water testing. An example of such curve series is given in Figure 1-2. Based on the curves it is clear that fixed shape propellers have a peak propulsive efficiency, which the propeller will deviate from if the advance ratio were to change. However, if such deviation occurred, the propeller can recover some of the reduced efficiency by adjusting its pitch and transiting to a curve with a different p/d in the curve series. This is the underlying philosophy in designing shape-adaptive variable pitch blades.

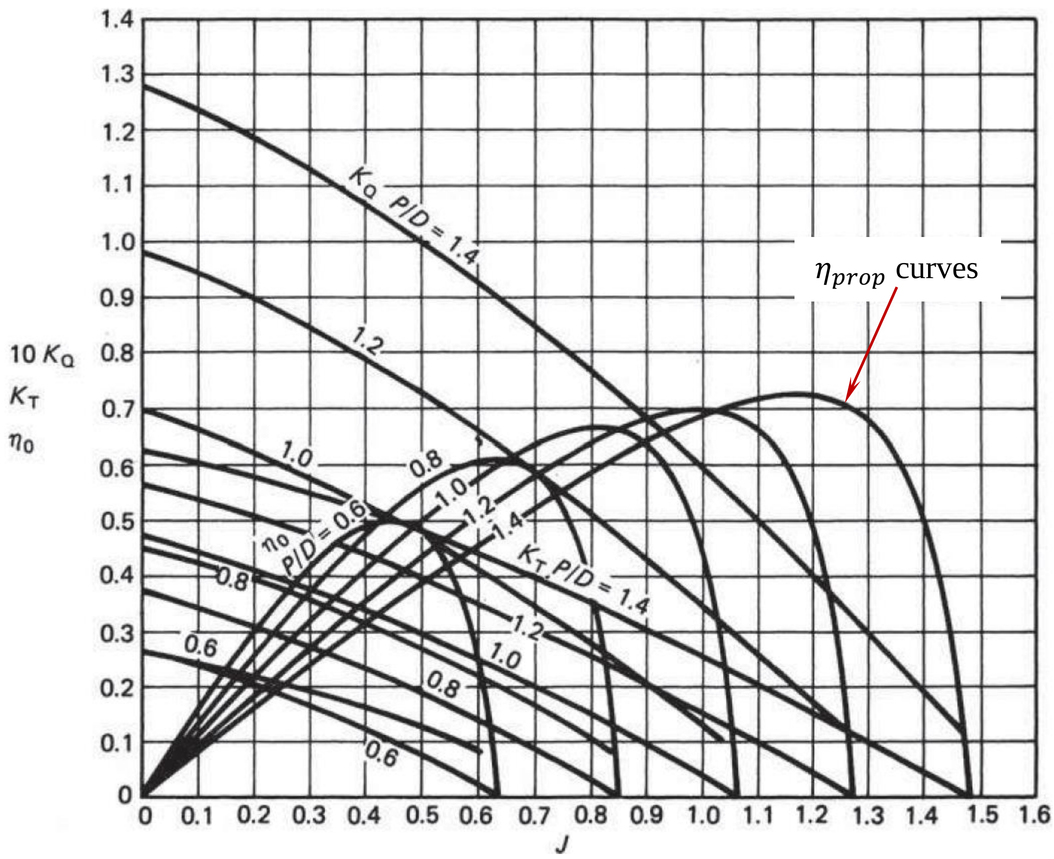

Figure 1-2: An example open-water curve series (Carlton, 2007)

As explained in proceeding chapters, the work undertaken in this research utilises hydrodynamic similarities between propeller blades and hydrofoil structures. Thus, it is necessary to draw a clear equivalence between the two entities. It can be argued that a propeller is in fact an object with hydrofoils arranged in a radial fashion around a hub. Propeller blades typically have more complex shapes compared to standard hydrofoils considered in proceeding discussions. However, the hydrodynamic similarity will remain consistent. Therefore, simpler hydrofoils with lower manufacturing costs and complexity are intended to be used as validating tools for the purposes of this thesis.

The two most commonly used hydrodynamic entities in the proceeding discussions are the advance ratio and the propulsive efficiency. The advance ratio represents the ratio between advance speed and radial velocity of the blade; thus, it is strongly correlated to the angle which the flow enters the propeller blade. Hence, it is taken that the angle of attack of flow incidence on the hydrofoil is a good representation of the advance ratio of a propeller blade. Furthermore, for small angles of attack, the thrust generated by a propeller blade is due to the lift generated by the blades, while the torque is required to overcome the moment caused by the drag on the blades. Thus, it is taken that the ratio between lift and drag of a hydrofoil is a good representation of the propulsive efficiency of a propeller. In fact, in the context of aerodynamics, L/D ratio of a wing is considered as its aerodynamic efficiency (Brandt, 2015), which further justifies the use of L/D of a hydrofoil as a representation of the propulsive efficiency of a propeller.

$$J = \frac{V_a}{2Rn} = \pi \frac{V_a}{V_r} = \pi \tan^{-1}(AOA) \leftrightarrow AOA$$
$$\eta_{prop} = \frac{TV_a}{Q\omega} \leftrightarrow \frac{L}{D}$$
Eq. 1-5

1.4. Research goals and approach

The primary objective of this research is to develop an optimisation scheme for the structural domain of a composite marine propeller and verify its change in performance using hydrofoils. This objective can be elaborated as follows:

1. Develop a robust optimisation scheme for composite marine propellers that is also applicable to composite hydrofoils
   - Construct an optimisation strategy and an objective function to improve the off-design propulsive efficiency of a composite propeller using bend-twist coupling characteristics of composites. The optimisation routine must be able to find the optimum fibre angle arrangement in the composite blade in order to provide best propulsive efficiency.

   - Investigate suitable optimisation algorithms and select an algorithm that is suited for the application
   - Investigate suitable methods to evaluate the structural response of a composite blade under the required loads
   - Device a strategy to calculate the unloaded shape of the blade such that the optimum shape is achieved at the design flow condition
2. Use experimental hydrodynamic results for a previously tested hydrofoil to optimise the layup and shape of a composite hydrofoil
   - Obtain hydrodynamic data for a standard hydrofoil that can be converted to a composite hydrofoil
   - Use the strategy devised previously to design a composite hydrofoil based on the standard alloy version
3. Use experiments to determine the structural properties of the optimised hydrofoil
   - Formulate a low cost, high quality composite manufacturing technique to manufacture the designed hydrofoil with the desired layup and initial shape
   - Conduct structural experiments on the manufactured hydrofoil to understand its strength properties and frequency characteristics. Use the experiments to gain insight into the safety of using composite hydrofoils in experiments and operation.
   - Use structural experiments to understand possible modes of failure of hydrofoils
4. Conduct cavitation tunnel results to characterise the performance of the optimised hydrofoil

- Understand the performance characteristics of the optimised hydrofoil and compare against non-optimised hydrofoils.
- Conduct fluid-structure interaction studies to validate findings
- Evaluate the outcome of the proposed optimisation scheme

1.5. Thesis Outline

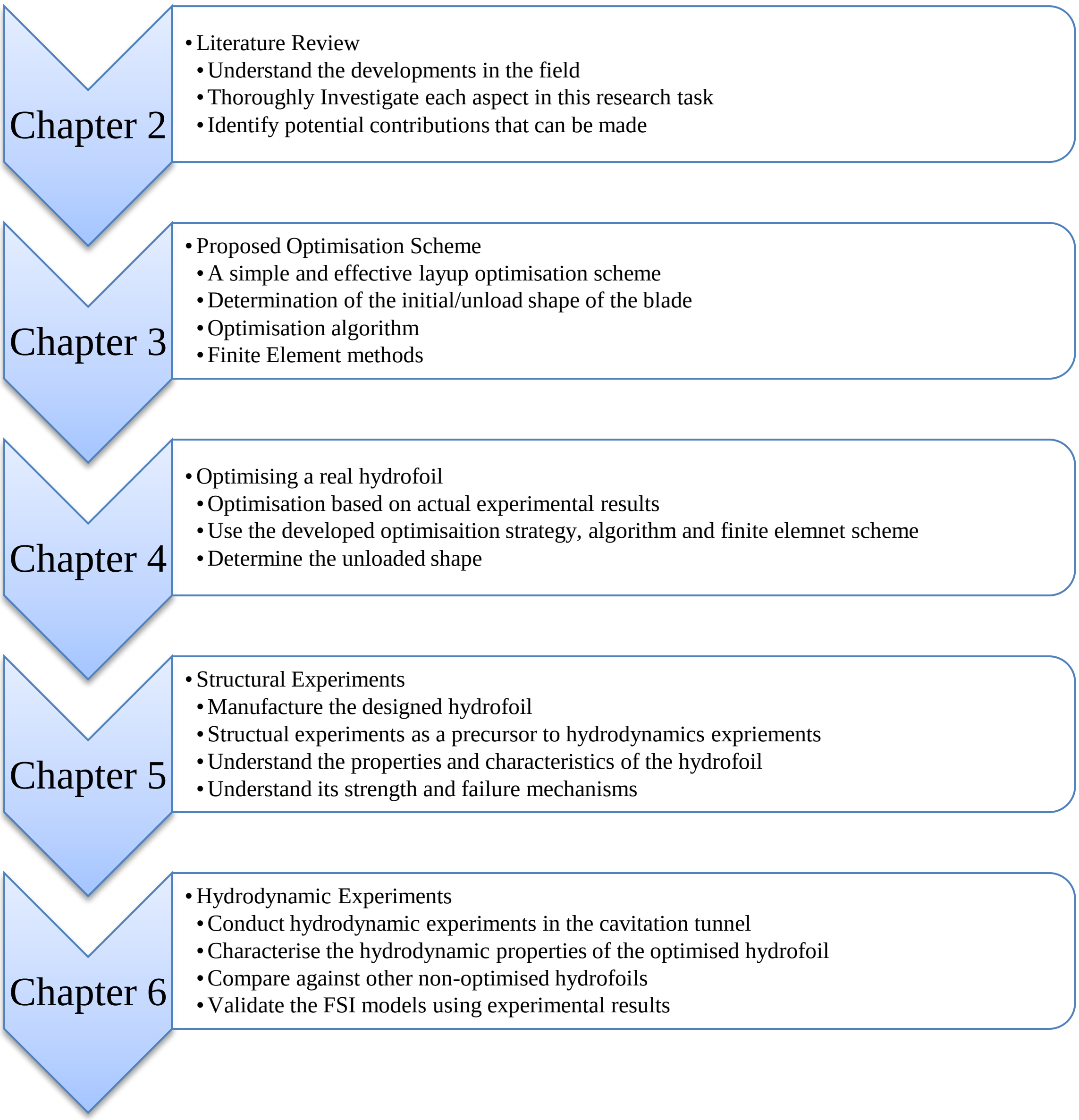

2. Literature review

2.1. Introduction

Designing marine propellers is a science that has been in existence for centuries. These marine propellers are traditionally made using Nickel Aluminium Bronze (NAB) or Manganese Nickel Aluminium Bronze (MAB) alloys. As many industries in modern engineering, there has been an increased interest towards using composites to develop marine propellers. This interest is mainly driven by the favourable properties of composites over traditional alloys. One such exceptional characteristic of layered composites is their bend-twist coupling characteristics. This is the ability of composites to twist under a pure transverse bending loading. This can potentially be used to improve the efficiency of the propeller by changing its pitch (twist) based on the incoming flow conditions.

However, little is known about the development and optimisation of composite propellers in order to achieve the best of bend-twist coupling characteristics. There is commercial development of shape-adaptive propellers, but their techniques are not available in open literature making it difficult to make improvements or understand the mechanics behind such propellers. In this light, there have been several research efforts in the past to fully understand the design process of shape-adaptive propellers and expand the knowledge making it available in open literature. Although these efforts are noteworthy and highly regarded in the field, these researches have not been able to compete against commercial level propellers.

The following is a literature review on composite propellers. Before discussing about research in the field of structural optimisation, it first outlines the hydrodynamics of propellers. The discussion is extended to fluid-structure interaction (FSI) coupling principle, which is an essential component in shape-adaptive propellers. This will be followed by an in-depth discussion about the structural optimisation efforts of past researchers both in and out of the context of composite propellers. Next, the experimental studies that have been undertaken thus far in this field of research are explained. Afterwards, numerical methods that are useful in implementing an accurate structural analysis scheme for the optimisation are explained. Finally, the review identifies the unexplored areas of research, in the context of composite marine propellers and the attempts that will be made as a part of this research.

2.2. Propeller Hydrodynamics

Propeller hydrodynamics is referred to the analytical/numerical study of fluid dynamics, focussing on the flow patterns and the resulting forces on the propeller. These methods have been in existence for over a century and have constantly been evolving to match the real performance of complex modern day propeller blades. Hydrodynamically, propeller blades differ from wing structures in that propeller blades have a much smaller span to chord ratio (aspect ratio). This demands the hydrodynamic analysis to be three dimensional unlike in the hydrodynamic analysis of wing structures (Bertram, 2000). Due to this, propeller hydrodynamics analyses have evolved greatly since the invention of the first theories of its kind.

Some of the first propeller hydrodynamic analyses techniques were developed by Rankine and Froude (Carlton, 2007) based on axial momentum theory. These techniques are highly idealized in that they assume that the propeller is equivalent to a rotating disk (can be thought of as a propeller with infinite number of blades) that produces thrust. In addition, the original formulation also assumes that the propeller operates in an idealized flow with no friction loss and that the propeller does not produce a rotation in the slipstream, out of which the latter assumption was proven to be not necessary by R. E. Froude. These theories, although extensively used in the past, are not used in modern day propeller design due to their highly idealized nature. However, they are still being used to arrive at general conclusions of the propeller at preliminary stages of design.

Simultaneous to the momentum theory, blade element theories were developed, in which the propeller blade is divided into a finite number of strips and each strip is analysed as an aerofoil subject to an incident velocity. Although there are several shortcomings in the original formulation, this method laid the foundation for more complex three dimensional numerical and finite element techniques that were introduced much later. One such technique is the boundary Element Method (BEM). In this method, the propeller blades and the hub are divided into a finite number of small hyperboloidal quadrilateral panels having a constant doublet distribution (Carlton, 2007). The panels follow the profile of the blade taking the thickness variation into account. Thus, it can provide highly accurate results with good correlation with experimental results (Carlton, 2007). However the main draw backs of this method is the demand for the computational resources and mathematical complexity (Bertram, 2000).

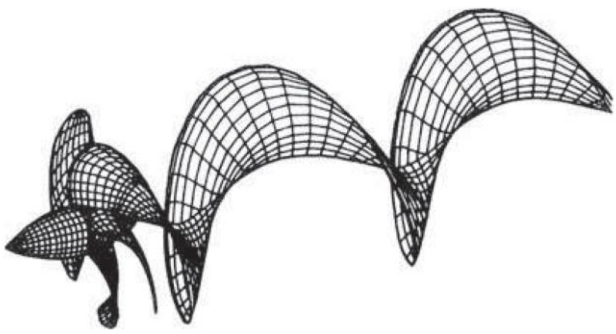

Figure 2-1: Panel distribution used for boundary element method on the complete propeller (Carlton, 2007)

Other major techniques of evaluating hydrodynamics are based on vortex theories implemented by Kutta and Joukowski (Carlton, 2007). These techniques directly correlate lift generation to vortex formation. The two most common vortex based propeller hydrodynamic analysis techniques are the lifting line method and the vortex lattice (lifting surface) method, of which the former is a one dimensional technique while the latter is a two dimensional technique. Lifting line technique (Lerbs, 1952) considers the lift generated by the vortex around the conjectural helical paths created by the rotating propeller (Figure 2-2(a)), whereas the lifting surfaces technique takes into account the two dimensional vortices on the blade surface (Carlton, 2007) (Figure 2-2.(b)). The major drawback of these techniques is that their accuracy is compromised near the hub (Bertram, 2000).

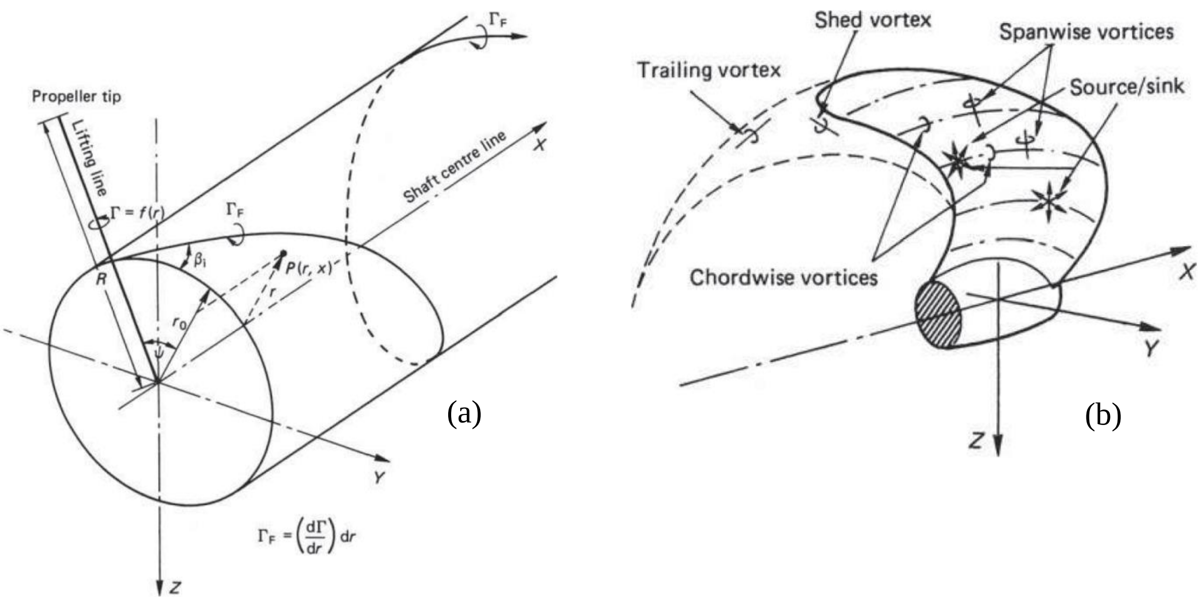

Figure 2-2: Vortex methods for evaluating propeller hydrodynamics (Carlton, 2007)

Although such numerical techniques exist, current propeller designs are predominantly based on Computational Fluid Dynamics (CFD). The complexity and accuracy of the models depend on the available computing power and time. Turbulence effects are modelled with turbulence models such as Reynolds Averaged Navier Stokes

(RANS), Large Eddy Simulations (LES), k – ω and Detached Eddy Simulations (DES), out of which RANS and k – ω models are more popular due to their high accuracy under a lesser computational time (Rhee and Joshi, 2003, Hsiao and Chahine, 2001).

Above mentioned techniques have been used for traditional propellers with a fixed geometry. In the case of flexible shape-adaptive propellers more advanced Fluid Structure Interaction (FSI) techniques are required. Fluid structure interaction is a fairly complex branch in structural and fluid mechanics; thus, most fluid-structure interaction problems depend on numerical methods and approximations. The basis of fluid-structure interaction is that the fluid domain is solved based on general Navier-Stokes based models and the structural domain is solved based on governing equations of the structure such that the normal stresses and velocities at the interface are balanced (Equations (2-1 and (2-2)) (Turek and Hron, 2006). Thus, the solution process is completely based on iterations over a large number of load steps and time steps.

$$\boldsymbol{\sigma}^f.\hat{\boldsymbol{n}} = \boldsymbol{\sigma}^s.\hat{\boldsymbol{n}} \quad \textbf{(2-1)}$$

$$\boldsymbol{v}^f = \boldsymbol{v}^s \quad \textbf{(2-2)}$$

where, $\boldsymbol{\sigma}$ is the stress tensor and $\boldsymbol{v}$ is the velocity vector, with f and s superscripts representing fluid domain and structural domain, respectively. Modern finite element packages are capable of handling fluid-structure coupled problems to give solutions with a good accuracy; however, such accurate solutions require extensive computing power and time. As a result, efforts have been taken to perform FSI using manual force coupling between specialized propeller hydrodynamic solvers and specialized structural solvers (Lee et al., 2005b, Lee and Lin, 2004).

2.3. Structural Design

This section discusses about the structural design of composite propellers. The section outlines the optimisation schemes demonstrating the various constraints that were imposed and the solution methodology. Prior to discussing about the optimisation schemes used for composite propellers, optimisation of composites in general to cater various requirements will be discussed.

2.3.1. Composite layup optimisation

Ability of layup arrangements to cater many different requirements is one of the major advantages of composites. This is achieved through numerical optimisation based on the requirements under specified constraints. Optimisation of composite layup has been in existence for many years to cater requirements such as best possible stiffness, strength, buckling resistance, lower cost, natural frequencies, etc. (Fang and Springer, 1993). Such optimisation has been achieved through various methods such as Heuristics, Non-Linear Programming (NLP), Genetic Algorithm (GA) Monte Carlo Method, Design Sensitivity Analysis, Simulated Annealing, Ant Colony Optimisation, etc. (Fang and Springer, 1993, Hammer et al., 1997, Kam and Snyman, 1991, Kameyama and Fukunaga, 2007, Awad et al., 2012). Each of these optimisation techniques has strengths and weaknesses, thus, must be used based on the nature of the task. For example, non-linear programming techniques are best with continuous variable problems, but have issues with convergence, integer variables, yield of spurious optima, etc. (Fang and Springer, 1993). On the other hand, Genetic Algorithms, for example, are predominantly used in situation where the optimisation variables (ply angles) are integers. Another importance of GA's is there capability to provide a "best" result, under computing constraints, rather than the single correct result of the problem. In addition, GA can be used for multi-objective optimisation. However, GA can be computationally expensive under large chromosomes and are also considered to be non-robust against uncontrolled parameters (Awad et al., 2012) (parameters that are not used in the optimisation process, but plays an important role in the physics of the structure). There are variations of GA that are continuous variable (Mühlenbein and Schlierkamp-Voosen, 1993), but if the problem is continuous variable, it is more desirable to use a non-linear programming method. Due to the attractive properties of GA, it is extensively used in the context of composite layup optimisation.

An example of using non-linear programming for ply optimisation is provided by Kam and Snyman (1991). The authors attempted to maximise the stiffness of a composite plate of a given thickness, made of a given composite material. Maximum stiffness was achieved by minimising the strain energy of the structure, as the two are equivalent (Tauchert and Adibhatla, 1984). Since the considered plate was under pure bending loading, strain energy was evaluated based on the curvature of the plate using the bending stiffness matrix [D].

A popular method in composite optimisation is the use of lamination parameters (Eqs. (2-3) - (2-7)). Composite lamination parameters are a simplified method of presenting the stiffness of a given layer independent of its fibre orientation. These parameters were first introduced by Tsai and Pagano (1968). They can be used to represent each layer as well as to form the stiffness matrix for the composite laminate.

$$U_1 = \frac{1}{8}(3Q_{11} + 3Q_{22} + 2Q_{12} + 4Q_{66}) \quad \textbf{(2-3)}$$

$$U_2 = \frac{1}{2}(Q_{11} - Q_{22}) \quad \textbf{(2-4)}$$

$$U_3 = \frac{1}{8}(Q_{11} + Q_{22} - 2Q_{12} - 4Q_{66}) \quad \textbf{(2-5)}$$

$$U_4 = \frac{1}{8}(Q_{11} + Q_{22} + 6Q_{12} - 4Q_{66}) \quad \textbf{(2-6)}$$

$$U_5 = \frac{1}{8}(Q_{11} + Q_{22} - 2Q_{12} + 4Q_{66}) = \frac{1}{2}(U_1 - U_4) \quad \textbf{(2-7)}$$

where, Q_{ij} are usual stiffness terms in the principal directions. Note that they avoid the use of non-linear sine and cosine terms that would usually occur if usual $Q_{x,y,s}$ were used. This makes the optimisation process much easier. Above parameters can then be used to express the complete stiffness matrix in a less complicated manner.

The use of lamination parameters is demonstrated by Kameyama and Fukunaga (Kameyama and Fukunaga, 2007). The authors attempted to minimize the weight of a high speed aircraft wing by minimising the thickness, while satisfying all required stiffness constraints based on lift generation, flutter, drag, composite strength, etc. Instead of using ply angles directly, lamination parameters and thickness of layer were used as optimisation variables and ply angles were calculated based on lamination parameters. A derivative of the Genetic Algorithm known as the Distributed Genetic Algorithm (DGA) was used to improve the solution speed through parallel processing. Examples of optimizing composite wing structures to meet various aerodynamic and design constraints are fairly common in open literature.

2.3.2. Ply optimisation and composite propeller design

As outlined in the previous section, shape adaptive propellers have the potential to be more efficient compared to rigid propellers. In order to achieve this, the composite propeller has to be designed such that its efficiency curve is tangential to the efficiency curves series of rigid propellers with different pitch angles (but with the same propeller geometry). As explained below, several research groups in the past attempted to design composite propellers primarily with the objective of fulfilling this requirement. This section discusses their efforts and how their methods can potentially be improved.

Based on the sources in open literature, probably the first time composite propellers were used to increase the efficiency using their flexibility is the carbon fibre aero propeller designed by Colclough and Russell (1972). These authors presented the design and testing process for a hovercraft propeller. Later, Atkinson and Glover (1988) demonstrated the deflection and resulting performance variations of NAB propellers, which are usually assumed to be rigid. They used lifting surfaces theory for the fluid domain and finite element method for the structural domain to analyse the performance of the models. This is one of the first Fluid-Structure Interaction attempts on propellers. However, the research was not extended into composite propellers.

Commercial production of composite propellers started in 1993 and completed the trials in 1995 by AIR Fertigung GmbH (Volante, 2005). Since then there have been several companies that produced composite propellers mainly targeting weight reduction. Some of these companies are Piranha™ Propellers, ProPulse™, QinetiQ™, etc. Shape adaptability is not a primary concern for the propeller built by these companies. Out of these QinetiQ built a composite propeller of 2.9 m diameter and is considered as the largest composite propeller to undergo sea trials (Marsh, 2004).

The only shape adaptive propellers that are currently in commercial production are propellers of the Contur-F Series, manufactured by AIR Fertigung GmbH (Marsh, 2004). Contur-F Series propellers are custom made up to 3.0 m (theoretically, but not manufactured thus far) in diameter according to the specifications of the customer. There seem to be a great interest in the market since they were first released in 2003. They are claimed to increase fuel efficiency by 15%, reduce the weight by about 25% -

35%, reduce noise by about 5 dB, reduce cavitation and improve smoothness of operation of the vessel (Marsh, 2004, Voith, 2004, Volante, 2005). Chen et al. (2006) experimentally tested these propellers and found that they have an efficiency gain of 5% compared to rigid propellers and cavitation can be delayed by 15% - 50%. In addition, United States Defence was interested in using these propellers in their submarines and initiated a project for testing the effectiveness of shape adaptive Contur-F Propellers (Defence, 2004). But the results of these experiments are not available in open literature. As this is commercial production, the design process and optimisation techniques are not available in open literature. Thus, there is a clear need of investigation into composite propellers and it may even enable to improve the designs beyond current commercially available Contur propellers.

The information available for the design and optimization of composite propellers is fairly limited. The primary goal of almost all of the researches that was found is improving the efficiency of the propeller in order to achieve an efficiency curve for the composite propeller that is as close as possible to a hypothetical ideal efficiency curve shown in Figure 2-3(b) (dashed line).

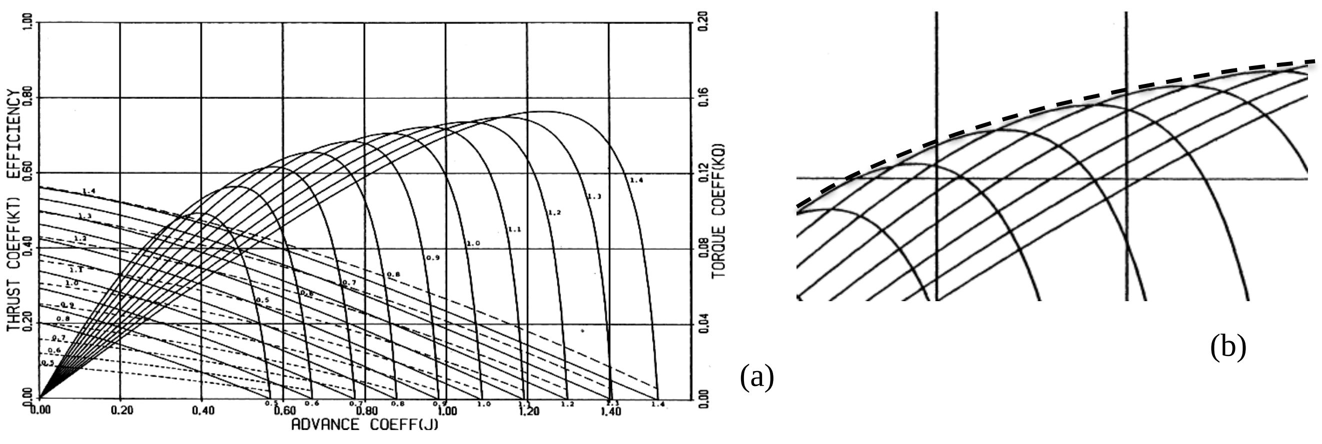

Figure 2-3: (a) Open water curves of a Wageningen B-series propeller; (b) ideal efficiency curve for a perfectly pitch varying propeller (Kuiper, 1992)

Lin and Lee (Lee and Lin, 2004, Lin et al., 2009, Lin and Lee, 2004) performed research with a similar goal (but not directly focussing at the efficiency) and attempted to validate their results using experiments. Young et al. (Liu and Young, 2009, Motley et al., 2009, Motley and Young, 2011b, Motley and Young, 2011a, Young, 2008, Young, 2007a, Young, 2010, Young et al., 2010) undertook research in this field investigating many aspects of design of composite propellers in terms of reliability, bend-twist coupling, fluid-structure interaction, experimentation, etc. A research group at University of New South Wales (Mulcahy et al., 2008, Mulcahy et al., 2011) performed their research focussed at a basic hydrofoil and attempted to optimise its performance through finite element analysis. The following discussion explains the achievements of the past researchers.

The main focus of Lin and Lee research group was minimising the variation of torque coefficient of the propeller (K_Q) (Lee and Lin, 2004) (Eq. 1-3). Their concept was to minimize the variation of torque of the engine at off-design conditions. It was considered that K_Q at optimum advance coefficient (non-dimensionalised advance velocity) must be the same for both rigid propeller and composite propeller. Thus, based on this constraint, the value of K_Q throughout the advance coefficient domain must remain close to the K_Q at optimum advance coefficient. The base alloy (fixed pitch) propeller was taken to be the DTNSRDC 4498 propeller (Nelka, 1974). The propeller that was considered (the initial rigid propeller) had its maximum efficiency at an advance coefficient (J) of 0.889, and at that J, K_Q of the original rigid propeller was 0.05204. As the off-design point $J = 0.6$ was chosen and it was attempted to minimize the difference between $K_Q|_{J=0.6}$ and $K_Q|_{J=0.889}$. In order to achieve this, the following objective function (Eq. (2-8)) was maximized with weightings $W_1 = 1$ and $W_2 = 2$ and tolerance level $C_0 = 0.1$ (Lee and Lin, 2004). Note that ply angles (fibre angles) being the variables of optimisation.

$$f = C_0 - \left[W_1\left(K_Q|_{J=0.6} - K_Q|_{J=0.889}\right) + W_2\left|K_Q|_{J=0.889} - 0.05204\right|\right] \quad \textbf{(2-8)}$$

The optimisation task was carried out using the genetic algorithm, with fibre angles constrained to only four possibilities (0^0, $+45^0$, -45^0 and 90^0), which the researchers state to be due to manufacturing constraints. From the optimisation process they found that the optimal layup is $[45_2/90_2/45_8/0_{10}/45_2]_s$.

It was witnessed that the propeller that was produced in this manner had a high pitch angle and required a large torque to drive at lower advance coefficients. To overcome this, the concept of pre-deformation was introduced. Pre-deformation is where the blade is negatively pre-deformed such that under the fluid loading it will achieve the required optimum shape (Figure 2-4).

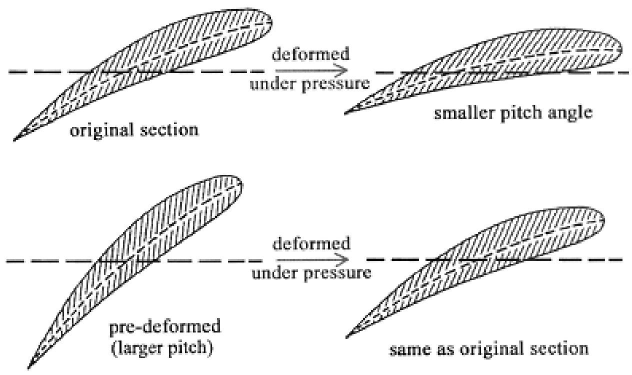

Figure 2-4: Pre-deformation of the blade (Lee and Lin, 2004)

The optimised layup technique was verified using finite element simulations performed using two different solvers for the structural domain and fluid domain. The structural domain was investigated using ABAQUS™ and the fluid loadings were evaluated using a solver developed by Massachusetts's Institute of Technology that dates back over 40 years. As it is coupling between two different solvers, it was performed semi-manually and iterations were performed until both deformation of the structure and load from the fluid domain do not change (converged) at the given time-step.

In addition to demonstrating the design and optimisation procedure, experiments were performed on manufactured carbon fibre propellers (Lin et al., 2009). There are many important aspects on manufacturing carbon fibre propellers and experimental measurement techniques that can be potentially used in this current thesis. However, the authors did not experimentally compare their composite propeller design to the rigid counterpart. The results were highly mixed with some experiments showing a good correlation between predicted results, while some experiments showing deviations of the order of 10 (1000%). Thus, there are clearly many improvements to be made in their design methodology.

Young et al. (Motley et al., 2009, Motley and Young, 2011b, Motley and Young, 2011a, Pluciński et al., 2007, Young, 2007a, Young, 2007b, Young, 2008, Young, 2010, Young et al., 2010) investigated the composite propeller in many different fronts. They introduced a more practical probabilistic approach in determining the operational speeds of the propeller (Motley and Young, 2011b). Furthermore, in-depth Fluid Structure Interaction analysis were performed using 3-dimensional boundary element methods (Young, 2008). The main concern in the scheme of optimisation was increasing the twist (φ) of the propeller (Equation (2-9)) under the fluid loadings. Increasing the twist inherently increases the flexibility of the blade, reducing its stiffness. Thus, it was attempted to maintain the stiffness above a minimum stiffness Equation (2-10) which later was defined (seemingly arbitrarily) as $0.5k_{max}$ (Liu and Young, 2009, Pluciński et al., 2007), where k_{max} is the maximum bending stiffness that can be achieved for the chosen composite. It is perhaps more sensible to define the term α based on the maximum allowable rake of the propeller and maximum permissible strain of the material. Additionally, the optimisation scheme ensured that the number of layers that has the same ply orientation does not exceed the critical number of plies of the same orientation in order to avoid delamination (2-11) (Pluciński et al., 2007, Liu and Young, 2009). These considerations are mathematically represented by Equations (2-9-(2-11) (Liu and Young, 2009, Pluciński et al., 2007).

$$\underset{\boldsymbol{\theta}}{max}\ \varphi(\boldsymbol{\theta})\ ;\ where\ \theta_i = \{90\ ,75\ ,60\ ,45\ ,30\ ,15\ ,0,-15\} \tag{2-9}$$

$$k(\boldsymbol{\theta}) \geq \alpha k_{max}\ ;\ \ 0 < \alpha < 1 \tag{2-10}$$

$$m(\boldsymbol{\theta}) \leq m_{max} \tag{2-11}$$

The authors implemented penalty functions based on the constraints (Equations (2-10 and (2-11) and modified the objective function to be,

$$\underset{\boldsymbol{\theta}}{max}\left\{\varphi(\boldsymbol{\theta})\lambda_1^{[m(\boldsymbol{\theta})-m_{max}]}\left[\frac{k(\theta)}{k_{max}}\right]^{\lambda_2}\right\} \tag{2-12}$$

Here, λ_1 and λ_2 are the severity of the penalty functions and were taken as 1 and 0, respectively, if the constraints are not violated. If in case the constraints were violated, $\lambda_1 < 1$ and $\lambda_2 > 0$.

The underlying argument of increasing the twist was that, increasing the twist (say for a given fixed loading) inherently increases the flexibility. Notably, a propeller achieves its maximum efficiency when the flow angle is equal to the pitch angle. Thus by increasing the flexibility, the propeller will flex by itself until the twist is aligned with the flow angle. This theory was shown to produce better results compared to rigid propellers at lower advance coefficients. However, when advanced speed was increased, as the propeller has to rotate faster to achieve that high advance speed, the propeller was observed to lose its efficiency. This is due to high resistance to rotation at high rotational speeds caused the propeller to reduce pitch, resulting a lower thrust production (Motley and Young, 2011b). Authors further state that in an ideal case this will not be an issue as the reduction of pitch will reduce the rotational resistance of the propeller allowing the propeller to rotate faster to achieve the same thrust. In addition, Young and Motley (Motley et al., 2012) also investigated to reduce the lifetime fuel consumption of the vessel taking into account a probabilistic approach to determine critical speeds the propeller should be designed for (Motley et al., 2012).

Furthermore, Liu and Young (2009) attempted to develop an optimisation scheme based on bend-twist coupling. The concepts that were used are based on general Classical Laminate Plate Theory (CLPT). The design process was of two steps, with step one attempting to determine the material properties and layup configurations and step two attempting to determine the unloaded shape of the propeller. Pluciński et al. (2007) also presented an optimisation scheme similar to this. They enforced additional constraints on the optimisation problem such as, minimum bending stiffness based on the maximum rake and maximum number of layers of the same fibre orientation in order to prevent delamination. Similar to Lee et al. (2005b) the problem was solved using a genetic algorithm.

Mulcahy et al. (Mulcahy et al., 2010b, Mulcahy et al., 2010a, Mulcahy et al., 2008, Mulcahy et al., 2011) investigated the problem taking a simplistic approach by focussing on a simple hydrofoil first. The optimisation method that was employed was fairly different to the optimisation schemes used by Young et al. (Pluciński et al., 2007) and Lin et al. (Lin and Lee, 2004). Mulcahy et al. (2008) based their optimisation on the unloaded shape. The idea was that the propeller should have the same unloaded (as it the same propeller) shape when the fluid loading at each advance coefficient is removed. They achieved this by defining a mesh for the propeller/hydrofoil blade and minimising the distance between nodes of each unloaded shape. Thus, this method was based on performing many finite element simulations for different advance coefficients of the propeller and applying those loads in a negative sense to find the unloaded shape, based on that advance coefficient. A similar approach is demonstrated by Chen et al (Chen et al., 2006) (Figure 2-5). However, experiments were not conducted and finite element simulations were performed only for laminar flow assuming the hydrofoil to be a 2-dimensional shell layer with no real thickness.

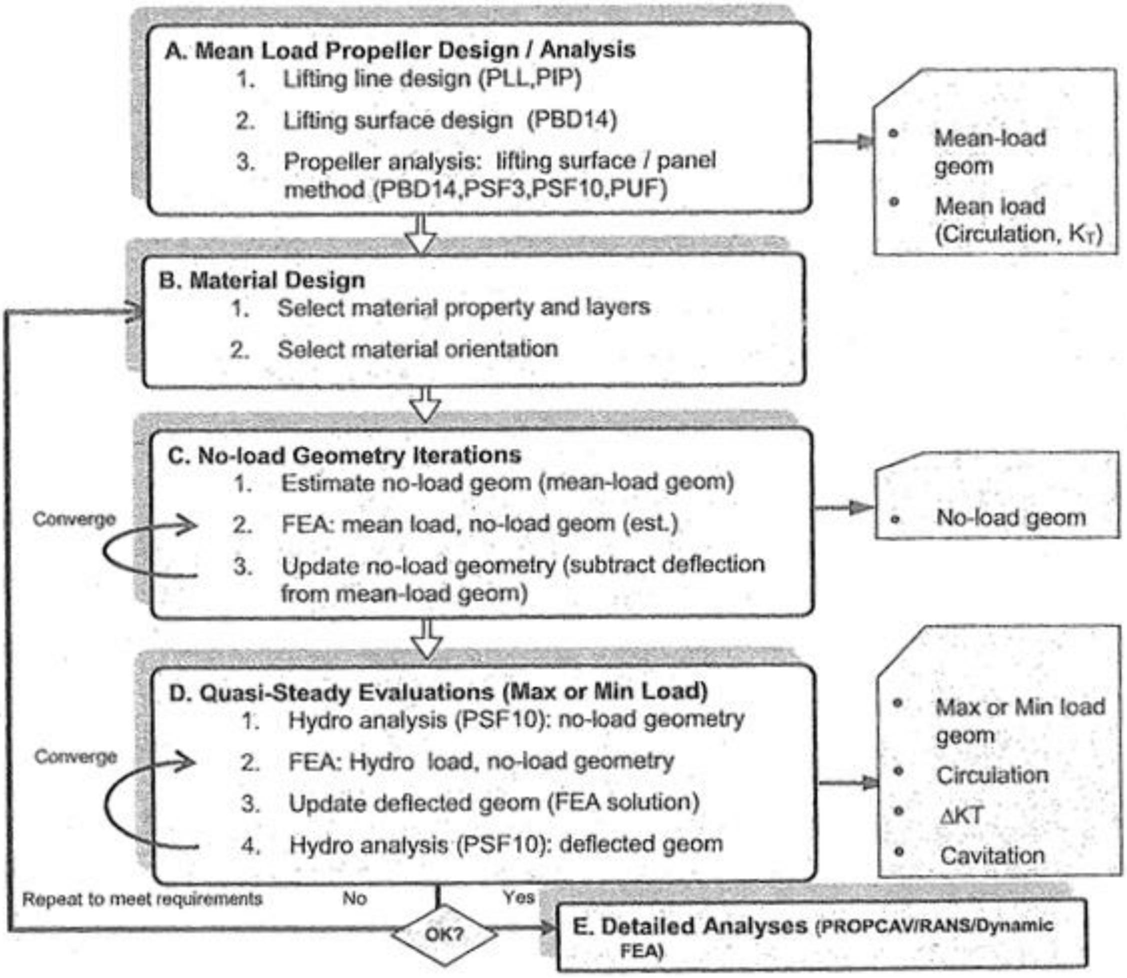

Figure 2-5: Design process demonstrated by Chen et al. (Chen et al., 2006), similar to Mulcahy et al. (Mulcahy et al., 2011)

Furthermore, Das and Kapuria (2016) performed a comprehensive CFD and FSI study on full scale composite propellers with a diameter of 4.2m. The study investigated the efficiency of carbon fibre propellers including the layups suggested by Mulcahy et al. (2011) and Motley et al. (2009). In addition, Das and Kapuria (2016) investigated propellers made out of glass-epoxy composite, graphite-epoxy composite and high tension carbon epoxy composite. The authors present results for both non-twisted and pre-twisted propeller blades. Authors report the observation of slight reduction in efficiency due to the large deformations that were observed in the blades at high rotational speeds, similar to the observations reported by Motley and Young (2011b).

In addition to the above mentioned major research specifically in the area of developing a shape-adaptive propeller with improved efficiency, there are further studies conducted with different goals. For example, companies such as QinetiQ and ProPulse have manufactured propellers optimised to give the best strength at the lowest possible mass, Gowing et al. (1998) attempted to use bend-twist coupled composites specifically to reduce cavitation in propellers. The authors used an elliptical hydrofoil with bend-twist coupling was used to reduce the pressure gradient between the leading edge and trailing edge. This resulted in a considerable reduction in cavitation.

2.4. Experiments

This section discusses about the experimentation techniques used by various researchers in performing experiments on marine propellers. For simplicity the section will be divided into two subsections, measurement techniques and experimental results in the context of flexible composite propellers. The measurement technique section will be further subdivided into two parts to outline measurements in the fluid domain and measurements in the structural domain.

2.4.1. Measurement Techniques

2.4.1.1. Hydrodynamic Measurements

Two of the most common and important hydrodynamic measurements in the context of marine propellers are flow velocity and pressure distribution at various locations of the fluid domain. Flow velocity is predominantly measured using Hotwire Anemometry, Laser Doppler Anemometry (LDA), Particle Tracking Velocimetry (PTV) and Particle Imaging Velocimetry (PIV) (Lee et al., 2005a, Lee et al., 2004, Maas et al., 1993). A comparison between these techniques is given in Table 2-1.

	Hotwire	**LDA**	**PIV**	**PTV**
Spatial Resolution	Low	Low	Very high	High
Temporal Resolution	High	Very high	Very Low	Low
Velocity Range	High	Very high	Very high	Low
Observation volume dimensions	-	-	2	2 or 3
Velocity field dimensions	1 – 3	1 – 3	2	2 or 3
Result	Vectors	Vectors	Vectors	Trajectories

Table 2-1: Comparison between flow velocity measurement techniques (Maas et al., 1993)

PIV and PTV have been extremely popular in the context of propeller hydrodynamic experiments due to their high spatial resolution non-intrusiveness. PIV takes images of a fixed volume and resolves the particle location in each image (frame) to evaluate the velocity vectors of each particle using consecutive frames (analogous with Eulerian flow field view), whereas in PTV each individual particle is tracked to find its path and velocity variations over time (analogous to Lagrangian flow field view) (Kim and Lee, 2002). Lee et al. (Lee et al., 2005a, Kim and Lee, 2002) developed a hybrid technique that combines the best of both PIV and PTV techniques. To achieve this, the authors used a high resolution Charge-Coupled Device (CCD) camera with a Nd:YAG laser synchronized with the blade locations of a 54 mm KP505 propeller to study the flow patterns in the wake. Velocity measurements were taken at advance ratios of 0.59, 0.72 and 0.88. The hybrid method is claimed to have a better spatial resolution, measurement accuracy and less computing time compared to the regular PTV and PIV methods.

Although basic PIV based methods can measure velocities in a two dimensional plane, PIV methods that utilize two or three CCD cameras have the ability to capture velocity patterns in all three directions. The schematic of the dual camera PTV hybrid method used by Lee et al. (Lee et al., 2004) is given in Figure 2-6. This method can inherently measure velocity components in two dimensions (out of plane measurement is not possible optically with just two cameras). However, strain rate continuity condition of the fluid states that, $\frac{\partial w}{\partial z} = -\frac{\partial u}{\partial x} - \frac{\partial v}{\partial y}$, by which, the out of plane strain component (w) of the fluid flow can be evaluated. If a triple camera system is used, all three components are possible to be measured optically. The dual camera setup was used to measure the three dimensional flow velocities in the wake of the propeller for the same propeller (KP505) explained in Lee et al. (Lee et al., 2004).

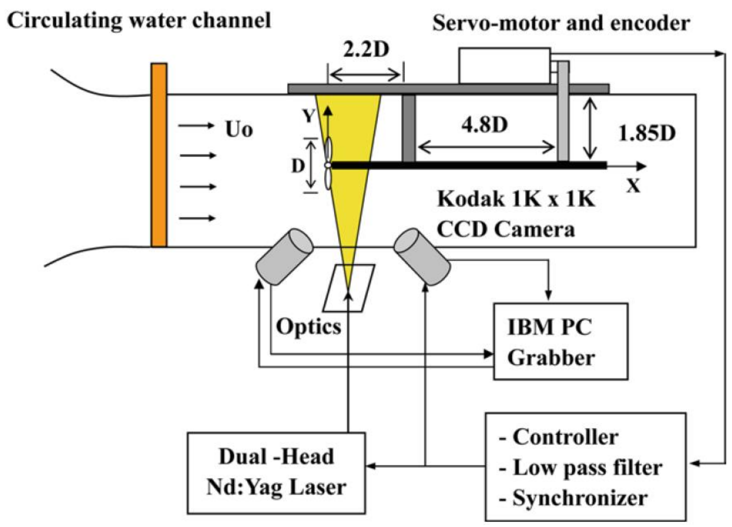

Figure 2-6: Experimental setup of the dual camera PIV+PTV hybrid flow measurements (Lee et al., 2004)

Pressure measurement is an important but challenging measurement in propeller experiments. Pressure measurements are usually achieved by high sensitivity pressure transducers (Duttweiler and Brennen, 1999, Huang et al., 1976). However, pressure transducers have difficulties is mapping the pressure in the vicinity of the propeller blades. Thus, if pressure measurements are required extremely close to the propeller blades, such as in the case of investigation of cavitation, Jessup (Jessup, 1986) used a single pressure gauge placed at a certain radial position with a series of channels embedded into the propeller blade model. The channels were open (through orifices) to the flow at various chordwise positions and were connected to the pressure gauge at that radial location via pressure taps. Pressure taps were opened and closed to obtain pressure readings at various chordwise locations. This technique, although complicated in terms of manufacturing, has produced extremely accurate results that correlate well with BEM analysis and CFD analysis (Jessup, 1986). A rather different technique has been used by Felli et al. (Felli et al., 2004), in which hydrophones were used to record fluctuations in noise around the propeller that were decoded to obtain pressure fluctuations. However, such a method is intrusive; thus, special care must be taken in choosing the size and the shape of hydrophones. Note further that, in the regions where flow is not highly turbulent, it is possible to use the simple Bernoulli's Theorem to evaluate the static pressure. This is done by first measuring the velocity at the interested location using a velocity measurement technique, such PIV or PTV, and using Bernoulli's Theorem to evaluate pressure.

2.4.1.2. Structural Measurements

In the context of alloy propellers there are no significant structural measurements to be made, as long as the flow speed and the speed of rotation of the propeller are not large enough to cause large strains. However, for flexible composite propellers, structural measurements are of utmost importance. The main parameters of importance are structural deformations and strains. There are many experimental techniques by which deformations can be measured accurately. Mulcahy et al. (2008) used Linear Variable Differential Transformers (LVDT) to measure displacement of a composite plate and strain gauges for the surface strains. Use of Fibre Bragg Gratings (FBG) has also become popular in the past two decades. In FBGs, when the original fibre length is expanded or contracted, the wavelength of the resulting output signal also increases or reduces accordingly. FBGs are popular in composite strain measurements as fibres can be embedded into the laminate structure during the manufacturing process.

Deviating from these classical methods of displacement measurement techniques, Lin et al. (Lin et al., 2009) employed a photogrammetry technique to evaluate deformation of the tested composite propeller. They first marked the hub and captured images of the propeller from various angles at every 0.5^0. When the propeller was in operation (during rotation), images were captured and superimposed with the stationary images making sure that the marking at the hub are perfectly overlapped each other. The superimposed image (Figure 2-7) was then used to determine the deflection of the propeller during operation.

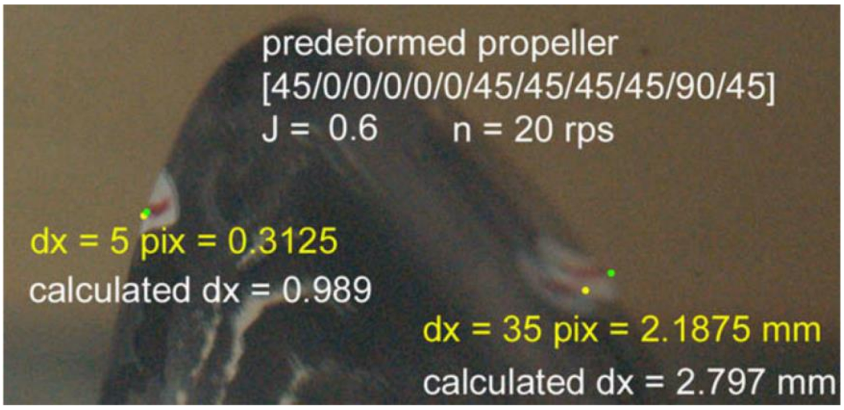

Figure 2-7: Superimposed image of the rotating propeller to show the deflection (Lin et al., 2009)

2.4.2. Experimental Results of Shape Adaptive Propellers

Chen et al. (2006) conducted comprehensive experiments on the only commercial shape-adaptive propeller series, Contur-F Series. Experiments were conducted in a 36 inch cavitation tunnel facility. In these experiments, three propellers were tested, one rigid and two shape-adaptive. Velocity measurements were taken using Laser Doppler Vibrometry. Blade deflections were measured using high speed video cameras. Altogether, thrust, torque, cavitation inception and blade deflection were measured during experiments. These measurements were then used to evaluate efficiency, torque coefficient, thrust coefficient and cavitation number.

Propellers were manufactured using CFRP with a design methodology similar to that of Mulcahy et al. (Mulcahy et al., 2008, Mulcahy et al., 2011). In essence, the no-load geometry was calculated by evaluating the fluid loads at several advance ratios and applying the strains in a negative sense. Contur Propellers P5474 and P5487R were used as the reference rigid propellers and the flexible propellers P5475 and P5487 are the flexible propellers manufactured, respectively.

The experiments revealed that the shape-adaptive propellers are indeed superior to fixed pitch propellers. It was found that the two flexible propellers gave 3% and 5% extra efficiencies compared to their rigid counterpart. In addition, cavitation performance was enhanced by 15% - 50%. Chen et al. (2006) also notes that not every rigid propeller can be turned into a flexible shape adaptive propeller. Propellers with a large skew and a smaller thickness are the best to reap the benefits of shape-adaptivity. It was witnessed that thrust coefficient and torque coefficient can provide a good indication as to how much the propeller blade is deforming, higher the deformation, higher the change in Thrust and Torque Coefficients. Thus, the design objective function of Lee et al. (Lee and Lin, 2004, Lin et al., 2009), which was based on maintaining the Torque Coefficient constant, is disputed.

An experimental study has also been done by Lin et al. (2009) on flexible composite propellers. The authors performed experimental analysis on two optimally laid up propellers, one with pre-deformation while the other without pre-deformation. The cavitation tunnel had size and measurement limitations; thus, torque and thrust as high speeds could not be measured. The propellers that were tested were fairly small with a diameter of 305 mm. Similar to the experiments performed by Chen et al. (2006), the propellers were manufactured using CFRP using a similar mould technique. The shape of the composite propellers was based on fixed pitch alloy propeller DTNSRDC 4498. One of the major drawbacks of the experimental technique is that the authors have not made a comparison against a fixed pitch propeller.

The main parameters of measurement of these experiments are the deflections of the propellers under the operating conditions, thrusts and torques under low rotational frequencies, pressure difference at free stream and inlet (inlet velocity is resolved from this using Bernoulli’s theorem. The deflection measurement technique of the propeller is the photogrammetry method explained earlier in the discussion (Figure 2-7). Based on these measurements the authors have evaluated all the major non-dimensional parameters. An example of the graphs is given in Figure 2-8.

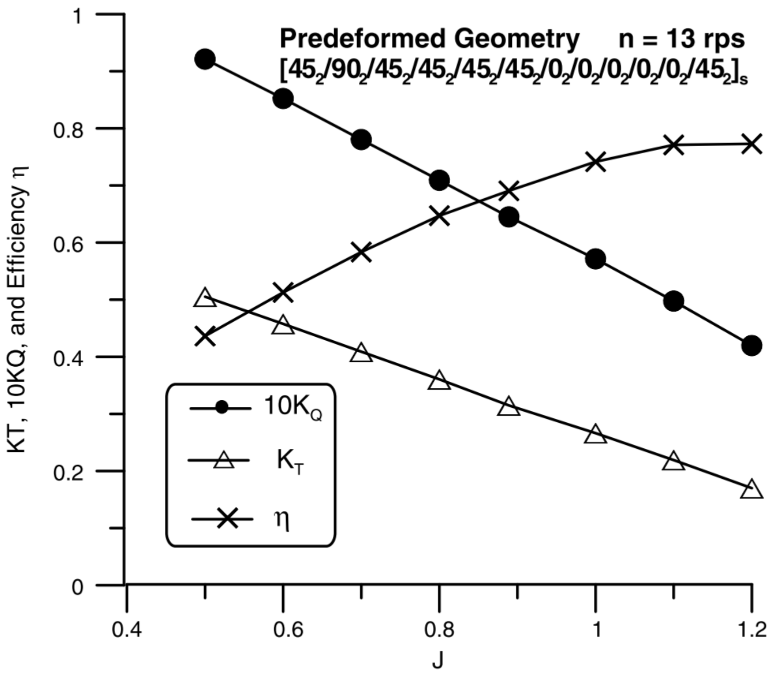

Figure 2-8: Experimentally measured K_T, K_Q and η (Lin et al., 2009)

Experimental measurements of this study do not match very well with predicted results. Some deflections that were measured experimentally are less than 1/10th of what was experimentally predicted. In addition, these results cannot conclusively prove the existence of a higher efficiency due to the use of composites, as a fixed pitch alloy propeller has not been used as the control experiment. Therefore, although there is much valuable knowledge that can be learned from their experimental procedure, there are many aspects that can be improved upon.

2.5. Manufacturing Techniques

Specific manufacturing processes and techniques used by composite marine propellers are fairly limited in open literature. The methodology adapted by the commercial producer AIR Fertigung is outlined by Chen et al. (2006). The process has four basic steps. First, the mould is created based on accurately cut (using Numerically Controlled Cutting) metal blades. Next, the carbon fibre layers are cut using NC cutting to the required shape (Figure 2-9(a)). Thirdly, the carbon fibre layers are laid in the mould with the resin and pressed and heated up inside the mould (Figure 2-9(b)). After the press is completed, the blade is removed from the mould and excess material is cut off from the edges and a thin epoxy layer is applied to create hydro-dynamically smooth surfaces and edges on the blade (Figure 2-9(c)).

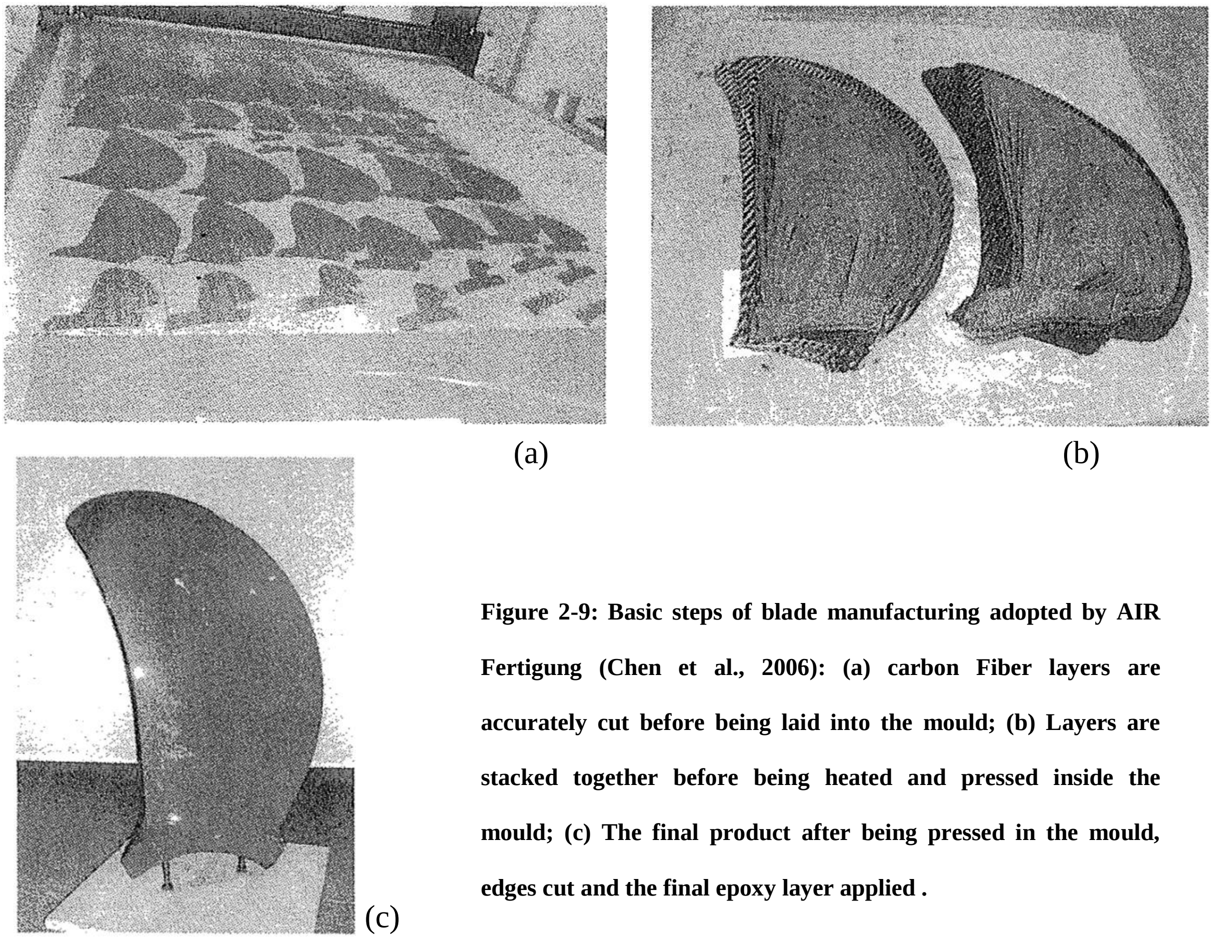

(a) (b) (c)

Figure 2-9: Basic steps of blade manufacturing adopted by AIR Fertigung (Chen et al., 2006): (a) carbon Fiber layers are accurately cut before being laid into the mould; (b) Layers are stacked together before being heated and pressed inside the mould; (c) The final product after being pressed in the mould, edges cut and the final epoxy layer applied .

Finally, the metal hub is manufactured using NAB alloy with slots to accommodate the composite blades. Afterwards, the blades are inserted into the hub slots to complete the propeller.

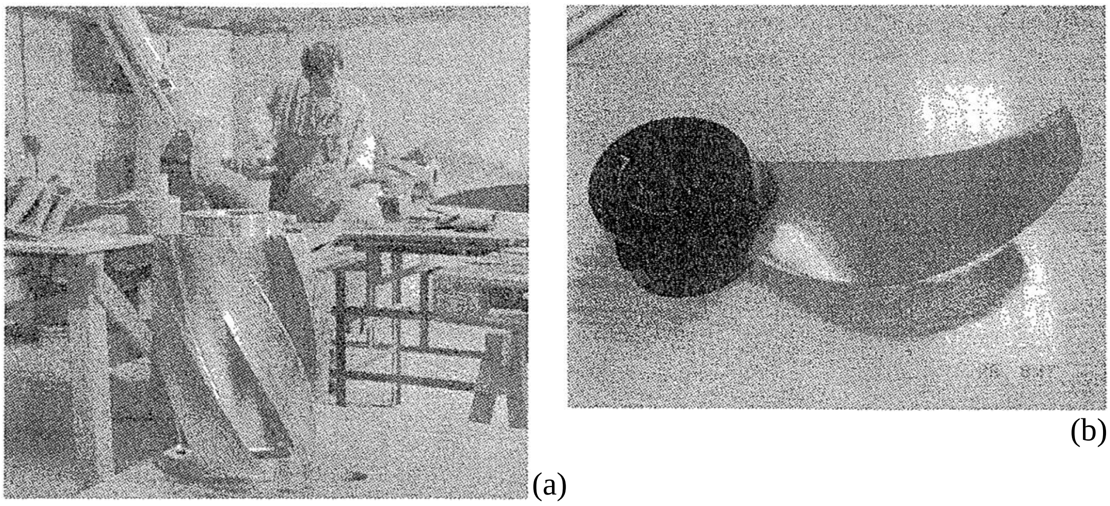

(a) (b)

Figure 2-10: Final steps of Contur Propeller manufacture: (a) Hub manufacture; (b) Completed propeller blade

Composite propellers manufactured by Lin et al. (Lin et al., 2009) were manufactured using a similar process. However, since the authors tested a highly scaled-down propeller in the cavitation tunnel facility, it can be thought that the manufacturing process was less challenging compared to Chen et al. Chen et al. (2006).

The chosen composite for the manufacturing process was pre-impregnated Toho HTA1200 carbon fiber / ACD8801 epoxy layers. The mould was constructed using aluminium alloy (Figure 2-11). Prepreg CFRP layers were accurately cut and laid on the bottom half of the mould. Afterwards, the top half was placed on top and the mould was secured. The assembly was then heated to 130^{o}C at 30 psi pressure for 40 minutes. Once the moulding process was completed, the blade was taken out of the mould and the edges were smoothed using an epoxy clay (Figure 2-11(b)). Finally the hub was manufactured using stainless steel and the blades were fitted into the slots of the hub to complete the propeller (Figure 2-11(c)).

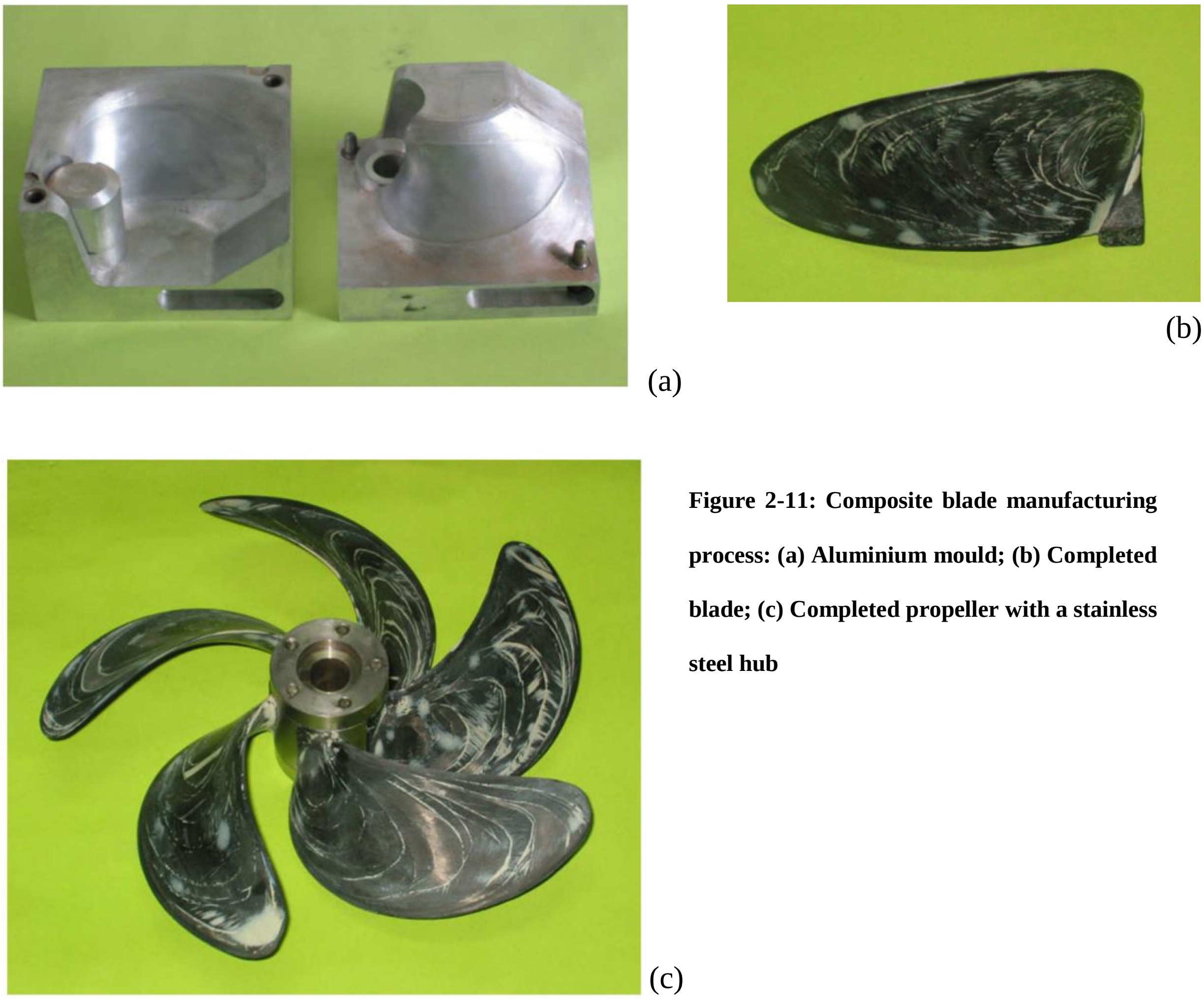

(a) (b) (c)

Figure 2-11: Composite blade manufacturing process: (a) Aluminium mould; (b) Completed blade; (c) Completed propeller with a stainless steel hub

In addition, Wozniak Wozniak (2005) constructed a carbon fibre propeller using a method almost identical to the methods outlines above. Markaide (2005) constructed composite marine propellers for fishing boats with the main focus of comparing manufacturing using prepreg layers in a mould and manufacturing using Resin Transfer Moulding (RTM) for practical commercial composite propellers. The author constructed two CFRP composite propellers, one using prepreg composite layers (similar to Lin et al. (2009)) and the other using a RTM technique (apart from this major difference, the manufacturing process used by Lin et al. Lin et al. (2009) and Markaide (2005) are identical). The author concludes that the RTM technique has the following advantages:

1. Reduced raw-material and labour costs,
2. Uniform mechanical properties and
3. Excellent surface finish for the coating
4. High manufacturing tolerance

Whereas, the issue in using prepreg composites is their typically high material cost. This information can potentially be helpful during manufacturing stages of the project.

2.6. Numerical Methods

In order to construct a robust optimisation scheme it is necessary to understand the mathematical techniques that are capable of analysing structures similar to propeller blades. Here, analytical schemes will not be considered viable as the analytical solution for even a simple clamped plate-like structure with bend-twist coupling is mathematically complex (Tian et al., 2011); hence, deriving such expressions for a complex shape such as propeller blades can be impractical. Furthermore, such an approach may negatively impact the scope of the optimisation scheme to a few selected propeller blade shapes that can be mathematically described.

Therefore, robust finite element schemes are proposed to be adopted that are applicable to any general propeller shape with just the change in mesh for each blade that is being analysed. In past research related to propeller optimisation, a number of different commercial finite element codes were used to evaluate the response of the propeller blade under a given fluid load for a certain composite layup. In order to solve the structural domain Motley and Young (2011b) used Abaqus™ coupled with a BEM solver for the fluid domain, while Lee and Lin (2004) used the NASTRAN^{TM} coupled with PSF2 solver to solve the fluid domain. Furthermore, Mulcahy et al. (2011) used SYSPLY^{TM} code to solve the structural domain. One drawback in using different solvers coupled with each other is the solution time when two different solvers communicate with each other and invoke each other for each iteration step. Therefore, developing a fast and robust in-house finite element solver was considered as the preferred approach.

The first step was to select a structural theory for the finite element formulation. Various structural theories proposed for evaluating the characteristics of composite laminates under different loading situations were reviewed by Noor and Burton (1989), (Mallikarjuna and Kant, 1993), (Kant and Swaminathan, 2000) and by (Khandan et al., 2012). These reviews discuss about various structural formulations applicable to similar structures, ranging from the simplest Kirchhoff-Love formulation for thin plates to more complex higher order formulations with up to 12 degrees of freedom per node. The higher degree formulations are particularly suited for thick plate structures. However, the drawback is the solution time of such high order formulations. The reviews suggest that for general purpose formulations for moderately thick structures with small deformations relative to their size the first order shear deformation theory, also known as the Mindlin-Reissner plate theory, is adequate to provide accurate solutions given that the thickness to length (for a plate this is the dimension in the bending direction) of the blade is kept below 0.2, while the ratio between longitudinal and transverse moduli of the composite laminate (E_L/E_T) is kept below 15, the maximum error that was witnessed in the result was 9.87%. The first order shear deformation theory can be used to give much more accurate results for even thick plates by adjusting the shear correction factors of the formulation (Noor and Burton, 1989). However, the applications discussed in this thesis and the optimisation scheme is developed for propeller blades and hydrofoils do not exceed the ratios specified earlier. Thus, the first-order shear deformation theory was deemed adequate for the application. In fact, most general purpose shell elements in commercial finite element codes (including shell elements in ANSYS and Abaqus) are based on the first order shear deformation theory.

Once the structural theory was evaluated and established, a Finite Element procedure was investigated. Finite element techniques that are applicable for shell element formulation have been formulated and developed for several decades. There are numerous publications in existence that discuss about conventional FEM (Zienkiewicz et al., 1977, Hughes, 2012, Strang and Fix, 1973). However, the focus of this investigation is to identify more recent developments in FE techniques and evaluate their applicability to composite blades and hydrofoils keeping in mind the accuracy and speed of the implementation. There have been a number of developments in mesh-free finite element methods and iso-geometric finite element methods.

Mesh free methods have recently become popular due to their primary benefit over traditional FEM, which is not being dependent on the quality of the mesh and being able to provide accurate results when the original mesh is highly distorted or when the mesh becomes highly distorted during deformation (Liu et al., 2007, Liu, 2009). In mesh free methods, integration is performed over the points known as field-nodes, which in some cases lead to numerical instabilities and inaccuracies due to disappearing derivatives of shape functions (Chen et al., 2001). As a result Chen et al. (2001) introduced strain smoothing techniques to the Galerkin weak form. However, this required high order shape-functions and field variable approximations which led to a higher computational cost. In order to alleviate this problem, Liu et al. (2007) introduced a technique where conventional FEM is combined with strain smoothing technique formulated for meshless methods. This FE method is known as the Smoothed Finite Element Method (SFEM).

Another important consideration in Finite Element methods is the shear locking phenomenon that may be present in the finite element formulation. Locking is a numerical phenomenon where the structure becomes overly stiff when the thickness is reduced. A set of methods have emerged to address the shear locking in the FEM. By incorporating the strain smoothing technique into the finite element method (FEM), Liu et al. (2007) have formulated a series of smoothed finite element methods (SFEM), named as cell-based SFEM (CS-FEM) (Nguyen-Xuan et al., 2008, Bordas and Natarajan, 2010) node-based SFEM (Liu et al., 2009b), edge-based SFEM (Liu et al., 2009a), face-based SFEM (Nguyen-Thoi et al., 2009) and α-FEM (Liu et al., 2008). And recently, edge based imbricate finite element method (EI-FEM) was proposed in (Cazes and Meschke, 2012) that shares common features with the ES-FEM. As the SFEM can be recast within a Hellinger-Reissner variational principle, suitable choices of the assumed strain/gradient space provides stable solutions. Depending on the number and geometry of the sub-cells used, a spectrum of methods exhibiting a spectrum of properties is obtained. Further details can be found in other literature Nguyen-Xuan et al. (2008) and references therein.

Nguyen-Thanh et al. (2008) employed CS-FEM for Mindlin-Reissner plates. The curvature at each point is obtained by a non-local approximation via a smoothing function. From the numerical studies presented, it was concluded that the CS-FEM technique is robust, computationally inexpensive, free of locking and importantly insensitive to mesh distortions. The SFEM was extended to various problems such as shells (Nguyen-Thanh et al., 2008), heat transfer (Wu et al., 2010), fracture mechanics (Nguyen-Xuan et al., 2013) and structural acoustics (He et al., 2011) among others. Furthermore, Bordas et al. (2011) has combined CS-FEM with the extended FEM to address problems involving discontinuities.

Another contemporary finite element method is iso-geometric finite element method presented by Hughes et al. (2005). A major drawback of conventional finite element meshing and basis functions is their inability to represent the geometry in its exact form which the original CAD model built. Conventional finite element meshes are sensitive to the mesh density and the order of the mesh when representing a geometry. Iso-geometric finite element analysis alleviates this problem by using the exact basis functions that were used to construct the geometry to construct the mesh. This is seen as a major advantage when analysing complex geometries such as propeller blades. One of the most popular implementations of iso-geometric analysis is based on NURBS basis functions. The primary reason for this is due to most CAD software use NURBS basis functions to construct edges, surfaces and solids in the CAD environment. Hughes et al. (2005) and Cottrell et al. (2009) presented a methodology by which these basis functions can be used to construct the mesh for the finite element discretisation, with further mesh refinements if necessary. Several NURBS meshes generated by various other researchers are given in Figure 2-12

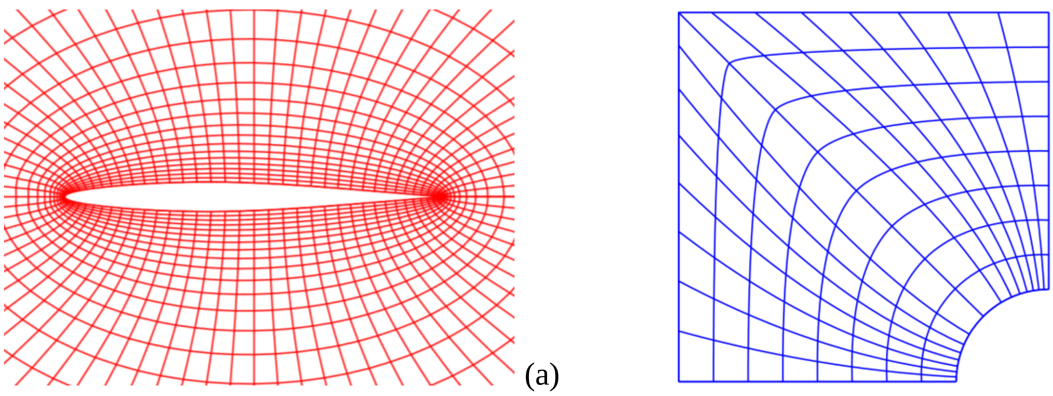

(a) (b)

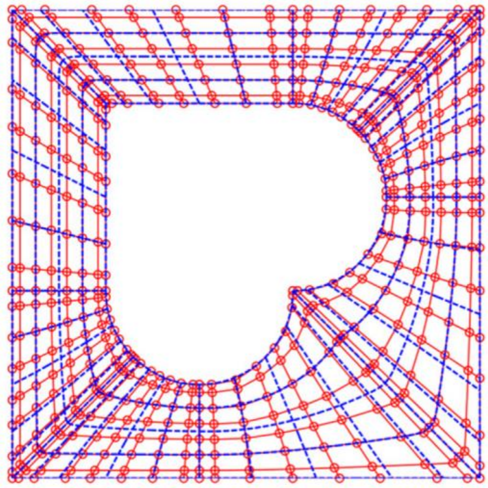
(c)

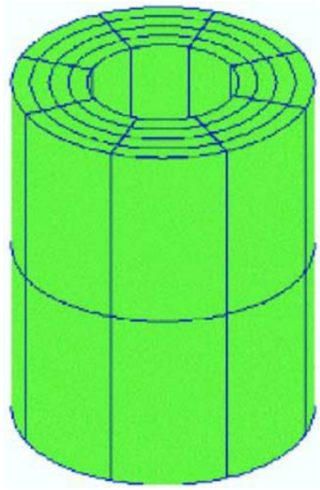
(d)

Figure 2-12: Examples of NURBS meshes: (a) Aerofoil fluid boundary (Hughes et al., 2005), (b) quarter model of a circular hole in a plate (Hughes et al., 2005), (c) Mesh of a heart shaped hole (Shojaee et al., 2012), (d) 3D hollow cylinder mesh (Hughes et al., 2005)

In the context of this optimisation task, in addition to the novelty, a NURBS based FEM solver can enable the exact representation of a propeller blade mesh while keeping the element count to a minimum. This enables faster convergence and lower computing resource consumption. This is especially important when an iterative optimisation procedure such as the GA is coupled with FE code to find optimal solutions to the problem. As the GA will conduct many iterations and invoke the FE solver many times during its solution stage, even a small saving in computational cost in the FE solver translates into a large time savings in the optimisation process.

2.7. Ply termination of tapered composites

Composite structures inherently require a ply termination strategy to accommodate thickness changes and tapers. A ply termination is a process where certain plies of the laminate are discontinued in order to reduce the thickness of the laminate. The strategy by which this termination sequence is designed is important to construct a laminate that does not compromise the strength due to discontinuities formed in the structure. Many research efforts have been dedicated to understand the stress fields developed in ply termination areas and effective methods of modelling such effects (Mukherjee and Varughese, 1999, He et al., 2000, Mukherjee and Varughese, 2001, Vidyashankar and Krishna Murty, 2001, Her, 2002).

When selecting a ply termination scheme, a particular attention must be paid to the stress developed at the ply termination point. Ply termination locations act as discontinuities in the structure that cause stress amplifications. Wu and Webber (1986) showed that these stress amplifications can be reduced by including resin fills (resin pockets) within the regions of ply terminations. In a continuation of the study, Wu (1987) demonstrate that taking into account the non-linear material behaviour of resins, the peak stress developed in the termination regions can be further reduced by about 50%. This is due to the large strain and stress distribution that emulates the process that occurs in reality in such regions. The higher stresses developed in the ply termination regions can result in the initiation of delaminations through the laminate. Thus, a ply termination strategy that does not impact the strength of the laminate must be chosen.

There are number of commonly used ply termination strategies used for tapering of composite laminates. These strategies are shown in Figure 2-13.

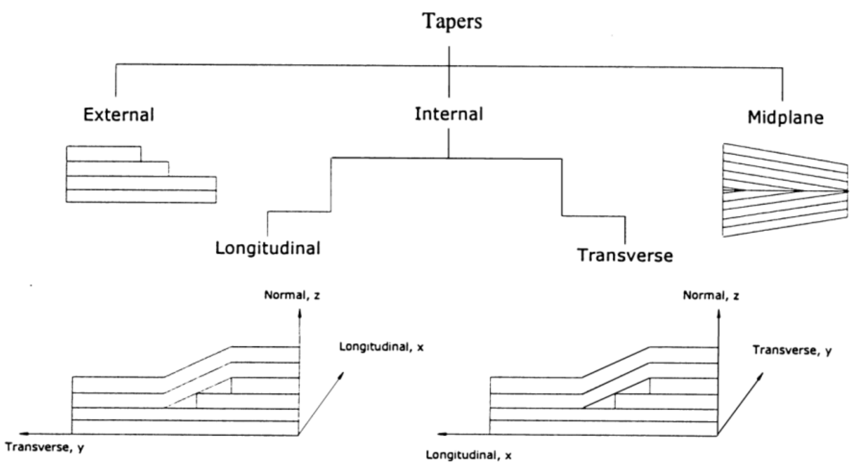

Figure 2-13: Common ply tapering/termination strategies (He et al., 2000)

An external ply termination is strategy where the ply terminations occur on the external surface of the laminate. These ply terminations are relatively easy to manufacture as they can be precisely cut from a thick pre-infused composite laminate using a CNC mills or a router without the need for a mould. However, based on the finite element models developed by Daoust and Hoa (1989), the strength of external ply termination is half as much as of internal ply terminations under tension, bending and torsion loads. Furthermore, an additional surface finish operation might be necessary in order to achieve the smooth surface required for fluid dynamic applications. Internal ply terminations eliminate these disadvantages of external ply terminations. They provide a higher strength and a better surface finish. However, the manufacturing process will require good shape accuracy and arrangement of each ply in order to accurately achieve the required thickness change in the laminate. Depending on the loading direction, internal ply terminations are divided into two categories: longitudinal and transverse (He et al., 2000). Longitudinal internal termination is a strategy where ply termination discontinuities (resin pockets) run parallel to the loading direction. Pogue and Vizzini (1990) used longitudinal internal ply termination close and parallel to the stress free edge of a laminate to reduce and strengthen the laminate against delaminations originating from the stress free edge of the laminate. Transverse internal ply termination is where ply termination is used to achieve thickness change in the direction of loading. In other words, ply termination fronts are located internally and transverse to the loading direction. This ply terminations strategy is widely used in engineering and has been extensively investigated in research. The final ply termination strategy, mid-plane ply termination, is a strategy where composite layers are terminated from the mid-plane of the laminate.

The application of composite hydrofoils and blades has a number of requirements that must be taken into account when choosing a ply termination scheme. It is desirable to have a smooth surface finish in order to reduce the drag and nucleation points for cavitation. In addition, the structural strength and reliability are of utmost importance. Therefore, external ply termination will be avoided in this application.

2.8. Summary and Proposed Improvements based on the Review

There are already shape-adaptive propellers in existence in commercial production. However, as the design process is commercially confidential, from research perspective it is worthwhile to understand the process and formulate a design process which may even have room for improvements over commercial propellers. Although there is much research done in this field, there are still improvements that can be made. One major improvement that can be made is developing an optimisation technique that focuses specifically on bend-twist coupling and bending stiffness matrix ($\boldsymbol{M} = [D]\boldsymbol{\kappa}$ for a symmetric layup). The method of optimisation presented by Liu and Young (2009) and Mulcahy et al. (2011) is focussed on improving the flexibility of the blade. In addition, this method has already given negative results in terms of efficiency at high rotational speeds (Motley and Young, 2011b) due to de-pitching. Thus, it is possible to formulate a technique where exact optimum pitch angles required at off-design condition are attempted to be achieved, rather than focussing on making the blade flexible. This is an improvement that can be attempted.

The optimisation technique used by all previous researchers is the Genetic Algorithm scheme. This is due the optimisation problems being non-linear, multi-dimensional, discrete variable. Furthermore, previous research efforts were conducted using commercial finite element solvers coupled with Genetic Algorithm codes. Coupling two different solvers within two different software platforms usually result in longer solution. Thus, it is possible to attempt to develop an in-house finite element scheme coupled with the GA within the same software platform such as Matlab™. Furthermore, discrete variable optimisation is typically more difficult to achieve due to the limited domain of possibilities variables can take. Therefore, it is intended to develop a solver that can handle both continuous variable and discrete variables. Furthermore, the manufacturing difficulties for avoiding continuous variable ply angles by previous researchers is not seen to be significant as the manufacturing techniques used in this research can develop blades with any ply angle.

The finite element technique used in the optimisation routine will use both smoothed finite element method and NURBS based FEM. Both codes are to be developed in-house and couple with the GA in the same software package, which can lead to significant speed up in the solution process. The SFEM method will be based on triangular elements such that it can mesh any propeller blade geometry with acceptable shape accuracy, while the NURBS based FEM will based on NURBS information from the CAD geometry to construct the mesh. The finite element techniques will incorporate ply terminations to account for the change in thickness. Hygrothermal effect of composites is a field that previous researchers did not address. This will also be attempted to be incorporated into the finite element solvers. The optimisation technique will also be able to handle multi-material optimisation

After the optimisation is performed it is essential to characterise the performance of the optimised blades with the help of Fluid-Structure Interaction capabilities of a commercial finite element solver. In terms of finite element modelling, Mulcahy et al.

(Mulcahy et al., 2011) used a highly simplified model assuming that the complex shape of the hydrofoil can be represented by a shell layer that has no real thickness, Lin et al. (Lin and Lee, 2004) performed modelling using two different software for performing fluid structure interaction (different solvers for structural and fluid domains). In addition, the fluid solver that was used is over four decades old. Moreover, there was a considerable deviation in their numerical results and experimental results. In terms of simulations performed by Young et al. (Young, 2008), they were performed by taking an equivalent ply angle and net properties for the propeller blade, instead of using all the ply angles for all the layers. It can be shown with the help of general theories in composite mechanics that it is not accurate to use an equivalent ply angle and net material properties for a structure that has a complex shape such as a hydrofoil. In addition, the propeller blade was constructed as a hollow body with the outer surface modelled as a shell layer.

However, in this research such simplifications will be avoided with the help of latest finite element modelling tools available commercially for constructing composite structures and hydrodynamic simulations. Furthermore, the use of cluster computing systems can further improve the accuracy of the solutions and their speed. Commercial finite element package ANSYS provides specialised composite modelling tools (ANSYS Composite PrePost) and supports fluid-structure interaction analyses along with high performance computing using parallel processing in cluster computers.

In terms of manufacturing, it is possible to use carbon fabric and vacuum infuse with epoxy resin instead of using prepreg carbon materials in order to keep the costs down. It is not necessary to have a fixed ply angle domain in this method of manufacturing. It is intended to perfect the manufacturing technique using simpler hydrofoil blades before attempting complex propeller blade shapes. Manufactured optimised hydrofoils are then intended to be subjected to both structural testing and hydrodynamic testing. Structural testing will characterise strength of the structure, another important step in the construction of composite blades.

The hydrodynamic experiments are to be conducted in a cavitation tunnel facility with the capability of monitoring deflections of the structure. The photogrammetry method adopted by past researchers is a viable and promising method. The hydrodynamic performance is then characterised of the optimised hydrofoil and compared against non-optimised hydrofoils.

3. Proposed Optimisation Scheme

Preface

In the previous chapter, a critical review of published literature on the development of shape adaptive propellers was discussed. Based on the discussions, it is evident that there is a clear advantage in using composites in the development of propeller blades and hydrofoils. This advantage can be further enhanced by optimising the propeller blade to be an adaptive structure to improve its efficiency or any other hydrodynamic parameter. The literature review discussed the requirements for a robust optimisation scheme in the development of composite propeller blades and hydrofoils. The problem involves many aspects of physics of fluids, structures and their interaction. Depending on the detail of accuracy, the optimisation strategy can be formulated to incorporate many of these intricacies and complications. The idea of this optimisation scheme is to develop a methodology that is relatively easy to implement at a low computing cost.

3.1. Introduction

This chapter explains the proposed optimisation scheme and the mathematical formulations involved in it. The primary goal of the proposed optimisation scheme is to widen the envelope of the efficiency of a propeller blade or the lift to drag (L/D) ratio of a hydrofoil using adaptive pitch change/twist of the blade. The twist is a result of the change in deflection due to the changes in flow conditions. The optimisation process will seek for the optimal layup angle sequence of the propeller blade or the hydrofoil. The objective function for the optimisation routine was formulated based on the design curve of the propeller blade or the underlying hydrofoil blade. The reliability of the structure was improved by limiting its flexibility to improve the structural health and strains during operation. Furthermore, the optimisation process will also seek for the pre-deformation required for the blade from its original idealistic shape.

In order to achieve this, two shell element based finite element codes were written in-house and were coupled with the Genetic Algorithm (GA). The first code was Cell based Smoothed Finite Element Method based on a 3-noded triangular element formulation while the second was an iso-geometric formulation based on Non-Uniform Rational B-Spline (NURBS) basis functions. A triangular element was used in the first FE implementation due to its ability to mesh any geometry, whereas, the second FE implementation based NURBS was more superior as a NURBS based mesh is able to capture the exact geometry of a complex propeller blade in the exact form it was modelled by the CAD software. The NURBS based approach also took into account the hygrothermal effects of composites due to possible changes in temperature and moisture content of the laminate during manufacturing and operation. Furthermore, the thickness variation of the hydrofoil was accounted for by estimating the number of plies required to match the local thickness of each element at its centroid.

The Genetic Algorithm was chosen as the preferred optimisation algorithm in the optimisation scheme. The GA was investigated in both continuous variable and discrete variable configurations with the intention that it gives the freedom for the analyst to optimise the structure depending on the manufacturing requirements and layup angle limitations of the manufacturing process of the hydrofoil or propeller blades.

Various researchers in the past (Lee and Lin, 2004, Liu and Young, 2009, Motley and Young, 2011b, Mulcahy et al., 2011, Young, 2007a) have used flexibility and bend-twist coupling characteristics of composites to design marine propellers that have the capability of self-varying pitch (shape adaptable) based on out of plane bending moments caused by the incoming flow. The approach taken by Lin and Lee (Lee and Lin, 2004, Lin and Lee, 2004, Lin et al., 2009) was to minimize the change of torque coefficient of the propeller when moving from the design advance ratio to one other off-design advance ratio. The reason behind this strategy was maintaining the torque, thrust and efficiency the same as the design value when moving away from the design point. However, only one off-design point was considered. The optimization process used by Motley and Young (2011b), Pluciński et al. (2007), Liu and Young (2009) attempted to ensure that the ply configuration was chosen such that the blade can achieve the maximum possible pitch variation when moving from unloaded to loaded state. Essentially, the optimization technique attempted to make the blade more flexible while maintaining strain and shape limitations.

3.2. Overview of the optimisation scheme

It is a well-known fact that composites demonstrate twisting strains due to out of plane bending moments at certain layup configurations. This effect is referred to as bend-twist coupling. The required degree/amount of bend-twist coupling must be achieved using a layup optimisation strategy to cater the requirement of the application. The shape-adaptive technique presented in this thesis predominantly relies on bend-twist coupling characteristics of laminated composites to change the pitch of the blade based on bending caused by fluid loadings at different flow speeds. In a macro-mechanical sense, bend-twist coupling characteristics can be demonstrated using the standard stiffness $[A], [B], [D]$ matrix system for composite materials (Eq. (3-1)). Here, $[A]$, $[B]$ and $[D]$ matrices have their usual laminate stiffness definitions.

$$\begin{Bmatrix} \boldsymbol{N} \\ \boldsymbol{M} \end{Bmatrix} = \begin{bmatrix} [A] & [B] \\ [B] & [D] \end{bmatrix} \begin{Bmatrix} \boldsymbol{\epsilon} \\ \boldsymbol{\kappa} \end{Bmatrix} \text{ where;}$$
$$\boldsymbol{N} = \{N_x \quad N_y \quad N_{xy}\}^T, \boldsymbol{M} = \{M_x \quad M_y \quad M_{xy}\}^T \qquad \textbf{(3-1)}$$
$$\boldsymbol{\epsilon} = \{\epsilon_x \quad \epsilon_y \quad \epsilon_{xy}\}^T, \boldsymbol{\kappa} = \{\kappa_{xx} \quad \kappa_{yy} \quad \kappa_{xy}\}^T$$

The proposed optimisation scheme consists of two stages. The first stage attempts to optimize the ply angles of the layers such that optimum bend-twist coupling performance can be achieved around the standard operating condition (cruise speed). Once the required ply configuration to enable pitch change is obtained, the second stage of the design scheme is to determine the unloaded shape of the propeller blade. This is an iterative process where the pre-twist of the blade is changed such that it reaches the required pitch at the cruise speed under cruise speed fluid loadings. A popular propeller series, the Wageningen-B series (Kuiper, 1992), is used as the reference for shape and performance characteristics of the composite propeller in the development process of the optimisation scheme. The use of Wageningen-B series is also due to the availability of extensive experimental data in open literature.

3.2.1. Stage One: Ply angle optimisation

The key idea behind the proposed optimization scheme for a marine propeller or a hydrofoil is to construct a "difference-scheme" relative to the operating point in terms of pressure and twist. The operating point is defined as the cruise advance ratio for a propeller blade or for a hydrofoil it is defined as the incidence angle where peak Lift/Drag ratio is achieved. The optimum alloy propeller geometry must be chosen for the application before it is further developed as a composite propeller. The process can be summarized as:

1. Evaluate pressure maps on the propeller blade surface for various speeds including and around the operating/cruise speed.
2. Construct pressure difference functions with respect to the operating condition for every chosen point around the operating point.
3. Assess the pitch changes required relative to the operating point for the chosen points to maintain an optimum efficiency. Pitch differences can be assessed using standard propeller efficiency curves for a propeller series, which the alloy propeller is based upon or a L/D curve series for a hydrofoil.
4. The objective function of optimization will attempt to minimize the total difference (corresponding to the respective pressure difference) between the optimum pitch that is required and the pitch that was obtained by the chosen ply configuration (3-2). Weightages (w_i) can be assigned to each off design point based on the likelihood of the propeller operating at each off-design point.

$$\min_{\boldsymbol{\theta}} f(\boldsymbol{\theta}) = Penalty \times \frac{\sum_{i=1}^{n} w_i \left| \Delta\phi^{i}_{tip_{Required}}(\Delta P_i) - \Delta\phi^{i}_{tip_{GA}}(\Delta P_i) \right|}{\sum_{i=1}^{n} w_i} \quad \textbf{(3-2)}$$

Here, *n* is the total number of points chosen above and below the operating condition. Penalty functions are used to improve the reliability of the optimization by limiting the deflection or resulting stresses. Stresses and/or strains can be used within the penalty function to artificially increase the value of the objective function if the stresses and strains in the iterative step in GA is not acceptable. This ensures that the structure does not violate any important failure criteria chosen for the application.

In step 1, it is intended to use a standard fluid solver, to obtain pressure maps on the propeller blade surface for various advance ratios in the vicinity of operating/cruise condition (advance ratio). The pressure difference functions are then to be converted to nodal force differences to be used in the finite element based optimization process. The required ideal pitch variation required to maintain the optimum efficiency can then also be assessed relative to the pitch at the ideal operating condition. These pitch changes can be obtained using standard propeller efficiency curves for the propeller series, which the composite propeller is based upon. Figure 3-1.(a) represents a typical efficiency curve series for Wageningen-B series propellers. The figure demonstrates the variation of efficiency with the change in advance ratio for fixed pitch propellers with different pitch to diameter (p/d) ratio. An optimally bend-twist coupled propeller must, in theory, be able to change its pitch (twist) with the change in advance ratio in such a way that it follows a tangential curve.

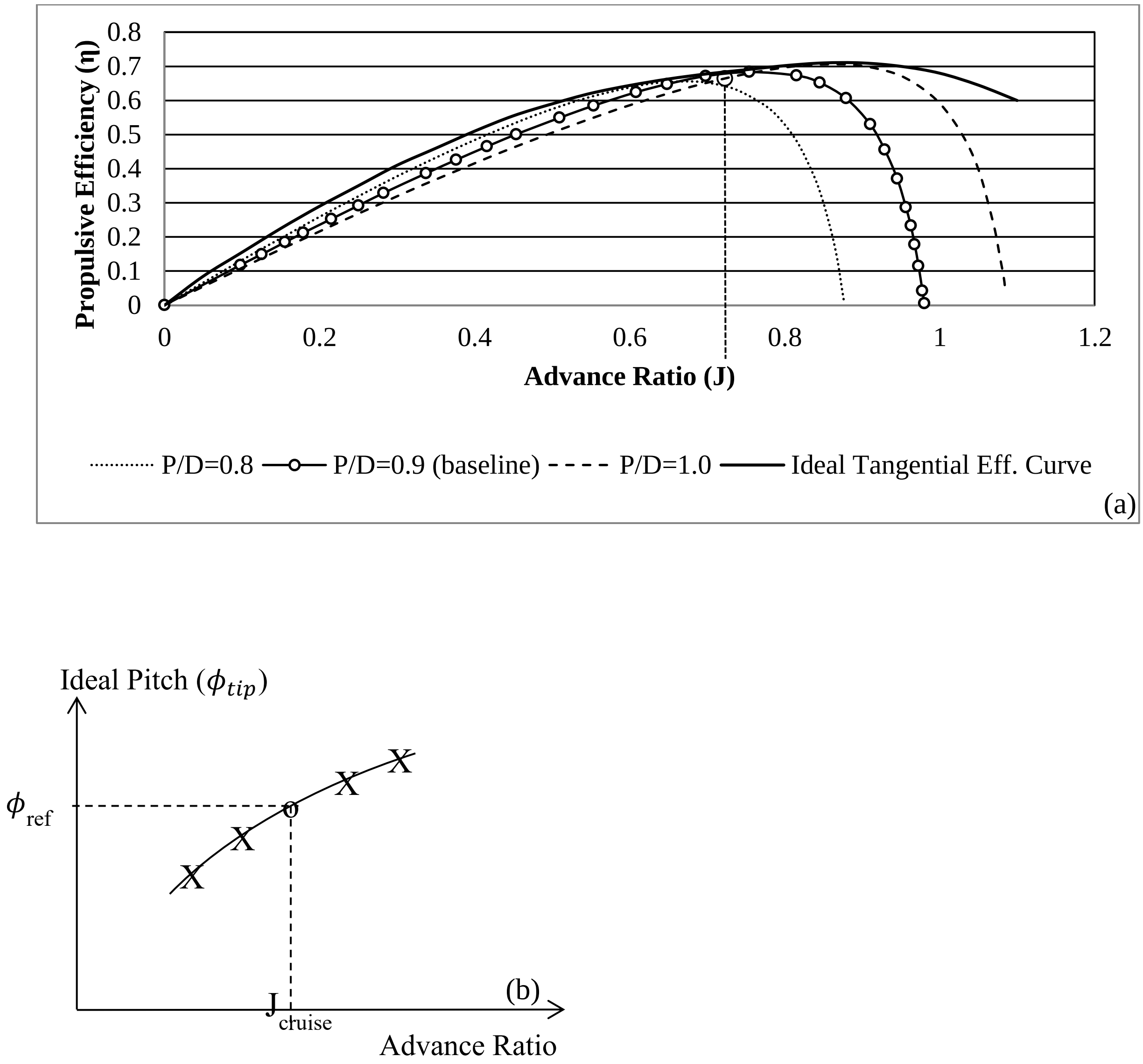

Figure 3-1: Typical propeller efficiency relationships: (a) Standard Wagenigen-B Series curves and the ideal tangential curve (b) Ideal pitch vs Advance Ratio constructed using the tangential curve

After the optimisation scheme was developed, it was important to decide the mathematical optimisation algorithm employed in the optimisation scheme. The optimization algorithm must be capable of handling non-linear objective functions, non-linear constraints and both discrete and continuous variables. Thus, the Genetic Algorithm (GA) was chosen as it can satisfy all these requirements. The GA has been used by several authors (Soremekun et al., 2001, Pluciński et al., 2007, Kameyama and

Fukunaga, 2007) in composite ply optimization tasks proving its attractiveness and credibility.

The process of GA involves applying mutations to the ply angle configuration and evaluating whether the blade can achieve the required angle at the tip. This gives rise to the requirement of having an accurate means of calculating deflections and rotations of the blade structure for an applied loading. Thus, two in-house FE codes based on the first order shear theory were developed. One of the codes used Cell Based Smoothed FEM with Discrete Shear Gap method, while the other used an iso-geometric formulation. These codes were then coupled with the GA. Figure 3-2 shows a summary of the optimization process coupled with FEM. Both the GA and the FE solver were coded in the commercial numerical processing software Matlab™. Although it is possible to couple the GA with an existing commercial FEM solver as attempted by several authors in similar research (Lee et al., 2005b, Lin and Lee, 2004, Motley and Young, 2011b, Mulcahy et al., 2008, Pluciński et al., 2007), a coupled fully in-house solver is seen as a fast and future proof approach. This is due to the inherent freedom the user has within such a solver and capability of improvement and further streamlining in the future.

The objective function of the optimization attempts to minimize the total difference (corresponding to the respective pressure difference) between the optimum pitch that is required and the pitch that was obtained by the chosen ply configuration (Eq. (3-2)) at each iteration step (chromosome) in the Genetic Algorithm. Weightages (w_i) can also be specified based on the probability of the occurrence of each off-design condition.

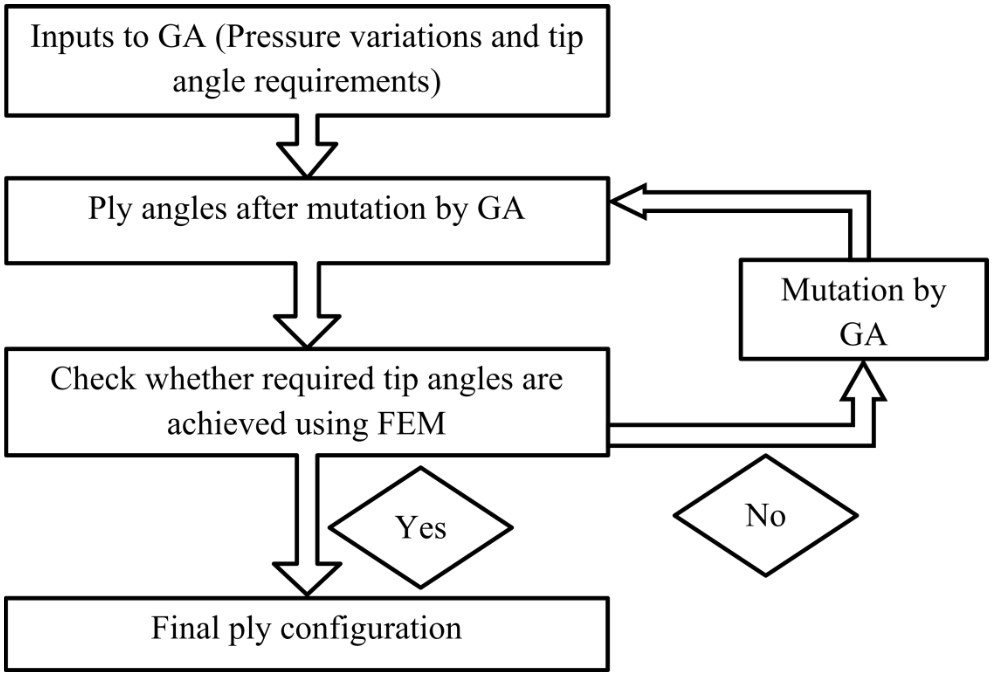

Figure 3-2: FEM coupled with GA flow

3.2.2. Stage Two: Unloaded shape

Unlike rigid alloy propellers, composite propellers cannot be manufactured at their optimum shape due to the flexibility which results in change in shape occurring over the transition from unloaded to optimally loaded condition. Thus, the objective of stage two is to achieve the pre-deformation required in the blade, such that it reaches the optimal geometry at the operating condition. The proposed methodology is iterative as summarized in Figure 3-3. The basic idea is to first apply repulsive strains to the blade and iterate the shape applying the loadings at the operating condition until the required shape at the operating loading condition is achieved, an approach that has previously been adopted by other researchers (Mulcahy et al. (2008), Pluciński et al. (2007)) in their earlier work.

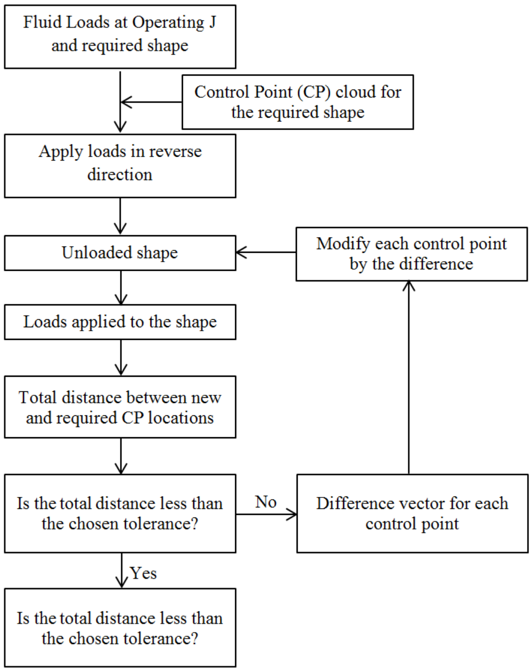

Figure 3-3: Propeller undeformed shape calculation

The process can be automated by coding into the NURBS based finite element solver. The locations in space for the i^{th} control point in the required shape is represented by $\boldsymbol{x}_i^r$. In each iteration, the control point cloud for the next iteration ($\boldsymbol{x}_i^{n+1}$) is updated as shown in Eq. (4-3). $\boldsymbol{x}_i^d$ represents the location of the i^{th} control point after applying the load on to the current shape iteration. The location of the i^{th} control point in the current iteration is represented by $\boldsymbol{x}_i^n$.

$$\boldsymbol{x}_i^{n+1} = \boldsymbol{x}_i^n + \left(\boldsymbol{x}_i^d - \boldsymbol{x}_i^r\right) \tag{3-3}$$

The shape iteration continues until the total distance between the required and achieved shape is less than the threshold set for the iteration process. The total distance is the sum of all distances between required and achieved control points, as calculated by Eq. (4-4). For the iteration process to terminate, Eq. (4-4) must be satisfied.

$$\sum_i \left|\boldsymbol{x}_i^d - \boldsymbol{x}_i^r\right| < threshold \tag{3-4}$$

3.3. The Genetic Algorithm

The developed FEM solvers were coupled with the Genetic Algorithm (GA) in order to optimise the ply stacking sequence required for the blades. The GA was considered because many of the classical gradient-based methods encounter difficulties when handling complex problems such as optimising composite layups and several other researchers have used GA based optimisation strategies in schemes for composite layups (Goupee and Vel, 2006, Lee et al., 2005b, Lin and Lee, 2004, Liu and Young, 2009). GAs are capable of handling both continuous variable and integer variable optimisation problems. Out of the two popular classes of GA (binary coded and real coded), the work presented in this thesis uses real-coded genetic algorithm having the general flow illustrated in Figure 3-4. Originally GAs were formulated as binary coded, however, advantages such as faster convergence, better handling of variables in the continuous space, overcoming the difficulty of "Hamming Cliff" and applying crossovers and mutations directly to chromosome entities rather than to the binary coded versions of them make real-coded GAs highly applicable for practical applications (Deep et al., 2009, Deep and Thakur, 2007, Lee and Lin, 2004, Pluciński et al., 2007, Goupee and Vel, 2006). In this application, chromosomes are vectors consisting of the fibre angle of each layer of the laminate. The chromosomes are sent into to FEM routine to calculate the fitness function values based on Eq. (3-2). Operators and settings for continuous variable optimisation and mixed-integer optimisation were chosen based on published work and experience gained by applying them to this work.

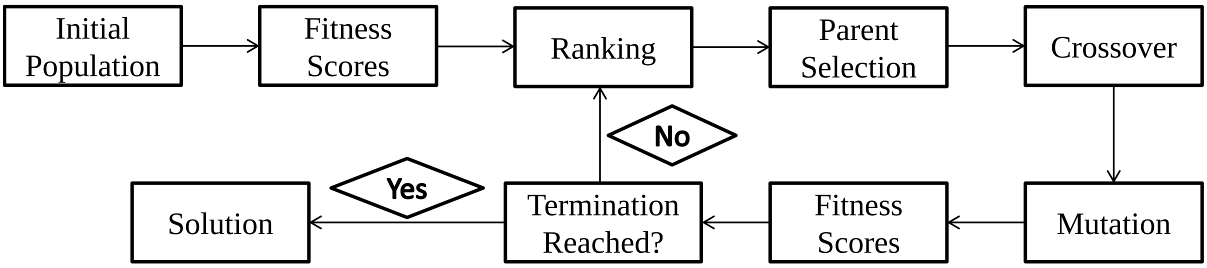

Figure 3-4: Basic layout of the GA

The GA used in this work utilised an elitist strategy to improve its efficiency. Based on numerous experiments, it was decided to carry on two elites and four elites to the next generation in continuous variable and mixed-integer optimisation cases, respectively. Additionally, the GA was modified to replace the worst child of the current generation by the next best elite of the parents' generation if crossover and mutation operators produced a worse child than the next best elite of the parents' generation. In other words, three and five elites, respectively, for continuous variable and mixed-integer cases were possible to be carried over to the next generation depending on the quality of off-springs. This strategy was observed to produce more diversity in populations compared to carrying three and five elites regardless of the quality of off-springs. At the same time, it enabled faster convergence by reducing unnecessary diversity of populations. In addition, parallelization was achieved by running the FEM solver in multiple threads for several chromosomes of the population at a time. The FEM solver was executed in serial mode in each thread.

3.3.1. Continuous variable optimisation

Continuous variable optimisation was performed assuming that there are no manufacturing limitations in laying the required angles. For such problems the Roulette Wheel (with stochastic Universal Sampling) parent selection operator, uniform crossover operator and adaptive mutation operator that satisfies upper and lower bound constraints of the problem were used. The standard Roulette wheel approach has to spin N times to select N parents; however, Roulette wheel with Stochastic Universal Sampling (SUS) picks N parents equally spaced from one spin. This operator is simple, extremely fast and has the same time complexity order, $O(N)$, as the Tournament selection operator (Baker, 1987, Herrera et al., 1998), which is widely considered as the most efficient selection operator (Goldberg and Deb, 1991). Uniform crossover employs random gene swaps between parents to produce offsprings. As investigated by Jong and Spears (1991) uniform crossover is efficient for population sizes of the order of 20, which was the population size chosen for continuous variable optimisation examples.

3.3.2. Mixed-integer optimisation

Mixed integer optimisation is a more practical approach for composite layup optimisation as in most cases fiber angles are preferred to be manufactured in certain fixed orientations. The mixed-integer GA implementation was implemented differently to the continuous variable implementation. Reproduction was carried out using the tournament selection method as it is proven to have same or enhanced performance compared to any other selection scheme in mixed-integer problems (Goupee and Vel, 2006, Goldberg and Deb, 1991, Deep et al., 2009). In this scheme, tournaments are held among randomly chosen contenders to pick the best parent for each slot in the mating pool. In this work the tournament size was set to be four. After the selection process, elites were chosen and Laplace crossover and Power mutation were performed based on the algorithm suggested by Deep et al. (2009) (MI-LXPM algorithm).

In the Laplace crossover, two off-springs ($\boldsymbol{y^1}$ and $\boldsymbol{y^2}$) are generated from two parents ($\boldsymbol{x^1}$ and $\boldsymbol{x^2}$) using random parameters β_i, u_i and r_i. Here, random β_i is first generated to satisfy the Laplace distribution using random numbers $u_i, r_i \in [0, 1]$.

$$\beta_i = \begin{cases} a - b\log(u_i), & r_i \leq 1/2 \\ a + b\log(u_i), & r_i > 1/2 \end{cases} \tag{3-5}$$

where a is the location variable and b is the scaling (integer for mixed integer problems) variable. Consequently, the two offsprings are generated as follows.

$$\begin{aligned} y_i^1 &= x_i^1 + \beta_i\left|x_i^1 - x_i^2\right| \\ y_i^2 &= x_i^2 + \beta_i\left|x_i^1 - x_i^2\right| \end{aligned} \tag{3-6}$$

Power mutation is a mutation technique based on the power distribution. First a random number s is created using the power distribution (Eq. (3-7)), based on a uniform random number t ($t \in [0, 1]$).

$$s = t^p \tag{3-7}$$

where p is the power parameter of the distribution that dictates the diversity of mutation. For mixed integer problems p is an integer number. After s is determined, children of the next generation y_i are determined using a parent x_i as follows:

$$y_i = \begin{cases} x_i - s\left(x_i - x_i^l\right), & t < r \\ x_i + s(x_i^u - x_i), & t \geq r \end{cases} \tag{3-8}$$

where $t = \frac{x_i - x_i^l}{x_i^u - x_i}$ and $\boldsymbol{x^u}, \boldsymbol{x^l}$ represent upper and lower bounds of decision variable vectors and r is a uniformly distributed number between 0 and 1.

3.4. Finite Element Method

As discussed earlier, two shell based finite element formulations were developed in this thesis in order to couple with the optimisation algorithm, one based on linear Lagrange basis functions based on 3-noded triangular (T3) elements and the other based on NURBS basis functions. Both finite element schemes have their merits, the T3 based method was easy to implement and, as it was developed based on Nguyen-Thoi et al. (2012), the formulation was highly stable and accurate. The solution speed was fast; thus, was ideal for an iterative optimisation scheme such as the GA. Furthermore, as the formulation was based on triangular elements, any area was able to be easily meshed with good shape accuracy. The second method, the NURBS based approach, was a much for challenging formulation to implement. However, it had the advantage of being able to create a mesh that represents the geometry with no disfeaturing. Here, it must be noted that NURBS basis functions are used by most CAD tools to constrict the geometry. By utilising the NURBS information from the CAD file and generating NURBS based mesh, the finite element solver was able to always capture the exact geometry of the structure that is being solved. This was especially important for complex geometries such as propeller blades. The NURBS based approach was also highly accurate and mathematically stable and was observed to achieve mesh convergence rapidly compared to other finite element methods (Chapter 3.4.2.3).

3.4.1. Triangular element based approach (CS-FEM with DSG)

In this study, the propeller blade was approximated by a hypothetical plate at the mid-plane of the blade. Three-noded triangular element with five degrees of freedom (dofs) $\delta = \{u, v, w, \theta_x, \theta_y\}$ per node was employed to discretise the plate domain. The displacement was approximated by,

$$\boldsymbol{u}^h = \sum_I N_I \boldsymbol{\delta}_I \qquad \textbf{3-9}$$

where δ_I are the nodal dofs and N_I are the standard finite element shape functions given by,

$$\boldsymbol{N} = [1 - \xi - \eta \quad \eta \quad \xi] \qquad \textbf{3-10}$$

In the CS-DSG3, each triangular element is divided into three sub-triangles. The displacement vector at the centre node is assumed to be the simple average of the three displacement vectors of the three field nodes. In each sub-triangle, the stabilized DSG3 is used to compute the strains and also to avoid the transverse shear locking. Then the strain smoothing technique on the whole triangular element is used to smooth the strains on the three sub-triangles.

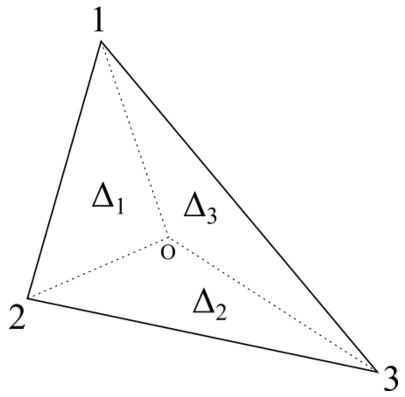

Figure 3-5: A triangular element is divided into three sub-triangles. $\boldsymbol{\Delta_1}$, $\boldsymbol{\Delta_2}$ and $\boldsymbol{\Delta_3}$ are the sub-triangles created by connecting the central point $\boldsymbol{O}$ with three field nodes

Consider a typical triangular element Ω_e as shown in Figure 3-5. This is first divided into three sub-triangles Δ_1, Δ_2 and Δ_3 such that $\Omega_e = \bigcup_{i=1}^{3} \Delta_i$. The coordinates of the centre-point $\boldsymbol{x_0} = (x_0, y_0)$ is given by:

$$(x_0, y_0) = \frac{1}{3}(x_I, y_I) \qquad \textbf{3-11}$$

The displacement vector of the centre-point is assumed to be a simple average of the nodal displacements as,

$$\boldsymbol{\delta_{e0}} = \frac{1}{3}\boldsymbol{\delta_{eI}} \qquad \textbf{3-12}$$

The constant membrane strains, the bending strains and the shear strains for sub-triangle Δ_1 is given by Eq. (3-21):

$$
\begin{aligned}
\epsilon_p &= \begin{bmatrix} p_1^{\Delta_1} & p_2^{\Delta_1} & p_3^{\Delta_1} \end{bmatrix} \begin{Bmatrix} \delta_{e0} \\ \delta_{e1} \\ \delta_{e2} \end{Bmatrix} \\
\epsilon_b &= \begin{bmatrix} b_1^{\Delta_1} & b_2^{\Delta_1} & b_3^{\Delta_1} \end{bmatrix} \begin{Bmatrix} \delta_{e0} \\ \delta_{e1} \\ \delta_{e2} \end{Bmatrix} \\
\epsilon_s &= \begin{bmatrix} s_1^{\Delta_1} & s_2^{\Delta_1} & s_3^{\Delta_1} \end{bmatrix} \begin{Bmatrix} \delta_{e0} \\ \delta_{e1} \\ \delta_{e2} \end{Bmatrix}
\end{aligned}
\qquad \textbf{3-13}
$$

Upon substituting the expression for $\boldsymbol{\delta_{e0}}$ in Eqs. (3-21), we obtain:

$$
\begin{aligned}
\epsilon_p^{\Delta_1} &= \begin{bmatrix} \frac{1}{3}\boldsymbol{p_1^{\Delta_1}} + \boldsymbol{p_2^{\Delta_1}} & \frac{1}{3}\boldsymbol{p_1^{\Delta_1}} + \boldsymbol{p_3^{\Delta_1}} & \frac{1}{3}\boldsymbol{p_1^{\Delta_1}} \end{bmatrix} \begin{Bmatrix} \boldsymbol{\delta_{e0}} \\ \boldsymbol{\delta_{e1}} \\ \boldsymbol{\delta_{e2}} \end{Bmatrix} = \boldsymbol{B_p^{\Delta_1}\delta_e} \\
\epsilon_b^{\Delta_1} &= \begin{bmatrix} \frac{1}{3}\boldsymbol{b_1^{\Delta_1}} + \boldsymbol{b_2^{\Delta_1}} & \frac{1}{3}\boldsymbol{b_1^{\Delta_1}} + \boldsymbol{b_3^{\Delta_1}} & \frac{1}{3}\boldsymbol{b_1^{\Delta_1}} \end{bmatrix} \begin{Bmatrix} \boldsymbol{\delta_{e0}} \\ \boldsymbol{\delta_{e1}} \\ \boldsymbol{\delta_{e2}} \end{Bmatrix} = \boldsymbol{B_b^{\Delta_1}\delta_e} \\
\epsilon_s^{\Delta_1} &= \begin{bmatrix} \frac{1}{3}\boldsymbol{s_1^{\Delta_1}} + \boldsymbol{s_2^{\Delta_1}} & \frac{1}{3}\boldsymbol{s_1^{\Delta_1}} + \boldsymbol{s_3^{\Delta_1}} & \frac{1}{3}\boldsymbol{s_1^{\Delta_1}} \end{bmatrix} \begin{Bmatrix} \boldsymbol{\delta_{e0}} \\ \boldsymbol{\delta_{e1}} \\ \boldsymbol{\delta_{e2}} \end{Bmatrix} = \boldsymbol{B_s^{\Delta_1}\delta_e}
\end{aligned}
\qquad \textbf{3-14}
$$

where p_i $(i = 1, 2, 3)$, b_i $(i = 1, 2, 3)$ and s_i $(i = 1, 2, 3)$ are given by:

$$
\begin{aligned}
B_p &= \frac{1}{2A_e} \begin{bmatrix} b-c & 0 & 0 & 0 & 0 & c & 0 & 0 & 0 & 0 & -b & 0 & 0 & 0 & 0 \\ 0 & d-a & 0 & 0 & 0 & 0 & -d & 0 & 0 & 0 & a & 0 & 0 & 0 & 0 \\ \underbrace{d-a}_{\boldsymbol{p_1}} & \underbrace{-d}_{\boldsymbol{p_2}} & \underbrace{a}_{\boldsymbol{p_3}} & 0 & 0 & 0 & 0 & 0 & 0 & 0 & 0 & 0 & 0 & 0 & 0 \end{bmatrix} \\
B_b &= \frac{1}{2A_e} \begin{bmatrix} 0 & 0 & 0 & b-c & 0 & c & 0 & 0 & c & 0 & 0 & 0 & 0 & -b & 0 \\ 0 & 0 & 0 & 0 & d-a & 0 & 0 & 0 & 0 & -d & 0 & 0 & 0 & 0 & a \\ \underbrace{0}_{\boldsymbol{b_1}} & \underbrace{0}_{\boldsymbol{b_2}} & \underbrace{0}_{\boldsymbol{b_3}} & 0 & 0 & 0 & 0 & 0 & 0 & 0 & 0 & 0 & 0 & 0 & 0 \end{bmatrix} \\
B_s &= \frac{1}{2A_e} \begin{bmatrix} 0 & 0 & b-c & A_e & 0 & 0 & 0 & c & \frac{ac}{2} & \frac{bc}{2} & 0 & 0 & -b & \frac{-bd}{2} & \frac{-bc}{2} \\ \underbrace{0}_{\boldsymbol{s_1}} & \underbrace{0}_{\boldsymbol{s_2}} & \underbrace{0}_{\boldsymbol{s_3}} & 0 & 0 & 0 & 0 & 0 & 0 & 0 & 0 & 0 & 0 & 0 & 0 \end{bmatrix}
\end{aligned}
\qquad \textbf{3-15}
$$

where $a = x_2 - x_1;\ b = y_2 - y_1; c = y_3 - y_1$ and $d = x_3 - x_1$ (see Figure 3-6), A_e is the area of the triangular element and B_s is altered shear strains (Bletzinger et al., 2000). The strain-displacement matrix for the other two triangles can be obtained by cyclic permutation.

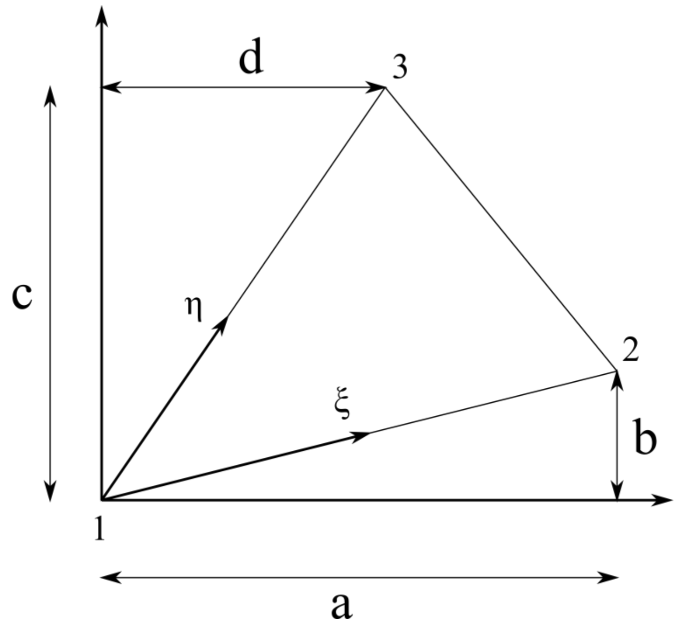

Figure 3-6: Three-noded triangular element and local coordinates in discrete shear gap method

Now applying the cell-based strain smoothing (Bordas and Natarajan, 2010), the constant membrane strains, the bending strains and the shear strains are respectively employed to create a smoothed membrane strain $\overline{\boldsymbol{\epsilon_p}}$, smoothed bending strain $\overline{\boldsymbol{\epsilon_b}}$ and smoothed shear strain $\overline{\boldsymbol{\epsilon_b}}$ on the triangular element Ω_e as:

$$\overline{\boldsymbol{\epsilon_p}} = \int_{\boldsymbol{\Omega_e}} \boldsymbol{\epsilon_p} \Phi_e(\boldsymbol{x}) d\Omega = \sum_{i=1}^{3} \boldsymbol{\epsilon_p}^{\Delta_i} \int_{\boldsymbol{\Delta_i}} \Phi_e(\boldsymbol{x}) d\Omega$$

3-16

$$\overline{\boldsymbol{\epsilon_b}} = \int_{\boldsymbol{\Omega_e}} \boldsymbol{\epsilon_b} \Phi_e(\boldsymbol{x}) d\Omega = \sum_{i=1}^{3} \boldsymbol{\epsilon_b}^{\Delta_i} \int_{\boldsymbol{\Delta_i}} \Phi_e(\boldsymbol{x}) d\Omega$$

$$\bar{\boldsymbol{\epsilon}}_{\boldsymbol{s}} = \int_{\boldsymbol{\Omega}_{\boldsymbol{e}}} \boldsymbol{\epsilon}_{\boldsymbol{s}} \Phi_e(\boldsymbol{x}) d\Omega = \sum_{i=1}^{3} \boldsymbol{\epsilon}_{\boldsymbol{s}}^{\boldsymbol{\Delta}_i} \int_{\boldsymbol{\Delta}_i} \Phi_e(\boldsymbol{x}) d\Omega$$

where $\Phi_e(\boldsymbol{x})$ is a given smoothing function that satisfies. In this study, following constant smoothing function is used:

$$\Phi(\boldsymbol{x}) = \begin{cases} 1/A_c & ; \boldsymbol{x} \in \Omega_c \\ 0 & ; \boldsymbol{x} \in \Omega_c \end{cases} \tag{3-17}$$

where A_c is the area of the triangular element, the smoothed membrane strain, the smoothed bending strain and the smoothed shear strain is then given by

$$\{\bar{\boldsymbol{\epsilon}}_{\boldsymbol{p}} \quad \bar{\boldsymbol{\epsilon}}_{\boldsymbol{b}} \quad \bar{\boldsymbol{\epsilon}}_{\boldsymbol{s}}\} = \sum_{i=1}^{3} \frac{A_{\Delta_i}\{\boldsymbol{\epsilon}_{\boldsymbol{p}}^{\boldsymbol{\Delta}_i} \quad \boldsymbol{\epsilon}_{\boldsymbol{b}}^{\boldsymbol{\Delta}_i} \quad \boldsymbol{\epsilon}_{\boldsymbol{s}}^{\boldsymbol{\Delta}_i}\}}{A_e} \tag{3-18}$$

The smoothed elemental stiffness matrix is given by,

$$\begin{aligned} K &= \int_{\Omega_e} \bar{B}_p A\, \bar{B}_p^T + \bar{B}_p B\, \bar{B}_b^T + \bar{B}_b B\, \bar{B}_p^T + \bar{B}_b D\, \bar{B}_b^T + \bar{B}_s E\, \bar{B}_s^T d\Omega \\ &= \left(\bar{B}_p A\, \bar{B}_p^T + \bar{B}_p B\, \bar{B}_b^T + \bar{B}_b B\, \bar{B}_p^T + \bar{B}_b D\, \bar{B}_b^T + \bar{B}_s E\, \bar{B}_s^T\right) A_e \end{aligned} \tag{3-19}$$

Where $\bar{B}_p, \bar{B}_b$ and $\bar{B}_s$ are the smoothed strain-displacement matrix.

A mesh convergence study was conducted to ensure that the cell-based smoothed finite element technique is stable and provides accurate results with the increase in the number of degrees of freedom. The mesh was refined by increasing the node number of the test structure (h-refinement). A simple rectangular plate with dimensions: 0.4 m (L) x 0.2 m (W) x 3 mm (t) was considered for the convergence study. It was assumed that the plate was made out of unidirectional CFRP (Table 3-1) and has 24 plies all having a fiber orientation of 40° counter clockwise from x-axis towards y-axis. The plate was assumed to be clamped at the left edge and a uniform pressure loading (normal to the surface) of 100 Pa (upwards) was applied on the top surface. Details of the meshes that were validated and their results are given in Table 3-1. As an independent verification, maximum deflection obtained using Q8 elements (using the commercial software ANSYS™, 8-noded shell 281) is also presented. Convergence results showed that CS-FEM was highly accurate with good stability and convergence. Thus, it can be used for complex shapes in further applications.

	Node Array	**Max. Deflection (mm)**
Mesh 1	5×5	4.296
Mesh 2	10×10	5.704
Mesh 3	20×20	6.087
Mesh 4	40×40	6.165
Mesh 5	80×80	6.194
ANSYS™ Q8 (9841 Nodes)		6.212

Table 3-1: Mesh convergence of CS-FEM

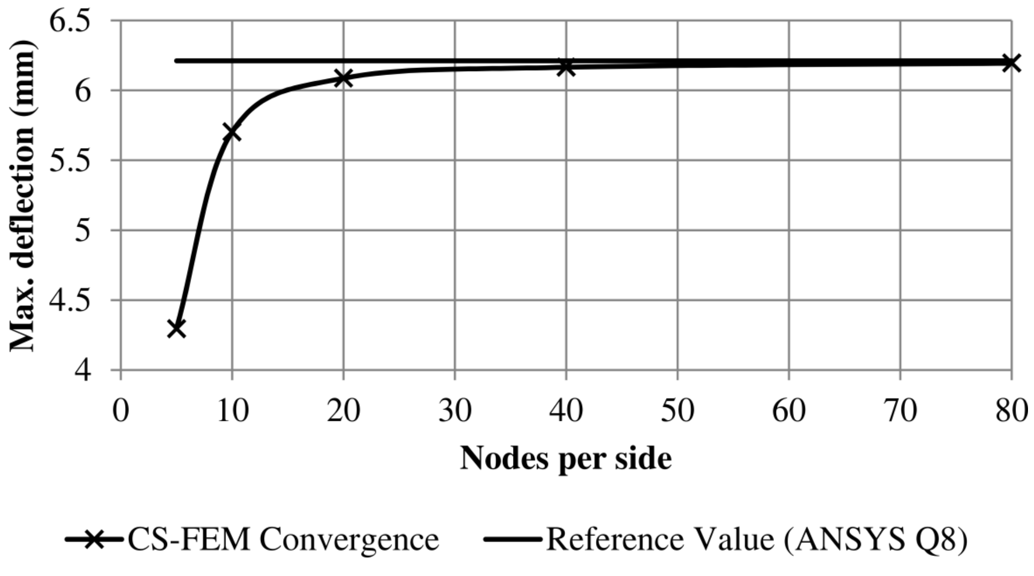

Figure 3-7: CS-FEM mesh convergence curve

3.4.2. NURBS based approach

The optimization technique developed in this work can accurately capture the complex blade profile that is required for the marine propellers. The optimization was performed using an in-house iso-geometric FEM code that was developed and coupled with the real-coded GA. In addition to the standard deformations due to loads, the iso-geometric analysis was enhanced to capture the deformations due to hygrothermal effects of composites.

3.4.2.1. NURBS FE formulation and Hygrothermal effects

The FEM was formulated using the Mindlin-Reissner static formulation incorporating hygrothermal effects. The displacements u, v and w at a point is expressed in terms of the displacement of the mid-plane u_0, v_0 and w_0 and independent rotations β_x and β_y of the normal in yz and xz planes, respectively as:

$$\begin{aligned} u(x,y,z) &= u_0(x,y) + z\beta_x(x,y) \\ v(x,y,z) &= v_0(x,y) + z\beta_y(x,y) \\ w(x,y,z) &= w_0(x,y) \end{aligned} \tag{3-20}$$

The strains were taken consistent with the standard formulation entailing planar (ϵ_p), bending (ϵ_b) and shear (ϵ_s) strains and additionally strains due to thermal and moisture effects ($\bar{\boldsymbol{\epsilon}}_{\mathbf{0}}$):

$$\begin{gathered} \boldsymbol{\epsilon} = \begin{Bmatrix} \boldsymbol{\epsilon_p} \\ \mathbf{0} \end{Bmatrix} + \begin{Bmatrix} z\boldsymbol{\epsilon_b} \\ \boldsymbol{\epsilon_s} \end{Bmatrix} - \{\bar{\boldsymbol{\epsilon}}_{\mathbf{0}}\} \\ \boldsymbol{\epsilon_p} = \begin{Bmatrix} u_{0,x} \\ v_{0,y} \\ u_{0,y} + v_{0,x} \end{Bmatrix}, \quad \boldsymbol{\epsilon_b} = \begin{Bmatrix} \beta_{x,x} \\ \beta_{y,y} \\ \beta_{x,y} + \beta_{y,x} \end{Bmatrix}, \quad \boldsymbol{\epsilon_s} = \begin{Bmatrix} \beta_x + w_{0,x} \\ \beta_y + w_{0,y} \end{Bmatrix} \end{gathered} \tag{3-21}$$

The subscript represents the partial derivative with respect to the spatial coordinate. Additionally, the strain due to hygrothermal effects are given by,

$$\bar{\boldsymbol{\epsilon}}_{\mathbf{0}} = \begin{Bmatrix} \bar{\epsilon}_{xx} \\ \bar{\epsilon}_{yy} \\ \bar{\epsilon}_{xy} \end{Bmatrix} = \Delta T \begin{Bmatrix} \alpha_x \\ \alpha_y \\ \alpha_{xy} \end{Bmatrix} + \Delta C \begin{Bmatrix} \gamma_x \\ \gamma_y \\ \gamma_{xy} \end{Bmatrix} \tag{3-22}$$

where ΔT and ΔC are the change in temperature and moisture concentrations, respectively, and α in x, y and xy directions can be expressed in terms of the principal direction properties as:

$$\begin{Bmatrix} \alpha_x \\ \alpha_y \\ \alpha_{xy} \end{Bmatrix} = \begin{Bmatrix} \alpha_1 \cos^2\theta + \alpha_2 \sin^2\theta \\ \alpha_1 \sin^2\theta + \alpha_2 \cos^2\theta \\ 2(\alpha_1 - \alpha_2)\cos\theta\sin\theta \end{Bmatrix} \tag{3-23}$$

Similar expressions can be given for moisture expansion coefficients in x, y and xy in terms of principal direction properties. The force and moment per unit width can then be given based on Eq. (3-1) as:

$$\begin{aligned} \boldsymbol{N} &= \begin{Bmatrix} N_{xx} \\ N_{yy} \\ N_{xy} \end{Bmatrix} = [A]\boldsymbol{\epsilon_p} + [B]\boldsymbol{\epsilon_b} - \boldsymbol{N^{HT}} \\ \boldsymbol{M} &= \begin{Bmatrix} M_{xx} \\ M_{yy} \\ M_{xy} \end{Bmatrix} = [B]\boldsymbol{\epsilon_p} + [D]\boldsymbol{\epsilon_b} - \boldsymbol{M^{HT}} \end{aligned} \tag{3-24}$$

With $\boldsymbol{N^{HT}}$ and $\boldsymbol{M^{HT}}$ representing the force and moment resulting from the hygrothermal effects, respectively. The hygrothermal forces and moments of the laminate can be given using the x, y directional stiffness matrix $\left([Q]_{xy}\right)$ and the hygrothermal strain of individual layers $\left(\boldsymbol{\bar{\epsilon}_0^k}\right)$ as,

$$\begin{aligned} \boldsymbol{N^{HT}} &= \begin{Bmatrix} N_{xx}^{HT} \\ N_{yy}^{HT} \\ N_{xy}^{HT} \end{Bmatrix} = \sum_{k=1}^{n} \int_{z_{k-1}}^{z_k} [Q]_{xy} \boldsymbol{\bar{\epsilon}_0^{\mathrm{k}}} dz \\ \boldsymbol{M^{HT}} &= \begin{Bmatrix} M_{xx}^{HT} \\ M_{yy}^{HT} \\ M_{xy}^{HT} \end{Bmatrix} = \sum_{k=1}^{n} \int_{z_{k-1}}^{z_k} [Q]_{xy} \boldsymbol{\bar{\epsilon}_0^{\mathrm{k}}} z dz \end{aligned} \tag{3-25}$$

The strain energy of the plate element is given by:

$$\begin{aligned} U(\boldsymbol{\delta}) = \frac{1}{2} \int_{A_e} \{ & \boldsymbol{\epsilon_p^T}[A]\boldsymbol{\epsilon_p} + \boldsymbol{\epsilon_p^T}[B]\boldsymbol{\epsilon_b} + \boldsymbol{\epsilon_b^T}[B]\boldsymbol{\epsilon_p} + \boldsymbol{\epsilon_b^T}[D]\boldsymbol{\epsilon_b} + \boldsymbol{\epsilon_s^T}[E]\boldsymbol{\epsilon_s} - \boldsymbol{\epsilon_b^T}\boldsymbol{N^{HT}} \\ & - \boldsymbol{\epsilon_b^T}\boldsymbol{M^{HT}} \} \, dA_e \end{aligned} \tag{3-26}$$

Where $\boldsymbol{\delta} = \{\mathrm{u}, \mathrm{v}, \mathrm{w}, \beta_\mathrm{x}, \beta_\mathrm{y}\}$ is the degree of freedom vector representing the displacement field in the discretised domain. For a static problem, Eq. (3-26) is followed by Eq. (3-27), where K is the linear stiffness matrix that satisfies $\boldsymbol{F} = [K]\boldsymbol{\delta}$ for a static finite element problem.

$$U(\boldsymbol{\delta}) = \frac{1}{2}\boldsymbol{\delta}^{\boldsymbol{T}}[K]\boldsymbol{\delta} \tag{3-27}$$

3.4.2.2. Iso-Geometric Analysis

Most existing approaches in structural optimisation use conventional FEM combined with optimization schemes (Motley et al., 2009, Mulcahy et al., 2011). Due to the complex shape of propellers, conventional Lagrange based FEM based approaches can only approximate the geometry. One of the main advantages of the proposed approach is that the geometry can be accurately modelled and the CAD and the FE analysis can be seamlessly integrated. In this investigation, the finite element approximation uses NURBS as the basis functions and the details on their use in FEM are given in (Cottrell et al., 2009). The key ingredients in the construction of NURBS basis functions are: the knot vector (a non-decreasing sequence of parameter values, $\xi_i \leq \xi_{i+1}, i = 0,1, \dots, m-1$), the control points, P_i, the degree of the curve, p, and the weight associated to a control point, w. The NURBS basis is constructed using B-Spline basis functions. The i^{th} B-spline basis function of degree p, denoted by $N_{i,p}$ is defined as,

$$N_{i,0}(\xi) = \begin{cases} 1 \; if \; \xi_i \leq \xi \leq \xi_{i+1} \\ \quad else \end{cases}$$
$$N_{i,p}(\xi) = \left(\frac{\xi - \xi_i}{\xi_{i+p} - \xi_i}\right)N_{i,p-1}(\xi) + \left(\frac{\xi_{i+p+1} - \xi}{\xi_{i+p+1} - \xi_{i+1}}\right)N_{i+1,p-1}(\xi) \tag{3-28}$$

A p^{th} degree NURBS curve is then defined as:

$$C(\xi) = \frac{\sum_{i=0}^{m} N_{i,p}(\xi) w_i \boldsymbol{P}_i}{\sum_{i=0}^{m} N_{i,p}(\xi) w_i} \tag{3-29}$$

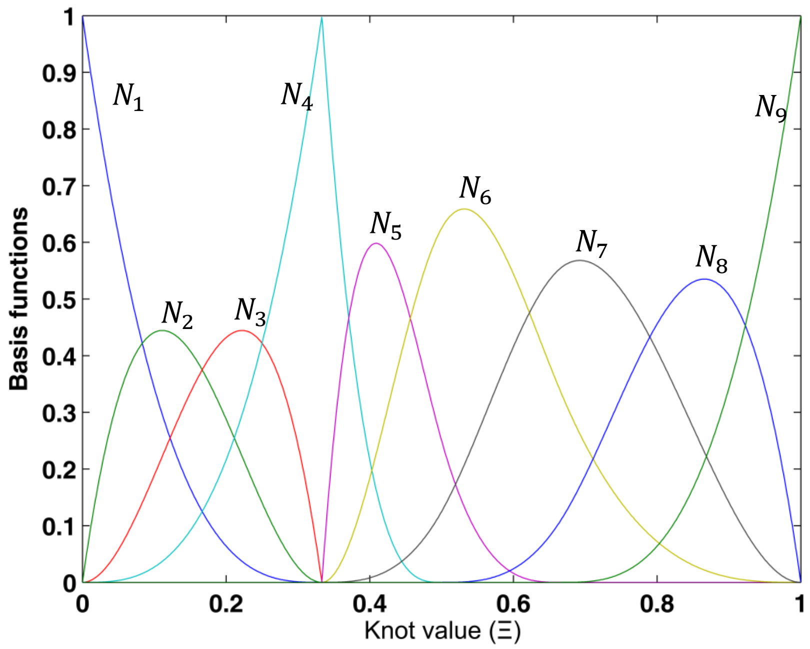

Figure 3-8. Non-uniform rational B-splines, order of the curve = 3

where P_i are the control points and w_i are the associated weights. Figure 3-8 shows the third order non-uniform rational B-spline for a knot vector, $\Xi = \left\{0, 0, 0, 0, \frac{1}{3}, \frac{1}{3}, \frac{1}{3}, \frac{1}{2}, \frac{2}{3}, 1,1,1,1\right\}$. NURBS basis functions have the following properties: (i) non-negativity, (ii) partition of unity, $\sum_i N_{i,p} = 1$; (iii) interpolatory at the end points. Iso-geometric analysis uses the same basis functions for the geometry and the field variables. Since the same NURBS bases used to construct the geometry are used to construct the mesh, a NURBS mesh is capable of representing the geometry accurately without any defeaturing introduced due to meshing. The B-spline surfaces are defined by the tensor product of basis functions in two parametric dimensions ξ and η with two knot vectors, one in each dimension as:

$$S(\xi, \eta) = \sum_{i=1}^{n} \sum_{j=1}^{m} N_{i,p}(\xi) M_{j,q}(\eta) \boldsymbol{P}_{i,j} \tag{3-30}$$

where $\boldsymbol{P}_{i,j}$ is the bidirectional control net and $N_{i,p}$ and $M_{j,q}$ are the B-spline basis functions defined on the knot vectors over an $m \times n$ net of control points $\boldsymbol{P}_{i,j}$. The NURBS surface is then defined by:

$$S(\xi,\eta) = \frac{\sum_{i=1}^{n}\sum_{j=1}^{m} N_{i,p}\,(\xi)M_{j,q}(\eta)P_{i,j}w_i w_j}{W(\xi,\eta)} \tag{3-31}$$

where $w(\xi,\eta)$ is the weighting function. The displacement field within the control mesh is approximated by:

$$\boldsymbol{u}_{\boldsymbol{\tau}}(x,y) = \boldsymbol{C}(\xi,\eta)\boldsymbol{q}_{\boldsymbol{\tau}}(x,y) \tag{3-32}$$

where $\boldsymbol{q}_{\boldsymbol{\tau}}(x,y)$ are the nodal variables and $\boldsymbol{C}(\xi,\eta)$ are the basis functions given by Eq. (3-31). Figure 3-9 shows the NURBS second order basis functions.

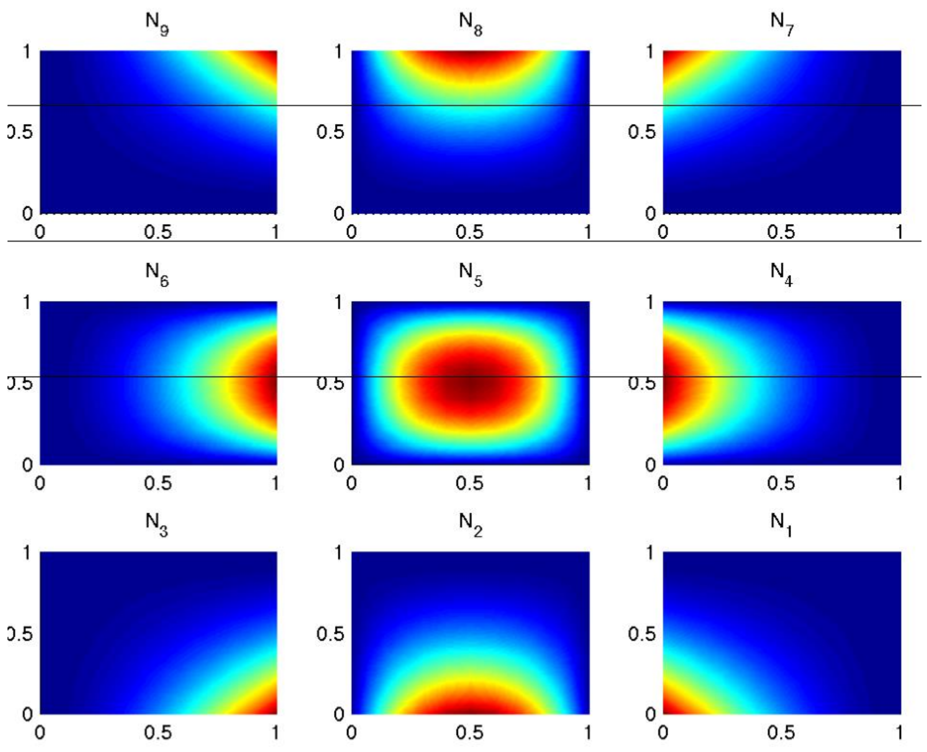

Figure 3-9: Shape function plot

For comparison purposes, Figure 3-10 is produced to emphasise the difference between a NURBS mesh with a standard T3 mesh with same number of DOFs. Figure

3-10 compares the 880 DoF NURBS mesh against the standard triangular element mesh with the same number of DoFs. As elaborated in Section 3.4.2.3 IGA has already achieved mesh convergence with 880 DoFs. The comparison clearly demonstrates that the triangular mesh fails to accurately capture the profile of the blade with the given low number of triangular elements. In other words, if a standard triangular element were used, a much higher element density is required to accurately capture the shape of the blade and to achieve results convergence.

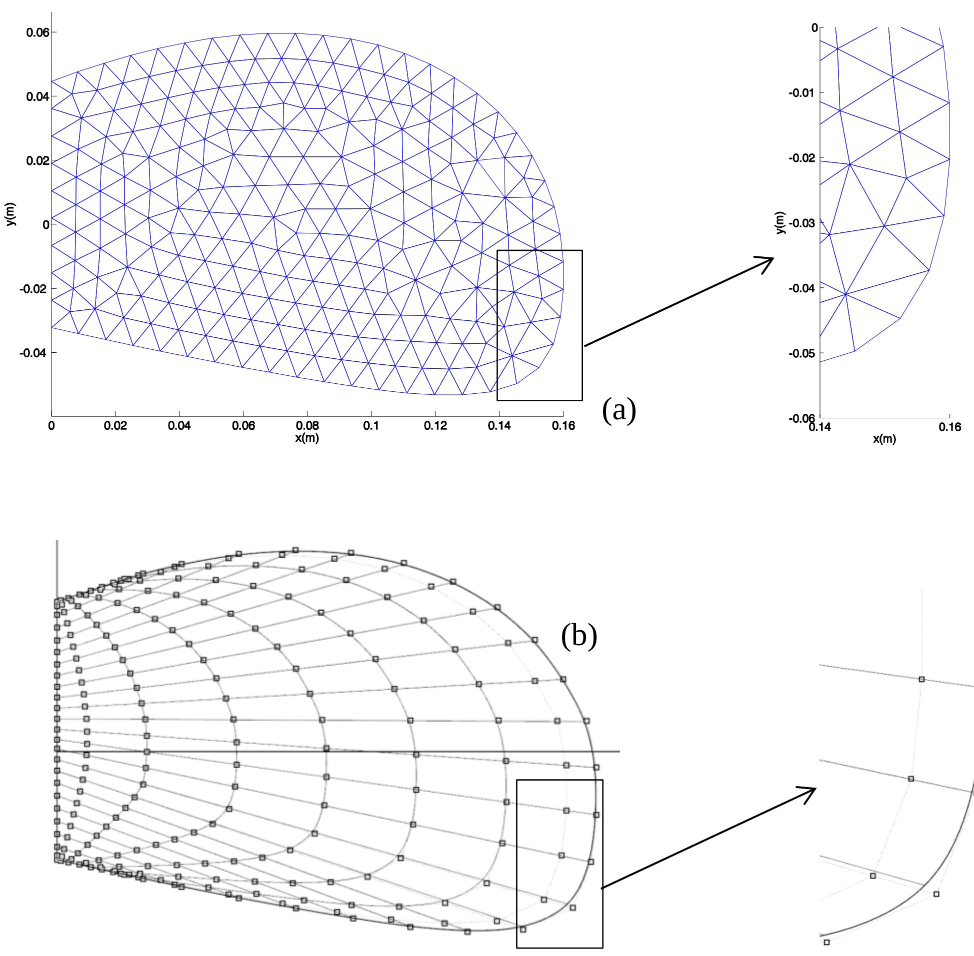

Figure 3-10: Standard T3 mesh compared against a NURBS mesh with same number of degrees of freedom: (a) standard T3 mesh and curve of the blade approximated by the triangular discretisation, (b) 3rd order NURBS mesh with perfect capture of geometry

Similar to the finite element based on Lagrange basis functions, shear locking may occur when lower order NURBS basis functions, such as quadratic, cubic and quartic elements[1], are employed (Beirão da Veiga et al., 2012, Valizadeh et al., 2013). One approach to alleviate the shear locking is to employ interpolation functions of order 5 or higher (Beirão da Veiga et al., 2012), but this inevitably increases the computational cost. A stabilization technique for several lower-order NURBS elements for plates was reported in (Thai et al., 2012). Here, the stabilization technique proposed by Kikuchi and Ishii (1999) and later used by Valizadeh et al. (2013) to study the response of Reissner-Mindlin plates is adopted. In this approach, the material matrix related to the shear terms are multiplied by the following shear factor:

$$shearfactor = \frac{h^2}{h^2 + \alpha^2 l^2} \tag{3-33}$$

where l is the longest length of the edges of the NURBS element and α is a positive constant given in the interval $0.05 \leq \alpha \leq 0.15$. It is found from numerical experiments of NURBS-based iso-geometric plate elements that α can be fixed at 0.1, which provide reasonably accurate solutions. It should also be noted that the continuity of the NURBS functions could be custom tailored to suit the needs of the problem.

3.4.2.3. NURBS mesh convergence and stability

A mesh convergence study was conducted to ensure that the NURBS based finite element technique is stable and provides accurate results with the increase in the number of degrees of freedom. Additionally, the study provided an assessment for the minimum level of refinement required for achieving mesh independent results. This was important in reducing computational time for subsequent GA based optimisations

[1] Linear NURBS basis functions are same as the linear Lagrange basis functions and are not discussed here. Approaches employed for Lagrange basis functions can readily be applied to NURBS basis functions with order 1

without compromising the accuracy of results. Typically, NURBS meshes can be refined in three ways: *h*-refinement (knot insertion), *p*-refinement (elevation of degree of NURBS bases) and *k*-refinement (a combination of both *h* and *p*-refinements) (Cottrell et al., 2009). It is beyond the scope of this thesis to discuss these refinement techniques in detail and interested readers are referred to the literature on the applications of NURBS based partition of unity method to analyse plate structures (Valizadeh et al., 2013, Shojaee et al., 2012, Scott et al., 2013). However, for the purposes of mesh convergence and stability, h-refinement and p-refinement will be presented and the convergence of maximum displacement was investigated.

The convergence of the NURBS mesh was compared to Cell-based Smoothed FEM with Discrete Shear Gap Method (CS-FEM with DSG), Lagrange linear and second order shell elements of commercially available FEM software ANSYS™ ("Shell181" and "Shell281" in their triangular form). For brevity, only the results for Wagengingen B-Series B5-60 blade will be presented. It was assumed that the blades were constructed using 40 CFRP layers all laid at an angle of 30º measured counter-clockwise positive *x*-axis to the positive *y*-axis. The blade was assumed to be clamped at the left edge with a uniform pressure of 100Pa applied over the blade surface. The change in temperature and moisture content were considered to be zero for the mesh convergence study.

Meshes were created for NURBS orders 1, 2 and 3 with a varying number of control points for each order (Table 3-2). In the case of propeller blade, there are two dominant directions for the mesh – radial and circumferential. It was evident that out of these two directions, the radial direction of the NURBS mesh was significantly more sensitive to deflection results. In other words, the initial mesh, which was 3rd order with 22 control points in the circumferential direction, was adequate to accurately capture deflection.

Due to the requirement of capturing the accurate curvature in the circumferential direction, the order or the number of control points were not reduced. Figure 3-11 illustrates several meshes that were created with different NURBS orders and control points.

Details of the meshes that were validated and their results are given in Table 3-2. Figure 3-12 illustrates the convergence of these results. It was evident that 3rd order NURBS elements have a much faster convergence; thus, lowering the number of degrees of freedom required for an accurate solution. For the purpose of comparison, the results obtained using a much higher mesh density (88825 DoFs with drilling DoF suppressed) is also presented in the table for CS-FEM and standard ANSYS™ elements. It was clear that the result achieved by the 3rd order NURBS mesh was eventually achieved by CS-FEM and Lagrange based elements with a much higher element density.

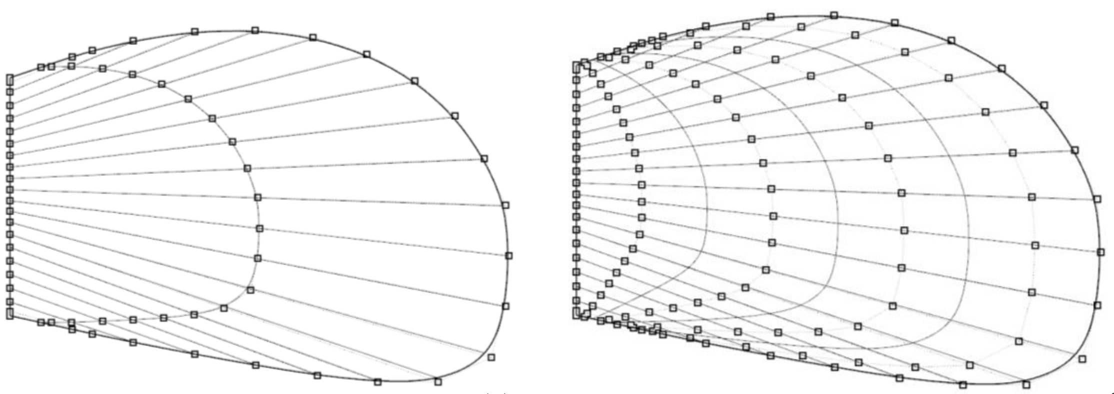

(a) (b)

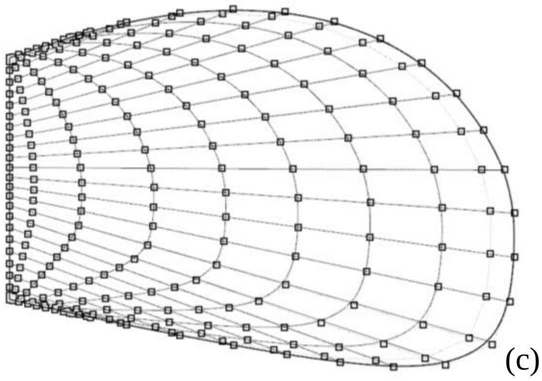

Figure 3-11: B5-60 blade mesh refinement steps

Degrees of Freedom	Max. Displacement (µm)			
	NURBS mesh (Radial Order = 3)	CS-FEM T3 (linear)	ANSYS™ shell181 (triangular linear)	ANSYS™ shell281 (triangular 2nd order)
440	25.1	24.5	24.5	24.8
660	25.6	24.9	24.8	25.2
880	25.7	24.8	25.0	25.2
1100	25.7	25	25.1	25.4
2200	25.7	25.3	25.4	25.4
4400	25.7	25.4	25.5	25.5
8250	25.7	25.5	25.6	25.6
88825		25.7	25.7	25.7

Table 3-2: Mesh convergence results of blade shapes

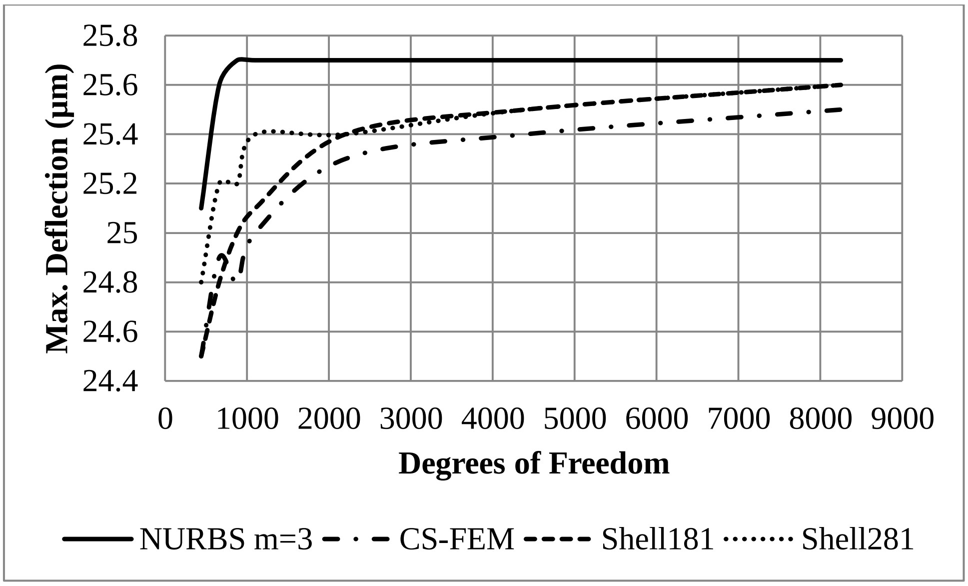

Figure 3-12: Mesh convergence study (displayed up to 8250 DoF)

In addition to the faster convergence in results, as expected, the NURBS mesh was able to capture the complex geometry of the propeller blade with a high accuracy. Further higher orders were also investigated and were found to have rapid convergence. For the sake of brevity, results for higher order basis functions are not shown here. Based on the results obtained, it was clear that the in-house solver has good stability and convergence.

3.4.3. Thickness change and ply termination

Ply termination is required to accommodate the change in thickness of a composite blade. In this analysis, ply termination was accounted for in the FE codes by reducing the number of layers in each element of the FE mesh. This was achieved by first calculating the thickness at the centroid of each element using the thickness function of the hydrofoil and then assigning the minimum number (integer) of plies required to satisfy the thickness at the centroid of the element. The stacking sequence passed through into FE solver from GA was then modified accordingly based on elemental thickness. Elemental stiffness matrices were then calculated and the global stiffness matrix was assembled (Figure 3-13).

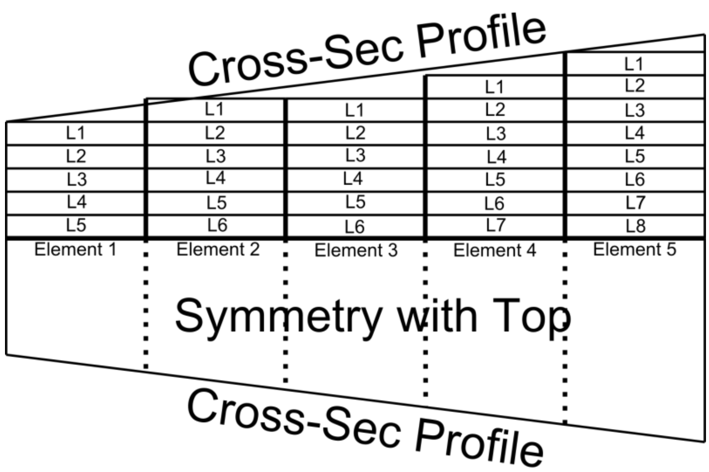

Figure 3-13: Ply drop-off process in FE modelling

As described later in Chapter 4, the designed hydrofoil has a thickness variation that must be accounted for using appropriate ply terminations. In order to achieve a continuous ply on the outer surface of the hydrofoil where stresses due to bending are highest, internal ply termination strategy was used as opposed to external ply termination. As explained later in Chapter 5, an infusion mat was added to the layup to act as the flow media to improve the consistency of resin flow within the laminate. The infusion mat layer was continued for a larger area in order to enable consistent resin flow in the specimen. The Matlab routine ensured the continuity of the infusion mat layer at the symmetry plane of the layup while terminating the next closest layers to the symmetry plane based on element thickness. The flow of GA coupled with FE code with ply termination is shown in Figure 3-14.

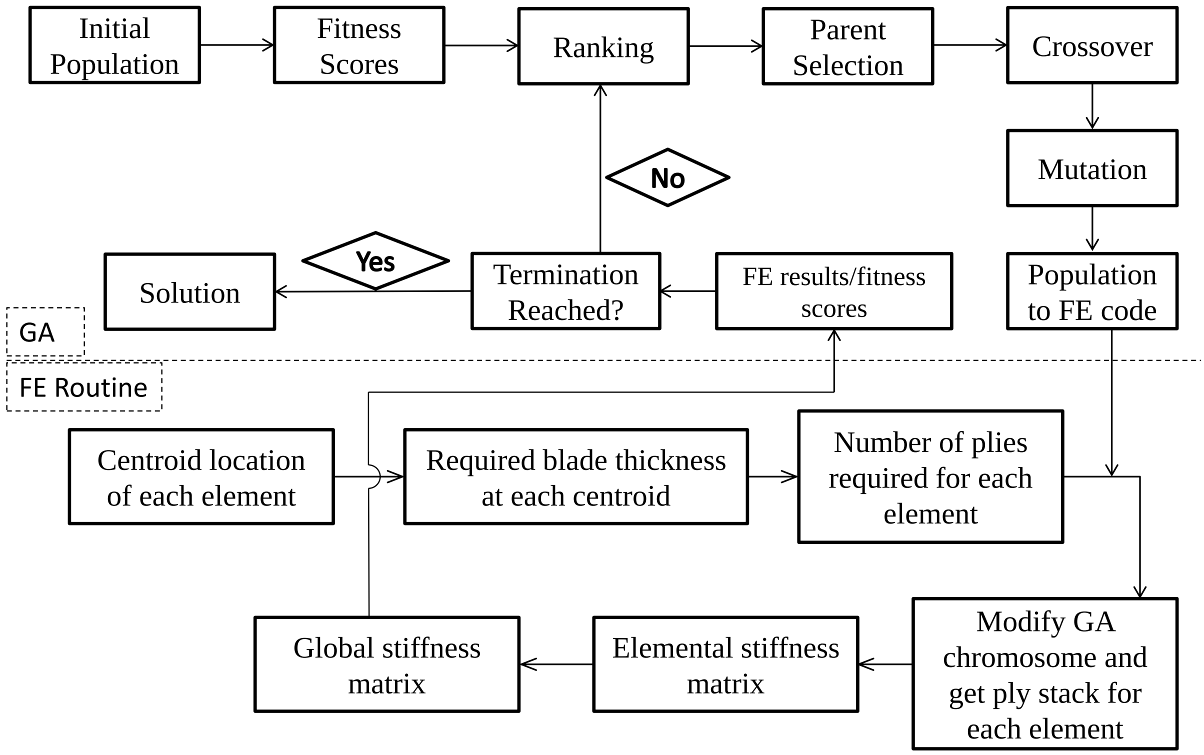

Figure 3-14: Process flow for GA coupled with the FE code with ply termination routine

3.5. Conclusion

The chapter presented an optimisation scheme developed for the layup optimisation of composite propeller blades and hydrofoils. The optimisation process was performed by a Finite Element solver coupled with the Genetic Algorithm. Two finite element codes based on shell element formulation were developed in-house to achieve this. One finite element solver was based on linear triangular elements using Cell-Based Smoothed Finite Element method using Discrete Shear Gap method, while the second finite element method was based on a NURBS based mesh. The CS-FEM code was less complicated to implement and as it was based on triangular elements, any shape was able to be meshed. The NURBS based finite element method had the advantage of being able to capture the exact shape of the geometry without any mesh defeaturing. Hygrothermal effects were also taken into account for the added accuracy of the solution process. The thickness variation of the blade geometry was accounted for by eliminating composite layers from the element to closely approximate the local thickness at the location of the element.

The finite element codes were coupled with the Genetic Algorithm to solve for the ideal ply angles of the blade. The Genetic Algorithm was used in both continuous variable and discrete variable settings in order to account for the manufacturing requirements of specific applications. The Genetic Algorithm worked robustly coupled with finite element solvers and was able to provide accurate layup angle based on twist change requirements. Further note that the chapter was dedicated to presenting the optimisation techniques and mathematical algorithms developed in this research.

4. Optimising a hydrofoil based on previous cavitation tunnel tests

Preface

The purpose of this chapter is to present the functionality and processes involved in optimising a hydrofoil blade using the optimisation technique outlined in Chapter 3. The chapter discusses all steps involved in the design process in detail with relevant attention given to validation studies where necessary. The design process outlined here is based on actual experimental results rather than pure simulation based results in order to further improve the confidence of the process and expected outcomes of the experiments that will be performed on the optimised hydrofoil. A summary of the optimisation steps detailed in Chapter 3 is given below:

1. Construct a relationship between required change in pitch/twist versus the change in flow conditions
2. Generate equivalent pressure maps for the idealised mid-plane of the structural domain
3. Construct nodal pressure difference maps relative to the design flow condition, using pressure maps generated in Step 2.
4. Select weightages based on the importance of off-design conditions and select deformation structural constraints that must be imposed on the hydrofoil.
5. Use the GA coupled FEM optimisation routine to converge to the best possible ply angle combination that can provide the required change in twist for the change in pressures.

6. Use the unloaded shape iteration scheme to find the required unloaded shape such that the optimised hydrofoil blade reaches the twist of the baseline hydrofoil blade at its design flow condition.

4.1. Introduction

In order to validate the layup optimisation technique and the unloaded shape iteration scheme, an optimised hydrofoil was designed based on conventional hydrofoils that underwent cavitation tunnel hydrodynamic experiments. The specific motive behind the optimisation effort was to design a hydrofoil that performs better, in other words demonstrates a wider lift to drag ratio curve compared to non-optimised hydrofoils. Prior to optimisation, hydrodynamic results obtained by cavitation tunnel testing were verified using ANSYS CFX™. These results were then used as the basis for optimisation of hydrofoils.

The hydrofoil that was tested is a modified NACA0009 (Eq.(4-1)) with the chord linearly tapering from 120mm (root) to 60mm (tip) over a span of 300mm. Additionally, the clamp was 110mm in order to fit within the clamping mechanism of the load cell. The modification had been made to the standard NACA 00XX[2] profile in order to account for the extra thickness formed during the manufacturing process of the composite foil and avoid a shape resin edge at the trailing edge. The modified equation and the resulting half-thickness distribution for the hydrofoil are given in Eq. (4-1) and Figure 4-1, respectively (Zarruk et al., 2014)

$$\frac{y}{c} = 5t(0.2969\bar{x}^{0.5} - 0.126\bar{x} - 0.3516\bar{x}^2 + 0.2843\bar{x}^3 - 0.08890\bar{x}^4) \qquad \textbf{(4-1)}$$

[2] Refers to the profile of a standard NACA 4-digit series hydrofoil with no camber

where y is the height to the top surface measured from the mid-plane, t is the maximum thickness to chord ratio (for NACA0009 $t = 0.09$) and $\bar{x}$ is the distance measured from the leading edge normalized with respect to the chord length $\left(\bar{x} = \frac{x}{c}\right)$.

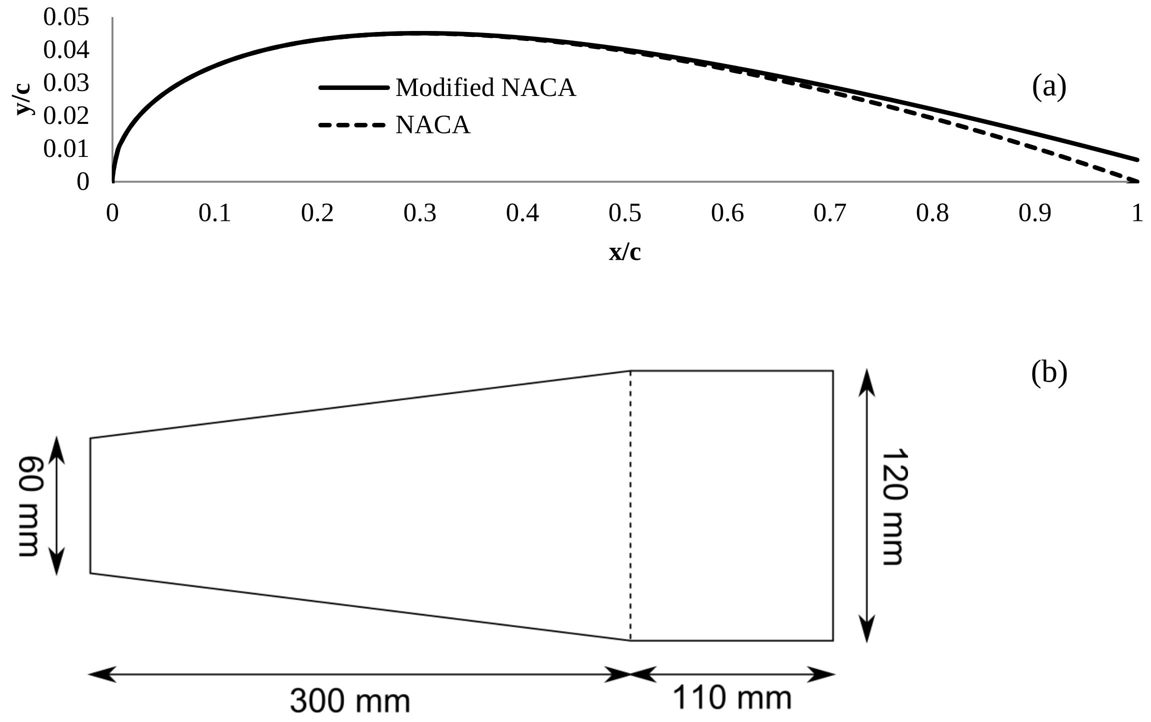

Figure 4-1: The profile of the optimised modified NACA0009 hydrofoil: (a) Cross-section & (b) plane-form

Verification of the CFD technique

4.2. Verification of the CFD technique

Prior to generating ideal efficiency curves and pressure maps for the optimisation process, the accuracy of the CFD technique was verified against hydrodynamic results obtained from cavitation tunnel experiments. The tests were performed on similar hydrofoils by Zarruk et al. (2014). CFD simulations required for the optimisation process were performed using the commercial CFD code ANSYS CFX™.

Two fluid domains were created for verification purposes: one that is identical in dimensions to the test section (0.6m × 0.6m × 2.6m) of the Australian Maritime

College (AMC), Tasmania cavitation tunnel facility and another that has a parabolic domain. The parabolic domain was used so that the changes in angle of attack can be implemented relatively easily without the interference of the side-walls of the domain. Although the parabolic domain is different to the actual test section, since the specimen is placed such that there were no considerable wall effects due to the limited experimental domain, both domains produced identical results in terms of hydrodynamic measurements. Thus, for later analysis the parabolic domain was used to obtain measurements by varying the angle of attack (AoA). Following initial mesh

convergence tests, the rectangular domain was meshed with just under 40 million cells while the parabolic domain was meshed with approximately 55.5 million cells. All simulations were performed as steady state analysis with governing equation residual targets set to 10^{-5}. The Shear Stress Transport (SST) turbulence model was employed to capture the turbulence effects. Under these general settings, the models were solved in a cluster computing system using 96 cores (Leonardi cluster computing system at University of New South Wales, Australia).

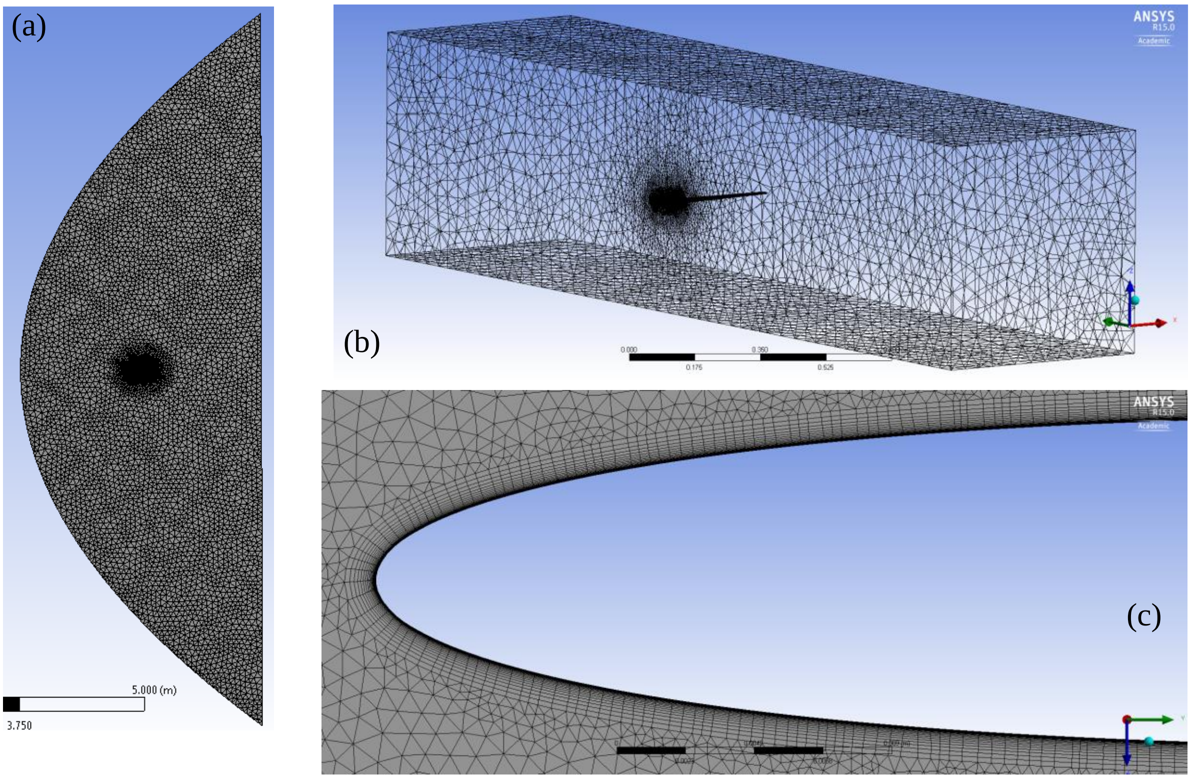

Figure 4-2: CFD Domains used for validation studies: (a) The parabolic fluid domain, (b) The rectangular fluid domain and (c) Mesh around the hydrofoil cavity

A major advantage of a parabolic domain is that the control of angle of attack (AoA) is much easier compared to the control of AoA of a rectangular domain. On a parabolic domain, change in AoA meant simply changing the vector components of the velocity at the inlet. Due to the inlet completely surrounding the foil specimen in the middle, there were no wall effects due to the change in AoA. However, in the rectangular domain, in order to change the AoA, the model had to be reconstructed with the change in the angle of hydrofoil cavity of the fluid domain followed by remeshing for each change in AoA. Changing components at the inlet is not recommended due to the prevalence of wall effects from top and bottom walls resulted by the flow not being parallel to the walls. Although changing the AoA of the cavity is in line with the experimental procedure, the parabolic domain did not demonstrate a measureable difference in results when compared against the rectangular domain. Thus, for validation purposes the parabolic domain was utilized.

For validation purposes, the lift coefficient and the drag coefficient were evaluated at Reynold's Number 0.6×10^6. The angle of attack was varied on the parabolic domain by 2º increment from 2º to 12º. Figure 4-3 shows the results obtained from CFD simulations, while comparing them to C_L and C_D values calculated based on measurements taken during experiments, as demonstrated by (Zarruk et al., 2014). Figure 4-4 summarises the complete spectrum of C_L and C_D curves obtained for the stainless steel modified NACA hydrofoil.

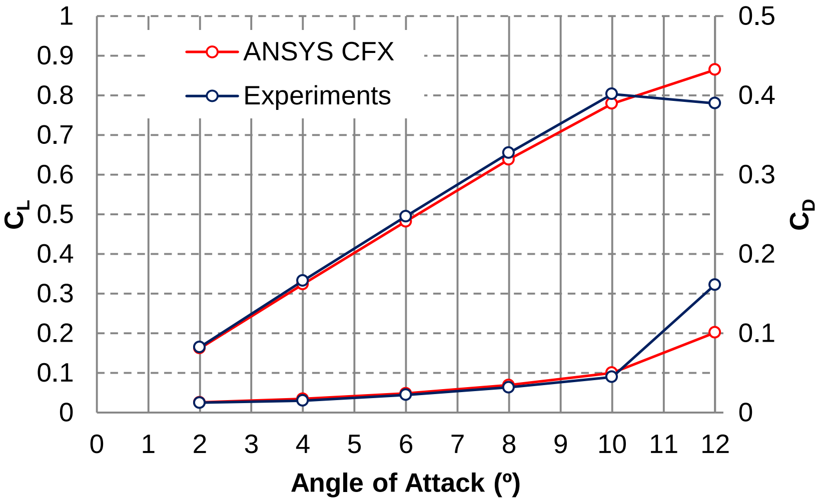

Figure 4-3: Results obtained for lift coefficient and drag coefficient against AoA

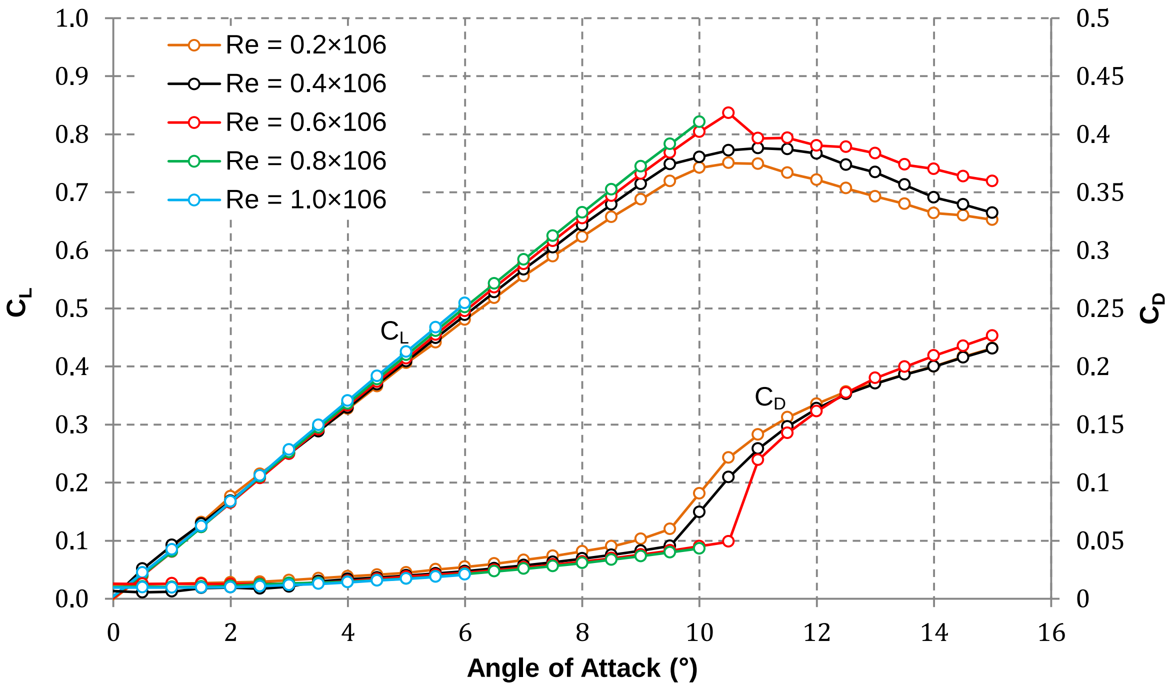

Figure 4-4: Variation of C_L and C_D for modified NACA profile at various Reynold's Numbers (Zarruk et al., 2014)

It is clear that the results correlation is satisfactory with CFD simulations being able to accurately determine C_L and C_D value as well as the break-away points (stall points) from their inherent linear trends. From Figure 4-4 it is also evident that non-dimensional hydrodynamic measurements do not depend on the speed of the flow, but rather the angle of attack sufficiently away from stall conditions. This is, in fact an established concept for rigid aero and hydrofoils at moderately high Reynold's numbers disregarding high speed and low speed Reynold's number effects. However, this establishment cannot be maintained for shape-adaptive hydrofoils as later explained in Chapter 6. With the confidence gained from these simulations, further models were constructed to develop L/D curves for optimisation tasks.

4.3. Construction of efficiency curves

Step 1 of the proposed optimisation scheme is to develop a relationship between the change in flow conditions (and the resulting pressure changes) and the required change in twist. This was achieved by using a series of efficiency curves for various pitch/twist angles. In the case of marine propellers, most standard propeller series have propulsion efficiency curves at various twist angles constructed as a result of prior open-water experiments. A typical series of efficiency curves for a marine propeller is given in Figure 4-5. In Figure 4-5, different curves represent propulsion efficiency variations against AoA for blades with different pitch values.

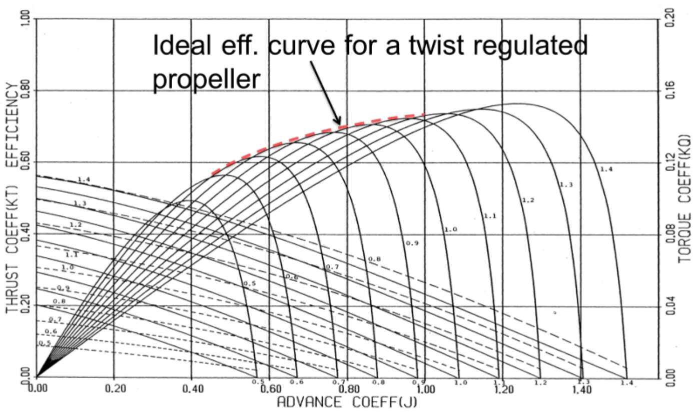

Figure 4-5: A typical propeller efficiency curve series

However, for the hydrofoil considered in this design and optimization task, such curves do not exist. In fact, for the case of hydrofoils, it is ambiguous to define a term named efficiency. Therefore, the lift to drag ratio was chosen as the efficiency, the equivalency between propulsive efficiency of a propeller and the lift to drag ratio of a hydrofoil is explained in Chapter 1. Typical propeller series have efficiency curves constructed against the advance ratio of the propeller. The advance ratio is proportional to the ratio between advance speed and rotational speed. Thus, advance ratio is strongly correlated to the angle of attack (Chapter 1). As stated earlier, AoA is the governing factor of non-dimensional quantities to a greater extent for NACA shapes for Reynold's numbers sufficiently away from extremely low or extremely high. The optimisation scheme outlined in Chapter 2.1 is reliant on such efficiency curves. Thus, L/D curves had to be generated for the hydrofoil that was tested before being optimised.

In order to generate L/D curves, CFD simulations were performed for twisted hydrofoils at various angles of attack. These twisted hydrofoils emulate the differently pitched propeller blades in a typical series of open water propeller efficiency curves. Five different twist conditions were considered for simulations:

1. Flat (no twist) hydrofoil
2. A hydrofoil with tip angled 1° upwards (Tip: +1°)
3. A hydrofoil with tip angled 2° upwards (Tip: +2°) (Figure 4-6)
4. A hydrofoil with tip angled 1° downwards (Tip: -1°)
5. A hydrofoil with tip angled 2° downwards (Tip: -2°)

Figure 4-6: Hydrofoil with tip angled +2° relative to the root

For each of these hydrofoils the angle of attack was varied from 2° to 12° at 2° increments and L/D variation was investigated. Figure 4-7 demonstrates the L/D curves obtained as a result of these CFD simulations.

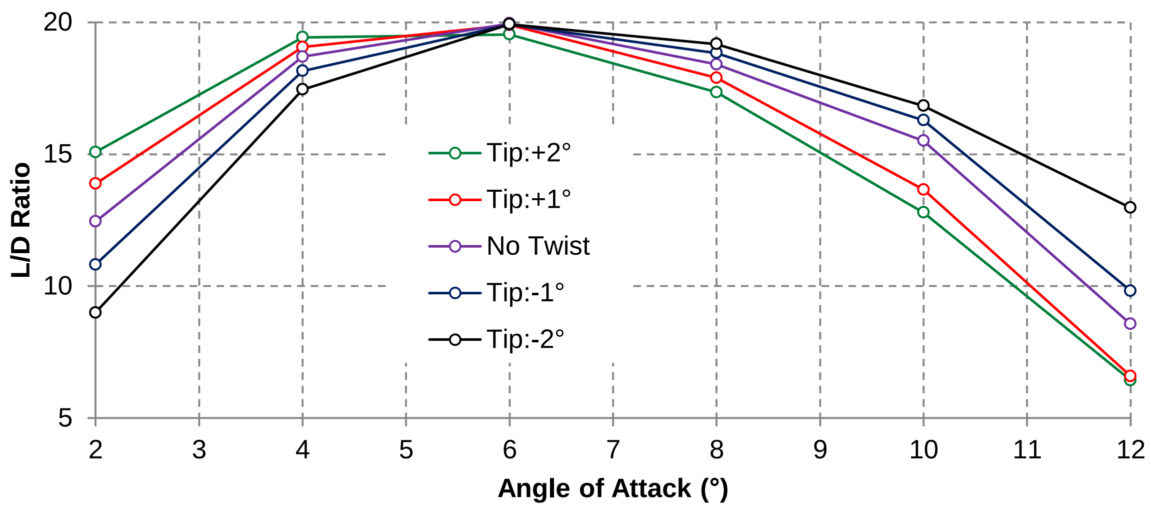

Figure 4-7: L/D curve series generated for the tested hydrofoil

It was observed from the L/D curves that there was a convergent point at approximately 6º angle of attack. Here, a convergent point in the L/D curves refers to a point on the curves where most hydrofoil twist values appear to converge towards and diverge away from each other. At this point, the non-twisted hydrofoil performs with its peak L/D ratio (efficiency). This point can be defined as the **operating condition** for the hydrofoil. If the operating conditions/AoA deviate from this point it is clear that the non-twisted hydrofoil does not perform as well as other twist hydrofoils. For example, if the angle of attack is reduced to 4º, the best performing hydrofoil is the foil that is twisted 2º upwards and if the angle of attack is increased to 8º, the best performing hydrofoil is the foil that is twisted 2º downwards. Thus the idea of optimisation is to achieve a layup that can produce the required twist under the changes in pressure. In addition to the better L/D response, it is also clear, with the help of Figure 4-4, that the stall point can also be potentially delayed as a result of optimum pitch variation. In the context of a propeller, the delay in stall may translate to a reduction in turbulence, cavitation and noise. Thus, by optimising the layup the expectation is that the L/D curve will widen performing better than a simple rigid untwisted hydrofoil.

4.4. Generation of pressure maps from CFD

Steps 2 of the optimisation process requires the extraction of pressure maps from CFD domain to be applied on to the structural domain idealised to the mid-plane of the hydrofoil. The optimisation technique developed depends upon the correct application of pressure loads at different angles of attack. Thus, pressure loads around the hydrofoil calculated in the previous CFD simulations had to be applied on to the structural domain. In order to achieve this, the pressure normal to the hydrofoil surface at each CFD domain node at the hydrofoil cavity was obtained from ANSYS CFX along with the normal vector at the corresponding point. Afterwards, individual vector components of pressure were calculated and each fluid node was projected on to the plane of the structural domain. Additionally, the pressure moment resulted due to the projection distance was also calculated and stored with the location of the projected fluid node. Two projections were performed based on the top and bottom surfaces of the hydrofoil.

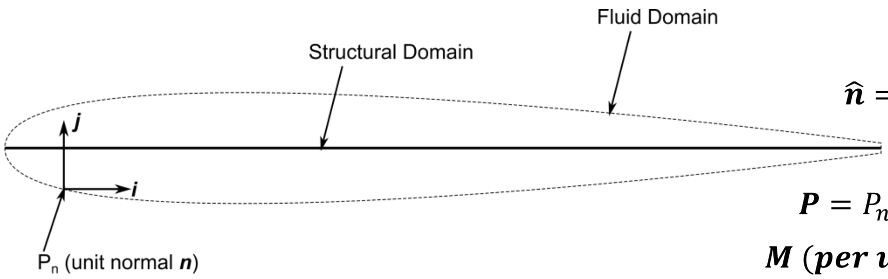

$$\hat{\boldsymbol{n}} = x\hat{\boldsymbol{\imath}} + y\hat{\boldsymbol{\jmath}} + z\hat{\boldsymbol{k}}$$

$$\boldsymbol{P} = P_n.\hat{\boldsymbol{n}}$$

$$\boldsymbol{P} = P_n x\hat{\boldsymbol{\imath}} + P_n y\hat{\boldsymbol{\jmath}} + P_n z\hat{\boldsymbol{k}}$$

$$\boldsymbol{M}\ (\boldsymbol{per\ unit\ area}) = \boldsymbol{d} \times \boldsymbol{P}$$

Figure 4-8: Load transfer from fluid domain to the structural domain

However, there arises a difficulty in transferring loads between two domains which do not have perfectly coinciding nodes. This difficulty was overcome using triangular interpolation between nodes. Prior to interpolation, projected fluid domain nodes were first arranged according to Delaunay triangulation to improve the quality of triangles that are used for interpolation (originally presented by Delaunay (1934)). The purpose of Delaunay triangulation is to eliminate highly skewed triangles being used in the interpolation process. Lee and Schachter (1980) presented a fast and efficient methodology for performing Delaunay triangulation. In Euclidean 2-D space this idea can be explained as constructing the circumcircle by taking three nodal points making sure that no other nodal points lie within the constructed circumcircle. If a nodal point lies within the circle, construct a circumcircle using the point that lied within the previous circle and re-check for any points lying within the new circle. If no points lie within the circle, the triangle formed by the three points is a Delaunay triangle. This process has to be repeated until all points are arranged using Delaunay triangulation, in other words, all circumcircles are empty. The solid black lines in REF _Ref416618026 \h Figure 4-9 demonstrate correct division of Delaunay triangles. It is clear that each of the two circles is empty. The two triangles formed by the dashed blue line represent incorrect division of Delaunay triangles. It is clear that in such a division of triangles, the circumcircles are not empty. Furthermore, the two triangles formed by such a division are more skewed compared to the Delaunay triangles. This task was performed using Matlab™ using the built-in Delaunay triangulation toolbox.

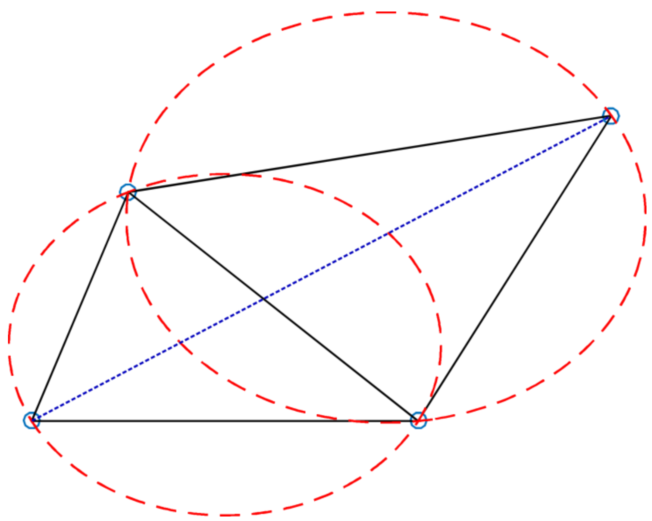

Figure 4-9: Delaunay triangulation triangle selection

After triangulation was performed, components of pressure and pressure moment at each Gauss point were estimated using triangular interpolation using the triangle surrounding the required Gauss point (Figure 4-10). Interpolation was performed for the projection of top hydrofoil surface and bottom hydrofoil surface individually and the vector sum of each component was taken as the final value on each Gauss point. Further note that, as pressure is extracted, values at Gauss points of the structural domain have to be considered rather than nodal points. Within the FE solver the surface integral will then calculate the force on each structural node using numerical integration using Gauss point values.

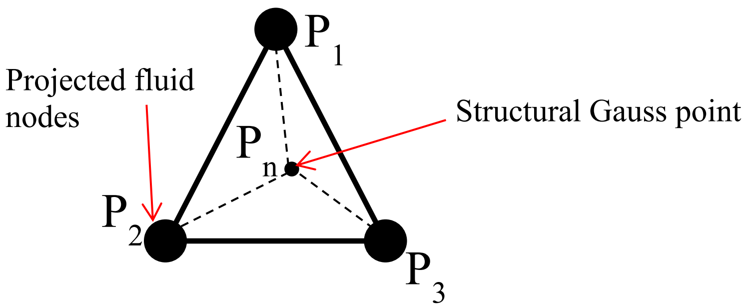

Figure 4-10: Triangular interpolation to find P_n at the Gauss point

In Triangular interpolation, the interpolant is based on the areas of the triangle formed by the Gauss point in the middle. The value at the point can be estimated by taking the area ratio of each small triangle with respect to the large triangle (Figure 4-11).

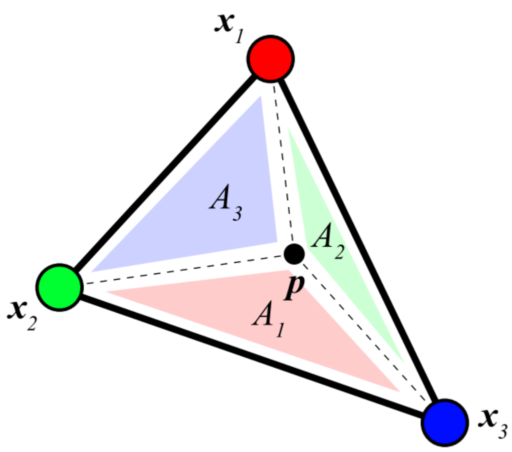

If x_1, x_2 and x_3 are the values at the three external nodes, the value at the internal Gauss point p is:

$$p = \frac{1}{A}(A_1 x_1 + A_2 x_2 + A_3 x_3)$$

Figure 4-11: The concept of triangular interpolation

Step 3 of optimisation scheme was to generate pressure difference maps for each off-design point relative to the design point. Generating pressure difference maps was a straight forward task after pressure values were obtained at each Gauss point. The difference between off-design and design pressure (along with pressure moment) for each gauss point was calculated by taking component-wise difference. Pressure difference maps were then used in the optimisation scheme to optimise for the required angle change at the tip.

4.5. Layup optimisation

After the fundamentals of optimisation were established, the hydrofoil layup optimisation was performed using overall material properties listed in Table 4-1. These properties were obtained by DSTO based on coupon testing performed according to relevant ASTM standards. Here ASTM D3039 was used to evaluate axial tensile properties, ASTM D3518 was used evaluate shear properties for all materials except the Infusion Mat and ASTM D5379 was used to evaluate shear properties of the glass infusion mat.

1. Unidirectional 300gsm/12k carbon fibre
2. Bi-axial 130gsm glass basket weave (not included in the optimisation process due to the negligible effect towards laminate stiffness)
3. Random short fibre 780gsm glass infusion Mat
4. Kinetix™ R118/H103 resin/hardener system

	Carbon UD	**Infusion Mat**	**Glass Basket weave**	**Resin**
E_{11} (GPa)	117.8	6.8	15.3	3.27
E_{22} (GPa)	11.4	5.0	12.8	3.27
E_{33} (GPa)	11.4	5.0	4	3.27
G_{12} (GPa)	3.9	2.5	3	1.26
G_{13} (GPa)	3.9	2.5	3.2	1.26
G_{23} (GPa)	4.786	1.92	3.2	1.26
$\boldsymbol{\nu_{12}}$	0.253	0.301	0.13	0.3
$\boldsymbol{\nu_{13}}$	0.253	0.301	0.25	0.3
$\boldsymbol{\nu_{23}}$	0.2	0.301	0.25	0.3
Density (kg/m^3)	1590	1380	1690	1130
Thickness (mm)	0.25	2.5 (nominal)	0.1	N/A

Table 4-1: Material properties used for optimisation

The purpose of the infusion mat layer was to promote efficient resin distribution during the infusion process reducing the chances of developing any resin dry regions in the laminate. The extent of the infusion mat layer was determined by a combination of manufacturing experience and the commercial composite part modeller ANSYS Composite PrePost™. The ply termination scheme explained in Chapter 3.4.3 was then used to internally terminate carbon layers used in the optimisation routine based on the size and distribution of the infusion mat layer and the locational total thickness of the hydrofoil. The shape of the infusion mat layer generated by ANSYS Composite PrePost™ is given in Figure 4-12.

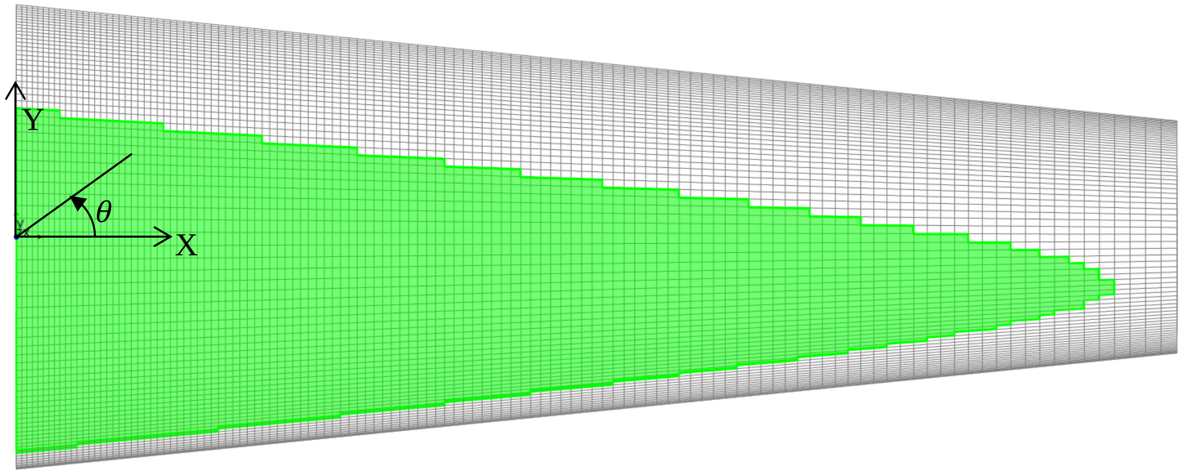

Figure 4-12: Extent of the infusion mat layer (approximately 275mm in length measured from the origin)

As explained in detail in Chapter 3, the optimisation technique proposed in this work attempts to achieve the ideal required change in twist under the change in pressure due to the change in AoA. The ideal required change in twist was estimated using the L/D curve series generated for the hydrofoil (Figure 4-7). The design point was chosen as the 6° AoA point due to the convergence of curves in the vicinity of 6° AoA and due to baseline non-twisted hydrofoil achieves its peak L/D at this AoA. Using Figure 4-7 the following relationship between change in AoA and required change in tip angle was formed:

Angle of Attack	**Pressure change (ΔP)**	**Ideal change in tip angle relative to root**
4°	$\sum_i (P_{Gauss_{4^0}} - P_{Gauss_{6^0}})$	+2°
6° (Design AoA)	0	0°
8°	$\sum_i (P_{Gauss_{8^0}} - P_{Gauss_{6^0}})$	-2°

Table 4-2: Change in angle of attack vs ideal required change in tip angle

Step 4 in the optimisation scheme is to select structural constraints and weightages. For this a rather conservative maximum deflection constraint was set on the hydrofoil when transiting between design AoA and off-design AoA. This rather conservative target was set to be 2mm between two points. The choice of 2mm was governed by deflection observed by Zarruk et al. (2014). The baseline carbon hydrofoil with a predominantly 0° carbon layup was observed to deflect 1.81mm for a change of 2° in AoA at $Re = 0.6 \times 10^6$ flow speed. It was assumed that the optimised hydrofoil was allowed to deflect 10% higher than the baseline hydrofoil without compromising the safety of running cavitation tunnel experiments. Here, it must be noted that 2mm is the deflection when transiting from design to off-design conditions at a Reynold's Number of 0.6×10^6. The actual deflection throughout the operation of the hydrofoil is in fact much larger. Furthermore, both off-design points were considered to be of equal importance; thus, an equal weightage of 1 was assigned for both off-design points.

Based on this information, the objective function was setup as given in Eq. (4-2) and **Step 5**, layup optimisation using GA coupled FEM, was performed.

$$\min_{\boldsymbol{\theta}} f(\boldsymbol{\theta}) = 10^{1000|d_{max}(in\ mm)-2|} \times \frac{\sum_{i=1}^{2} w_i \left| \Delta\phi_{Optimum}^{i}(\Delta P) - \Delta\phi_{GA}^{i}(\boldsymbol{\theta}, \Delta P) \right|}{\sum_{i=1}^{n} w_i} \tag{4-2}$$

Optimisation was performed using the GA coupled FEM solver as mixed-integer optimisation with allowable angles being 5° or 15° fibre angles. The main driving factor in choosing mixed-integer optimisation was simplifying the hand-layup process during manufacturing. The final ply angle results and the achieved objective function values are given in Table 4-3. The angles in this optimisation task were measured counter-clockwise from positive x-axis to the positive y-axis (coordinate system given in Figure 4-12). The convergence plot of GA for the 15° increment case is given in Figure 4-13.

The maximum deflection observed was 2mm, in compliance with the penalty criterion in the objective function (Eq. (4-2). This was observed when the hydrofoil increased the angle of attack from 6° to 8°. It was observed that much higher twist values can be obtained by releasing this constraint, however, for safety and reliability the deflection constraint was imposed. Further improvements in the FEM can be made with composite failure criteria taken into account instead of deflection based constraints.

Increment	**Layup**	**Obj. Function (Rad)**
5 deg	$[(-25)_2/30/(-25)_4/(75)_3/(-25)_4/-15/\overline{Mat}]_S$	0.0282
15 deg	$[(-30)_2/30/-30/75/-30/75/(-30)_4/75/(-30)_2/-15/\overline{Mat}]_S$	0.0283

Table 4-3: Optimum ply angles based on GA optimisation

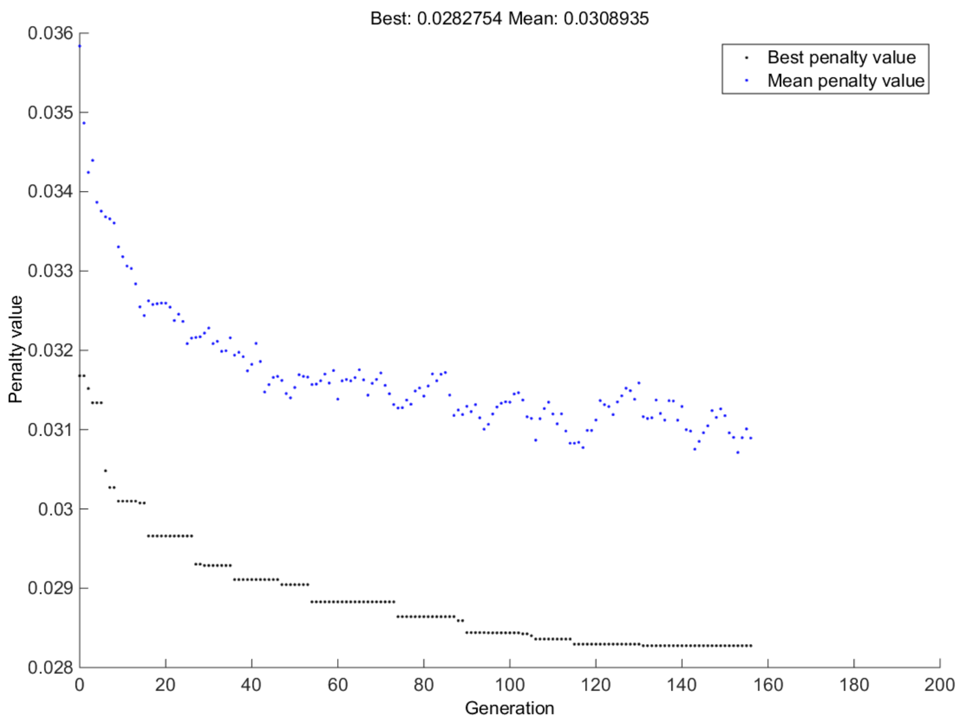

Figure 4-13: GA convergence for 15° increment case

The above results take into account ply termination based on the thickness variation of the hydrofoil. Ply drop-offs were assumed to be starting from the inner-most layers, in other words, the inner layers starting from angle -15º terminate first, while the outer layers starting from -30º continue without termination.

4.6. Unloaded Shape

Achieving the unloaded shape was a separate iteration process after the GA had converged to an optimum ply stacking sequence. The unloaded shape iteration process was automated by coding into the finite element solver developed in Matlab. The location in space for the i^{th} node in the required shape (flat shape) is represented by $\boldsymbol{x_i^r}$. In each iteration, the node cloud for the next iteration ($\boldsymbol{x_i^{n+1}}$) was updated as presented in Eq. (4-3).

$$\boldsymbol{x}_i^{\boldsymbol{n+1}} = \boldsymbol{x}_i^{\boldsymbol{n}} + \left(\boldsymbol{x}_i^{\boldsymbol{d}} - \boldsymbol{x}_i^{r}\right) \tag{4-3}$$

$\boldsymbol{x_i^d}$ represents the location of the i^{th} node after applying the load on to the current shape iteration. The location of the i^{th} node in the current iteration is represented by $\boldsymbol{x_i^n}$.

The shape iteration continues until the total distance between the required and achieved shape is less than the threshold set for the iteration process. The total distance is the sum of all distances between required and achieved nodes, as calculated by Eq. (4-4). For the iteration process to terminate, Eq. (4-4) must be satisfied. In these iterations, the threshold was taken as 0.1mm. The iteration process converged in four iteration steps. The element plot of the unloaded shape is given in Figure 4-14. The final unloaded shape the Matlab routine converged to have a sag just over 11mm with a tip angle of +1.34º.

$$\sum_i \left| x_i^d - x_i^r \right| < threshold \tag{4-4}$$

After the unloaded shape was achieved, the mould was constructed in the CAD software ProEngineer Wildfire using the exact nodal points given by the Matlab routine.

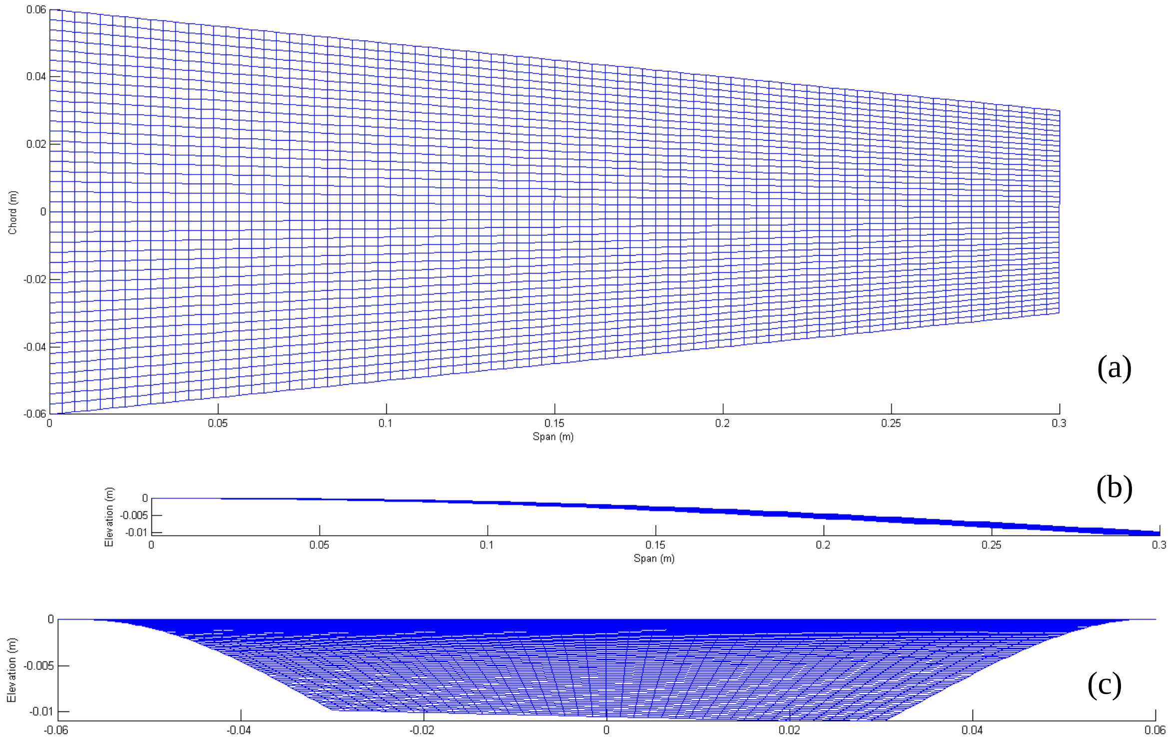

Figure 4-14: Unloaded shape the Matlab routine converged to: (a) Top view, (b) Front view & (c) Side view

4.7. Mould Design

The mould was manufactured an assembly of four major components: the top plate with the cavity, the bottom plate with the cavity and the two support plates used to maintain the shape under vacuum during the infusion process. All standard accessories required for a mould, such as release pins, locating pins, handles, etc. were included in the mould. Aluminium 6061-T6 was decided to be used due to its good strength, light weight and manufacturability. The hydrofoil cavity was constructed based on the mid-surface of the unloaded shape given in Figure 4-14. The modified NACA0009 profile

(Figure 4-1) was constructed around the mid-surface. Detailed technical drawings of the mould are given in Appendix A. A rendered image of the mould is given in Figure 4-15.

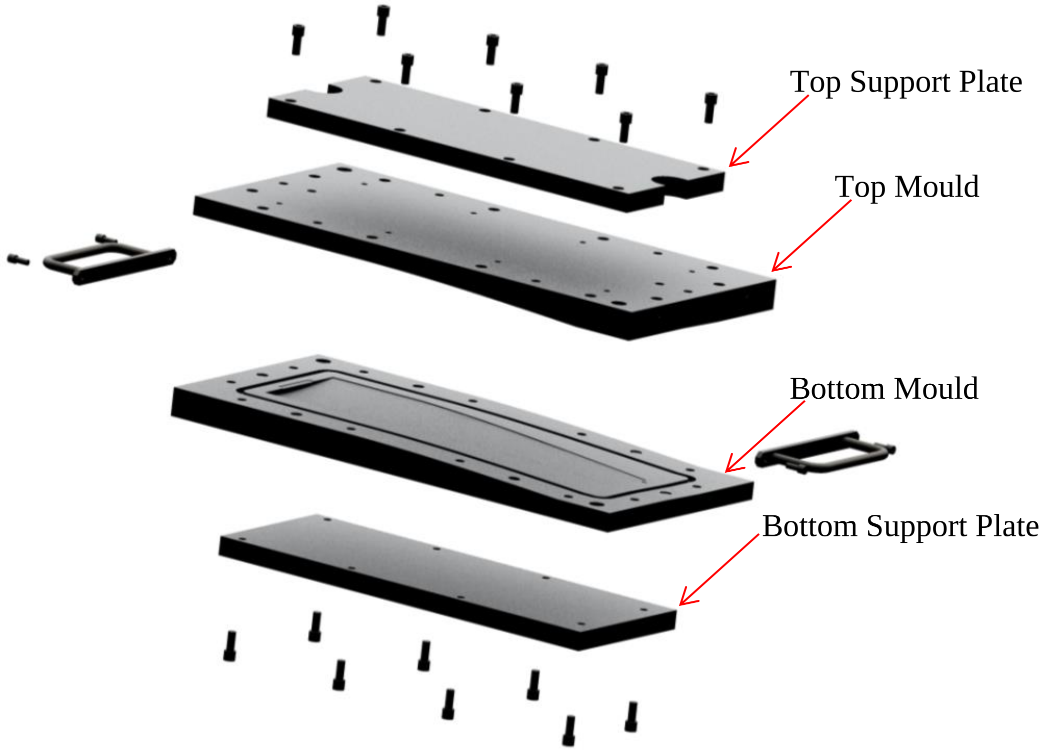

Figure 4-15: Software render of mould assembly

A 3-axis CNC mill (Figure 4-16) was used to create the mould hydrofoil cavity up to an accuracy of 0.05mm and a surface finish of N6. Due to the use of a 3-axis mill, there were difficulties in generating a sharp flat trailing edge prescribed for a modified NACA profile (Figure 4-1). As a result, a rounded trailing edge of a radius of 0.5mm was created. Furthermore, a radius of 1mm was created at the tip of the hydrofoil cavity. The O-ring cavity was also created as a part of the milling process.

After the construction of the mould was completed, the cavity of the hydrofoil was hand polished progressively down to a surface finish of 0.05 micron. The final polishing stage of 0.05 micron was achieved using alumina paste (Figure 4-17). Afterwards, permanent and temporary mould release agent layers were coated in the cavity surfaces and around the cavity where resin flashing is expected during the infusion process. The final step was installing the O-ring for proper sealing during the vacuum infusion process. An open ended solid silicone rubber O-ring with an outer diameter of 6.5mm was used as the O-ring for the mould. Sealant tape typically used in composite vacuum bagging was used at the open ends of the O-ring to complete the O-ring loop and prevent any vacuum leakage during infusion.

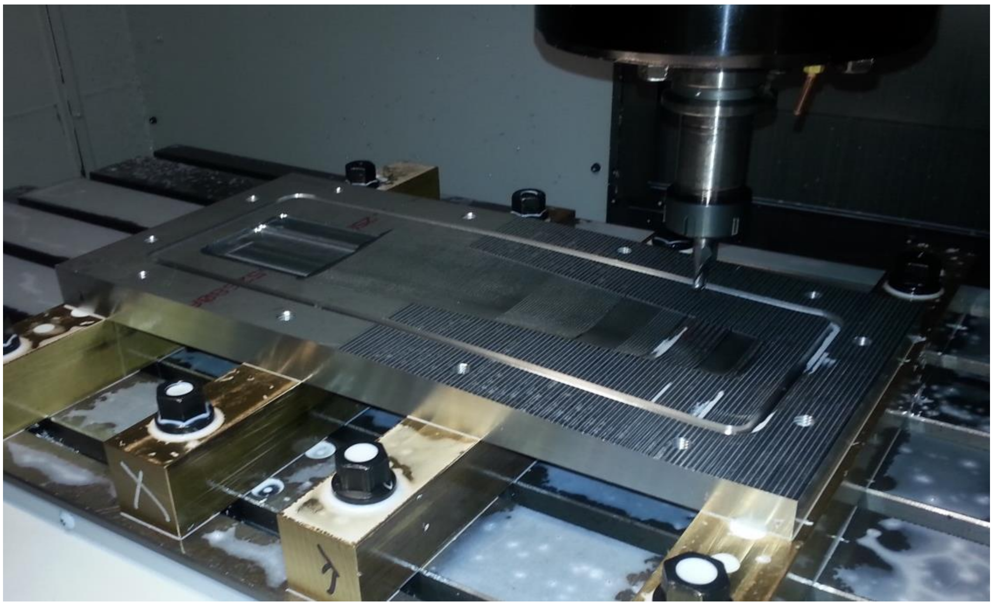

Figure 4-16: CNC milling of the mould

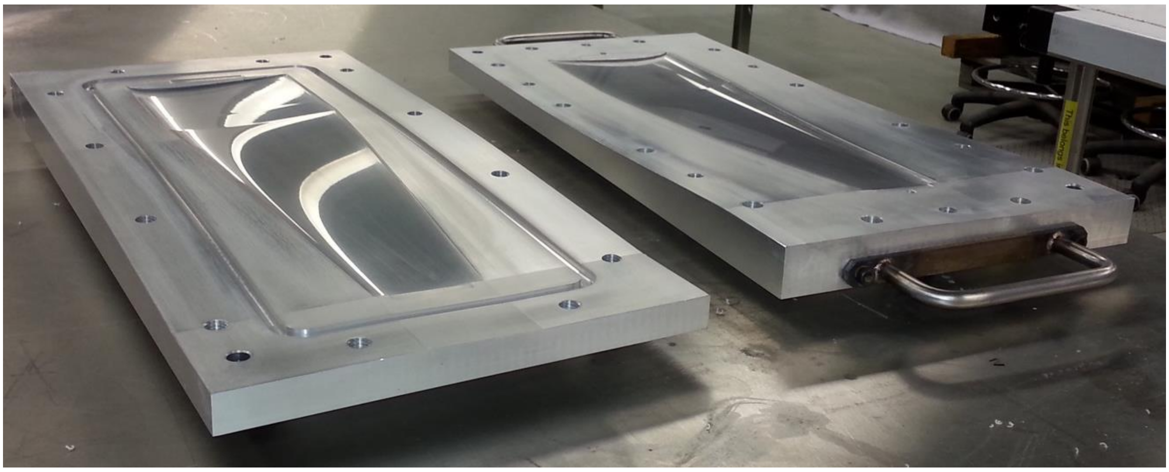

Figure 4-17: Mould halves manufactured and hydrofoil cavity polished

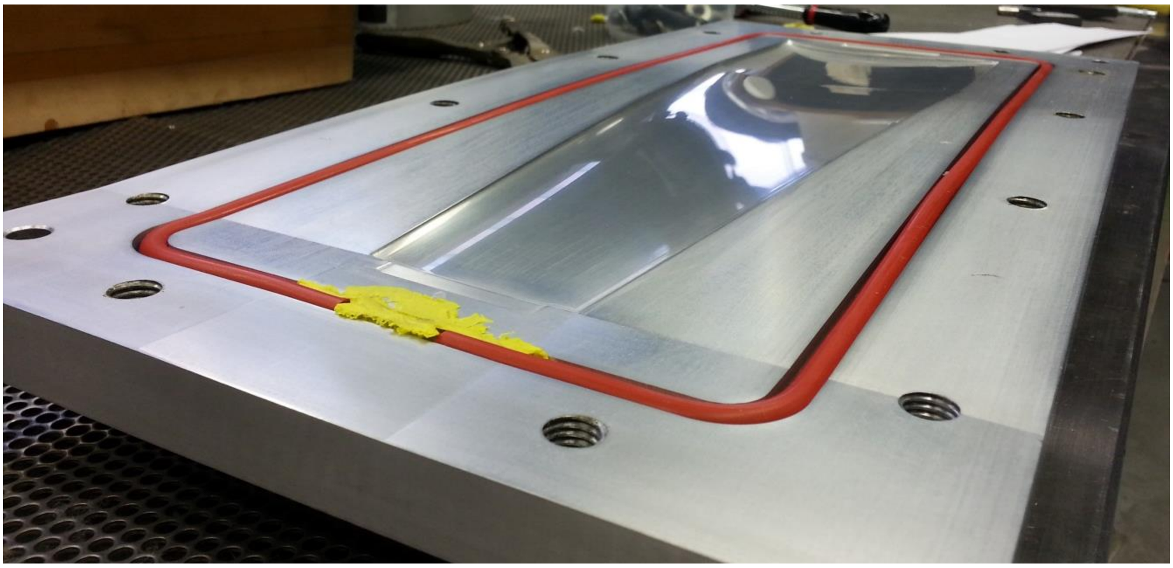

Figure 4-18: Mould with O-ring installed

4.8. Conclusion

The chapter discussed the tasks and processes involved in optimising a hydrofoil based on the optimisation algorithm and tools discussed in Chapter 2.1. The optimisation was based on experimental data obtained from cavitation tunnel tests (Zarruk et al., 2014) performed on similar non-optimised hydrofoils. Since this was an application for hydrofoils, efficiency (L/D) curves had to be generated based on CFD simulations for hydrofoils with different twisting profiles more and less than the baseline flat hydrofoil. Prior to the generation of efficiency curves, the used CFD tools were validated against experimental results and found to match experimental results to a very high accuracy. Based on the L/D curves, the relationship between the required twist change vs the change in AoA was established.

Afterwards, pressure maps at design and off-design conditions were applied on to the structural domain using a Delaunay triangulation based interpolation scheme. From the pressure maps, pressure difference maps for each off-design point relative to the design condition were established. Pressure maps and pressure difference maps were based on the Gauss point locations of the structural domain. This was followed by selecting appropriate structural constraints and weightages to the optimisation scheme. Structural deflection limitations were imposed based on observations in previous cavitation tunnel tests of baseline non-optimised CFRP hydrofoil which had carbon layers oriented in the span direction. In addition, equal weightings were used assuming that all off-design points are of equal importance.

Based on the data and assumptions, the objective function was constructed and the optimisation routine was used in the mixed-integer mode to simplify hand layup and manufacturing. The GA converged to the result $[(-30)_2/30/-30/75/-30/75/(-30)_4/75/(-30)_2/-15/\overline{\mathrm{Mat}}]_S$, based on which the unloaded shape of the hydrofoil was obtained. After the unloaded shape was obtained, the mould was designed for manufacturing of the hydrofoil.

The mould was designed and manufactured as an assembly of four individual components for the ease of manufacture and shape-stability. The mould was manufactured to a high accuracy using 3-axis CNC milling and was later hand polished for a high surface finish of the hydrofoil blade.

5. Structural Experiments

Preface

This chapter presents the hydrofoil manufacturing process and structural experiments that were performed on the optimised hydrofoil. The necessity for a comprehensive manufacturing technique for the hydrofoils and ensuring their strength and safety during cavitation tunnel tests were the motivations behind these endeavours. The ideal manufacturing technique for the hydrofoils was identified as Vacuum Assisted Resin Transfer Moulding (VARTM). However, especially due to the use of a pure carbon layup, the manufacturing technique had to be perfected in order to avoid any resin deficient regions in hydrofoil blades. Quality manufacture of a composite specimen with a complex shape with varying thickness, bend and twist was a challenging task that had to be undertaken with proper control and care.

The same layup derived in Chapter 4.5 was used for the manufacturing of the hydrofoil. To ensure the strength of the layup, the hydrofoil was loaded in cantilevered configuration, similar to what was to be expected in cavitation tunnel experiments, and loaded to failure.

5.1. Introduction

The optimised hydrofoil discussed in Chapter 4 was manufactured to further understand its structural response and failure conditions. Two hydrofoils were manufactured for testing purposes at DSTO's Integrated Composites Facility by using VARTM within a fully-closed mould. The manufactured hydrofoils were subjected to modal frequency testing to ensure the consistency of manufacturing and act as a validation result for the finite element model of the hydrofoil. Afterwards, the hydrofoil was fitted with strain gauges and acoustic emission sensors in preparation for load testing. One of the two manufactured hydrofoils was loaded in a cantilevered configuration to replicate the loads expected in the cavitation tunnel.

As a part of the cantilevered tests, material hysteresis of the specimen was investigated as it was important to ensure that the specimen remains within its elastic limits in the loading range of the cavitation tunnel. The hysteresis tests were performed by using repeated loadings and investigating any loss of stiffness or change in deflection response against load between each run. Hysteresis tests were followed by experiments to measure tip deflections and tip twists in order to investigate whether the bend-twist coupling effect was evident as expected. Strains were also recorded during experiments to understand the surface strain variation against applied load.

The final cantilevered test was performed to investigate the strength of the hydrofoil, by loading up to its failure point. The purpose of this experiment was to ensure that the hydrofoil had adequate strength with a sufficient safety margin to be used in cavitation tunnel experiments. The failed specimen was then tested for any changes in natural frequencies using the same modal frequency test setup. Afterwards, the failed specimen was partitioned into cross-sections and UV fluorescent optical microscopy and Neutron Tomography were used to investigate and understand the type of failure that occurred within the specimen.

The experimental results were used to develop a fully detailed finite element model using the commercial finite element code ANSYS™. Several different methods of modelling the composite hydrofoil were investigated with the intention of picking a modelling technique that has a good balance between solution time and accuracy to be used as the structural domain of FSI simulations. The results obtained from FEA were compared against experimental results to draw any further conclusions about the modelling technique.

5.2. Manufacturing Process

The hydrofoils were manufactured using Vacuum Assisted Resin Transfer moulding (VARTM) process inside a fully-closed mould. A fully-closed mould was necessary, as opposed to a one-sided mould process (such as vacuum bagging) due to the need for high quality surface finish on both sides of the hydrofoil. Two identical hydrofoils were manufactured using the same process with the intention of using one as the failure specimen and the other as the control specimen. In addition, the two hydrofoils also served the purpose of evaluating the consistency of the manufacturing procedure.

The layup was primarily unidirectional carbon fibre, with the addition of the glass infusion mat layer and the glass basket laid on the outside of the foil to provide a smooth surface finish. The glass infusion mat layer was used to achieve a consistent resin flow. The inclusion of the infusion mat layer was an essential part of manufacturing as the unidirectional carbon fabric used was not particularly favourable for vacuum infusion type manufacturing. The unidirectional carbon layer packed densely with each layer making it challenging to achieve a specimen with consistent resin distribution. The inclusion of the infusion mat in the middle of the layup alleviated this issue successfully. As explained in Section 4.5, the inclusion of the glass mat layer was taken into account in the optimisation process. However, the glass basket weave layer was not taken into account in the optimisation task as its stiffness and thickness are considerably lower compared to those of carbon layers. Thus, the contribution from the glass basket layer to the stiffness matrix (ABBD) is negligible. Materials used for the manufacturing process are as follows:

1. Unidirectional 300gsm/12k carbon fibre
2. Bi-axial 130gsm glass basket weave
3. Random short fibre 780gsm glass infusion Mat
4. Kinetix^{TM} R118/H103 resin/hardener system
5. BYK A-500 air release agent

Properties of composites made using above materials have been tested according ASTM standards by DSTO (Table 4-1). Here, ASTM D3039 was used to evaluate axial tensile properties, ASTM D3518 was used to evaluate shear properties for all materials except the infusion mat and ASTM D5379 was used to evaluate shear properties of the glass infusion mat.

Out of the numerous mixed integer optimisations that was performed, the 15^0 increment layup was chosen as the preferred layup to manufacture as it involved angle plies that were relatively easy to cut into shapes. However, it must be noted that the manufacturing technique does not rely on having specific angles for fabric layers. As the plies are cut manually, any ply angle is possible to be manufactured subject to the accuracy of the manufacturer. Thus, the limitation of using a given set of angles such as, 0, 90, 45, etc. does not exist for this type of manufacturing. As a consequence, limiting ply angles during optimisation to a discrete domain as performed by Liu and Young (2009), Lin and Lee (2004), Mulcahy et al. (2011) is not necessary. It is explained in their work that manufacturing difficulties was the primary purpose of limiting the ply angle domain.

The templates were generated using the Abaqus Composite Modeller™ plugin. This manufacturing process and layup strategy does not use a core material to achieve the required shape of the hydrofoil. Instead, the shape is obtained using the shape of the mould cavity and the accurate ply drop-off in order to enable the required thickness variation of the hydrofoil. Internal ply termination strategy was used as opposed to external ply termination in order to achieve a continuous ply on the outer layer of the hydrofoil where stresses due to bending are highest. Thus, these specimens have different, presumably better, strength and stiffness properties compared to an external ply termination strategy. Although internal ply termination was chosen, the infusion mat layer was continued for a larger area in order to enable consistent resin flow in the specimen. However Abaqus Composite Modeller by default does not support such an exception. The strategy that was employed was to use the template generated for a larger ply (ply no. 12) layer as the template for the infusion mat. Afterwards, the layup configuration file in Abaqus was appropriately modified to include this change. Additionally, the infusion mat was split into four layers in the finite element model in order to discretise the varying thickness due to its inherent compressibility. Figure 5-1 demonstrates the cross-section of the layup at the root for the per ply solid model.

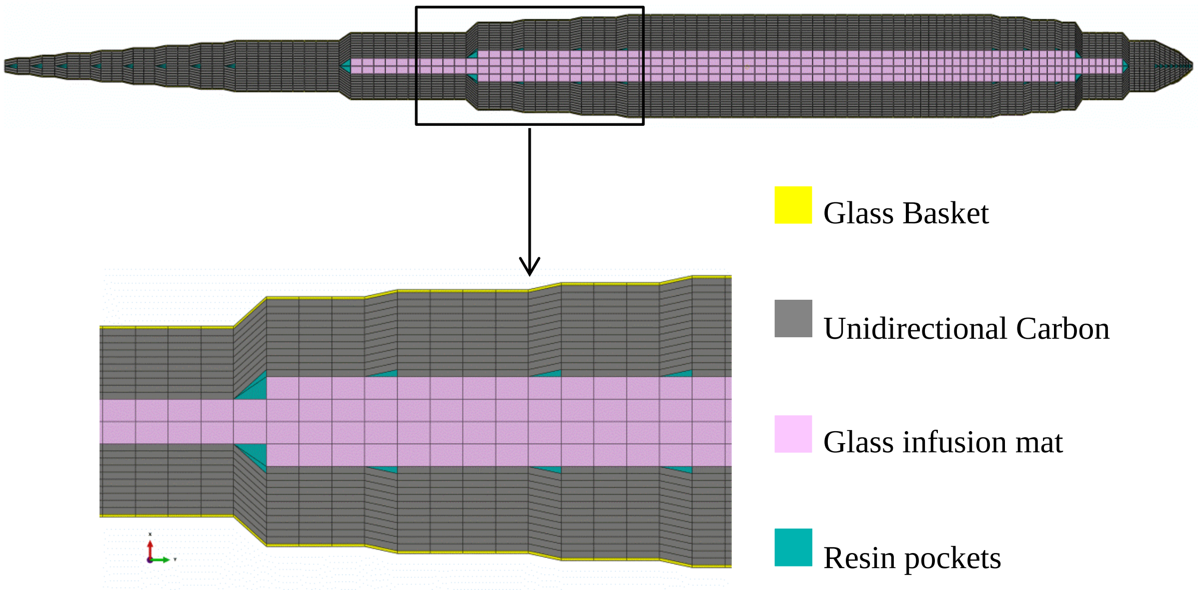

Figure 5-1: Composite ply layup of the root section

5.1.1. Detailed Manufacturing Steps

The first step of manufacturing was cutting carbon layers, glass basket and infusion mat layers to the required shapes and sizes based on the templates that were generated using Abaqus. The cutting process was performed using an octagonal fabric cutter. Although the angles produced by this process are subject to the accuracy of the operator, there are no limitations in terms of the angles that can be cut for each layer. Afterwards, the mould was prepared by removing resin deposits from previous infusion tasks and re-applying mould release agent, if necessary. Fabric layers were then placed inside the mould cavity and were further trimmed if needed. After all the layers, in the top half and the bottom half, were placed inside the mould cavity, the mould was carefully closed and sealed. The vacuum pump and resin reservoir (empty at this stage) were then connected to the mould and was let to consolidate under 5mbar (abs) overnight. This is an essential step for vacuum bagging type resin infusion processes in order to provide the exact shape of the mould and improve the fibre fraction. However, closed mould vacuum infusion processes, such as this, can also be benefitted by vacuum consolidation due to the removal of moisture and other contaminants. After consolidation, the resin was prepared.

The resin and hardener were mixed in 4:1 ratio with half a pipette of BYK A-500 air release agent mixed to enable better air escape during the degassing process. For the hydrofoils, 400g of resin and 100g of hardener (500g in total) was adequate to fill the cavity. Afterwards, the mix was degassed under 4mbar (abs) pressure until gas bubble release rate became considerably small. The resin mix was then connected to the resin inflow port of the mould while maintaining the same vacuum that the mould was left overnight. It was witnessed that the resin flow could take between 120 – 240 seconds, with the first hydrofoil taking 210 seconds and the second hydrofoil taking 130 seconds. Once the resin flow was complete, the hose on the vacuum port was sealed and the pressure on the resin reservoir was increased to 2atm (abs). This process further consolidated the resin inside the cavity while contracting any air bubbles that may have formed during resin infusion. The mould was kept under this positive pressure until the resin/hardener cured to a considerably brittle gel state. Post curing was then performed in an oven at $100^{0}C$ for 4 hours (based on the curing specifications for the R118/H103 system), with an initial temperature ramping of $3^{0}C/min$. After post-curing and sufficient cool down of the mould, the hydrofoil was de-moulded and resin flashing was sanded off.

(a)  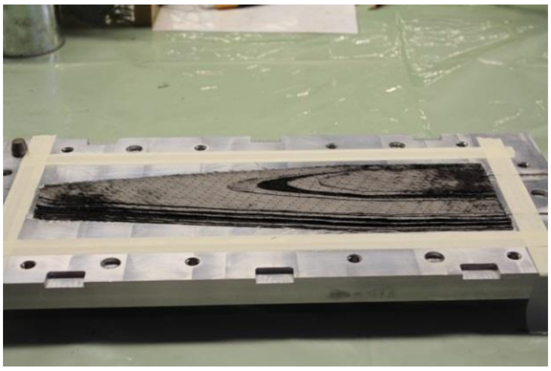 (b)

(c) 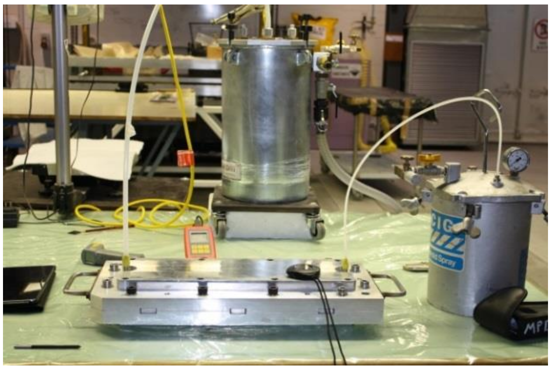  (d)

(e) 

Figure 5-2: Basic manufacturing steps (photos taken for a flat hydrofoil): (a) cutting fabric into required shapes and fibre angles using templates, (b) placing layers inside the mould, (c) vacuum consolidation followed by vacuum infusion, (d) demoulding after post-cure in the oven & (e) final specimen after light sanding and trimming resin

5.1.2. Specifications of the final specimen

After the infusion process, the dimensions and the mass of the hydrofoils were measured to ensure that the hydrofoil has the expected geometric accuracy. The mass of the hydrofoil was measured using a standard laboratory scale with an accuracy of 0.01g. The mass was measured to be 399.98g and 400.01g for the two specimens. Accuracy of the hydrofoil profile was evaluated by metrology performed using to a Coordinate Measuring Machine (CMM). The CMM used for this application was a LK G80C, which uses a Renishaw TP20 automatic positioning probe head. The datum coordinate was chosen at the mid-chord of start of the hydrofoil span, coinciding with the coordinate system given in Figure 4-12. The STEP-File (.stp format, ISO 10303-21) of the twisted hydrofoil was loaded into the CMM software and the probe was set to take measurements at 95 points along the surface of the hydrofoil. The measurements were compared to the geometry of the STEP-File and directional deviation (in 3-axes) and total 3D deviation were calculated. The tolerance limit of CMM was set to 0.3mm and 3 out of 95 points were observed to fail the tolerance test.

Two out of these three points were at the trailing edge of the hydrofoil while the third was in the vicinity of the leading edge within the area that is intended to be clamped during experiments. Inaccuracies in the trailing were expected as resin flashing that formed at the trailing edge during manufacturing was sanded by hand. The third inaccurate point was formed most likely due to an inaccuracy in the mould. However, as it was located within the clamped region, it was not expected make any significant impact to the experimental results obtained using the specimen. A summary of metrology scan measurement results is given in Table 5-1. The detailed list of deviation of each point is given in Appendix B. Figure 5-3 demonstrates the CMM scan points overlaid on to the Stereolithography (.stl) file of the hydrofoil reconstructed in Matlab. CMM scan points within tolerance are marked with blue open circles, while the three points out of tolerance are marked with red open circles.

95 CMM Points	DX	DY	DZ	3D
Maximum Deviation	0.153	0.206	0.299	0.307
Minimum Deviation	-0.110	-0.698	-0.306	-0.702
Deviation Range	0.263	0.904	0.605	1.008
Average Deviation	-0.000	-0.000	-0.000	0.066
RMS Deviation	0.026	0.097	0.155	0.185
Standard Deviation	0.026	0.097	0.156	0.173

Table 5-1: Summary of deviation results (in mm)

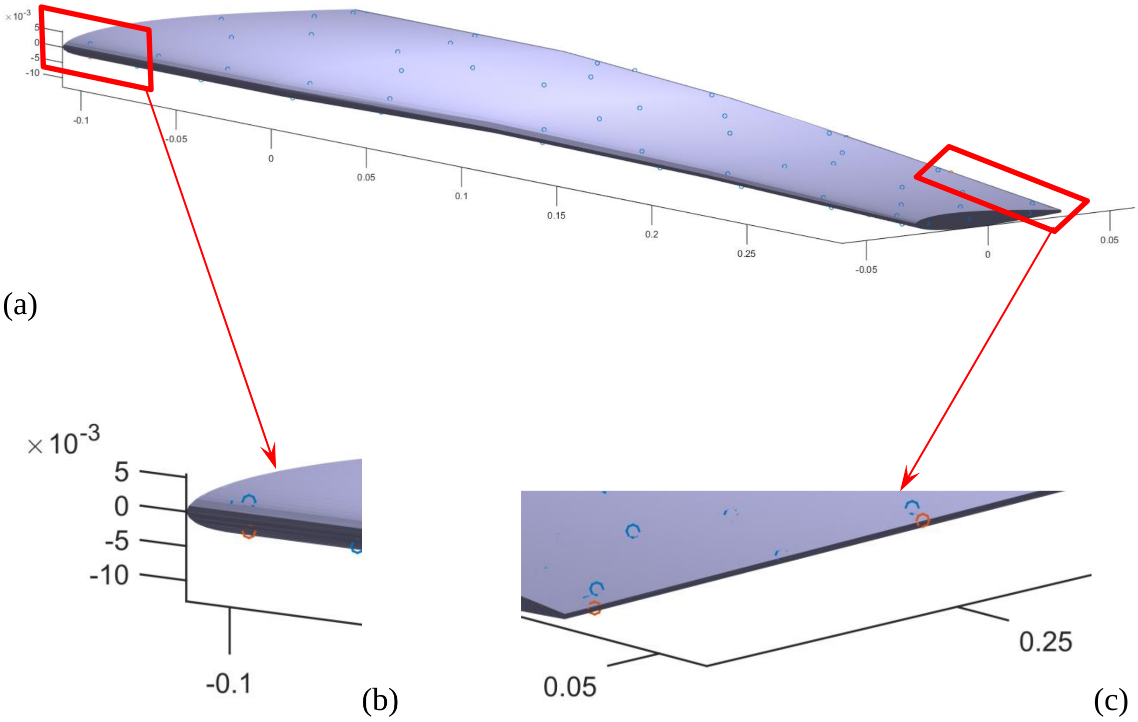

Figure 5-3: Metrology scans overlaid on to the Stereolithography model constructed in Matlab: (a) The complete model and scan points; (b) leading edge deviation & (c) trailing edge deviations

Based on metrology it was concluded that the surface quality and dimensional accuracy of the mould cavity was acceptable and on average, the tolerance was within 0.1mm. However, special care must be taken when trimming resin flashing as it may alter the profile at the leading edge, trailing edge and tip.

5.3. Structural experiments and strength testing

Experiments were focussed on two major aspects: modal frequencies and strength under quasi-static cantilevered loading. The purpose of modal testing was to act as a verification step for FEM and later investigate the shift in modal frequencies after the specimen is tested and failed. Cantilevered strength testing was performed as the optimised layup used for this specimen has never been tested for strength. As the layup mostly consisted of plies in one direction (30^0) there were concerns about its strength lateral to the fibres. Furthermore, all previous hydrofoils manufactured and tested as a part of the overall extended project had carbon/glass hybrid layups. In such hydrofoils, bi-axial glass layups were included to improve the ductility and the toughness of the specimen by adding further reinforcements in the lateral direction to the unidirectional carbon layups. These experiments were performed as an important safety precaution to investigate prior to the hydrofoil being tested in the cavitation tunnel in future.

5.3.1. Modal frequency testing

Modal frequencies of the hydrofoil were experimentally measured using tap testing, with a digital tap hammer and an accelerometer connected to the Dewetron™ DEWE-2521 system. The Dewetron is a compact 64-channel data acquisition system with DeweSoft™ and DeweFRF™ software preloaded for data analysis. The hydrofoil was suspended from elastic bands to simulate a free-free boundary condition. Elastic bands provided excellent isolation from the rest of the suspended structure. A template was used to mark grid points for hammer tapping on the hydrofoil. The template used and the coordinates of the grid points are given in Appendix C. Figure 5-4 shows the experimental setup and the equipment used. Modal tests were performed on both manufactured hydrofoils in order to compare the similarity and thus the consistency of the manufacturing process.

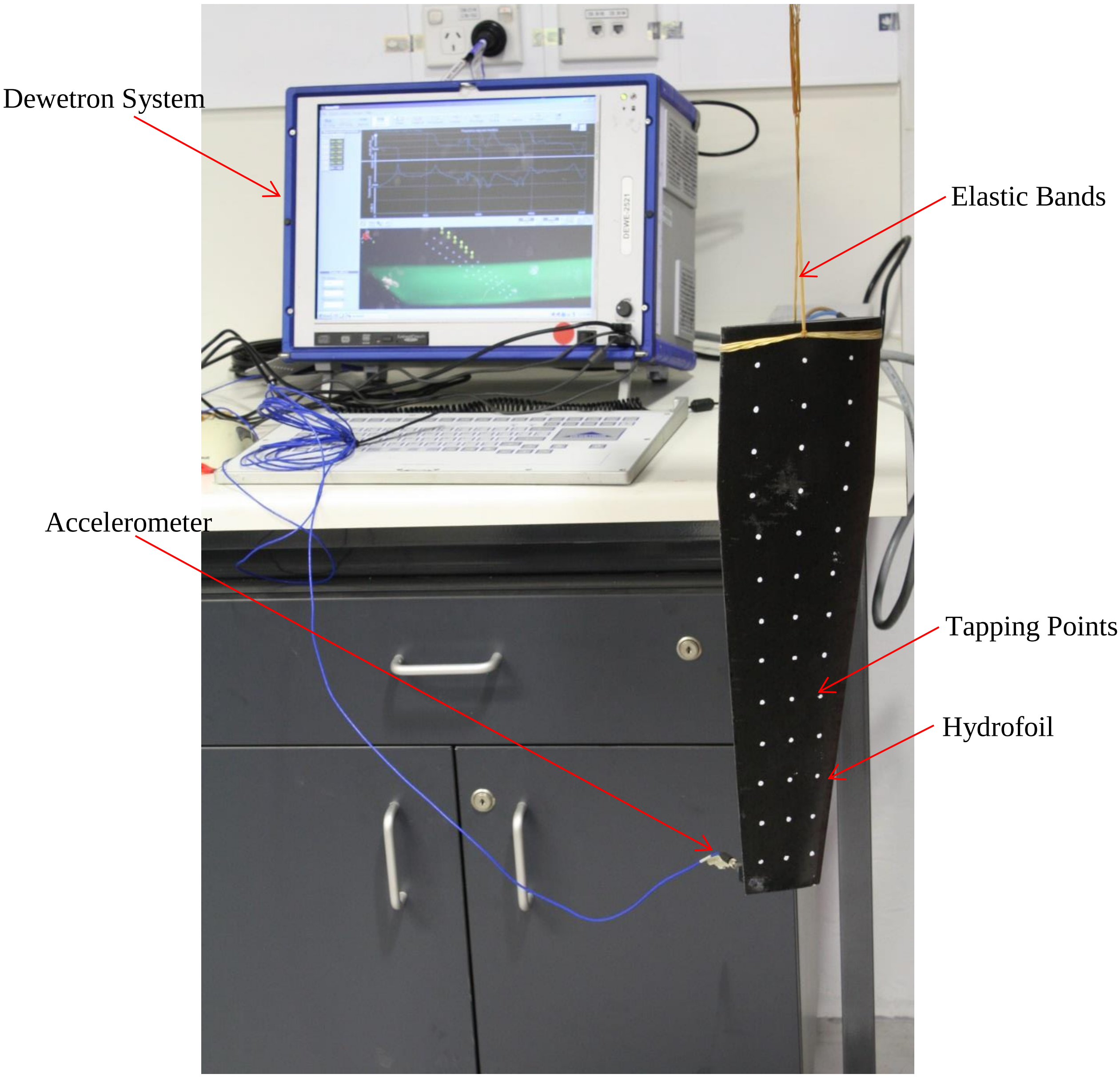

Figure 5-4: Modal testing experimental setup

The suspended specimen was tapped using the hammer 4 – 6 times at points that were marked using the grid. Multiple taps at the same point allowed the software to compare and cohere the response for each point. The acceleration response picked up by the accelerometer is then decomposed into the frequency domain using Fourier Transform by the software, from which the Transfer Function is constructed. Results obtained using modal testing can be considered excellent with good coherence and low noise even at high frequencies. Furthermore, the difference between the two specimens in modal frequencies was less than 1%. This proves the accuracy and consistency of modal experiments and the manufacturing process. Figure 5-5 demonstrates an example acceleration amplitude curve at one point obtained using the experimental setup. Table 5-2 summarises the first three modal frequencies obtained for the two specimens. In addition to the modal frequencies, the spectral analysis software was used to produce mode shapes. The first two shapes were modes in pure bending, while the third mode was in pure torsion. These mode shapes are demonstrated Figure 5-6.

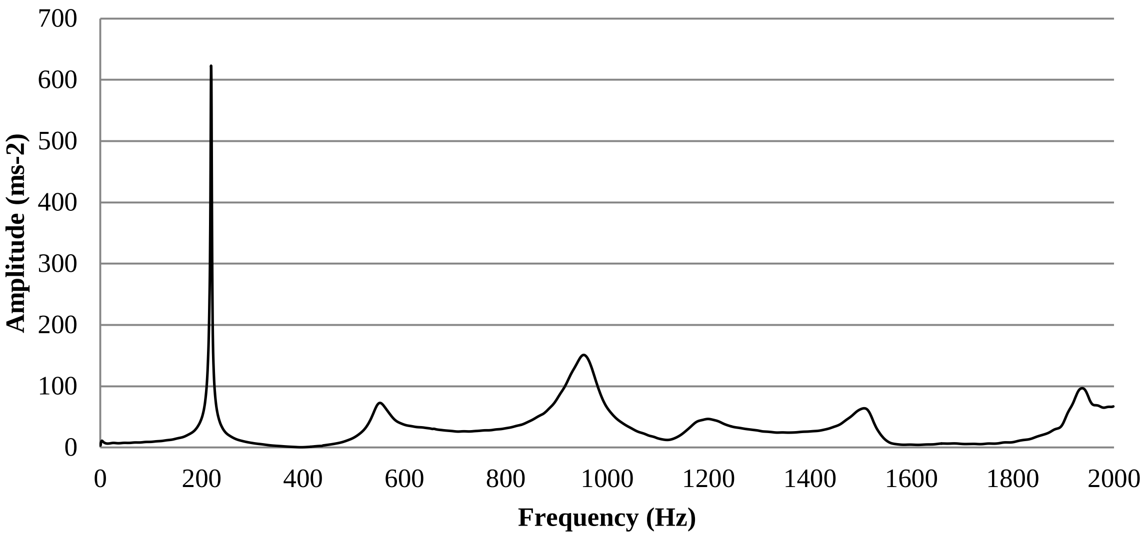

Figure 5-5: Acceleration amplitude plot for one point on the hydrofoil

Specimen	Mode 1	Mode 2	Mode 3
Specimen 1	221.21Hz	558.64Hz	962.94Hz
Specimen 2	219.96 Hz	555.52Hz	951.06Hz

Table 5-2: Modal frequencies obtained using tap testing

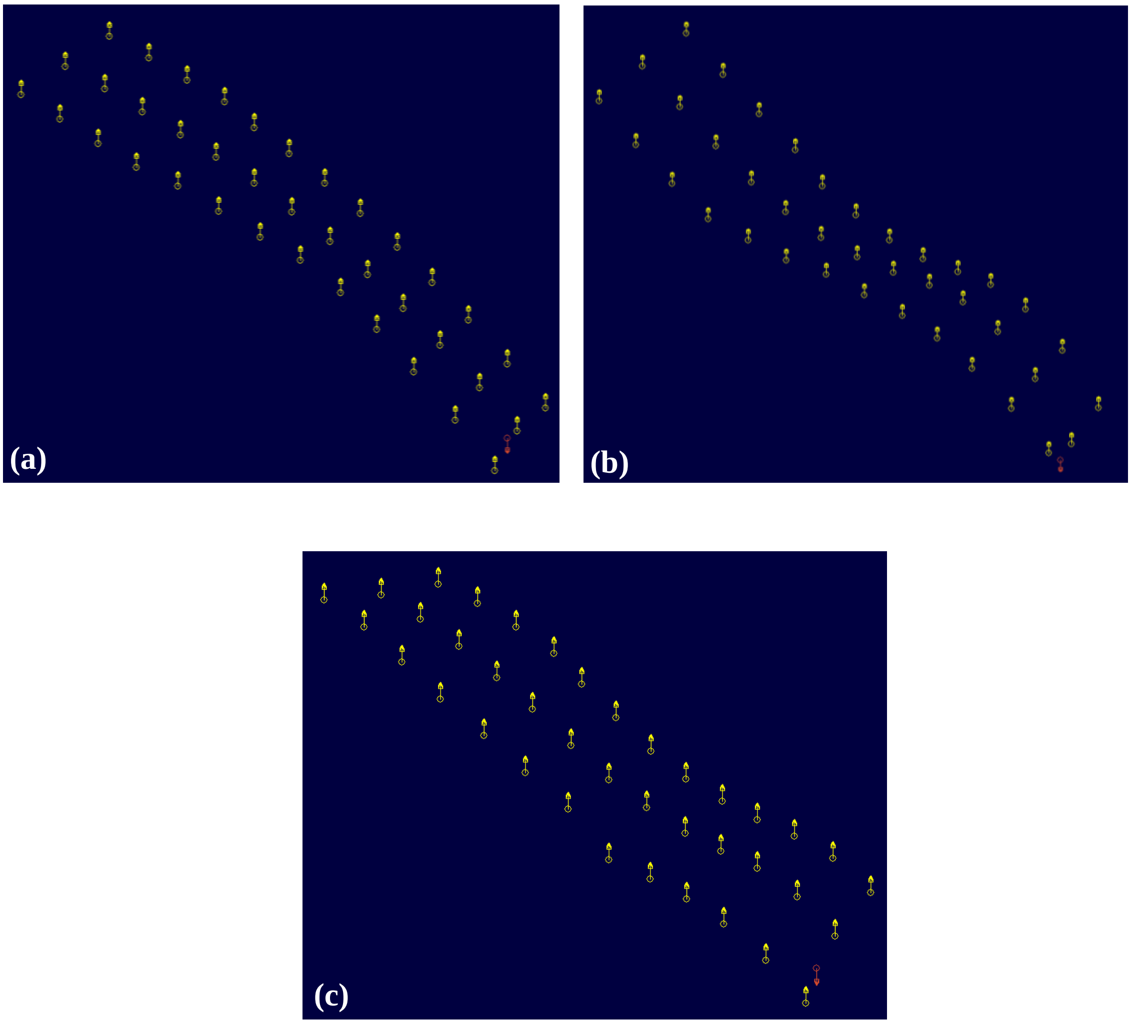

Figure 5-6: Mode shapes: (a) Mode 1, (b) Mode 2 & (c) Mode 3

As explained in the proceeding section, (Section 5.3.2), one of the two specimens was loaded in cantilever condition to test its strength. Tap testing was then performed again on the failed specimen in order to investigate the shift in modal frequencies due to structural damage that was caused during testing. Table 5-3 summarises results for undamaged specimen and the damaged specimen. The change in modal frequencies was not substantial. However, it was observed that there were some points that demonstrated vibrations almost independent from the rest of the structure, as if the structure were discontinuous. One such discontinuity was witnessed at approximately 864.8Hz, where two tapping points demonstrated much higher amplitudes compared to the rest of the structure. In fact, 864.8Hz was the frequency which this phenomenon was most prominently observed. However, frequencies such as 564.9Hz, 878.58Hz, 1139.2Hz and 1448.5Hz also clearly demonstrated the discontinuity at the same point. It is speculated that this discontinuity was due to the holes drilled to load the hydrofoil in the cantilevered configuration. Structural discontinuity due to the absence of material may have resulted in reduced local stiffness, which resulted in higher amplitudes in vibration. The vibration pattern at 864.8Hz is shown in Figure 5-7.

Specimen	Mode 1	Mode 2	Mode 3
Undamaged Specimen 1	221.21Hz	558.64Hz	962.94Hz
Damaged Specimen 1	216.83 Hz	548.64Hz	951.06Hz

Table 5-3: Comparison between undamaged and damaged specimen modal frequencies

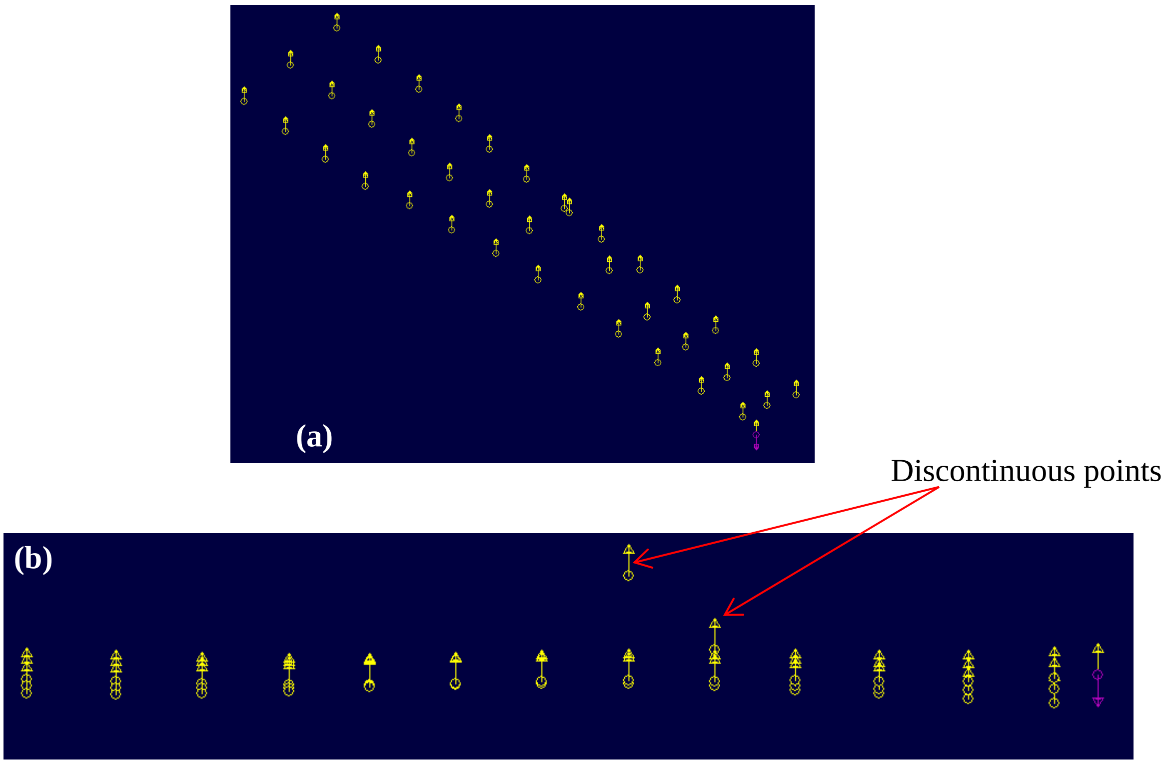

Figure 5-7: Two discontinuous points that were witnessed at 864.8Hz: (a) Perspective view & (b) Side view

5.3.2. Load response and strength testing

After modal tests were completed, specimen no. 1 was subjected to quasi-static load testing and strength testing under cantilevered loading conditions, which resembled the loading state in the cavitation tunnel. Prior to testing, strain gauges and acoustic emission sensors were attached to the hydrofoil. The strain gauges were attached to the tensile side of the specimen, while the acoustic emission sensors were attached to the compressive side. This strategy was employed based on past experience, as it was known that failure initiates on the compressive side as a result of fibre buckling. Thus, it was speculated that acoustic emission transducers will be able to detect noise due to failure much more efficiently. In addition, limited space in the loading rig was also a driving factor for this choice.

The load was applied at mid-span between the clamp and the tip of the hydrofoil, 15mm offset from mid-chord towards the leading edge (Figure 5-8). Loading was done using an MTS single axis loading system. The rig consisted of an aluminium capture block CNC milled to the outside profile of the hydrofoil and a loading pin. The loading pin was double jointed in perpendicular axes that emulated a universal joint. This load pin was chosen such that it provided freedom to rotate about two axes to provide freedom for both bending and twisting. The capture block was fixed to the loading stage of the MTS system using a 20mm thick aluminium slab. The slab was sufficient to ensure that the deflection of the rig during loading was negligible.

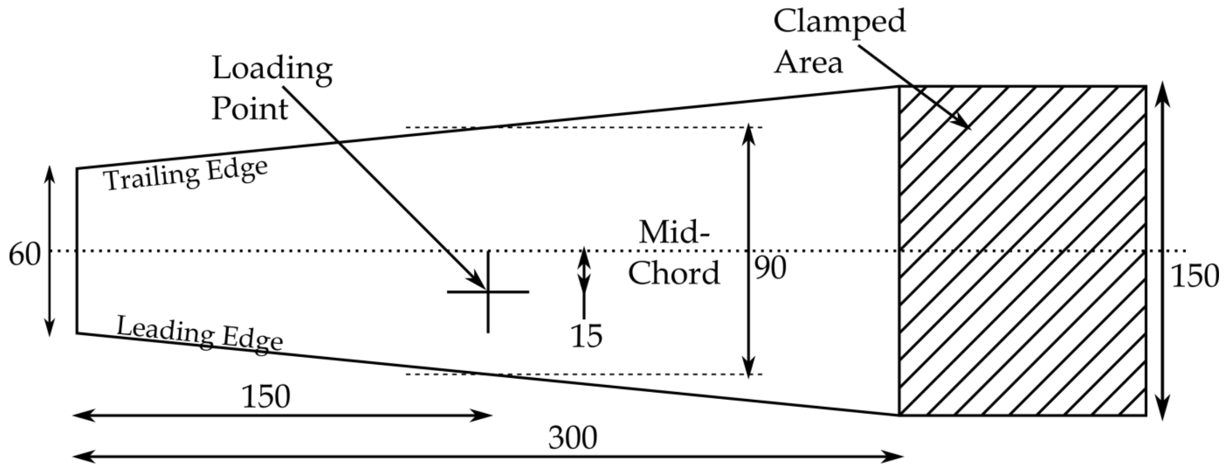

Figure 5-8: Loading configuration (in mm)

Several 350Ω strain gauges were used to read the strain values during the loading test. One strain rosette was used while all the others were unidirectional gauges. The gauges were connected to an HP data logger to collect real time data during tests. An auxiliary load output from the MTS system was also connected to the same data logger. Acoustic emission transducers were connected to a separate data processing computer via a low noise amplifier. A second auxiliary analogue load connection was provided to the acoustic emission data acquisition system. In addition, two dial gauges were placed at the leading and trailing edge of the tip of the hydrofoil to measure the tip deflections and the twist at the tip. The dial gauges had 0.01mm accuracy. The experimental setup is shown in Figure 5-9.

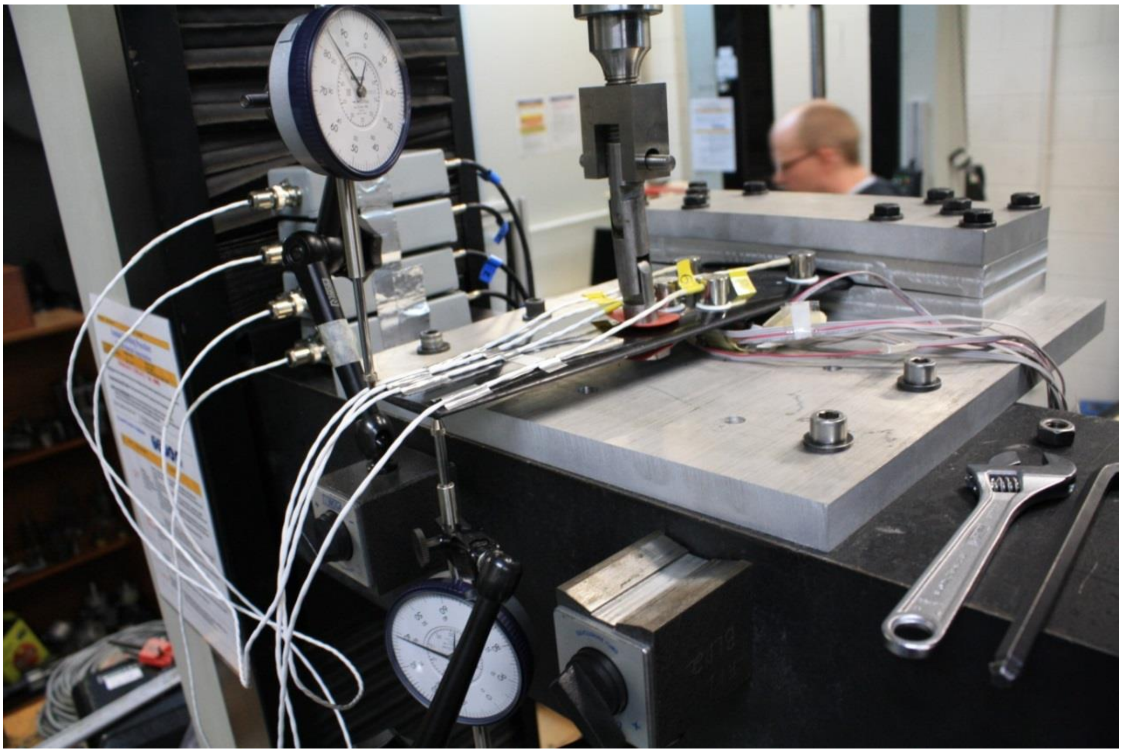

Figure 5-9: Experimental setup for static tests

5.3.2.1. *Investigation of hysteresis and possible loss of stiffness*

Several loading experiments were performed using the loading rig. Loading was applied as displacement controlled load, with a rate of 5mm/min. Two initial loadings were performed up to just above 1kN to test the hysteresis strain effects of the hydrofoils and detect any loss of stiffness due to loading. The loads measured by the MTS load cell against the deflection of the crosshead for both up stroke and down strokes are presented in Figure 5-10.

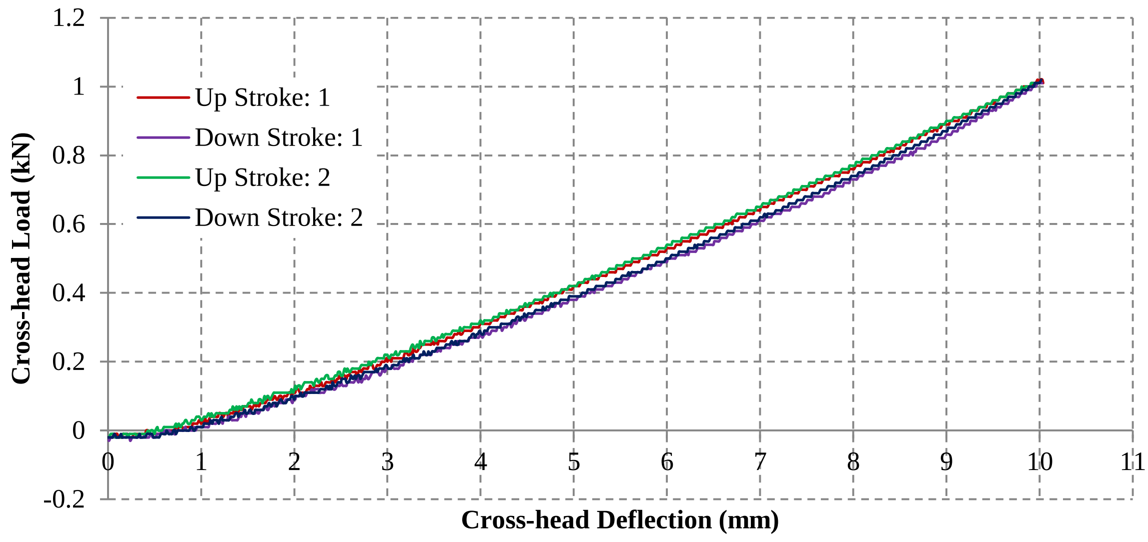

Figure 5-10: Testing hysteresis effect and loss of stiffness

Based on the deflections, it was clear that the hysteresis of the specimen was negligible. After the initial hysteresis test (Up Stroke 1 and Down Stroke 1), another load up to just above 1.0kN was applied (Up Stroke 2) at the same cross-head deflection rate and released (Down Stroke 2) at the same rate to ensure that there was no drop in stiffness in the structure due to the former hysteresis experiment. The load vs displacement curve for this loading case is also given in Figure 5-10. It is clear from the 2nd loading curve that, there is no noticeable change in the slope of the graph. To be exact, the loading curves (Figure 5-10) show that the upstroke of the second load follows the same curve of the first curve and the downstroke curve of the second load follows the same downstroke curve as the first loading curve. However, there is a maximum difference between the upstroke and downstroke of 2.5% in deflection for the same load. It is possible that this is due to the time taken to release internal stresses.

Thus, it was clear that there was no noticeable change in stiffness of the hydrofoil due to loading. It must be noted that the choice of 1kN was based on previous experiments that were performed in the cavitation tunnel (Zarruk et al., 2014). During those experiments it was observed that the highest lift that was produced by the hydrofoils was in the vicinity of 1kN. This limit was further confirmed by the CFD simulations performed explained in Section 4.2.

Thus, the static hysteresis test confirmed that up to around 1kN loading, the hydrofoil remains in its elastic region with no significant issues with hysteresis or loss of stiffness due to repeated loading.

5.3.2.2. Twist variation and failure

After the hysteresis test, the specimen was loaded to measure the twist variation at the tip of the specimen. As part of this same loading run, two more loading and unloading cycles were performed to further ensure that there was no hysteresis or loss of stiffness due to repeated loading. These two cycles will be ignored in the proceeding discussion as no change in results was observed due to repeated loading.

Two analogue dial gauges were used to measure the deflection at the leading and trailing edges at the tip of the hydrofoil. The use of analogue gauges was due to the difficulties experienced in setting up LVDTs, which were originally planned to be used for the experiments. Due to the use of dial gauges, loading had to be paused at displacement increments to manually read the dial gauges. Thus, every 1mm displacement increment, the MTS system was paused and readings on the two dial gauges were taken. Readings were taken for both the up stroke and down stroke of the experiment in order to ensure that there was no residual twisting strain in the specimen. Table 5-4 summarises all reading that were recorded during experiments and Figure 5-11 shows the variation of twist against load. Further note that the twist was such that the leading edge deflected less than the trailing edge. This direction of twist was witnessed even with the loading point being much further towards the leading edge from the mid-chord point of the hydrofoil. In the context of hydrodynamic loading, this is equivalent to reduction in angle of attack with the increase of lift. Such a reduction in angle of attack is what the L/D curves prescribe (Figure 4-7) to improve the L/D performance of the hydrofoil. Thus, it was clear that the optimisation effort was successful in proving a layup that can potentially fulfil that requirement. For comparison purposes another layup with no prior optimisation (glass layup with 0/90 plies) was also tested and the results are given in Table 5-4 and Figure 5-11. It was evident that the desirable twist of the optimised layup was over twice that of non-optimised layup, which may lead to better L/D performance of the optimised layup in cavitation tunnel tests.

Crosshead Def. (mm)	**Tip Def. CF foil (mm)**		**ΔTwist Angle: CF foil (deg)**	**Tip Def. GF foil (mm)**		**ΔTwist Angle: CF foil (deg)**
	Leading	**Trailing**		**Leading**	**Trailing**	
0	0	0	0	0	0	0
1	0.82	0.85	0.037367	1.56	1.61	0.062278
2	2.98	3.14	0.199289	3.75	3.86	0.137011
3	5.24	5.53	0.361208	5.99	6.15	0.199289
4	7.48	7.93	0.560484	8.24	8.45	0.261566
5	9.83	10.4	0.709933	10.53	10.8	0.336297
6	12.15	12.85	0.871825	12.78	13.08	0.373663
7	14.52	15.36	1.046154	15.12	15.48	0.448393
8	16.93	17.91	1.220465	17.43	17.85	0.523121
9	19.26	20.37	1.382304	19.8	20.29	0.610302
10	21.7	22.94	1.544121	22.11	22.66	0.685026
11	24.06	25.43	1.705914	23.85	24.5	0.80956
10	21.8	23.1	1.618798	22.7	23.33	0.784654
9	19.39	20.57	1.469439	20.36	20.92	0.697479
8	17.08	18.13	1.307611	17.99	18.46	0.585393
7	14.68	15.58	1.120861	15.7	16.11	0.510666
6	12.22	12.97	0.934088	13.38	13.72	0.423483
5	9.9	10.52	0.772201	11.12	11.42	0.373663
4	7.57	8.05	0.597847	8.72	8.95	0.286477
3	5.29	5.63	0.423483	6.44	6.61	0.211744
2	3.03	3.22	0.236655	4.24	4.36	0.149467
1	0.88	0.93	0.062278	2.07	2.13	0.074734
0	0.06	0.07	0.012456	0.03	0.04	0.012456

Table 5-4: Variation of deflection and twist angle in the optimised layup and a non-optimised layup

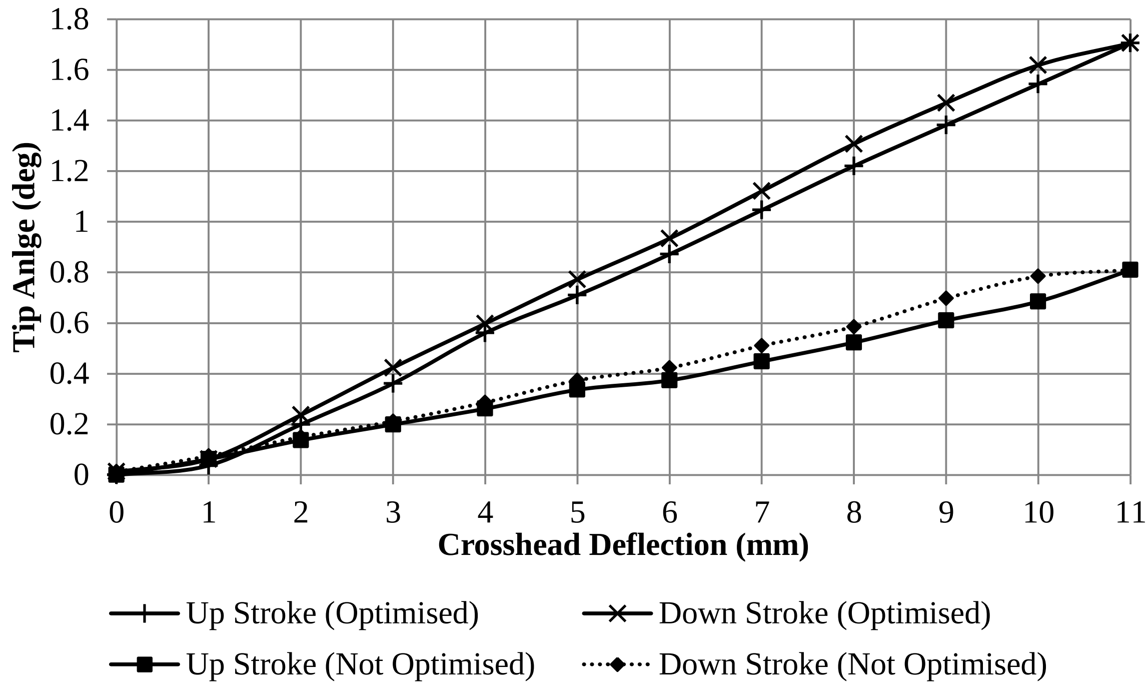

Figure 5-11: Variation of twist angle against crosshead deflection

After the twist experiment was completed, the specimen was loaded all the way up to the point of failure. The same deflection rate of 5mm/min was maintained. The load variation against crosshead displacement is shown in Figure 5-12. Failure was notied to occur at 4.2kN at a crosshead displacement of 32mm. This load and deflection are significantly higher than what had been witnessed in previous cavitation tunnel experiments on hydrofoils.

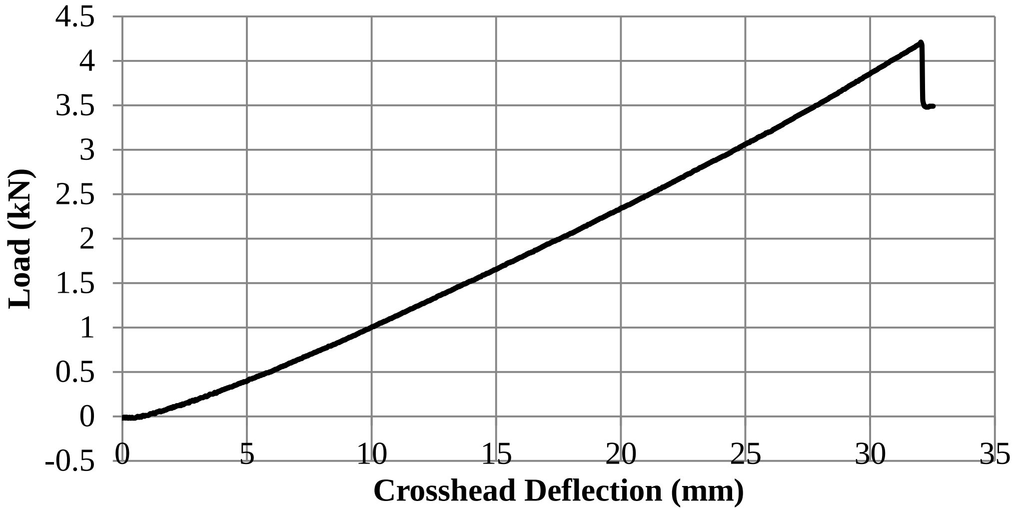

Figure 5-12: Load variation against deflection up to failure

5.3.2.3. Strain Variations

Strain gauges were attached to the tensile side of the hydrofoil and the variation of strain was measured against load during cantilevered tests. The purpose of strain measurement was to understand the surface strain variation of the hydrofoil in order to understand the stress field on the surface of the hydrofoil and validate the finite element models used to predict the response of the hydrofoil.

Five single axis strain gauges and one strain rosette were attached to the surface of the hydrofoil at locations given in Figure 5-13. Coordinate locations of strain gauges are given in Table 5-5. The chosen strain gauges were Vishay CEA-06-250UN-350 linear strain gauges with a gauge factor of 2.08±0.5% and CEA-06-250UR-350 rectangular rosette with a gauge factor of 2.05±0.5%. All strain gauges were of 350Ω impedance with a maximum strain range of ±5%, which translates to ±50000με. All strain gauges were connected to a HP data logger and strain data were captured at every 2s time interval. SG7 failed during assembly of the specimen on to the loading rig and was decided not to be included in subsequent data analyses.

Strain Gauge	X (mm)	Y (mm)
SG_R (Rosette)	75	-21
SG4	42	-21
SG5	42	0
SG6	75	0
SG7	110	-21
SG8	75	22.5

Table 5-5: Coordinates of strain gauges

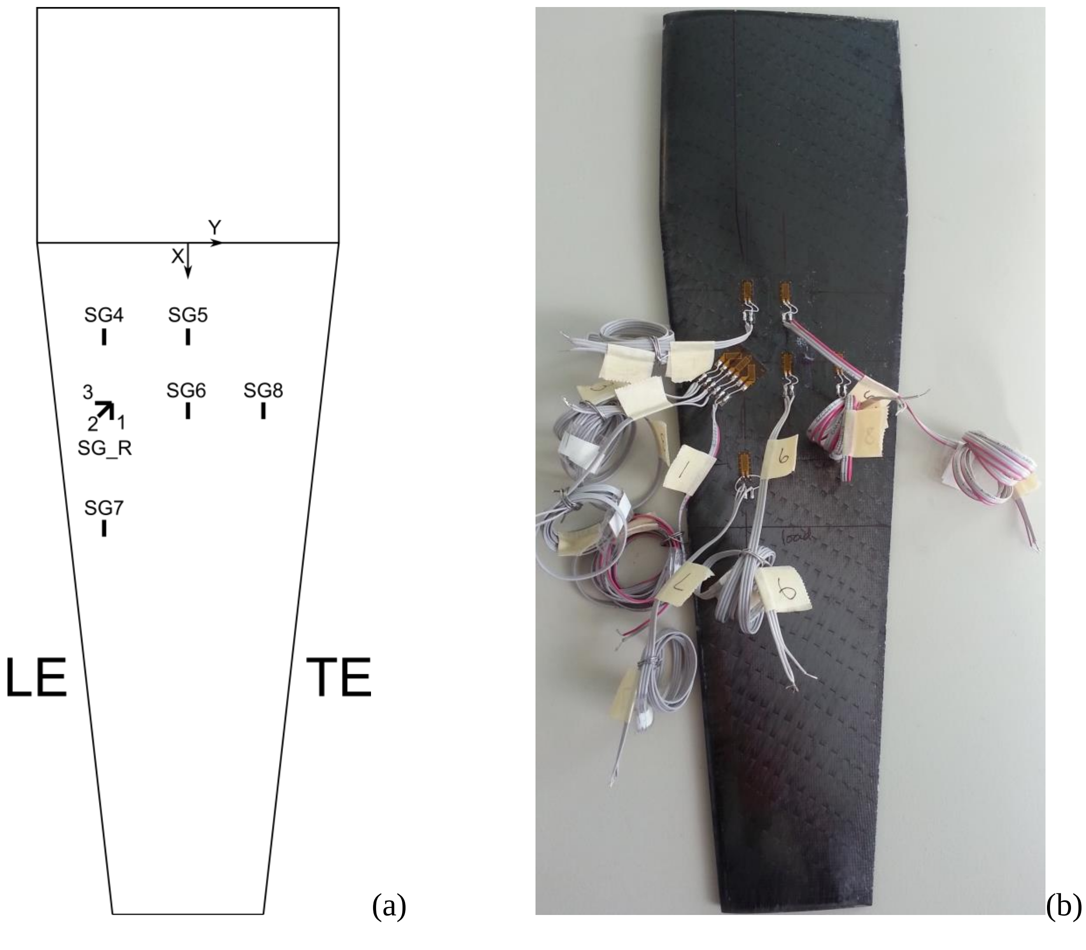

Figure 5-13: Strain gauge layout (a) Strain gauge locations (LE: Leading Edge, TE: Trailing Edge); (b) Actual image of strain gauges with wires attached

Strain data was recorded for the investigation of hysteresis (Section 5.3.2.1) and twist variation and failure (Section 5.3.2.2). The strain variation of each strain gauge for the hysteresis loading is given in Figure 5-14. Based on Figure 5-14 it was clear that in addition to the absence of global deformation hysteresis, the hydrofoil did not exhibit any localised strain hysteresis. However, similar to deflections (Figure 5-10) there was a slight difference in strain for the upstroke and downstroke. However, the same values were observed for each upstroke, while the same values were observed for each downstroke. Table 5-6 summarises averaged strain data at each twist measurement deflection increment. Figure 5-15 demonstrates the strain variation observed in each strain gauge for the cross-head deflections and the resulting load increments given in Table 5-6. Figure 5-16 summarises the strain variation observed for the loading case up to the failure point of the hydrofoil.

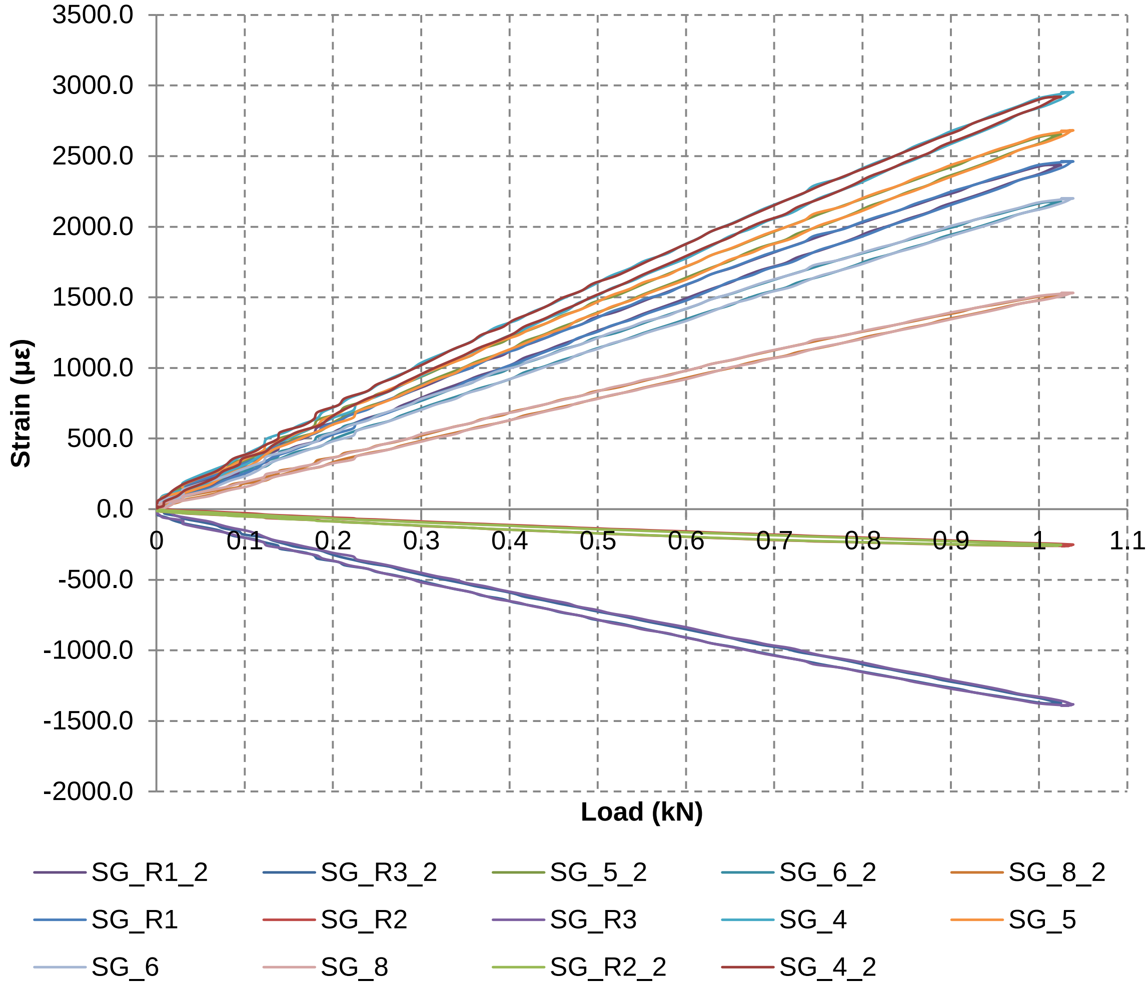

Figure 5-14: Strain variation for hysteresis loading test

Crosshead Def. (mm)	Load (kN)	SG_R1	SG_R2	SG_R3	SG_4	SG _5	SG_6	SG_8
0	0	4.2308	-3.3695	-8.1599	4.3284	2.9087	2.9004	1.8259
1	0.03	92.619	-12.116	-60.335	114.98	105.84	83.023	54.768
2	0.11	314.96	-37.87	-190.66	383.75	355.19	283.66	189.21
3	0.2	555.35	-64.84	-329.4	672.69	621.99	499.48	335.37
4	0.3	802.71	-93.026	-470.56	968.07	892.27	721.7	488.64
5	0.4	1067.9	-121.34	-617.96	1283.1	1177.3	959.23	655.22
6	0.52	1333.6	-147.18	-762.66	1598	1462	1197.3	822.9
7	0.63	1606.2	-174.28	-912.25	1921.4	1754.1	1440.9	995
8	0.76	1884.6	-202.54	-1067.1	2253.2	2053.3	1688	1169.2
9	0.88	2152.3	-227.42	-1216.1	2575.6	2343.4	1925.9	1337.3
10	1.01	2431.8	-255.36	-1374.2	2912.9	2645.4	2172.8	1511.6
11	1.13	2704.2	-279.07	-1526.8	3244.1	2941.5	2412.6	1680.8

Table 5-6: Strain variation against load for the deflection and twist measurement experiment

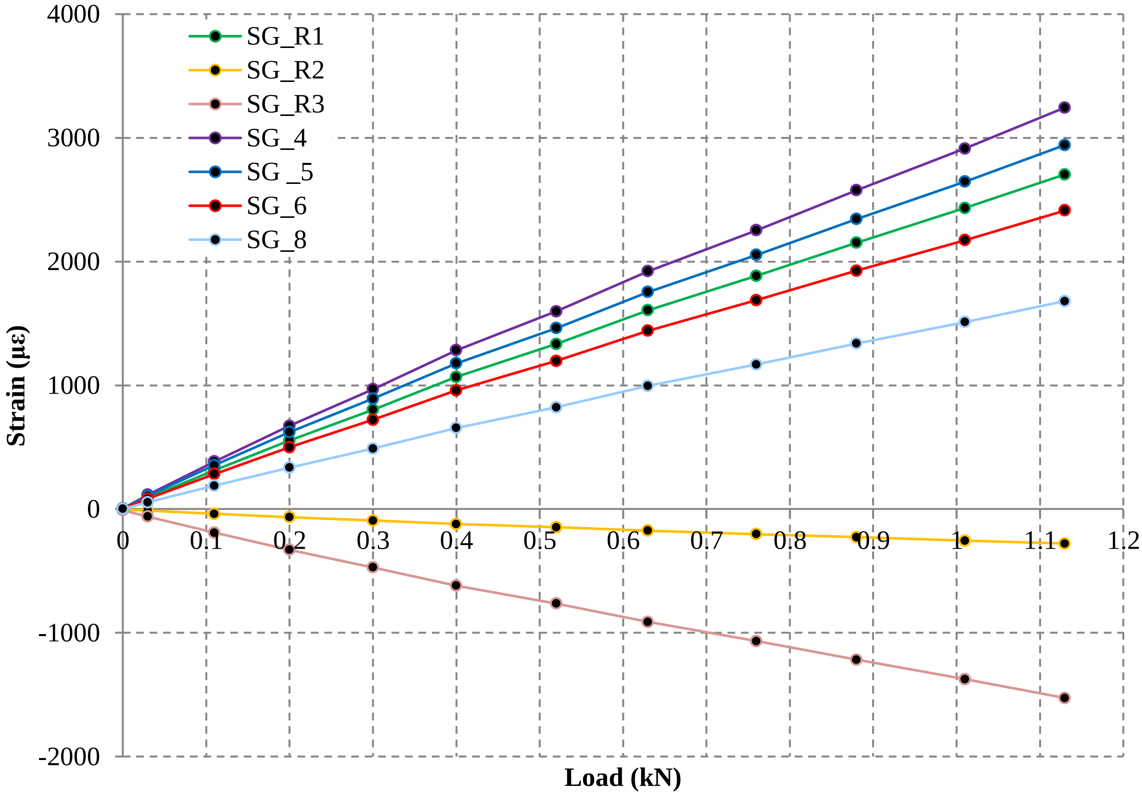

Figure 5-15: Averaged strain data for each twist measurement deflection increment

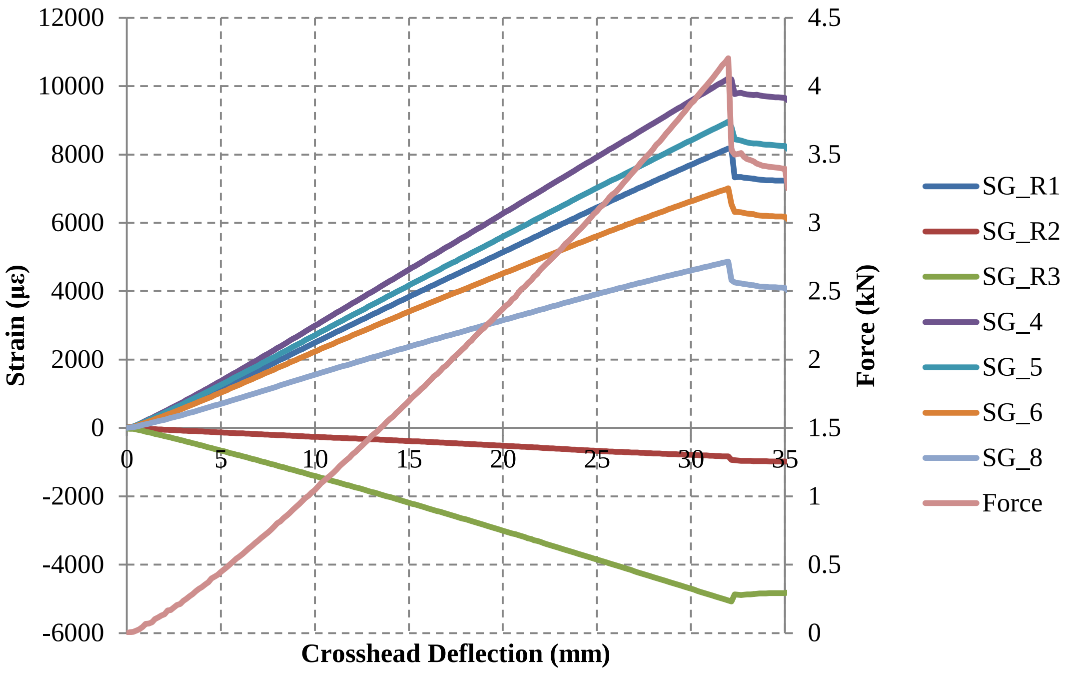

Figure 5-16: Strain variations up to failure load

5.4. Interrogation of the failed specimen

The ultimate failure of the hydrofoil was witnessed to be due to buckling of fibres on the compressive side of the hydrofoil. This was consistent with previous experiments that were performed by DSTO on other hydrofoils under cantilevered loading. Figure 5-17 illustrates the final failure that was witnessed on the foil. A major crack (possibly fibre kink) at approximately 30° degrees was witnessed on the external surface of the foil. In addition, a crack parallel to the clamped edge was also witnessed followed by another shorter crack along 30° fibres. Localised buckling of fibres was also witnessed, where fibre strands were separated and slightly raised from the resin matrix. It was anticipated that the whole failed region (Figure 5-17(b)) experienced an internal delamination as a result of failure.

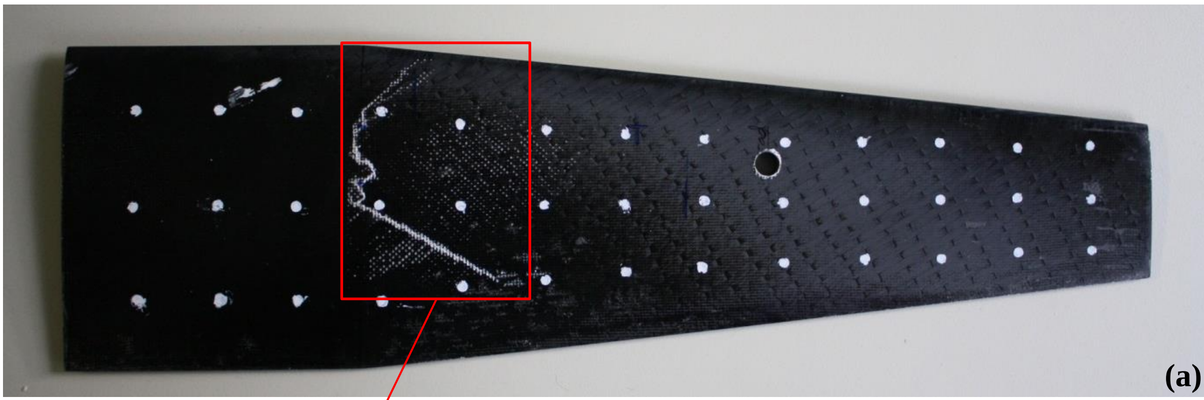

(a)

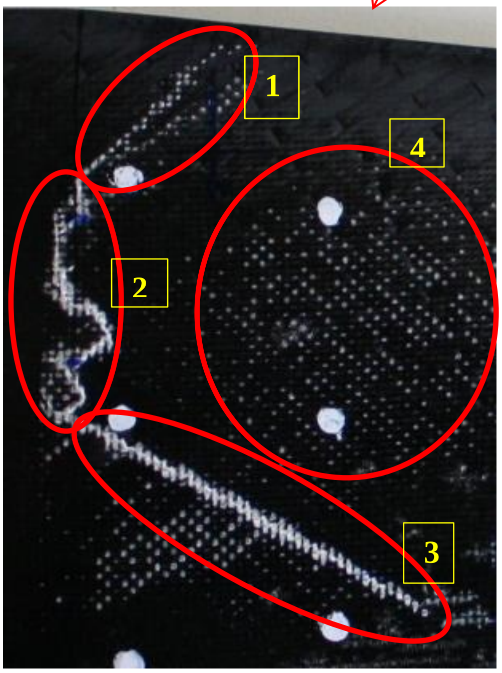

(b)

1. Short crack along fibres
2. Crack along the clamp interface
3. Crack at approximately 60°
4. Region with localized fibre buckling

Figure 5-17: Failed carbon fibre hydrofoil

5.4.1. UV Florescent Optical Microscopy

The failed hydrofoil was further investigated using UV fluorescent optical microscopy at cross-sections of interest. Cross-sections of the failed hydrofoil were cut using a circular diamond saw and the cross-section surfaces were polished down to a 0.05μm surface finish. For better visual of the localised failure, a UV fluorescent paint was applied to the cross-section surface and wiped off using solvent prior to inspection under microscope. The fluorescent material seeped into the cracks and provides a clear visual of the damage at the cross-section. A UV light was used during microscopy with ambient light kept at a minimum when fluoresce was necessary. As it was not possible to capture the whole chord of the hydrofoil in one scan, it was required to take multiple photos and stitch them together to generate the complete cross-section. Figure 5-18 demonstrates the damage at the leading edge portion of the cross-section. Further magnification into the region where crack has propagated to the surface is shown in Figure 5-18(b).

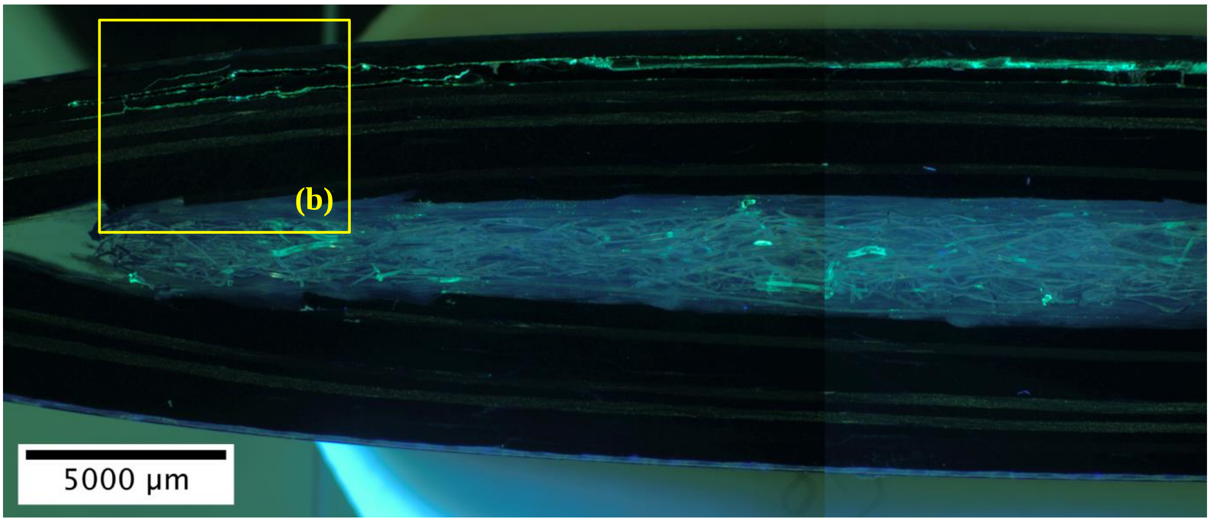

(a)

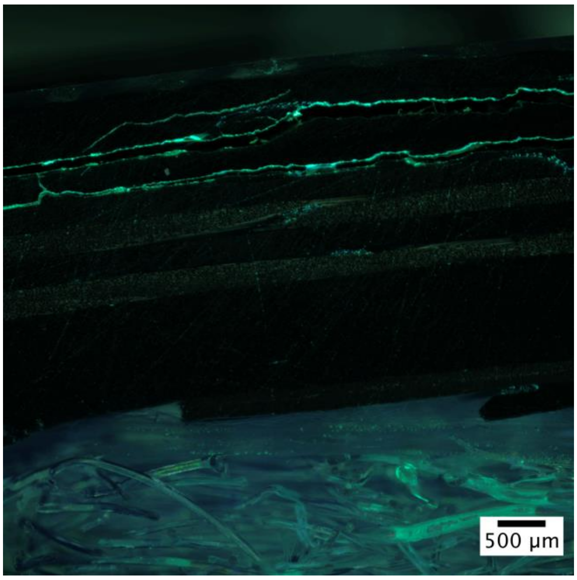

(b)

Figure 5-18: Delamination shown at the leading edge half of the cross-section: (a) fore-half of the cross-section, (b) region where through-thickness crack have propagated to the surface

It was clear from microscopic images that a major delamination occurred at the failure point of the hydrofoil. The major delaminations in this case occurred between the $2^{nd}/3^{rd}$ carbon layer interface and $3^{rd}/4^{th}$ carbon layer interface of the hydrofoil. This was likely due to the discontinuity of the laminate as the 2^{nd} layer is a -30° carbon layer, while the 3^{rd} was a +30° carbon layer and the 4^{th} layer was another -30° carbon layer (Table 4-3). As demonstrated by Figure 5-18(b), cracks have propagated through the thickness direction of 3^{rd}, 2^{nd} and 1^{st} carbon layers and caused a fibre kink in the glass basket layer on the surface. This fibre kink is the short crack that appeared on the surface of the hydrofoil near the leading edge depicted by crack no. 1 in Figure 5-17.

It was witnessed that the same major delamination had propagated to a great extent towards the trailing edge of the hydrofoil. The trailing edge portion of the cross-section is shown in Figure 5-19. Similar to the leading-edge portion, at one point, the cracks appeared to have propagated through the layers towards the surface of the hydrofoil to cause fibre kinks on the glass basket layer of the hydrofoil. The through-thickness crack propagation in the trailing edge portion of the hydrofoil is shown in Figure 5-19(b). This is the same surface crack witnessed in Figure 5-17 identified by crack no. 3. It appears that the delamination that propagated along the $3^{rd}/4^{th}$ carbon layer interface propagated through the 3^{rd} layer and continued to propagate along the $2^{nd}/3^{rd}$ carbon layer interface.

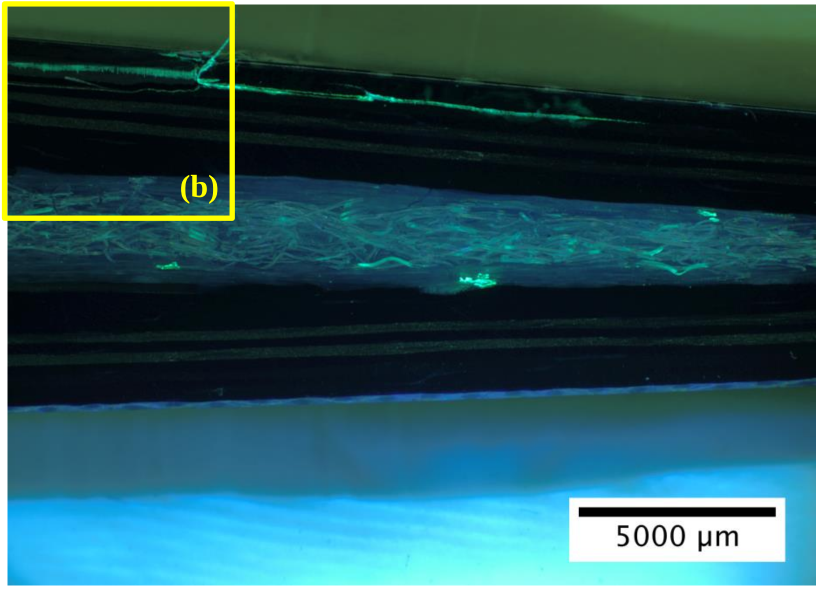

(a)

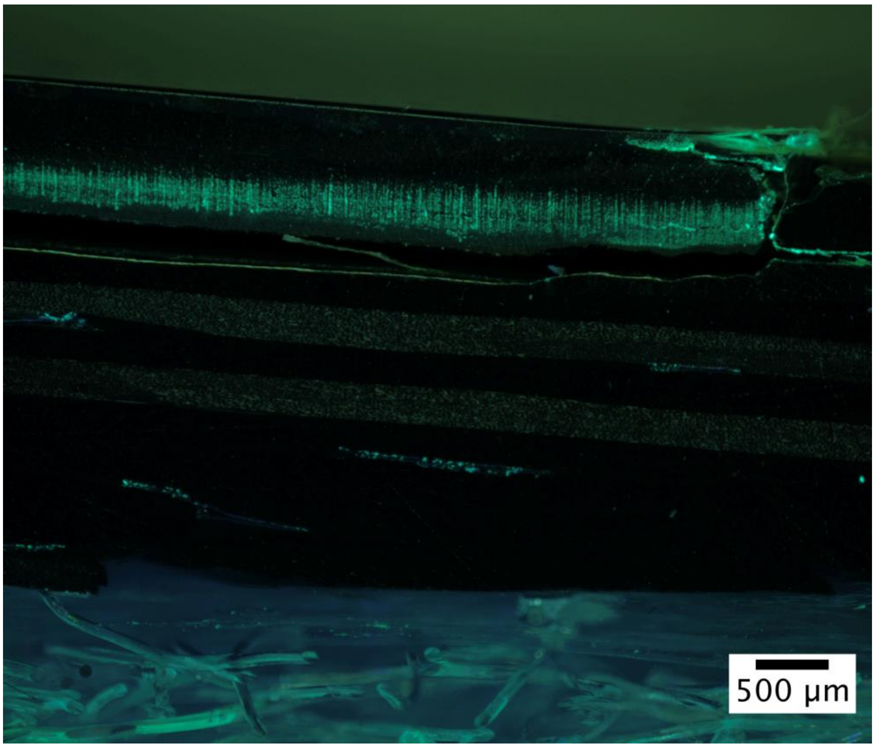

(b)

Figure 5-19: Delamination at the trailing edge portion of the hydrofoil (a) Trailing edge portion, (b) through-thickness crack propagation

5.4.2. Neutron Tomography Scanning

In addition to florescence microscopy, an attempt was made to scan the internal structure of the failed specimen using 'DINGO' Neutron Tomography scanning facility at the Australian Nuclear Science and Technology Organisation (ANSTO). Neutron tomography is similar to X-ray tomography in its fundamental principles. However, while x-ray is particularly suited for dense materials, neutron tomography can be used for less dense materials depending on the absorption of neutrons of the constituent elements of the composite material. The general principal is to project neutron beams on to the specimens and investigate the absorption of neutrons by analysing the neutron beam received by the neutron receiver. This methodology is used to obtain 2D scans of an object and afterwards, the 2D scans are combined together to form a 3D model of the object. The resolution of neutron tomography is usually in the order of 200μm - 500μm.

Neutron tomography is an attractive idea to evaluate the internals of failed composites. The idea was to obtain detailed microscopy images of the surface of failed specimens and use tomography to understand the propagation of cracks within the specimen. It can also be potentially used to evaluate the quality of the composite manufacturing technique and evaluate the void fraction.

Several preliminary neutron tomography scans were performed on the same specimens that were subjected to florescence microscopy. Some of these results are shown in Figure 5-20 and Figure 5-21. It must be noted here that the scans attempted here are preliminary studies to understand the feasibility of using neutron tomography to detect damage within carbon fibre reinforced composite structures. Extensive further work is necessary to understand this methodology and formulate a technique to detect damages within the composite structure.

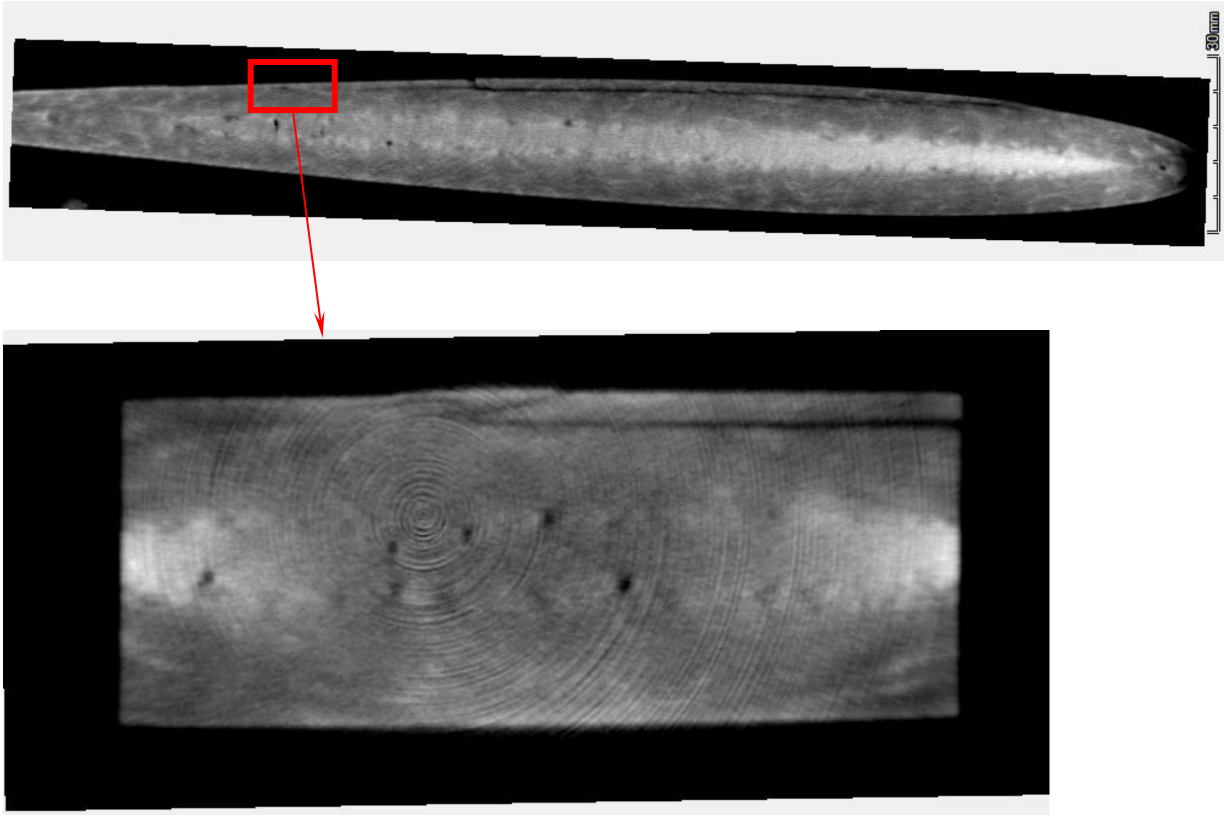

Figure 5-20: Cross-section tomography scan of the failed region

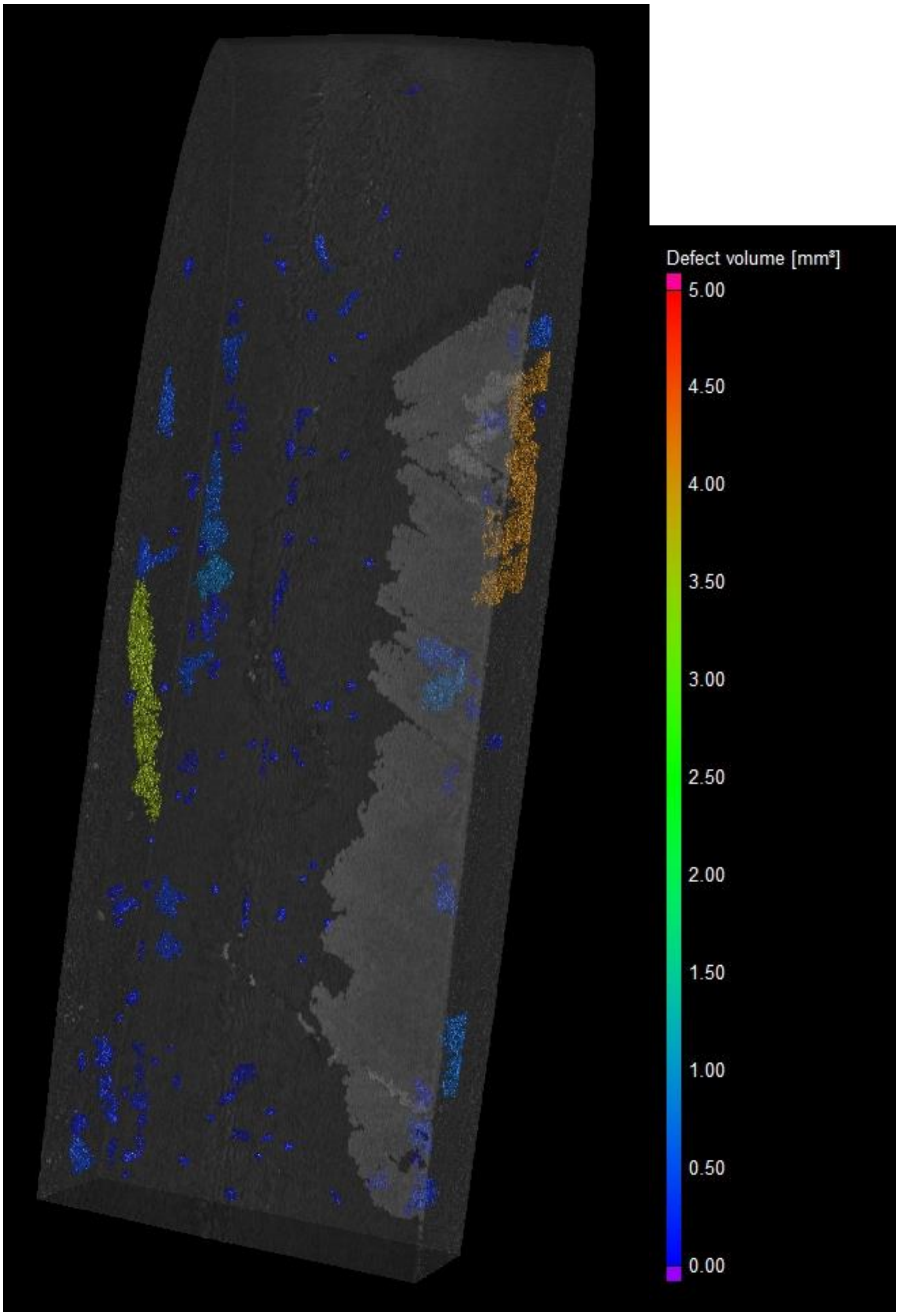

Figure 5-21: Defect volume contour map within a section of the hydrofoil

5.5. Finite Element modelling

Finite element modelling was performed in ANSYS with the help of ANSYS Composite PrePost (ACP) plugin in order to validate the observations and data collected during experiments. Finite Element modelling was performed to validate both modal analysis results and deflection results. Material properties used for the simulation are summarised in Table 4-1. The material properties for FE modelling were based on properties obtained using specimens manufactured using vacuum bagging, which is a slightly different process compared to closed mould vacuum infusion process.

ANSYS Composite PrePost provides freedom to model composite laminates in several different formulations. The three major formulations are:

1. Using shell elements
2. Using brick elements with only one element in the stacking direction (Monolithic)
3. Using brick elements split to represent each layer

The two brick element based discretizations can be chosen to follow either the solid-shell formulation or the pure solid formulation. Out of these options, solid element based formulations were investigated and compared against experimental results. The choice of solid element formulations was due to the requirement of performing FSI analysis on the same models. Performing FSI using solid FE structural models is more convenient and possibly more accurate, compared to shell element based models, due to the model having the exact shape of the hydrofoil cavity of the CFD domain. The mesh that was generated followed the stacking and ply termination strategy that was used during manufacture, explained in Chapter 5.2. Figure 5-1 illustrates the mesh that was created with the glass infusion mat placed at the mid-plane of the layup and glass basket layer on the outside. Figure 5-22 further illustrates the inside of the layup. This is exactly the sequence and appearance when the bottom layers were laid inside the mould cavity and the infusion mat layer was placed on top as shown in Figure 5-22(b).

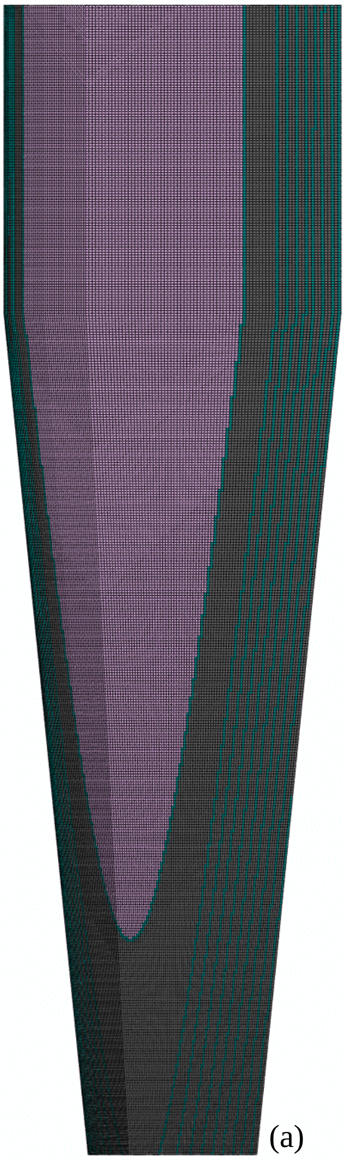
(a)

(b)
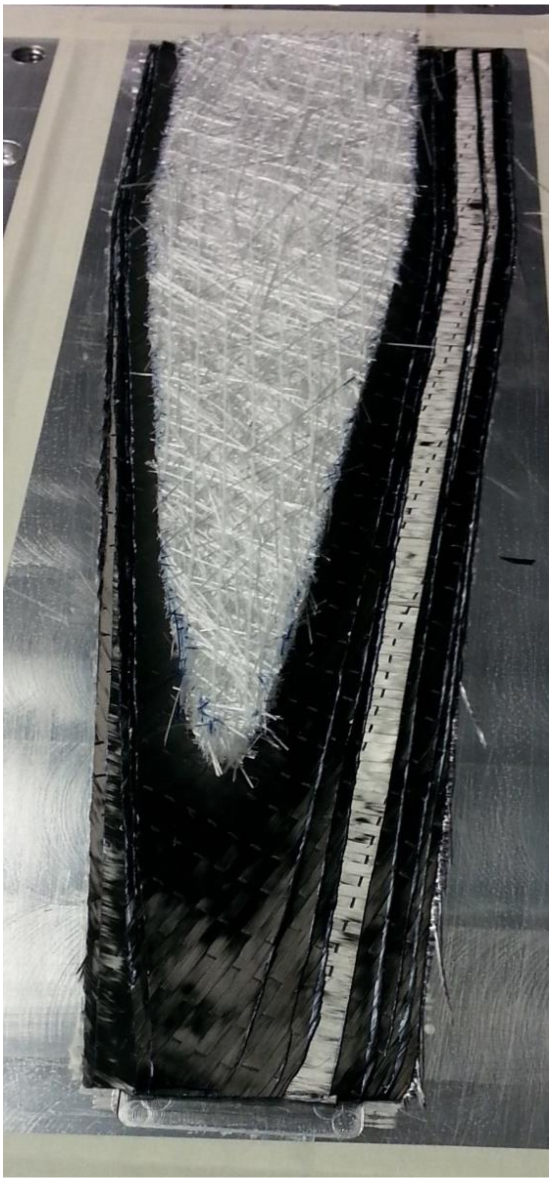

Figure 5-22: Cross-section cut with infusion mat layer placed on top (a) FE mesh, (b) Actual layup

5.5.1. Modal Analysis

Modal analysis was performed with free-free boundary condition setup similar to the experiments that were performed. The modal frequency results agreed to within 10% of what was measured during experiments. Table 5-7 summarises results obtained for modal frequencies for various Finite Element formulations in ANSYS. Although the difference between results observed for different formulations was almost negligible, the closest values to the experiments were observed in the per ply split brick element model. However, the CPU time taken by this model was excessively large. The mode shapes obtained using FEM were very similar to what were given by the frequency analysis software of the Dewetron system. These mode shapes are given in Figure 5-23 (compare against Figure 5-6). The first two were bending modes, while the third was a twisting mode.

Specimen	Mass (g)	Mode 1 (Hz)	Mode 2 (Hz)	Mode 3 (Hz)
Specimen 1 (Experiment)	400.01	221.21	558.64	962.94
Specimen 2 (Experiment)	399.98	219.96	555.52	951.06
FE solid per ply split, pure solid	408.23	214.27	557.05	897.12
FE Monolithic, 1st order solid	408.49	214.17	556.86	896.85
FE Monolithic, 1st order solid-shell	408.49	214.08	556.31	893.28
FE Monolithic, 2nd order solid	408.67	214.09	556.32	894.06

Table 5-7: Comparison between modal frequencies

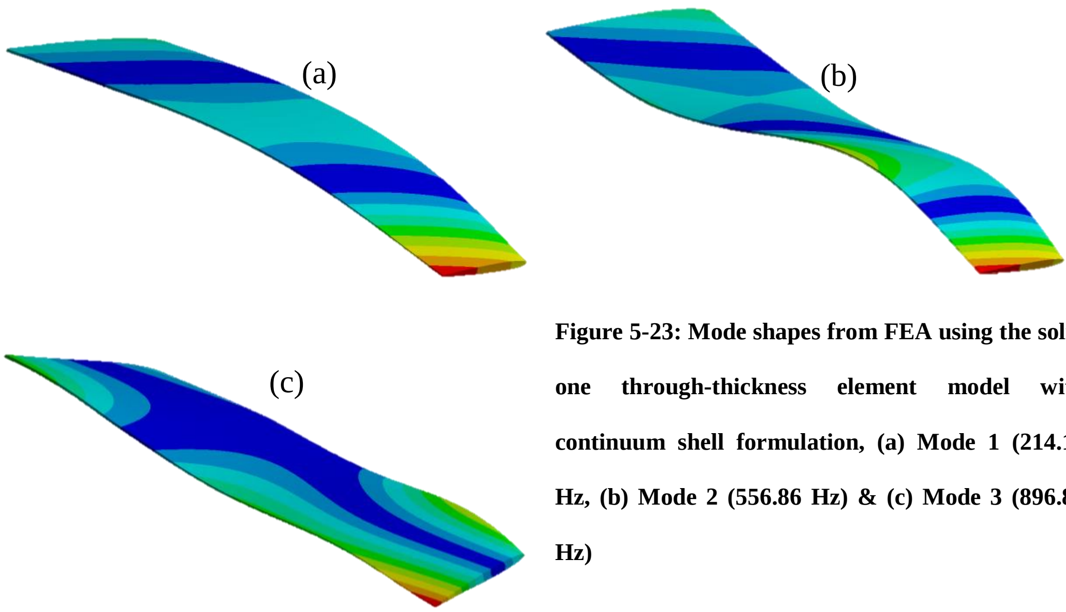

Figure 5-23: Mode shapes from FEA using the solid one through-thickness element model with continuum shell formulation, (a) Mode 1 (214.17 Hz, (b) Mode 2 (556.86 Hz) & (c) Mode 3 (896.85 Hz)

As outlined in Table 5-7, it was noticed that there is a slight discrepancy in the mass that was estimated by ANSYS based on individual material density data that were provided for the FE model. The mass of the specimen after manufacturing was 400g while the mass estimated by ANSYS was 408.67g. This is a difference of 2.17% relative to the manufactured specimen. In addition, there may be slight discrepancies in stiffness properties of materials due to the two different manufacturing methods used for the hydrofoil and the specimens which material properties were measured from. The properties were tested using specimens that were manufactured using vacuum bagging process. This may result in slightly different fibre fractions (likely higher) to closed mould vacuum infusion. In vacuum bagging it is possible to achieve a higher fibre fraction (lower resin fraction) doe to the pressure on the laminate bag and consolidation of the laminate over time. The nylon bagging film used in the process will further compress the laminate, reducing the volume and increasing the fibre fraction. However, this is not possible in closed mould vacuum infusion as the volume of the mould cavity will remain almost constant (deformation of aluminium under vacuum is negligible). Thus, in closed mould infusion, the fibre fraction is dominated by the stacking and ply termination strategy. This may result in slightly lower fibre fractions for closed mould vacuum infusion.

5.5.2. Deflection and twist validations

Deflection and twist validation studies were performed using FEA similar to modal analysis. The load was applied as a static load on the nodes from where the load pin nut was in contact with the specimen. A clamped (all degrees of freedom fixed) boundary condition was applied at the nodes inside the capture block (Figure 5-24). Similar to the modal studies, the results were obtained for all three brick element models. The comparison was made only at 0.4kN load. The comparison was made on the leading and trailing edge deflections at the tip of the hydrofoil, which were measured during experiments using dial gauges. The results obtained are summarised in Table 5-8. Results presented here were obtained using linear static analysis with load applied as one load step. Non-linear analysis was also performed to account for the large deflections and the resulting change in load paths. However, no considerable difference was witnessed in the results in the load range, which the twist was measured.

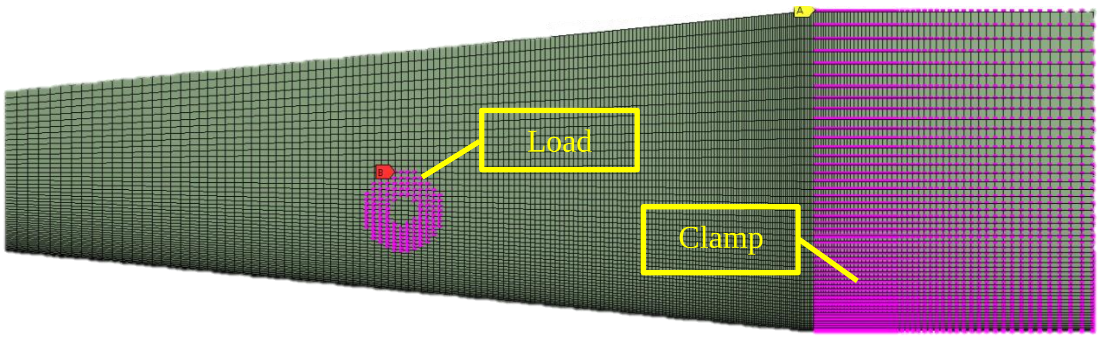

Figure 5-24: Loads and boundary conditions on the hydrofoil

Case	DOFs	Tip Def. (mm)		Twist Angle (deg)	CPU Time (s)[3]
		Leading	Trailing		
Experiments	N/A	9.83	10.4	0.71	N/A
FE solid one element, 2nd order solid elements	319,554	7.55	8.21	0.63	98.8
FE solid per ply split, Solid	3,602,016	7.83	8.52	0.66	90305
FE solid per ply split, Cont. Shell	3,602,016	7.84	8.54	0.67	91546

Table 5-8: Results summary for various FE formulations

Based on the results, it was clear that the per ply split solid models gave the most accurate, closest to experimentally observed results. However, the simulation times taken to achieve the results were considerably higher. This was due to the much larger

[3] CPU time is the aggregate time taken by all cores of the CPU for the task. This is different to the actual time taken for the simulation, which is given by "Wallclock Time"

number of degrees of freedom (DoFs) of the model. The improvement in accuracy as a percentage was roughly 3%, for an increase in CPU time of almost 1000-fold. Thus, considering the number of solutions that had to be obtained, it was decided to perform FEA using the model with one brick element in the thickness direction using the continuum shell approach. It is well understood that a one element thick brick model is not capable of achieving accurate results for stresses and especially through thickness stresses. Therefore, for stress evaluations, the per ply split model was used. Deflection results obtained from the one element thick brick model is summarised in Table 5-9 for each crosshead deflection and load recorded by the MTS load cell. The monolithic model provided adequate accuracy with fast solution times.

Load (kN)	**Tip Def. Exp. (mm)**		**Twist Angle: Exp. (deg)**	**Tip Def. FEA (mm)**		**Twist Angle: FEA (deg)**
	Leading	**Trailing**		**Leading**	**Trailing**	
0	0	0	0	0	0	0.00
0.03	0.82	0.85	0.04	0.57	0.62	0.05
0.11	2.98	3.14	0.20	2.08	2.22	0.13
0.2	5.24	5.53	0.36	3.78	4.12	0.32
0.3	7.48	7.93	0.56	5.66	6.16	0.48
0.4	9.83	10.4	0.71	7.55	8.21	0.63
0.52	12.15	12.85	0.87	9.8	10.66	0.82
0.63	14.52	15.36	1.05	11.87	12.91	0.99
0.76	16.93	17.91	1.22	14.3	15.55	1.19
0.88	19.26	20.37	1.38	16.53	17.98	1.38
1.01	21.7	22.94	1.54	18.94	20.6	1.58
1.13	24.06	25.43	1.71	21.14	22.99	1.77

Table 5-9: Deflection and twist values obtained from experiments and FEA

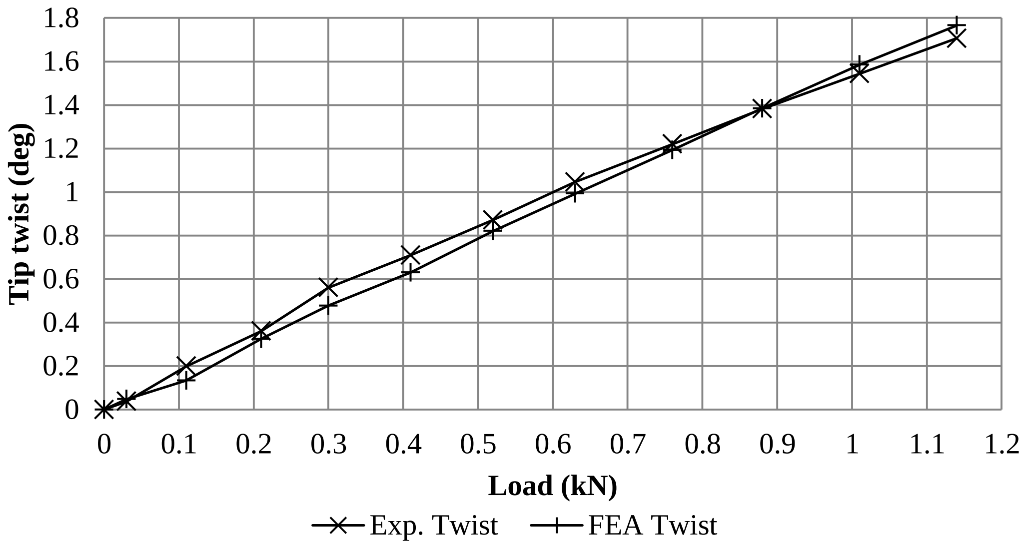

Figure 5-25: Comparison between the twist observed from experiments and FEA

In general, the deflection and twist results from FEA agreed to the results that were witnessed during experiments to an acceptable level. The twist values particularly agreed to the experimental values with a high degree of accuracy. It may be noted that the use of more accurate per ply split solid models can further improve the results as compared in Table 5-8. However, the time required to complete the analyses will be much higher.

5.5.3. Strain variations

The same monolithic model was used to determine the strains at the locations of strain gauges attached to the surface of the hydrofoil (Figure 5-13). Strains were calculated in ANSYS by selecting nodes on the bottom surface of the hydrofoil that lay within the geometric boundaries of the used strain gauges and rosette. Logic based precise node selection were made using ranges of the x and y coordinates of the strain gauges. Nodal strains obtained in required directions were then averaged within the strain gauge to obtain the required strain values and were compared against experimental values. This averaging process was necessary to obtain an acceptable comparison between strain values as the strains were witnessed to vary with high gradients at near some of the strain gauges. Figure 5-26 demonstrates the nodal locations of strain gauges, while Figure 5-27 summarises the comparison against strains measured by experiments. Loading was applied with identical boundary conditions to Figure 5-24.

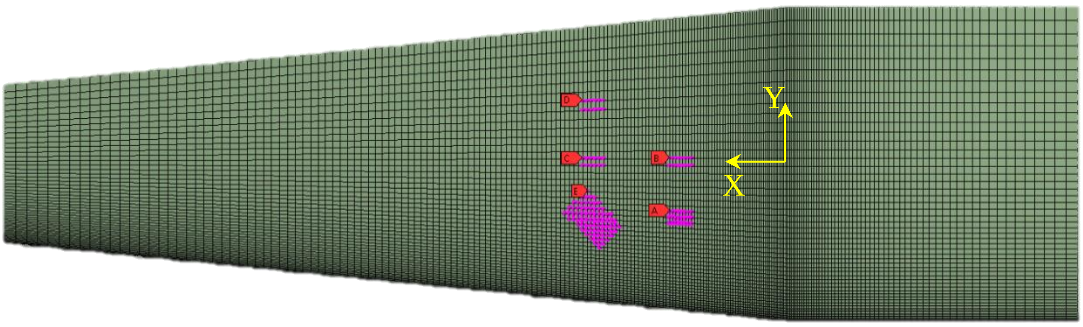

Figure 5-26: Nodes selected at each strain Gauge location in ANSYS

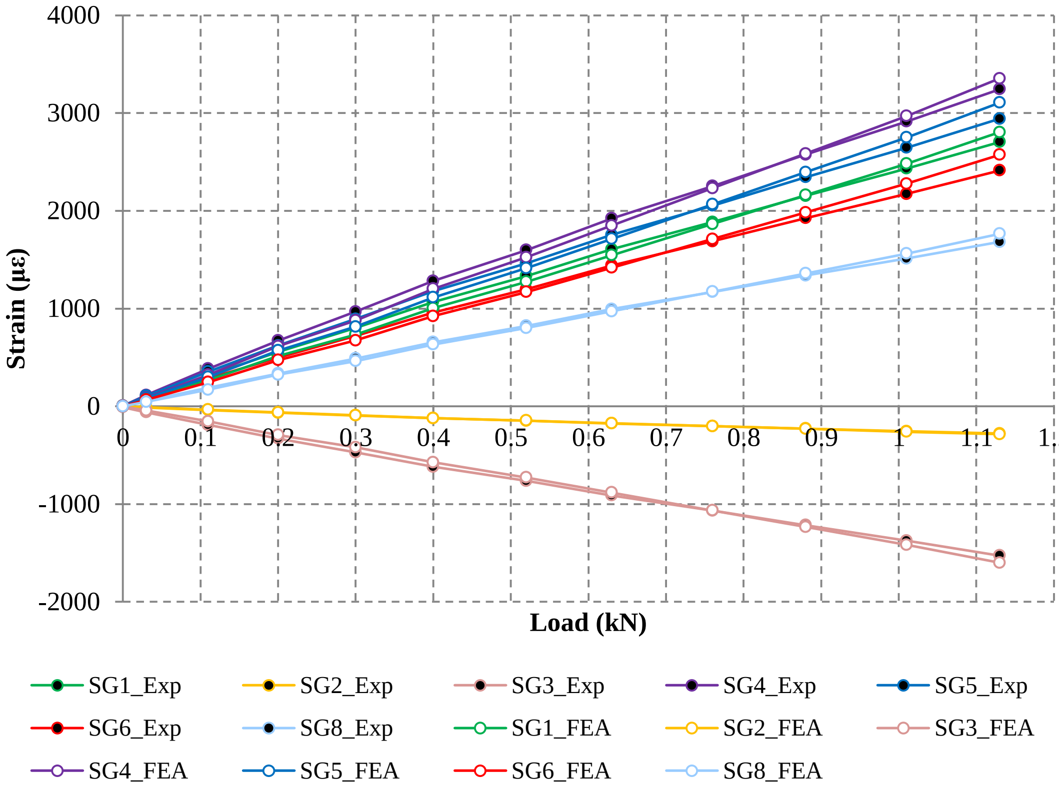

Figure 5-27: Comparison between strain variation in experiment and FEA

In general, strains obtained from FEA matched against experimental strain measurements with a good accuracy. In all strain gauge comparisons it was witnessed that the FEA model underestimated the strain values slightly at lower loads, while slightly overestimated at higher loads.

The witnessed discrepancies may be due to two major reasons: slightly different material properties due to the potentially different fibre fractions in specimens, changes in load angle due to the considerable bending and the resulting rotation that was witnessed during experiments. In summary, it can be considered that FE modelling provided acceptable and useful results particularly in terms of twist.

5.6. Conclusion

Based on the optimisation demonstrated in Chapter 4, hydrofoils were manufactured and tested. The manufacturing process was perfected using an infusion mat layer for efficient and consistent resin distribution and a glass basket layer on the surface of the hydrofoil for good surface finish of the hydrofoil. Experiments were performed on the manufactured hydrofoil to investigate the natural frequencies, load/deflection response, twisting response and ultimate failure point of the hydrofoil.

Natural frequencies were tested by using tap testing using a Dewetron data acquisition and processing system with a single accelerometer. The hydrofoil was suspended using elastic bands and tap testing was performed by tapping the hydrofoil at 39 locations on the surface. Tap testing experiments provided excellent results with low noise and good coherence between each tap. The first natural frequency of the hydrofoil was at around 220Hz. Natural frequency values were well confirmed by finite element analysis with less than 10% deviation in frequencies measured during experiments and frequencies obtained from FEA.

The hydrofoil was then loaded in cantilevered configuration using an MTS loading system to measure the deflection and twist against load. Any possible presence of hysteresis was also measured in the hydrofoil and was found to have no hysteresis up to a load of approximately 1kN, the load range expected in cavitation tunnel tests. Twisting was observed in the expected direction, with leading edge deflecting more than the trailing to unload itself during hydrodynamic testing. Both deflection and twisting values matched well with finite element predictions to further confirm their accuracy.

In the final test, the hydrofoil was loaded to its ultimate failure point. The ultimate failure occurred at a load of 4.2kN, which provided the hydrofoil a safety margin of 400% with respect to the maximum expected loading during cavitation tunnel testing. The failed specimen was then subjected to modal frequency testing and was found to have no significant change in modal frequencies. Afterwards, the failed specimen was partitioned into cross-sections and was scanned to detect cracks and internal damaged using UV florescent optical microscopy. Delaminations were observed to have occurred between ply interfaces of 2nd/3rd carbon layers and 3rd/4th carbon layers. This is believed to have occurred due to the 60° difference in ply angle of 3rd layer compared to 2nd and 4th layers. At two locations the delamination appeared to have propagated through the thickness towards the surface to cause kinks in the outer glass basket layer of the hydrofoil.

Finite element modelling was performed based on obtained experimental results in order to validate and enhance the finite element models. The modal FE simulations were able to predict the first three mode of the hydrofoil to within 10% of the experimental along with the correct modal shape for the first three modes. Deflection and twist predictions were also of good accuracy with most deflection values and all twisting values falling within the 10% range of experimental results. The accuracy of finite element models was proven satisfactory to be used in future FSI studies.

6. Cavitation Tunnel Experiments

Preface

A composite hydrofoil blade was optimized using the proposed optimisation scheme and was manufactured according to the layup and unloaded shape suggested by the optimisation scheme. The blade was then subjected to structural testing to understand its natural frequencies, structural response under cantilevered loading and failure load and deflection. These tests confirmed that the hydrofoil was safe for cavitation tunnel with a safety factor exceeding 400% based on the loading requirements observed in the previous experiments conducted by Zarruk et al. (2014). With the confidence gained from structural testing, the hydrofoil was subjected to cavitation tunnel testing in order to characterise its real-world hydrodynamic performance and validate the predictions made by FSI simulations conducted on the optimised blades and consequently to validate the effectiveness of the proposed optimisation scheme.

The opportunity to conduct cavitation tunnel tests can be considered as a rare and invaluable to validate the techniques detailed in the thesis. Therefore, in addition to validating the optimised hydrofoil, a flat hydrofoil with positive bend-twist coupling was also tested within the same experiment schedule. With the testing of the two hydrofoils, a complete set of hydrofoils was tested: no bend-twist coupling (Zarruk et al., 2014), negative bend-twist coupling (Zarruk et al., 2014), positive bend-twist coupling (current schedule) and optimised hydrofoil (current schedule). The positive bend-twist coupled hydrofoil was constructed of a glass and carbon hybrid layup. The hydrofoil also gave an understanding of the expected behaviour if the structure behaved with opposing characteristics to the optimised hydrofoil, whereby the twist is designed to increase with deflection. Due to its unstable coupling pattern, the hydrofoil demonstrated interesting and unexpected characteristics that was not demonstrated by any other hydrofoil.

6.1. Introduction

The chapter discusses the cavitation tunnel experiments that were performed on manufactured optimised composite hydrofoil specimens. The main objective of the experiments was to understand the response of the optimised composite hydrofoil and characterise its hydrodynamic properties and performance against previously tested carbon hydrofoils that were manufactured with no layup optimisation or unloaded shape design. The chapter first discusses about the cavitation tunnel facility and the experiment setup, which is the same tunnel and measurement systems used in the experiments by (Zarruk et al., 2014). The same systems were kept in place in order to make a fair comparison between the results. The optimised hydrofoil used for the experiments is explained in detail in Chapter 4. However, a brief description of the design philosophy of the hydrofoil, its layup and shape are given in this chapter for clarity. The second hydrofoil used in the experiments had a layup with angles opposite to the negative bend-twist coupled hydrofoil tested by Zarruk et al. (2014) and a flat shape similar to standard tapered NACA hydrofoils.

The loads during experiments were measured using 6-axis load system and converted to useful lift, drag, moment results using matrix transformations. The chapter presents the non-dimensional hydrodynamic entities and compared against previous composite hydrofoils that were tested. A hysteresis effect was witnessed in the positively bend-twist coupled hydrofoil and this phenomenon is also presented in the chapter in detail. The chapter also presented the uncertainty and the variation of hydrodynamic measurement and their non-dimensional derivatives due to measurement uncertainties and vibrations of the hydrofoil.

The observed hydrodynamic measurements were then compared to the results obtained from the finite element models utilising fluid-structure interaction (FSI) capabilities between the structural domain and the fluid domain. Hydrodynamic entries and deflection and twist readings of the FSI simulations are verified against experiments and presented briefly in the chapter. Furthermore, it was witnessed during experiments that the speed of the flow influences the performance of the hydrofoil rather than the standard dependence on the Reynold's number. This became apparent when comparing the experiments performed by Zarruk et al. (2014) to the current experiment schedule. Due to seasonal changes the ambient temperatures were considerably different during the two experiments schedules which resulted in different flow speeds to account for the change in viscosity of water in order to achieve the same Reynold's number. However, during experiments this was not validated; thus, in the chapter it will be validated using ANSYS FSI.

6.2. Test Setup and measurement techniques

Experiments were conducted at the Cavitation tunnel laboratory owned and managed by the Australian Maritime College, Launceston, Tasmania. The tunnel is a state-of-the-art cavitation tunnel facility with high uniformity and low turbulence in the test section. The tunnel provides fine control of velocity and pressure at the test section while maintaining a low cavitation number in the test section. It is also equipped with capabilities to reduce nuclear formation to further improve the uniformity of the flow and prevent delay the onset of cavitation (Brandner et al., 2007). Specifications of the cavitation tunnel can be summarised as follows:

- Test section 0.6 m square x 2.6 m long
- Max flow speed 12 m/s
- Pressure range from 4 to 400 kPa absolute
- Test section velocity uniformity at mid-section 0.25%
- Test section turbulence intensity at mid-section 0.3%
- Test section temporal stability of velocity 0.01%
- Test section temporal stability of pressure 0.01%

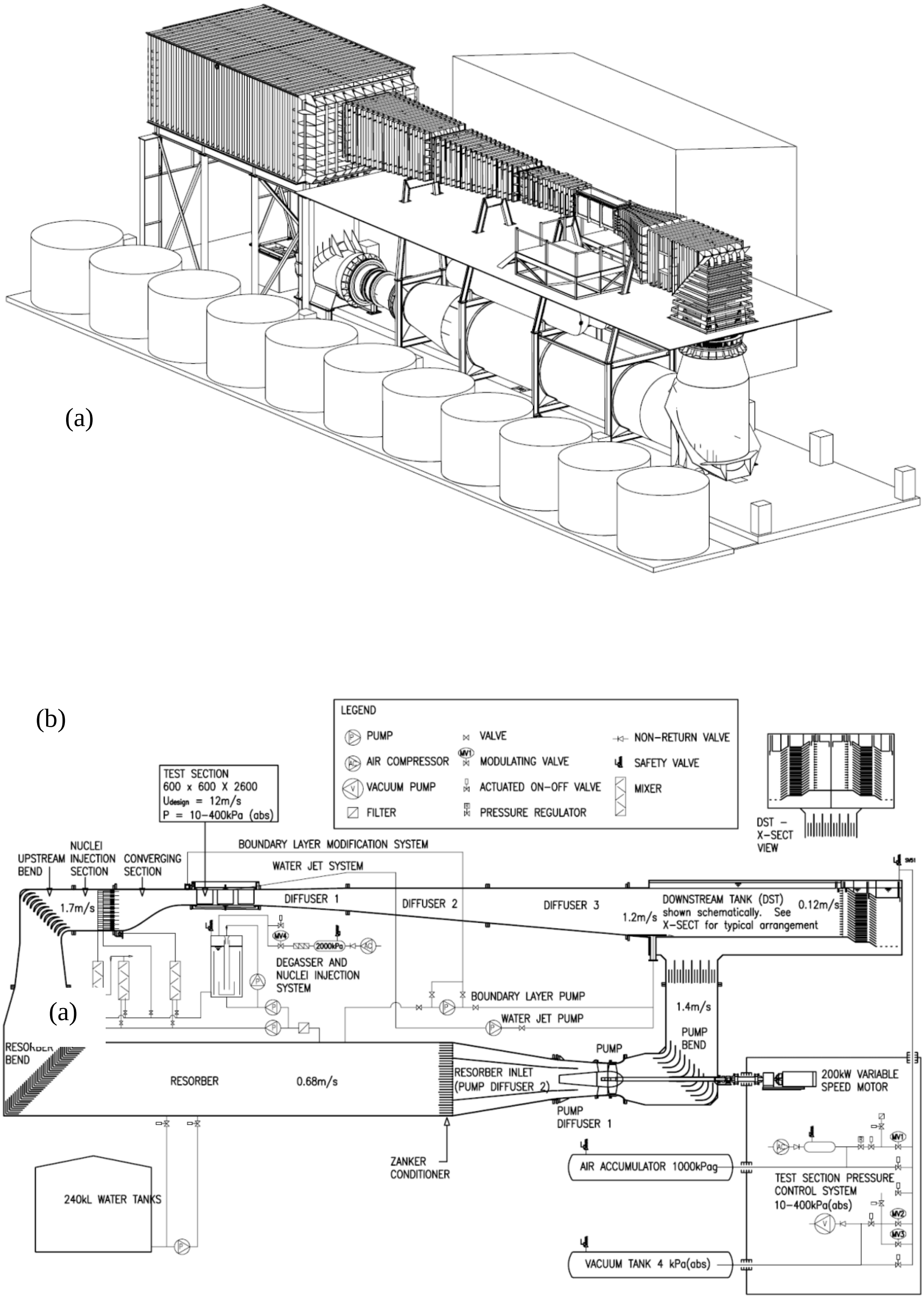

Figure 6-1: Cavitation Tunnel facility (Brandner et al., 2007): (a) Overview & (b) cross-section of the facility and components

For the experiments, the following flow conditions and parameters were observed:

- Water density : 997.28 ± 0.02 kgm^{-3}
- Temperature : 24.06 ± 0.06 °C
- Dynamic viscosity : 8.8738×10^{-4} $kgm^{-1}s^{-1}$
- Reynold's numbers (Re) used[4] : 0.25 Mil., 0.4 Mil., 0.6 Mil., 0.8 Mil. and 1.0 Mil.
- Avg. flow speeds (free stream) : 2.5 m/s, 4.002 m/s, 6.044 m/s, 8.018 m/s, 10.019 m/s
- Angle of Attack : [-15°,15°] at 0.5° inc. and 10 seconds at each inc. for all Re except 1 Mil.; [-9°, 9°] at 0.5° inc. and 10 seconds at each inc. for Re 1 Mil.
- Tunnel Pressure : 200kPa (to delay the onset of cavitation)

6.2.1. Load Balance

The load balance used for the experiments was a six axis system with the clamping system being designed to hold hydrofoils of similar profile and size. The load balance and subsequent calculations are based on two different coordinate reference systems: one being the flow-fixed coordinate system, while the other being the body-fixed coordinate system. The two coordinate systems are demonstrated in Figure 6-2.

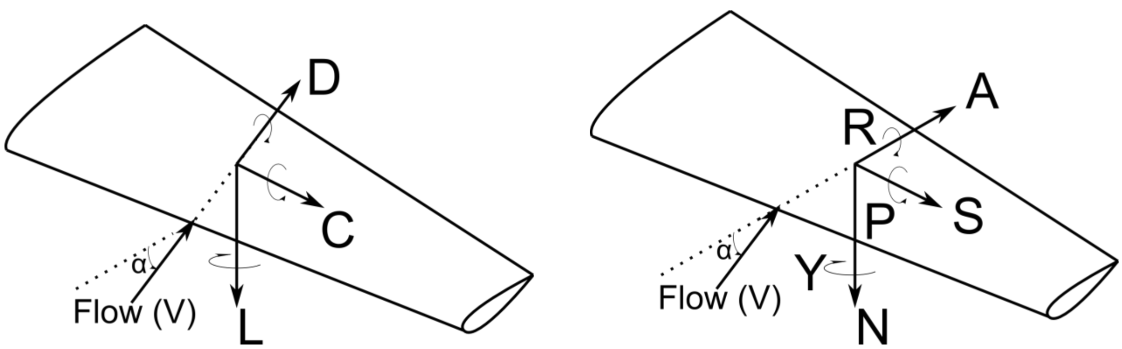

[4] Based on the average chord of the hydrofoil: 0.09m

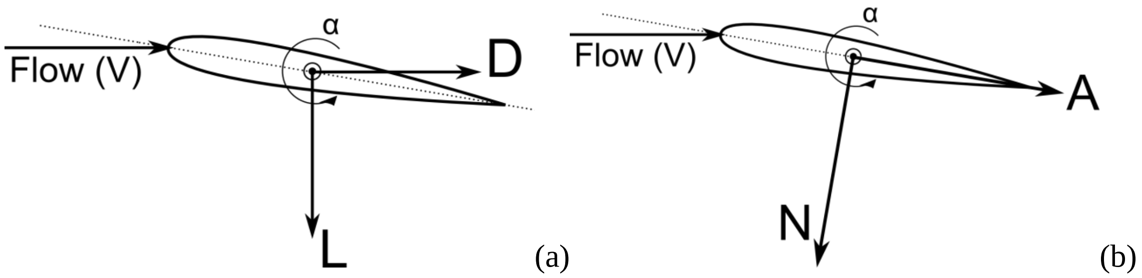

Figure 6-2: Coordinate system used for measurements: (a) Flow-fixed & (b) Body-fixed

The load balance used six independent load cells for accurate measurement of forces. The load cells were configured inside the balance as shown in Figure 6-3. The three load cells in the plane of the chord of the hydrofoil (L1, L2 and L3) are capable of measuring loads parallel to the chord-plane, while the load cells normal to the chord-plane (L4, L5 and L6) measure the loads out-of-plan. Based on raw measurements from the six load cells, a simple coordinate transformation can be performed to obtain loads in three directions and moments about three axes. The hydrofoil was mounted on to the load balance using a pre-made rig given in Figure 6-4. The optimised foil was designed such that it fits the same pre-made rig that was used for previous hydrofoil experiments (Zarruk et al., 2014). Figure 6-5 shows the hydrofoil clamped into the load balance.

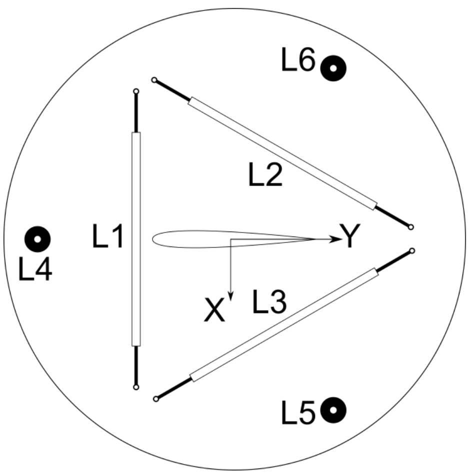

Figure 6-3: Load-cell setup of the load balance

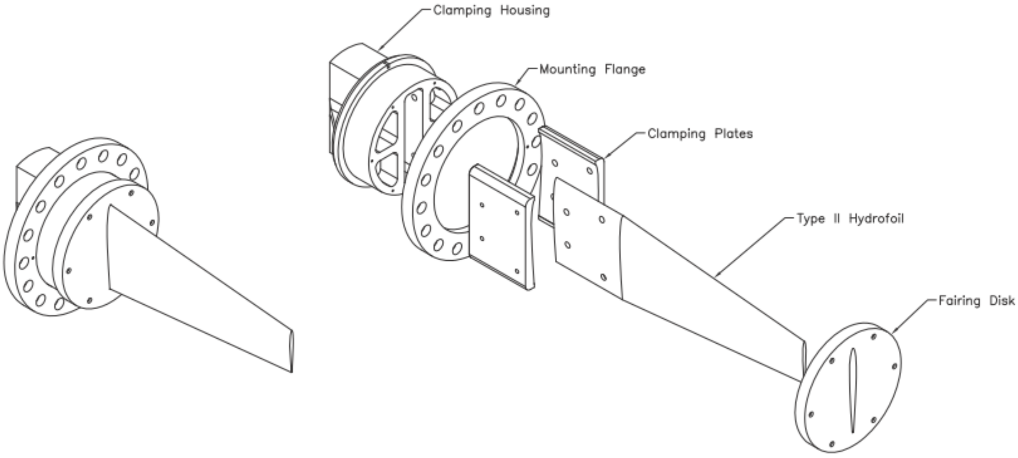

Figure 6-4: Clamping system assembly used on the load balance

Figure 6-5: Hydrofoil fastened into the load balance

The load cells were calibrated using known weights prior to loading. The calibration process was performed using a calibration rig and air bearings. Based on prior studies it was known that the accuracy of calibration does not substantially change with the load range. Therefore, mass up to 5kg (at 1kg increments) for Y and Z axis and mass up to 20kg (at 5kg increments) for X axis were used to calibrate the forces. A moment arm with the length of 350mm was used to calibrate the moments. Moments about the three axes were calibrated using masses up to 5kg (at 1kg increments), with moments resulting up to 1.75kg.m. Calibration was performed using a calibration software written for the load balance, where voltages from load cells were recorded for the known masses in both loading and offloading cycles.

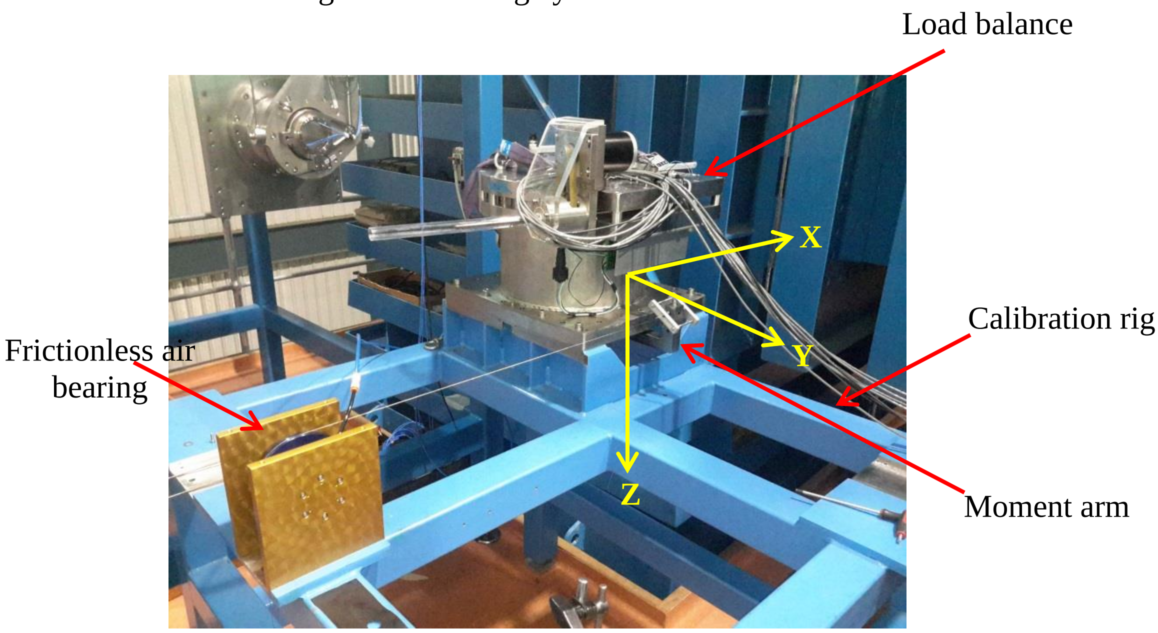

Figure 6-6: Calibration process of the load balance (at the given instance calibration is being performed for moment about Z-axis)

6.2.2. Deflection Measurement

Tip deflections were of particular interest in these experiments. Tip deflections were measured by photogrammetry using a Nikon D8000 camera mounted facing the tip of the hydrofoil (Figure 6-7(a)). Two circular trip strips were glued close to the leading edge and trailing edge of the hydrofoil for the image recognition routine to easily recognise the extremities of the tip of the hydrofoil. The camera was adjusted to shallow depth of field with appropriate lighting and zoom levels in order for the image recognition software be able to easily recognise the trip strips glued to the tip. Prior to taking measurements a calibration plate with 5mm x 5mm grid size was used to calibrate the camera pixel ratio to length at the same distance the hydrofoil tip was located from the camera lens.

The image recognition routine was written on C++ using OpenCV (Open Computer Vision), an open-source image recognition library for C++ and C languages. The routine was set to recognise the locations the pixels of red hue and calculate pixel that corresponds to the centroid of each red hue (trip strip dot). After the two centroids were recognised, the centroid pixels locations were compared to the original image with zero flow velocity to find the deflection and twist at the tip of the hydrofoil. For these experiments only tip deflections were measured, while the full-field deflection pattern was not considered. Full-field deflection and strain patterns can be obtained using ARAMIS strain measurements, as recently demonstrated by Butler et al. and DSTO.

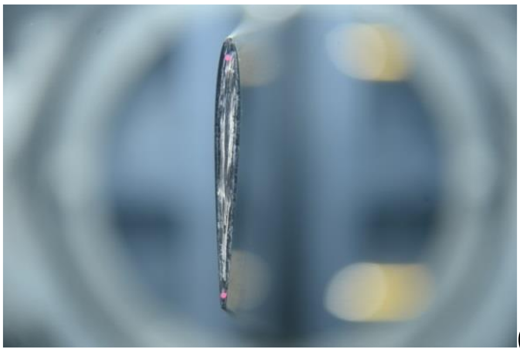
(a)
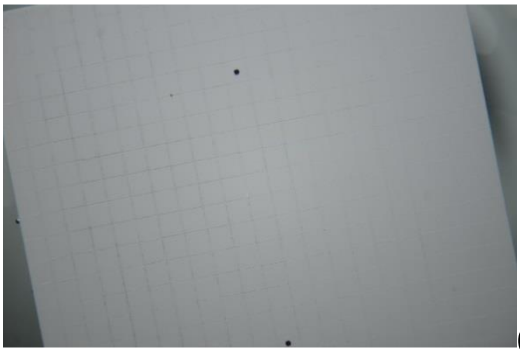
(b)

Figure 6-7: Camera setup for photogrammetry: (a) Tip of the hydrofoil, (b) Calibration plate

6.2.3. Summary of specimens used

The hydrofoil tested was a modified NACA0009 (Eq.(4-1) with the chord linearly tapering from 0.12m (root) to 0.06m (tip) over a span of 0.3m. The modification had been made to the standard NACA 0009 profile in order to account for the extra thickness formed during the manufacturing process of the composite foil. The modified equation and the resulting half-thickness distribution for the hydrofoil are given in Eq. (4-1) and Figure 4-1, respectively (Zarruk et al., 2014).

The optimised hydrofoil was designed based on a specific layup optimisation and pre-loaded shape design algorithms based on pressure distributions obtained from previously tested hydrofoils in the cavitation tunnel. Chapter 3.2 discussed in detail the proposed optimisation scheme with the required mathematical background, while Chapter 4 discussed the processes involved in optimising a hydrofoil based actual cavitation tunnel tests that were conducted in the same AMC cavitation tunnel with no-optimised hydrofoils. Finally, Chapter 5 explained the manufacturing process of the hydrofoils and the structural tests to validate its safety under cavitation tunnel loads.

The optimisation process elaborated in Chapters 3 and 4 was used to achieve the composite layup required to optimally change the twist deformation based on generated lift. Exact pressure distributions derived using ANSYS CFX^{TM} fluid solver at different AoAs in the vicinity of the operating AoA of 6º were used in the optimisation process. Optimisation was performed using the Genetic Algorithm with mixed integer formulation to achieve ply angles that are relatively straight forward to cut and manufacture. During manufacturing a biaxial carbon layer was used to improve the resin flow during the infusion process in order to obtain a better surface finish. Results achieved using the optimisation scheme and the manufactured layup are summarised in Table 6-1. It must be noted that, using a biaxial carbon layer of similar surface density as opposed to using [30, -30] unidirectional layers does not produce a layup that is considerably different in terms of mechanical properties.

Increment	Layup
5 deg	$[(-25)_2/30/(-25)_4/(75)_3/(-25)_4/-15/\overline{\mathrm{Mat}}]_S$
15 deg	$[(-30)_2/30/-30/75/-30/75/(-30)_4/\ 75/(-30)_2/-15/\overline{\mathrm{Mat}}]_S$
Actual Manufactured	$[0^{GB}/(-30)_2/30^{Bi}/75/-30/75/(-30)_4/\ 75/(-30)_2/-15/\overline{\mathrm{Mat}}]_S$[5]

Table 6-1: Results obtained from the optimisation algorithm

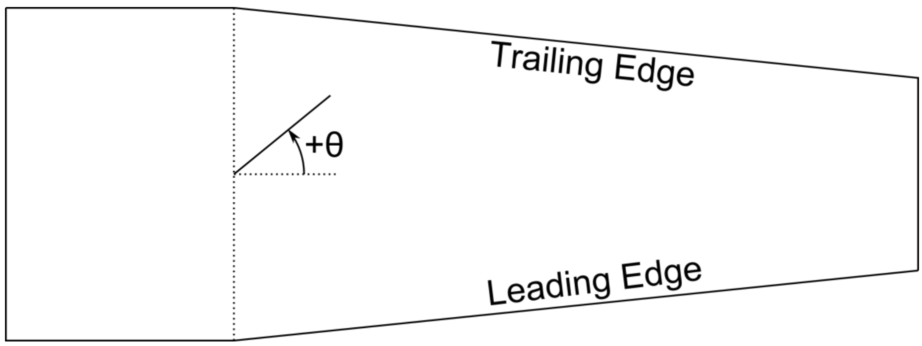

Figure 6-8: The convention of fibre direction

After the layup was optimised, the unloaded shape required for the layup was determined. Since it is intended to compare the optimised layup against previously manufactured and tested flat hydrofoils, the required shape at the operating condition was considered as the flat planar trapezoidal shape, but with the slight positive twist obtained by the flat hydrofoils. In other words, the hydrofoil had to achieve the shape of the flat hydrofoil at the operating condition.

A second hydrofoil was constructed with no optimisation, but with a layup arrangement that further loads itself with increased deflection/lift. In other words, the second hydrofoil had a layup that has positive bend-twist coupling performance. The layup for this hydrofoil was chosen to be the opposite of the bend-twist coupled layup that was tested by Zarruk et al. (2014). The layup chosen for the hydrofoil was $[0^{GB}/(30)_5^{CUD}/(0)_2^{GFB}/(30)_4^{CUD}/\overline{\mathrm{Mat}}]_S$[6].

[5] GB – Glass lasket layer, Bi – Carbon fibre Bi-axial layer
[6] GB – Glass basket, CUD – Unidirectional carbon, GFB – Glass fabric

6.3. Hydro-dynamic results

Hydrodynamic results were recorded for five different Reynold's Numbers (flow speeds) with root angle of attack as specified in Section 6.2. However, the starting and ending angles were changed accordingly, when needed, to investigate hysteresis effects and gear backlash issues of the servo controller of the load balance pitching mechanism. It must be noted that these experiments used the pitching mechanism with the rotary encoder feedback control system, in order to minimise backlash issues. Experiments for the optimised hydrofoil was done starting from $\alpha = -1°$ and ending at $\alpha = +1°$. For example, the experiment for Re = 0.25×10^{6} was performed by sweeping the root incidence angle in the sequence: $\alpha = -1° \rightarrow +15° \rightarrow -15° \rightarrow +1°$. All incidence angles were changed at an increment of 0.5° while maintaining each increment for a duration of 10 sec. Based on previous hydrofoil experiments (Zarruk et al., 2014), a 10 sec duration was deemed adequate for the hydrofoil to reach its steady state. Images were captured for deflection and twist measurement purposes at every 1° increment.

6.3.1. Non-Dimensional Hydrodynamic Parameters

Hydrodynamic results were first measured in the load balance coordinate frame and were converted to flow-fixed and body-fixed coordinate systems. Non-dimensional flow parameters were calculated using the following relationships (only presented for flow-fixed coordinates; body-fixed coordinate system will have similar interpretations).

$$\begin{gathered} Lift\ Coefficienct = C_L = \frac{2L}{\rho V^2 A} \\ Lift\ Coefficienct = C_D = \frac{2D}{\rho V^2 A} \\ Cross\ Coefficienct = C_C = \frac{2C}{\rho V^2 A} \\ Yaw\ Coefficienct = C_Y = \frac{2Y}{\rho V^2 Ab} \\ Roll\ Coefficienct = C_R = \frac{2R}{\rho V^2 Ab} \end{gathered} \tag{6-1}$$

$$Pitch\ Coefficienct = C_Y = \frac{2P}{\rho V^2 Ab}$$

where, A is the planform area and b is the span of the hydrofoil. $Y, R\ and\ P$ are yaw, roll and pitching moments, respectively and L, D and C are lift, drag and cross forces on the hydrofoil, respectively. During measurement, all forces and moments followed the sign convention given in Figure 6-2. However, for the purpose of presenting results, the sign convention has been changed to a more sensible system where lift is considered upwards. Results for both hydrofoils that were tested are presented and discussed here. The full AoA sweep is presented for +30Deg hydrofoil to demonstrate hysteresis effects observed that were observed. As no measureable hysteresis was observed for the optimised hydrofoil, average quantities for increasing and decreasing AoA sweep is presented here. Hysteresis is further discussed later in this chapter. Figure 6-9 and Figure 6-10 summarise the variation non-dimensional hydrodynamic entities with incidence angle for the optimised and +30deg hydrofoils, respectively.

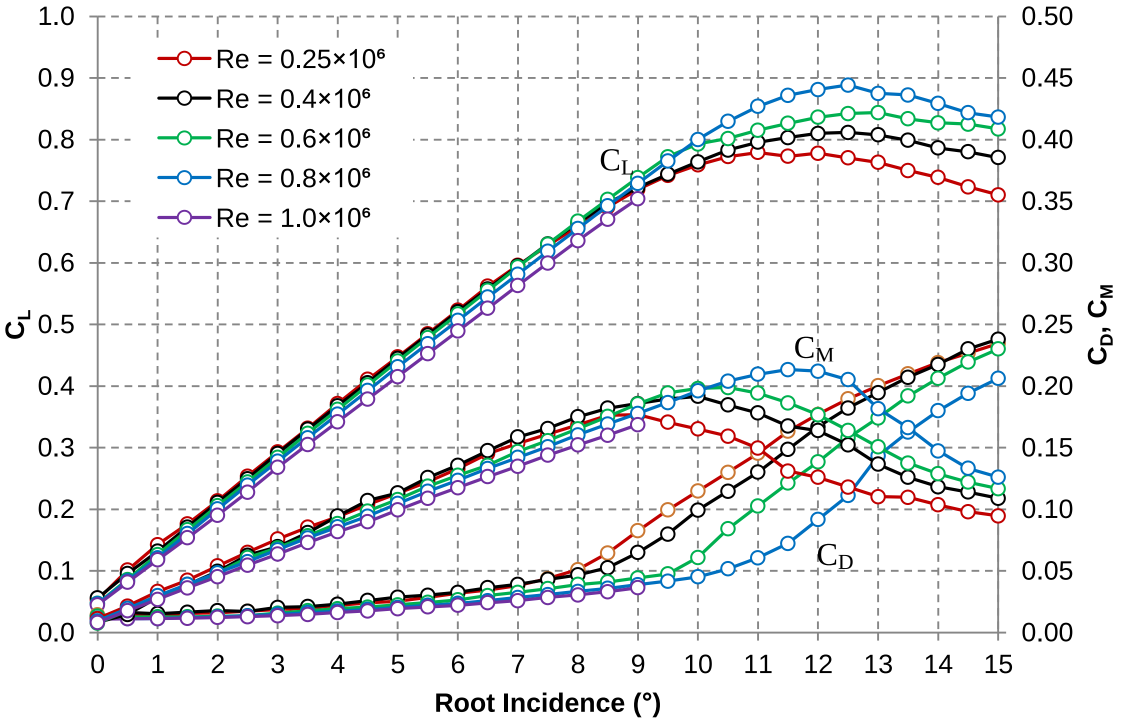

Figure 6-9: Lift, drag and pitching moment coefficients against incidence angle for optimised hydrofoil

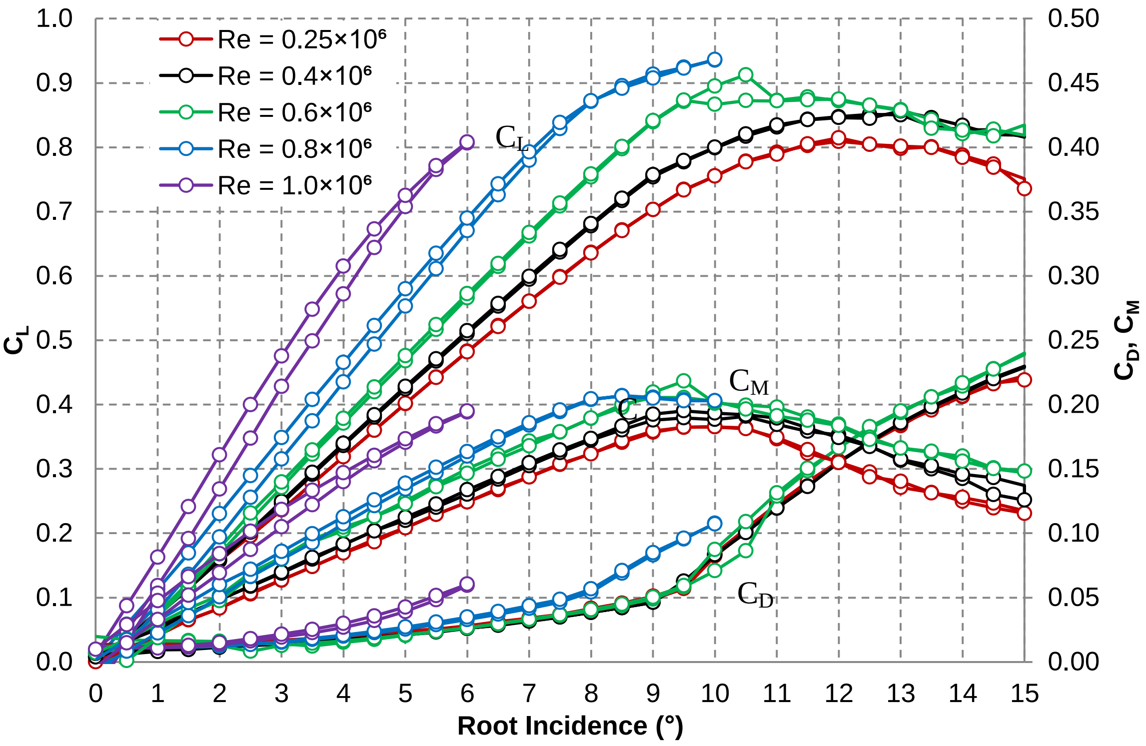

Figure 6-10: Lift, drag and pitching moment coefficients against incidence angle for +30deg hydrofoil

It must be noted that for the case where $Re = 1 \times 10^6$, the incidence angle was not taken up to 15° in order to maintain the force on the hydrofoil below 1kN. Several notable observations can be made based on the results presented above.

At pre-stall incidence angles, optimised hydrofoil behaves almost identically (in terms of non-dimensional hydrodynamic entities) at all Reynold's Numbers (Figure 6-11). The slight differences can be attributed to low Reynold's Number effects of flow and/or the shape adaptive nature of the hydrofoil. Low Reynold's number effects on NACA aerofoils are documented by Ohtake et al. (2007) and Selig et al. (1995). If low Reynold's Number flow effects were dominant, C_L can be expected slightly increase with Reynold's number. However, in this case, the opposite can be observed: C_L reduces with increasing Re. Furthermore, Zarruk et al. (2014) shows that low Reynold's number effects explained by Selig et al. (1995) and Ohtake et al. (2007) are not significant for the modified NACA profile used in these experiments. This could possibly be due to extended flow attachment observed at low speeds being hampered by the introduction of a flat edge at the trailing edge. Therefore, it is more likely that the observed difference between Reynold's numbers is due to the shape adaptive nature of the hydrofoil. The hydrofoil has a layup that reduces its incidence angle with increased deflection due to lift. In other words, at higher speeds, the hydrofoil will reduce the incidence angle at the tip by twisting downwards. This leads to lower C_L values with the increase in Reynold's number. This explanation is further substantiated by the delay in stall angle with the increase in Reynold's number. It can be seen that stall is substantially delayed for 0.8 million Reynold's number compared to 0.25 Million Reynold's number. In summary, the shape adaptive hydrofoil demonstrated decreases in C_L, C_D and C_M and delayed stall with increasing Reynold's number.

The pre-stall behaviour of the +30deg hydrofoil was significantly different in comparison to the optimised hydrofoil and all previous hydrofoils tested by Zarruk et al. (2014). The hydrofoil demonstrated strong Reynold's number dependencies in all three hydrodynamic parameters considered here. No such strong dependence between Re and C_L, C_D and C_M has ever been documented in this Reynold's number range purely due to flow effects. Thus, as with the optimised hydrofoil case, this has to be due to bend-twist coupling effects of the hydrofoil. The layup of the hydrofoil was arranged such that the tip AoA increases with increase in deflection and lift. Therefore, for the same root incidence angle, a higher Reynold's number gives a higher tip incidence angle. This essentially means that the hydrofoil has a different shape for each Reynold's number and it acts as a different hydrofoil altogether. As a result, the popular idea of Reynold's number independence on non-dimensional parameters does not hold in the case of shape-adaptive structures.

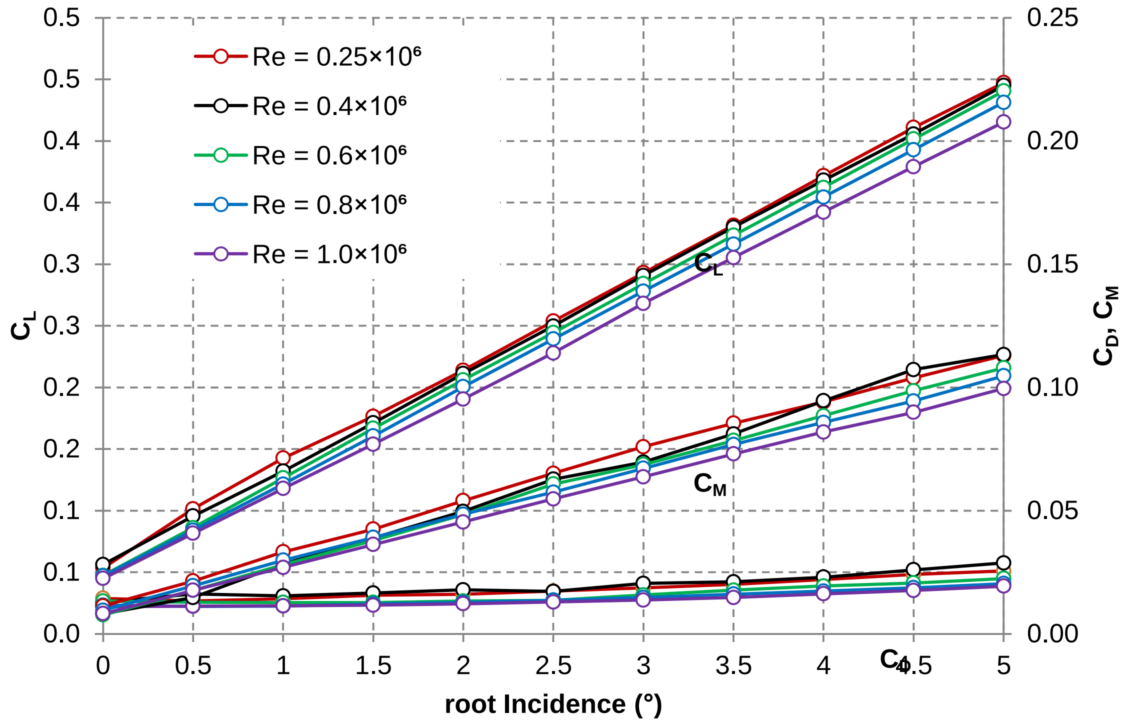

Figure 6-11: Pre-stall hydrodynamic behaviour of the optimised hydrofoil

6.3.2. Lift/Drag ratio and efficiency of Hydrofoils

The lift/drag performance of the hydrofoil was investigated and compared against each other. The lift to drag ratio can be considered as the efficiency of a hydrofoil due to its equivalence to the propulsive efficiency of a propeller. As stated in Section 6.2.3, the optimised blade was in fact designed with the intention of maintaining a higher L/D ratio over a wider range of incidence angles, in comparison to the baseline composite hydrofoil (CFRP 00 deg hydrofoil) with no coupling.

One major discrepancy that must be noted here is the conditions of flow that was prevalent during the previous set of experiments, where CFRP 00 deg foil and CFRP -30 deg foil were tested, and the current set of experiments, where Optimised foil and CFRP +30 deg foil were tested, is the water temperature and the resulting change in viscosity. The previous batch of experiments were conducted during winter at a water temperature of 17.8°C, while the current batch of experiments were conducted in late summer at an average water temperature of 24.06°C. As a result, the dynamic viscosity during previous experiments was $1.0523 \times 10^{-3} kgm^{-1}s^{-1}$, while during recent experiments it was $9.0411 \times 10^{-4} kgm^{-1}s^{-1}$. This was a change of 14%, with the implication being, the latest experiments having had to run at a 14% lower flow velocity to maintain the same Reynold's number compared to the previous set of experiments. As the lift force acting on the hydrofoil and the resulting structural deflection has a second order relationship to the flow velocity, this causes a considerable disadvantage to the optimised hydrofoil when comparing L/D performance if the same Reynold's numbers were to be considered. It must be noted here that the design of the optimised hydrofoil was based on the experimental and simulation data that were obtained during the previous set of experiment, which had higher flow speeds for the same Reynold's Number. As explained in Section 6.2.3, the optimised hydrofoil was designed for a Reynold's Number of 0.6×10^6 of previous set of experiments. During the experiments, due to the reduction in flow velocity, it was observed that the optimised hydrofoil behaved closer to its design objective at 0.8×10^6 Reynold's Number rather than 0.6×10^6. Consequently, due to the changes in structural deformations, it was decided that comparing 0.6×10^6 of previous set of experiments to 0.6×10^6 Reynold's Number in the current set of experiments is more pertinent. Figure 6-12 summarises the Lift/Drag ratio for the four composite hydrofoils: $Re = 0.6 \times 10^6$ for CFRP 00deg and CFRP -30deg and $Re = 0.8 \times 10^6$ for CFRP +30deg and Optimised hydrofoils are compared against each other.

The baseline hydrofoil achieves its peak L/D performance between 4° - 6° root incidence angle. However, beyond this range its efficiency starts decreasing considerably with a rapid drop L/D starting from 10° due to the characteristic drag bucket effect of these hydrofoils at stall. The -30deg hydrofoil tested before demonstrates a much wider L/D curve with the stall being delayed to around 12° AoA. However, the drawback of the -30deg hydrofoil is that it starts offloading too soon due to it being manufactured with an initial flat shape identical to the baseline 00deg hydrofoil. As a result, the -30deg hydrofoil demonstrates a lower L/D value compared to the baseline 00deg hydrofoil in the AoA range between 0° to 5°. The optimised hydrofoil demonstrates a wider L/D curve similar to -30deg hydrofoil due to its layup optimisation, but due to the initial shape optimisation, does not fall below the curve of the baseline hydrofoil. Thus, the importance of a two-step optimisation process is demonstrated. On the other hand, the +30deg hydrofoil achieves the peak L/D much earlier than all other hydrofoils and recedes rapidly as the AoA is increased. Further, due to considerable hysteresis of the +30deg hydrofoil, the average L/D value for each AoA was taken for clarity. It must be noted here that there is a narrow range where the baseline hydrofoil has a slightly higher L/D compared to the optimised hydrofoil. This could likely be attributed to differences in mould quality and edge quality as all hydrofoils manufactured using the flat mould was observed to achieve the same peak L/D at some AoA point regardless of the layup.

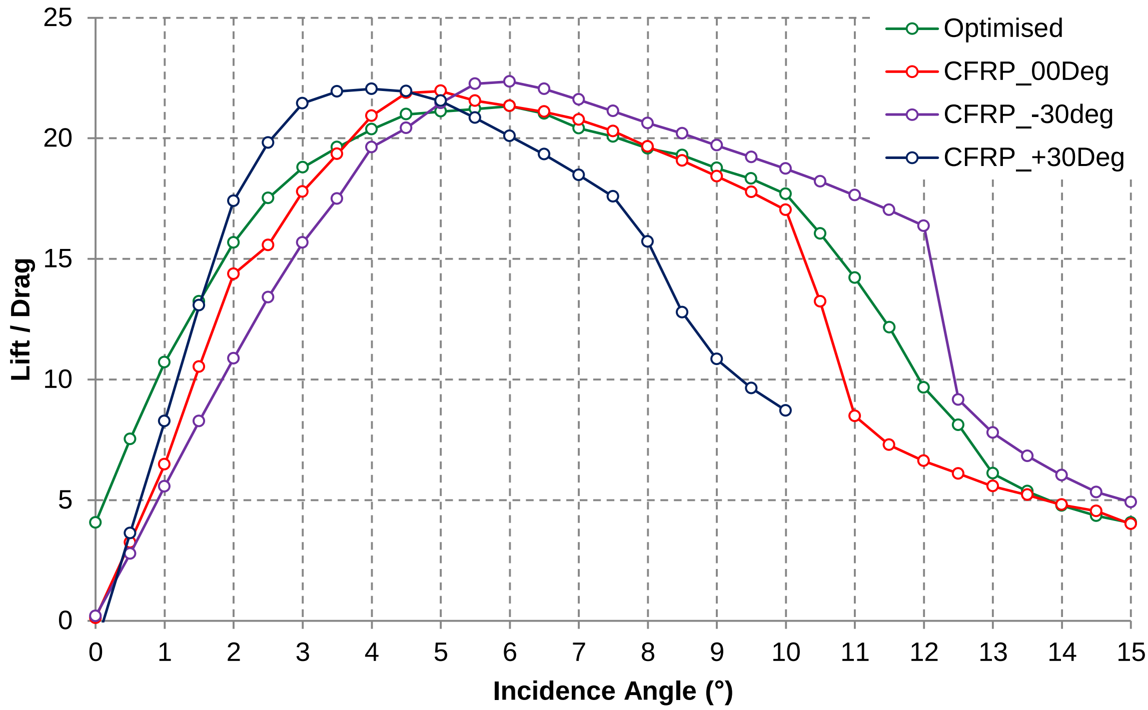

Figure 6-12: Lift/Drag comparison for different hydrofoils

6.3.3. Stall Angles and Peak Lift

An important advantage of offloading is the delay in stall that can be achieved. Stall usually begins at the tip for non-offloading type aero and hydrofoils. The reason for this is that even for steel structures where deformation can be negligible, due to the lift centre being close to leading edge of the hydrofoil, the tip will always have a slightly higher incidence angle compared to the root. However, offloading type aero and hydrofoils, such as the optimised hydrofoil and the -30deg hydrofoil, due to their layup arrangement will have a lower incidence (washout) sat the tip. However, too large of a washout can be detrimental to the amount of lift generated by the hydrofoil. This is in fact the disadvantage of the -30deg hydrofoil, which the optimised hydrofoil mitigates by the initial positive twist as a result of its shape optimisation and by having a layup just enough to provide the required amount of bend-twist coupling as a result of its layup optimisation.

Due to offloading, the optimised hydrofoil reaches stall at around 12.5° root incidence for $Re = 0.8 \times 10^6$, whereas the stall angle of the baseline hydrofoil is at around 10.5° (Zarruk et al., 2014). Furthermore, the maximum C_L of the optimised hydrofoil is 0.89, whereas of the baseline hydrofoil and -30deg hydrofoil they are 0.868 and 0.871, respectively. Thus, it is clear that offloading does not reduce the overall lift generation, but has the potential to increase it, due to the delay in stall.

6.3.4. Hysteresis Effects

Another important and interesting observation was the significant amount of hysteresis that was present in the +30 degree hydrofoil. In comparison to the optimised hydrofoil, the +30deg hydrofoil demonstrated a significant amount of hysteresis. This effect was more prominent with the increase in flow speed. Figure 6-13 compares hysteresis between the two hydrofoils using lift coefficient (C_L) for a full sweep of -1° → +6° → -6° → +1° at 1.0×10^6 Reynold's number. It is clear that the optimised hydrofoil demonstrated almost the same C_L for a given root incidence angle regardless of whether the incidence angle was increasing or decreasing. However, the +30deg demonstrated differing C_L values for the same root incidence angle with a maximum absolute difference of 0.0583 occurring at 0° root incidence. To further understand this phenomenon, several experiments were performed on the +30deg hydrofoil with different starting points and different AoA limits set for the sweep. In the 1st run the incidence angle was changed in the sequence -1° → +6° → -6° → +1°, in the 2nd run the incidence angle was changed in the sequence +1° → -6° → +6° → -1° and in the 3rd run the incidence angle was changed in the sequence +1° → -3° → +3° → -1°. This was performed to understand of effect of loading history on the amount of hysteresis that was observed. The results are summarised in Figure 6-14.

Runs 1 and 2 were performed with angle sweeps in opposite directions to each other in order to verify that the witnessed hysteresis effect was not a result of gear backlash in the automated indexing mechanism. These two runs gave C_L paths that almost perfectly coincide with each other, which provided a closed loop envelope for C_L. The fact that the same envelope was obtained for the two runs ruled out any possibilities of gear backlash in the indexing system. Run 3 was conducted afterwards to investigate the effect of incidence angle range on the amount of hysteresis. Based on 3rd run it observed that the hydrofoil attempts to take the same path when the incidence angle is increasing in either direction, regardless of the starting and ending incidence. However, depending on the starting point and extremities, the path taken to converge at the C_L path of increasing incidence may be different.

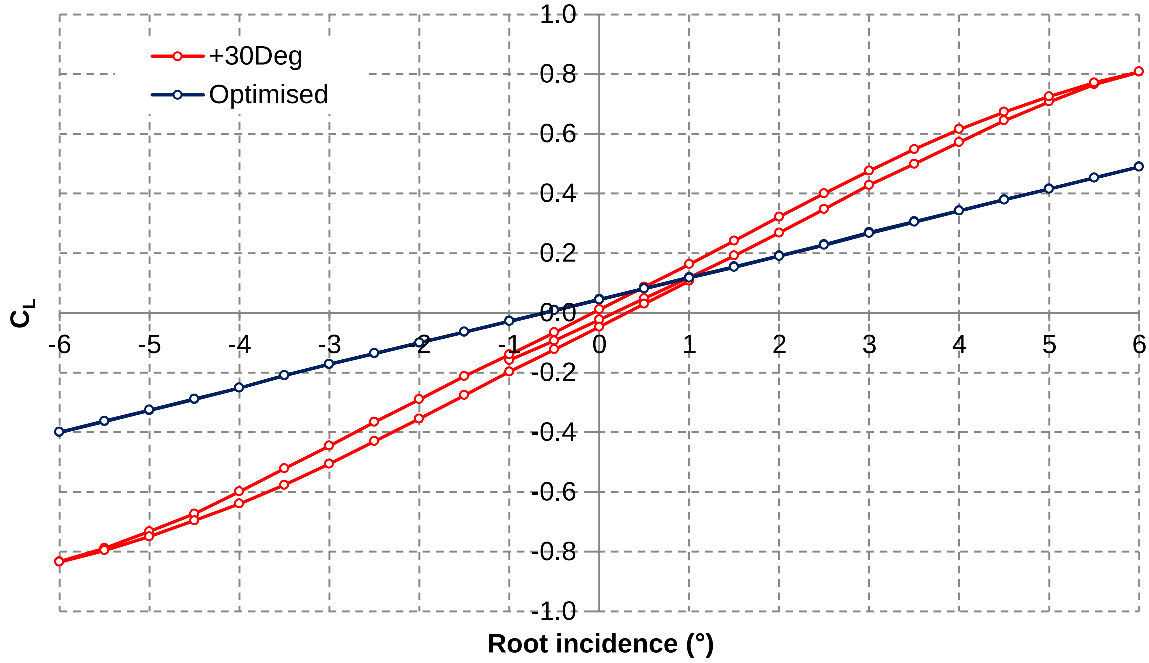

Figure 6-13: Hysteresis comparison between the two hydrofoils at $Re = 1.0 \times 10^6$

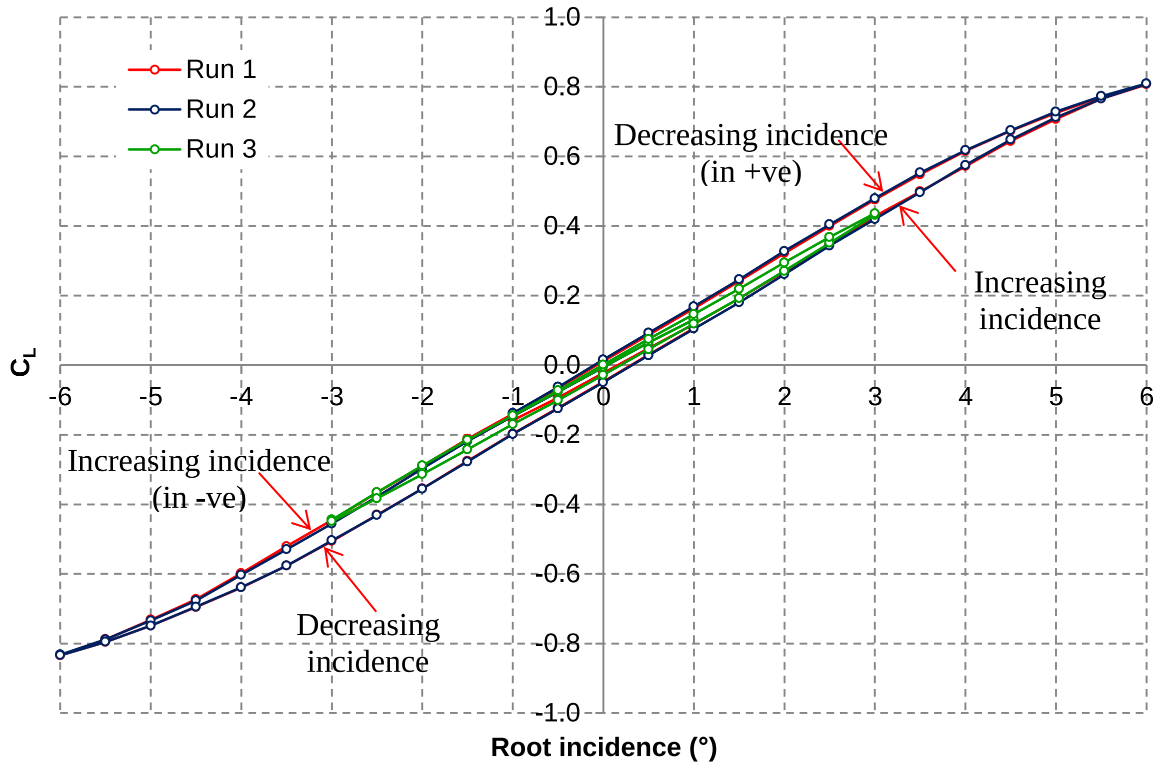

Figure 6-14: Effect of loading history on hysteresis

This is a particularly interesting phenomenon as it implies that for the same hydrodynamic setup, there could be two or more performance and structural deformation solutions. These are observations that to the best of author's knowledge have not been documented for hydrofoils before. However, a similar hysteresis phenomenon is reported by Augier et al. (2014) for flexible sails at relatively low pitching periods ($T = 1.5, 2, 3, 6s$). One could expect such hysteresis in the inherently unstable dynamic model created in high speed cycles of pitch change due to the fast movement of lift centre, which results in further positive twisting and increase in lift. However, in the context of these experiments, where the incidence was changed 0.5° per every 10s, observing hysteresis was an unexpected outcome. A concrete explanation for this hysteresis effect is still under investigation. However, an attempt is made here to narrow down the cause of this effect and present the hypothesis the author has to explain this effect.

The first possibility is the hysteresis of the materials used to construct the hydrofoil, which causes the material to retain a certain amount of positive angle of attack when the incidence is reduced from its peak. It is a known fact that most materials demonstrate such hysteresis behaviours due to plasticity effects after a certain strain is exceeded. However, these hydrofoils were tested for hysteresis using static testing and was concluded that they exhibit very little, almost negligible amounts of hysteresis for loads up to 1kN (Figure 6-15). The maximum hysteresis was less than 5% occurring at around 6mm of cross-head (at mid-span), and approximately 15mm deflection at the tip. This is considerably different in shape and magnitude to the hysteresis observed during tunnel testing, especially for the +30deg hydrofoil. Thus, it can be safely concluded that the hysteresis effect is not due to material alone. There can clearly be no hysteresis due to fluid alone, as such a phenomenon was not observed for the steel hydrofoil, which can be safely assumed to have no structural deformation. Furthermore, among all the extensive research that has taken place in the long history of research in similar NACA profiles, no such hysteresis has ever been documented in the Reynold’s number range considered in these experiments due to pure hydrodynamic loadings. Thus, the best explanation is that the observed hysteresis is due to a coupled effect between the fluid domain and the structural domain.

During down sweep, when the incidence is gradually reduced, the hydrofoil reduces its lift, from the previous higher incidence with higher lift. Consequently, for a normal hydrofoil with no positive bend-twist coupling, when the root incidence is reduced and lift is reduced, due to the structural stiffness of the hydrofoil, it is expected that the tip will retract its deflection and twist, falling back to the deflection curve it took during up sweep of the hydrofoil. The current hypothesis is that this may not necessarily be true for a hydrofoil with positive coupling between bending and twisting. In such a hydrofoil, it is maybe possible that during down sweep of root incidence, the tip does not follow the change in root incidence as expected. In other words, the system finds a stable (or quasi-stable) point where the attempt from structural stiffness to retract the tip deflection and twist is counteracted by the higher fluid forces by the oncoming fluid at the tip due to the positive twist encouraged by the composite layup. However, the argument against this hypothesis is that if the hydrofoil is held at each root incidence for a long enough period during its up-sweep, due to the unstable divergent loop of "lift increase → deflection increase → twist increase → tip incidence increase → lift increase...", the hydrofoil should eventually achieve the higher deflection it achieved during its down-sweep. This was not tested during the current set of experiments.

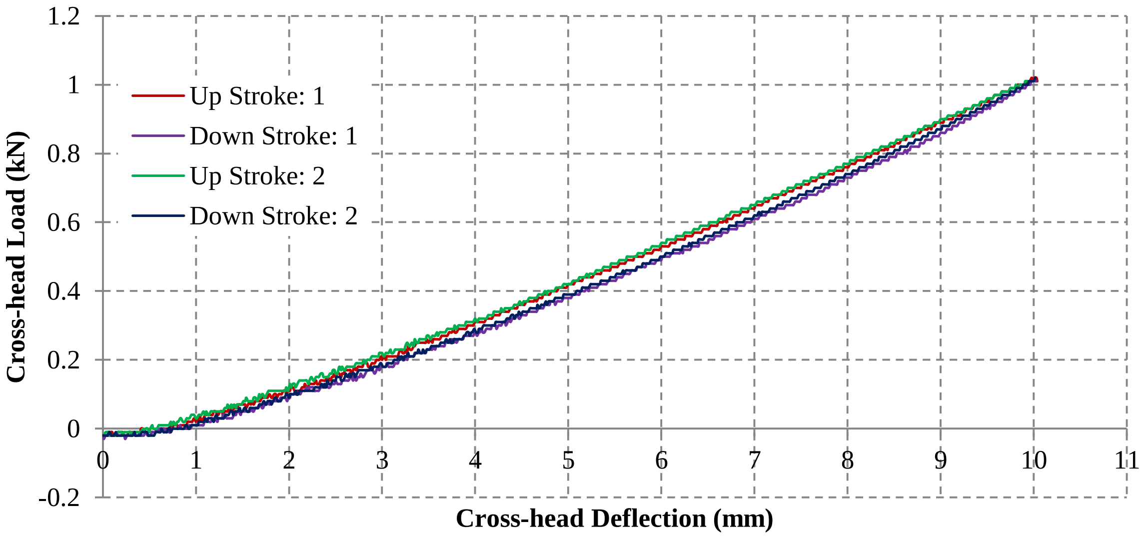

Figure 6-15: Hysteresis of the structural domain measured using static loading

6.4. Deflection and Twist of hydrofoils

Deflection measurements were taken using photogrammetry explained in Section 6.2.2. The orientation and trip-strip locations for the stationary (no flow) hydrofoil were first recorded by changing the root angle from -15° to 15° at 0.5° increments under no flow conditions and capturing images. These images were then cross-correlated against the locations of the trip-strips under required flow conditions for the same root angle of attack.

The deflection and twist profile obtained at $Re = 0.8 \times 10^6$ and $Re = 1.0 \times 10^6$for the optimised hydrofoil is shown in Figure 6-17. The ratio between deflection and the change in angle is also plotted to further understand the coupled structural behaviour of the hydrofoil. The deflection maintains an approximately linear relationship with the angle of attack at pre-stall conditions. This is expected due to the linear variation of lift coefficient against angle of attack (Figure 6-9). Consequently, the variation of twist appears to remain linear with the change in in angle of attack. This is a result of the constant bending stiffness matrix of the hydrofoil that couples deflection with twist. However, one must be careful to understand that these are not strictly linear relationships due to the movement on the lift centre with the change in angle of attack. For NACA profiles the lift centre typically moves towards the leading edge of the hydrofoil with the increase in angle of attack. As a result, the downward pitch the hydrofoil is designed to produce will be slightly reduced with the increase in angle of attack. This is evident from the gradual decrease of the ratio between deflection and twist shown in Figure 6-17. It must be noted that there was no considerable amount of hysteresis observed in the optimised hydrofoil in terms of deflection and twist. Further note that beyond the stall point of the hydrofoil, the deflection and twist profiles appear to demonstrate a non-uniform behaviour. This is an inherent short coming of a photogrammetry type measurement system. A photogrammetry system does not measure an average deflection; rather, it simply measures the deflection and twist at the time a photo was taken. Thus, when the hydrofoil exhibits a considerable amount of vibration at its post-stall angles of incidence, as it did in these experiments, the photogrammetry system fails to capture minima, maxima and medians of the deflection profile. A possible solution to this shortcoming is the use of high frame rate camera to capture a series of photos at a sufficiently high frequency and cross-correlate against the photo captured at no flow condition for the same root incidence angle to understand the peaks and trough and the frequency spectrum of deflection and twist variation.

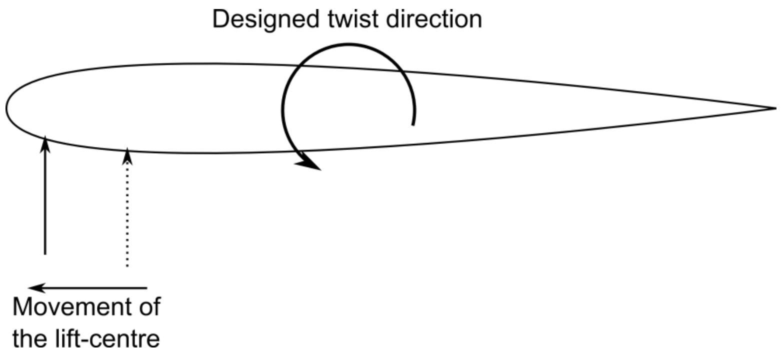

Figure 6-16: The movement of centre of lift relative to the hydrofoil cross-section

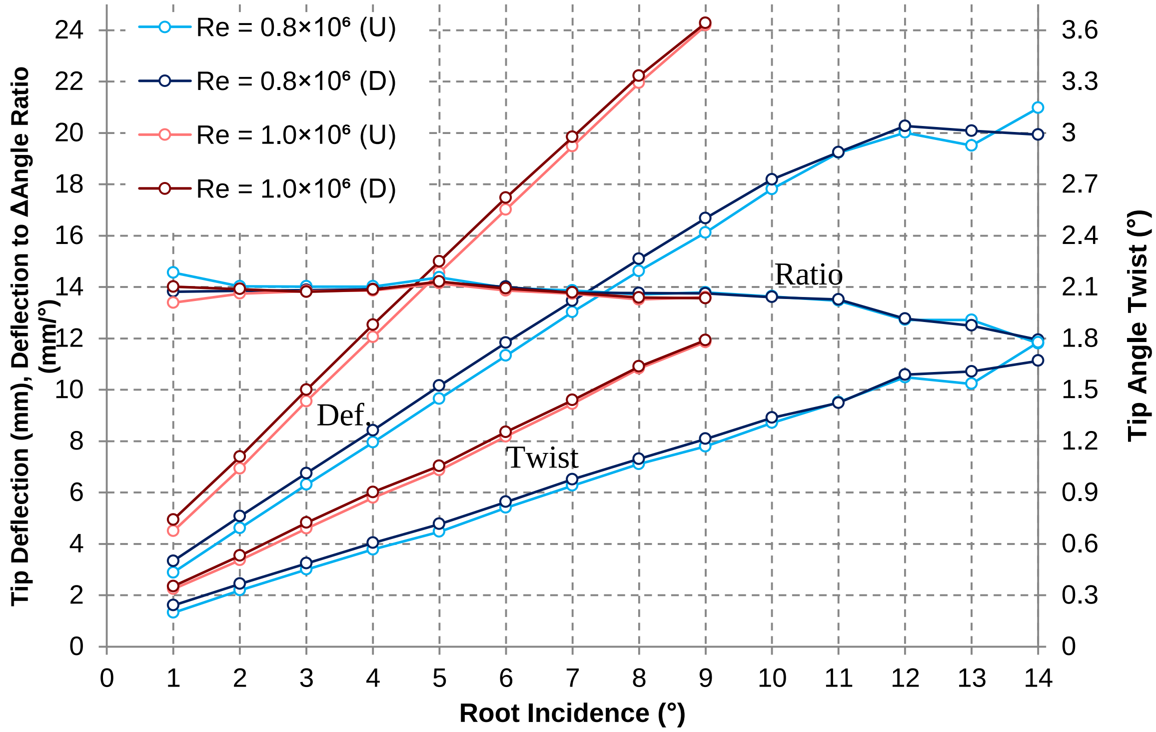

Figure 6-17: Deflection and tip angle change (downward twist is plotted as positive) of the optimised foil against change in root incidence

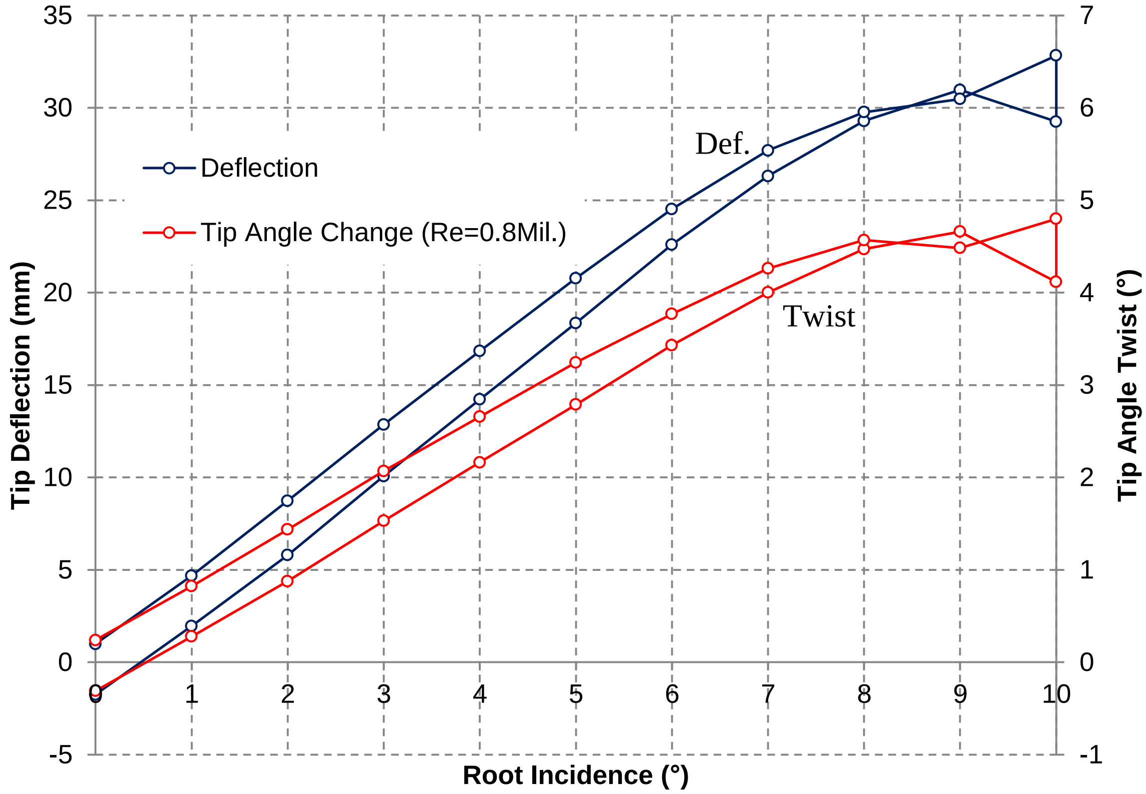

Figure 6-18: Deflection and tip angle (upward twist is plotted as positive) change of the +30deg hydrofoil against change in root incidence

The variation of twist and deflection for the +30deg hydrofoil with positive bend-twist coupling is given in Figure 6-18. The most noticeable aspect of this graph is the significant amount of hysteresis present in both deflection and twist. The highest absolute value of hysteresis for deflection and twist were measured to be 2.73mm and 0.55°, respectively. This occurred when the root incidence was 0° when the deflection and twist were ideally meant to be zero.

6.5. Uncertainty in non-dimensional coefficients

In any experiment, uncertainties in measurements and their derivatives have to be well scrutinised in order to fully understand their results and outcomes. In the case of hydrofoils, uncertainties arise due to usual random errors in measurement equipment and pitching mechanism, but more importantly due to the random vibrations demonstrated by the hydrofoil during the experiments. Here, the vibrations cause the hydrofoil to laterally deflect and change its twist. This is a complex fluid dynamics and structural dynamics coupled effect resulted by the turbulence of the flow passing the hydrofoil. It is hypothesised that the optimised hydrofoil has the capability to remain more stable and maintain a relatively low variation in hydrodynamic derivatives due to its offloading nature resulted by the layup. The optimised hydrofoil has the capability to reduce the lift by twisting downwards if the lateral deflection increases due to vibration; thus, maintaining a more stable range of operation. Figure 6-19(a)-(e) summarise the uncertainties of the measurements observed during experiments. For clarity the graphs were presented individually for each Reynold's number tested. The error bars represent the range of the measurement for a given root incidence angle.

The lift coefficient (C_L) in Figure 6-19(b)-(d) clearly demonstrate the onset of stall after around 10° root incidence angle. Due to the typical vibrations beyond the stall point the range of the (C_L) values is markedly increased compared to prior to stall condition. It is also clear that the first appearance of relatively large error bars delay with the increase in flow speed: 10° for $Re = 0.4 \times 10^6$, 10.5° for $Re = 0.6 \times 10^6$ and 11° for $Re = 0.8 \times 10^6$. The $Re = 1.0 \times 10^6$ experiment was not performed beyond 9° root incidence to prevent over loading the hydrofoil. The $Re = 0.25 \times 10^6$ experiment demonstrated a similar uncertainty range for many different root incidence angles. This is assumed to be due to the larger relative error when measuring small measurement quantities, rather than due to vibrations. During experiments the $Re = 0.25 \times 10^6$ case did not demonstrate considerable amounts of vibration even after the stall condition due to the low flow speed and Reynold's number. In all Reynold's number cases pitching moment coefficient appears to have the highest variation in values. This is due to the pitching moment being dependent on both lift and location of lift centre. The lift centre also changes considerably due to the change in twist as a result of the changes in lateral deflection of the hydrofoil. Also note the low uncertainty in C_D at all flow speeds.

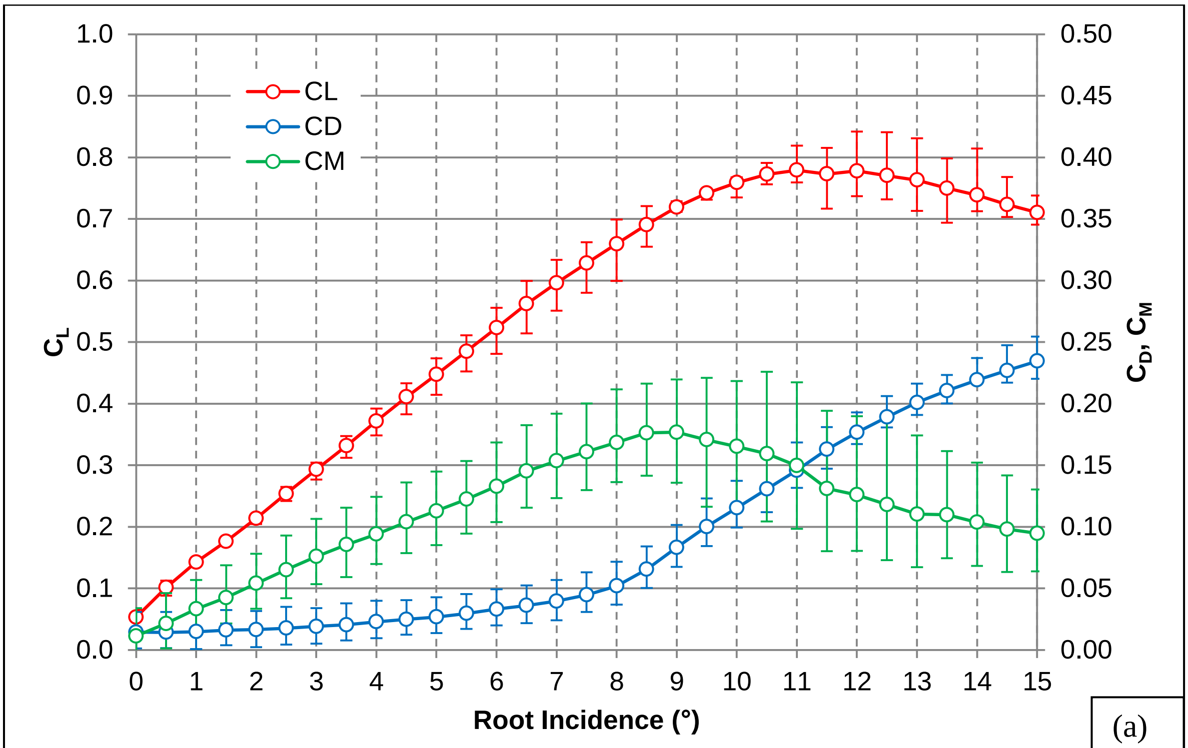

(a)

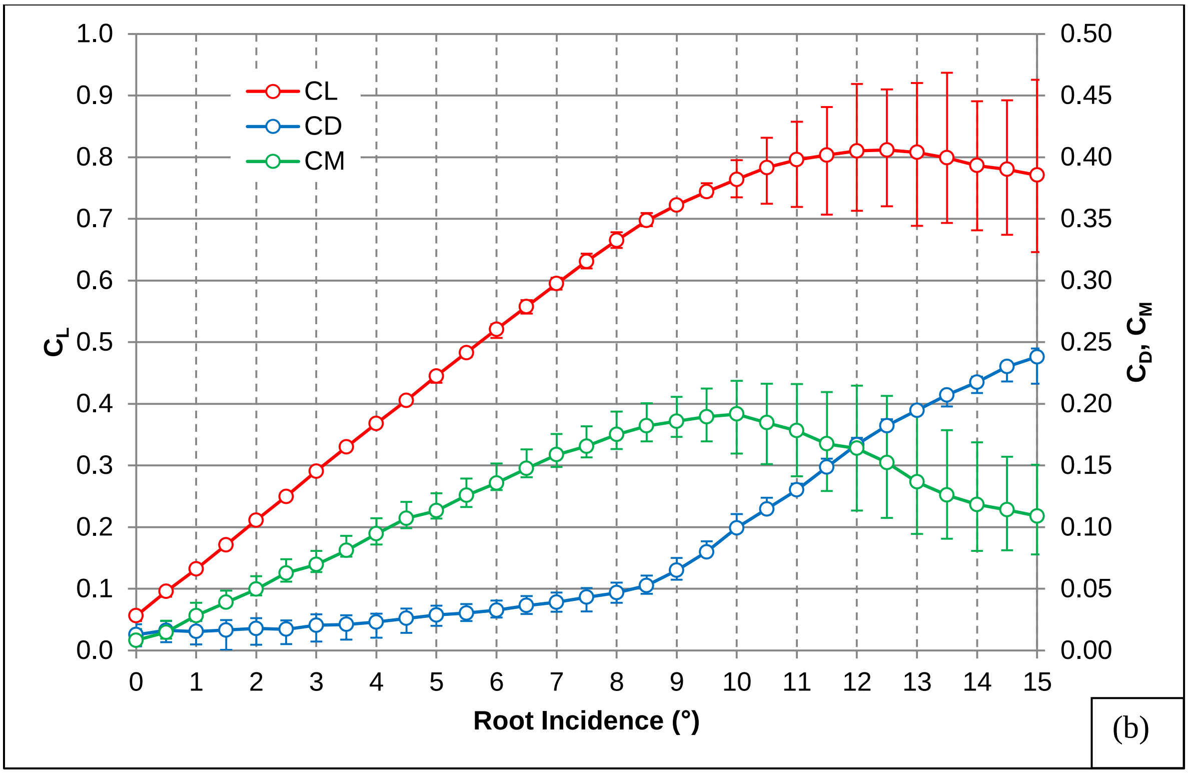
CL
CD
CM
C_L
C_D, C_M
Root Incidence (°)
(b)

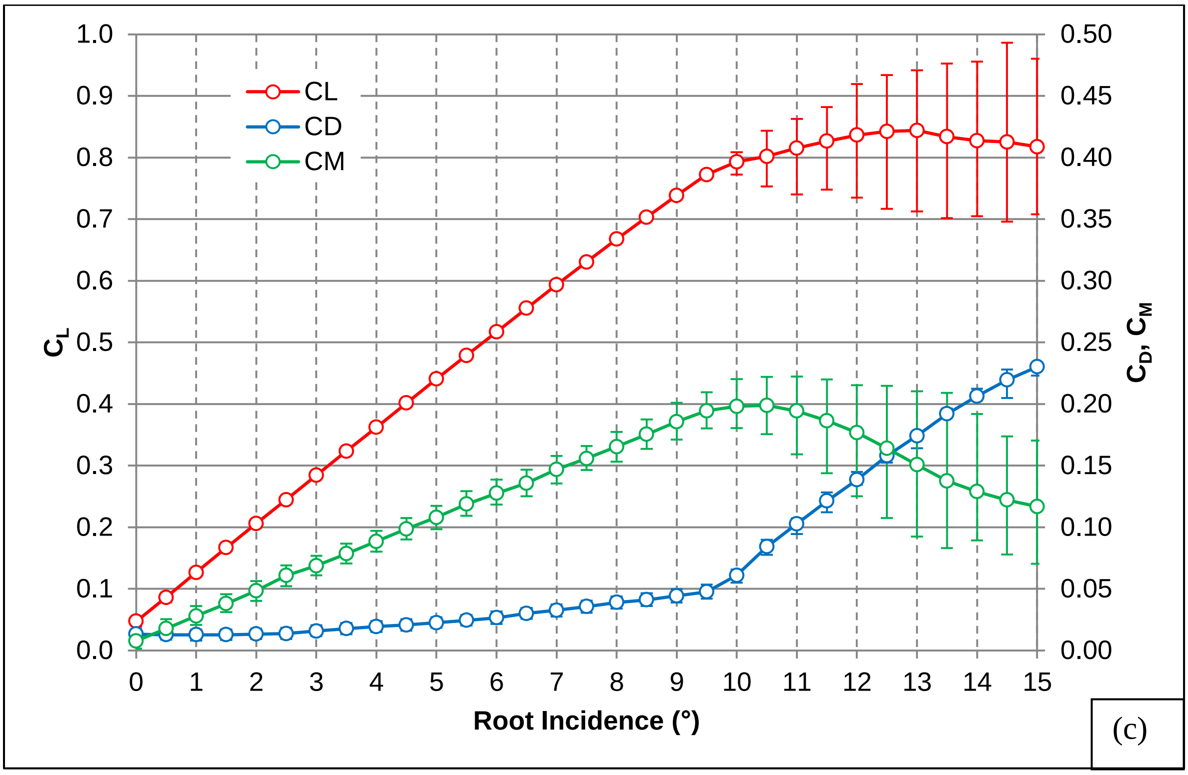
CL
CD
CM
C_L
C_D, C_M
Root Incidence (°)
(c)

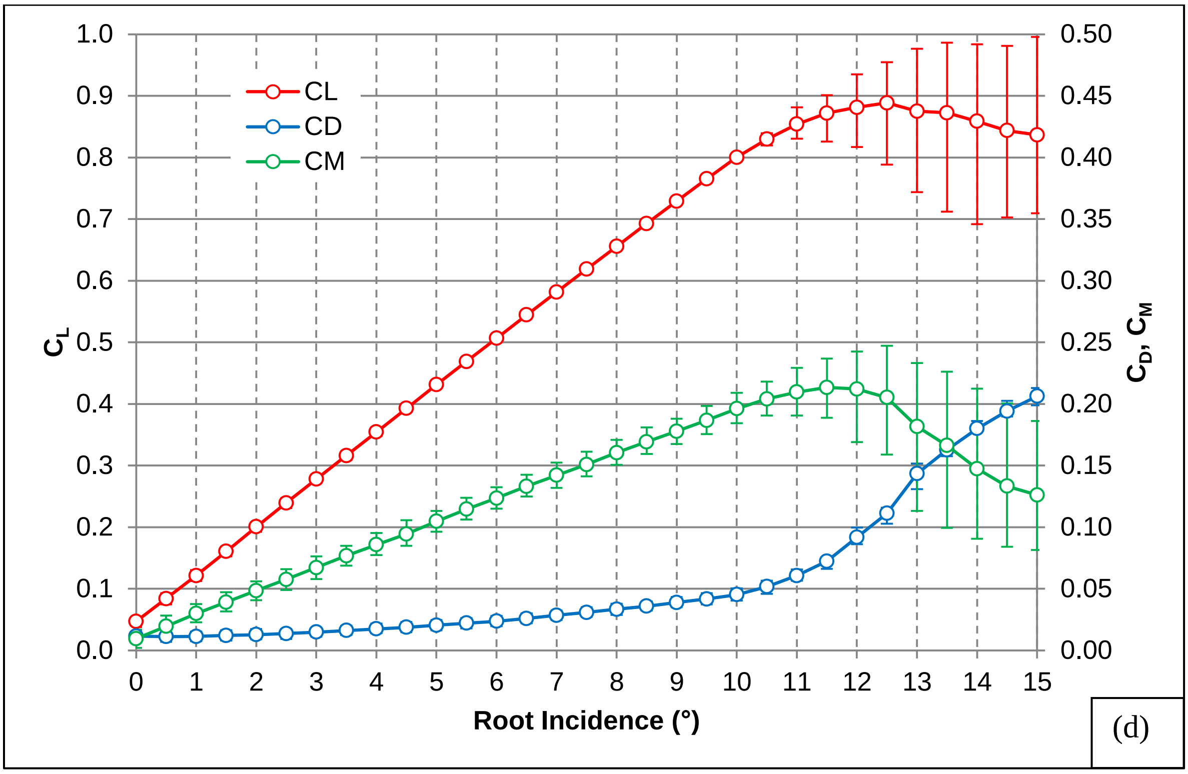

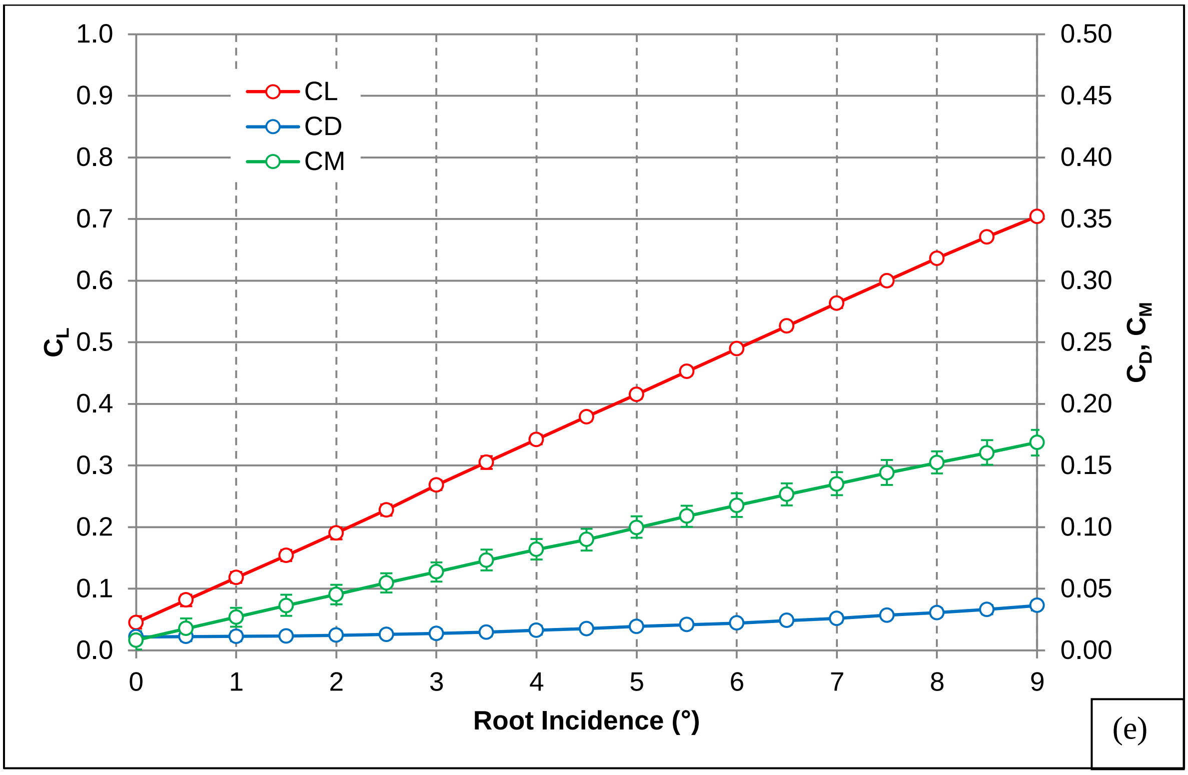

Figure 6-19: Uncertainties in hydrodynamic measurements of the optimised hydrofoil: (a) $Re = 0.25 \times 10^6$; (b) $Re = 0.4 \times 10^6$; (c) $Re = 0.6 \times 10^6$; (d) $Re = 0.8 \times 10^6$ & (e) $Re = 1.0 \times 10^6$

The uncertainty demonstrated by the positive bend-twist coupled hydrofoil was also investigated during experiments. Similar to the optimised hydrofoil, the $Re = 0.25 \times 10^6$ Figure 6-20(a) case demonstrated higher levels of uncertainty even prior to the stall point, which roughly occurred at 9.5° root incidence. However, unlike the optimised hydrofoil, after stall has reached, the uncertainty of the non-dimensional entities appeared to have greatly increased even for the low speed at $Re = 0.25 \times 10^6$. This is due to the instabilities caused by the positively bend-twist coupled layup of the hydrofoil. During experiments considerable amount of vibrations were witnessed for the hydrofoil after the stall condition. As a result, the range in both C_L and C_D were observed to be greatly increased. However, the average values of C_L and C_D were fairly similar to the optimised hydrofoil. A notable observation is the large range of C_D relative to the average value. The relative range of C_D was much lower for the optimised hydrofoil. Other Reynold's number cases - $Re = 0.4 \times 10^6$, $Re = 0.6 \times 10^6$ and $Re = 0.8 \times 10^6$ – demonstrated smaller variations in non-dimensional entities prior to stall. However, in all cases, the uncertainty in post-stall non-dimensional entities was much larger compared to the optimised hydrofoil. Furthermore, due to positive coupling, the stall root incidence angle was observed to get smaller with increased speed. Experiments with $Re = 0.8 \times 10^6$ and $Re = 1.0 \times 10^6$ were limited to root incidences 10° and 6° due to the instabilities of the hydrofoil and to prevent over-loading. High root incidences at high Reynold's numbers also instigated the typical screeching noise at the onset of cavitation, although the tunnel was pressurised to further delay cavitation related phenomena. Onset of cavitation was likely achieved faster by the hydrofoil compared to the optimised hydrofoil due to its positive coupled layup and also due to the surface finish, which may have caused nucleation at the onset of cavitation. In summary the positive coupled hydrofoil demonstrated more uncertainty in results due to structural vibrations, a much larger drag uncertainty relative to the average value of C_D, lower stall root incidence angles and even reached the onset of cavitation during experiments. All these observations made the optimised hydrofoil more hydrodynamically superior to the positive bend-twist coupled hydrofoil that was tested. It must be noted that during experiments, the uncertainty in deflections of the hydrofoils were not measured. In fact, as high speed photography was not used during experiments, capturing the variation in deflections due to vibrations was not feasible.

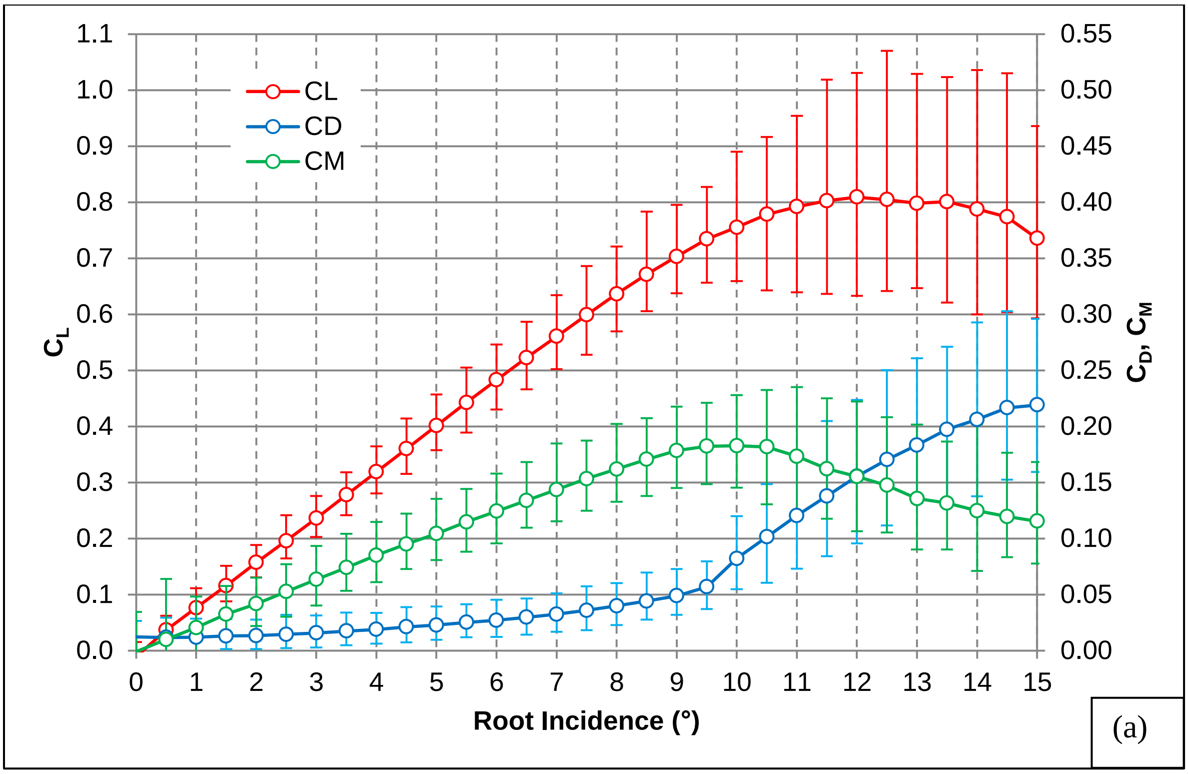

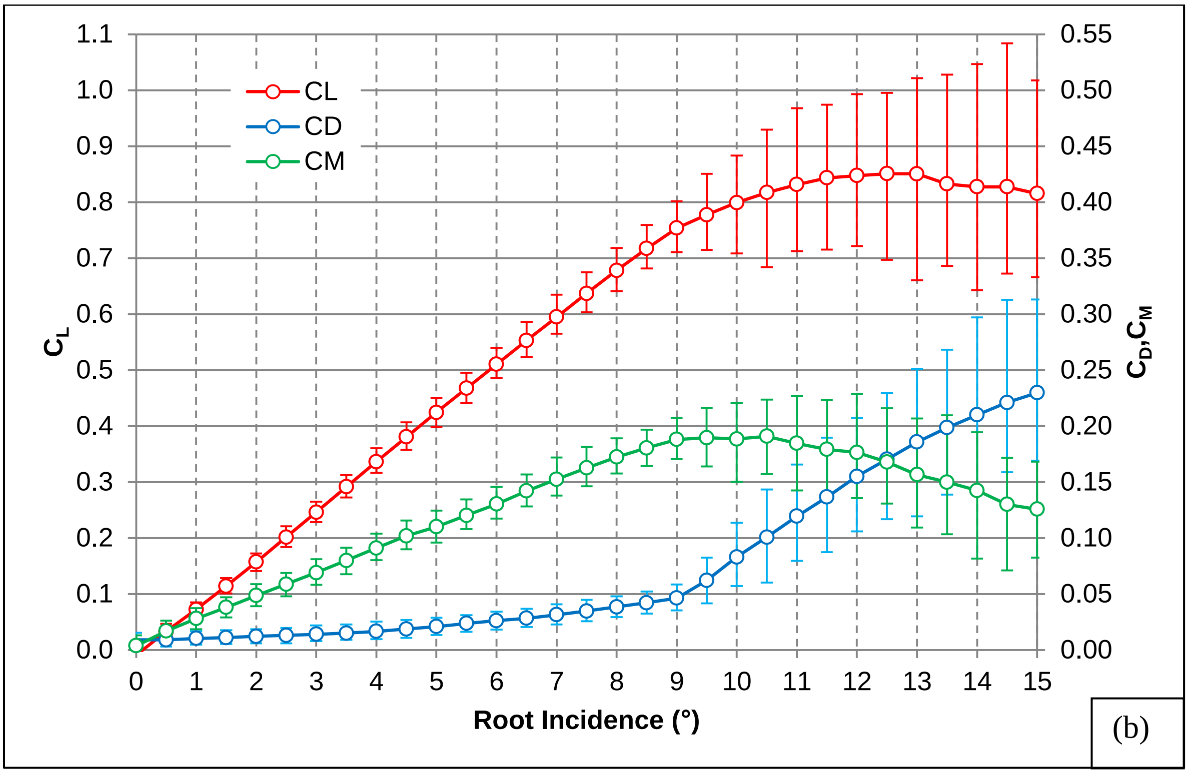
CL
CD
CM
C_L
C_D,C_M
Root Incidence (°)
(b)

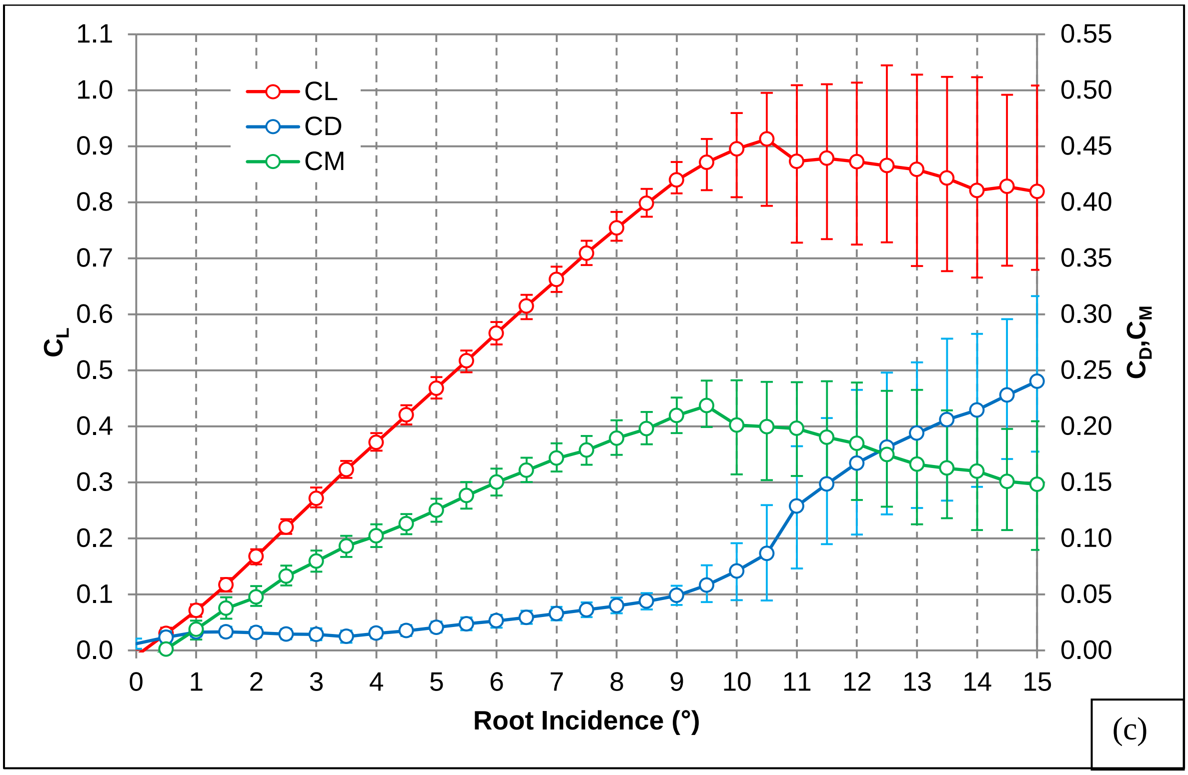
CL
CD
CM
C_L
C_D,C_M
Root Incidence (°)
(c)

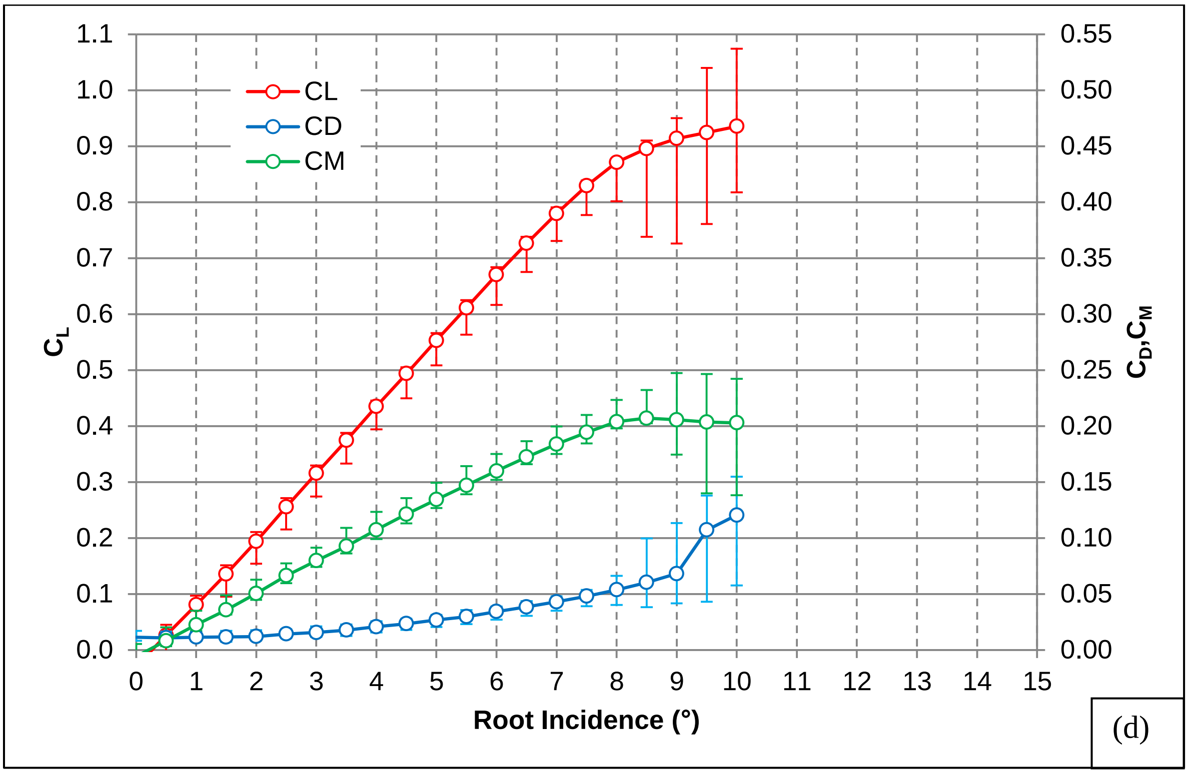

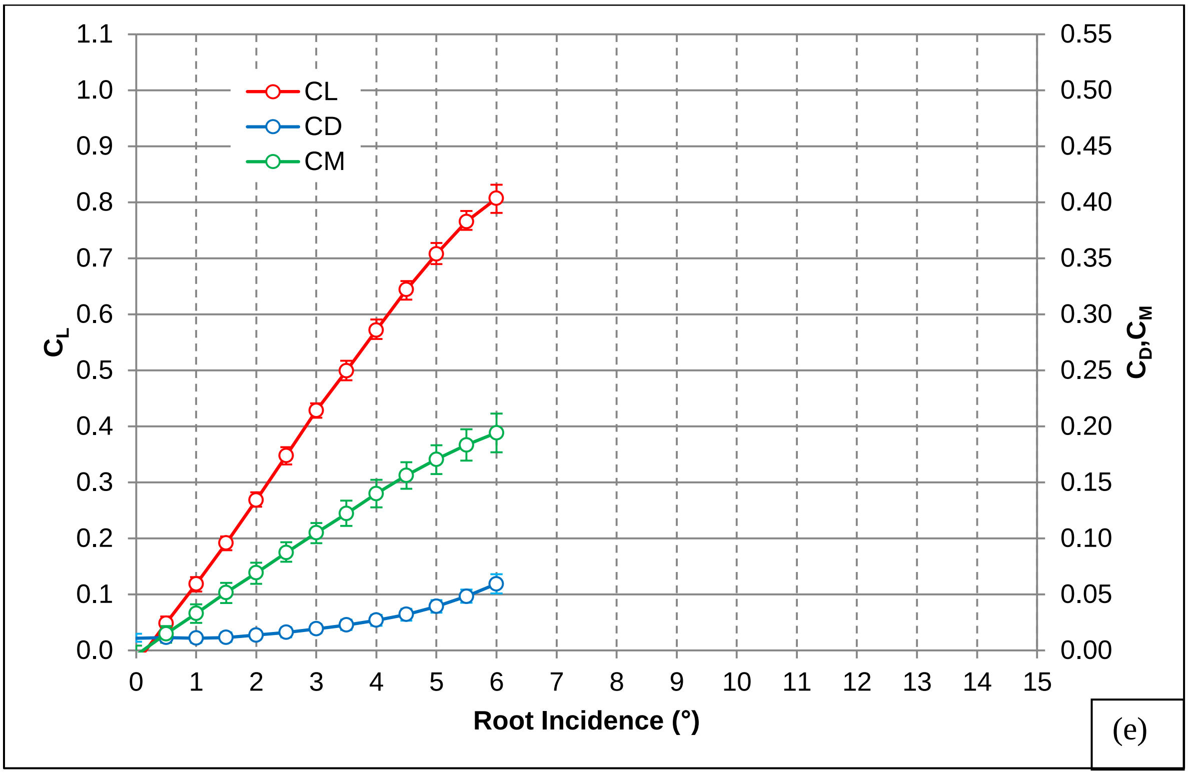

Figure 6-20: Uncertainties in hydrodynamic measurements of the positive twist coupled hydrofoil: (a) $Re = 0.25 \times 10^6$; (b) $Re = 0.4 \times 10^6$; (c) $Re = 0.6 \times 10^6$; (d) $Re = 0.8 \times 10^6$ & (e) $Re = 1.0 \times 10^6$

6.6. Fluid Structure interaction studies and comparisons against experiments

Fluid-Structure Interaction (FSI) studies were performed on tested hydrofoils to validate the obtained results and the FSI technique against each other. Developing an FSI technique is a crucial goal as it can be used to make accurate future predictions for scenarios that experiments cannot be performed. ANSYS software package was used to FSI simulations, with CFX used as the solver for fluid domain and the standard ANSYS transient structural solver used for the structural domain. The composite domain was modelled using the ANSYS Composite PrePost™ (ACP) plugin.

6.6.1. Simulation Setup

FSI simulations were performed as 2-way FSI for maximum accuracy, with both solvers run in the transient state. 2-way FSI refers to the simulation technique where the fluid domain mesh is updated at each time-iteration depending on the deformation of the structural domain of the previous iteration step. The Leonardi cluster computing system available at UNSW was used for running simulations with resource allocations of up to 128 cores per simulation depending on the availability of resources and queue time.

Although the tunnel test section was of square cross-section, due to the ease of changing incidence angle, the CFD domain was modelled as a sufficiently large parabolic domain (Figure 6-21). The assumption made here is that there were no considerable wall effects on the hydrofoil. The application of the parabolic domain was explained in Chapter 4. Using the parabolic domain, the simulation setup was verified against the previously tested stainless steel hydrofoils and the results were found to match experimental results very closely. The simulation time was set to 2s with time increments of 0.05s on both domains. Each root incidence case was treated a separate simulation and, being a parabolic domain, the angle of flow was conveniently changed by changing the vector components of the inlet flow without the need for changing the actual angle of the hydrofoil inside the domain, which would require constructing a different model and a mesh for each incidence angle. If a square domain similar to the actual dimensions of the tunnel were used, a new model has to be constructed for each incidence angle, as changing flow components at the inlet is not a viable option as it will result in different flow physics compared to the experiments. The parabolic domain was meshed with approximately 30.5 Million cells with inflation layers used to capture boundary layer of the hydrofoil. The mesh is a particularly important consideration in FSI type simulation as low quality meshes may lead to warped and sometimes negative volume elements in the fluid domain during mesh deformation near the hydrofoil cavity, The 30.5 Mil. mesh was found to produce to good results without facing such difficulties. Turbulence was captured using Large Eddie Simulation (LES) using Wall-adapting Local Eddie-Viscosity (WALE) model. This was found to run smoothly for this application without causing convergence issues during simulation. LES was used for these models as the previously used Shear-Stress Transport (SST) model was observed to not capture vibrations of the hydrofoil that were observed in real-life testing. This was expected as the SST model tends to average and overly smoothen the turbulence numerics of the CFD domain. However, the used 0.05s time increment for the solution was not adequate to fully capture the frequencies of vibration of hydrofoil during its operation. To fully capture the vibration frequencies, a much smaller time-step needs to be used, which dramatically increases the solution time of the simulation. It may be highlighted, 2-way FSI in ANSYS performs three iteration steps for each time increment: fluid domain iterations, structural domain iterations and force and displacement iterations at the fluid and structural interface. As a result, reducing time-stepping by a factor of $\frac{1}{n}$th will increase the number of total iterations by a factor of n^3, which will in turn increase the solution time by roughly n^3. Furthermore, in order to capture the full vibrational pattern, simulations must be performed with at least two times the frequency of the major vibration frequencies of the spectrum ($< \frac{1}{2f}$ time increment). This requires a considerable amount of computing resources.

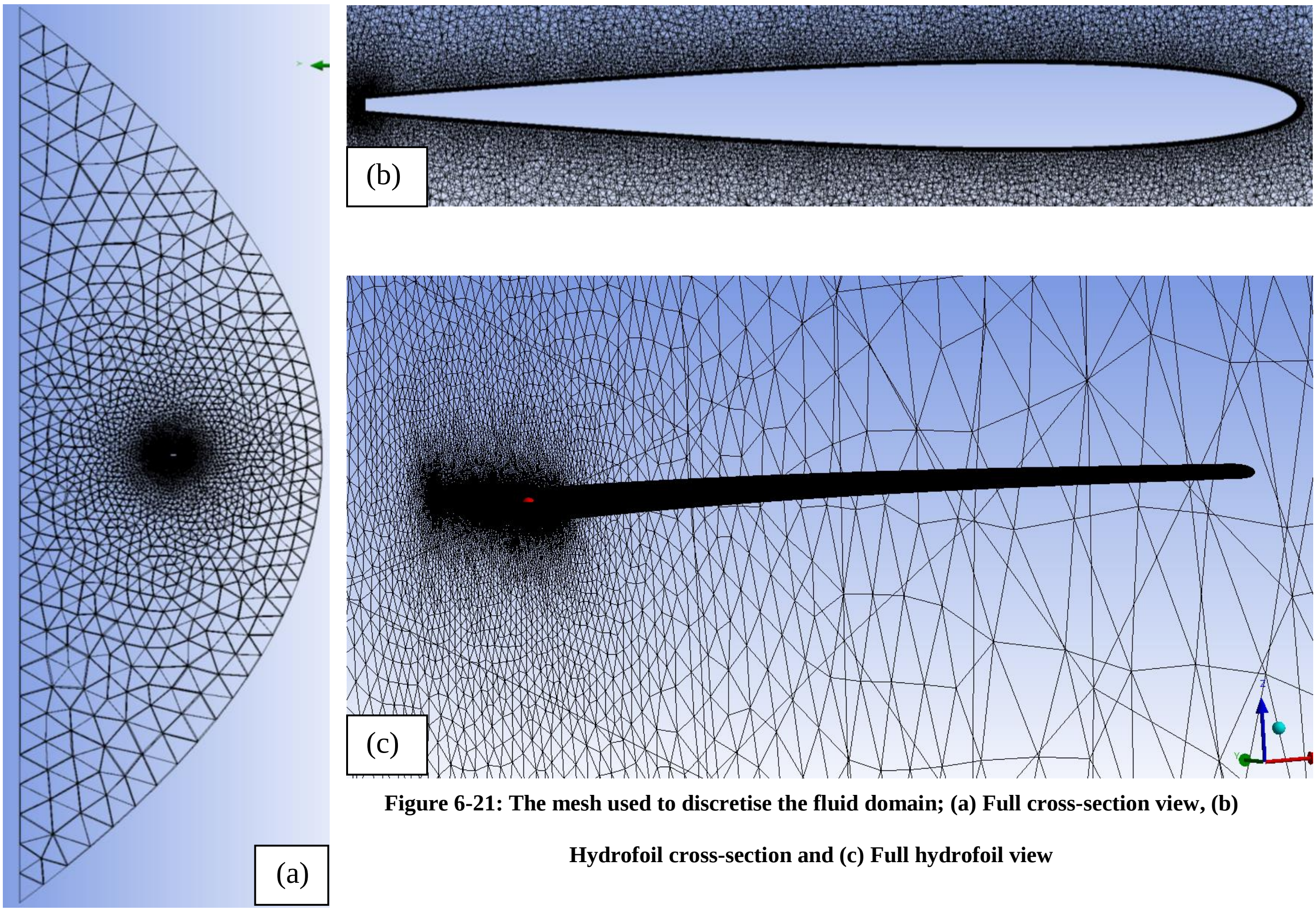

Figure 6-21: The mesh used to discretise the fluid domain; (a) Full cross-section view, (b) Hydrofoil cross-section and (c) Full hydrofoil view

The inlet flow specified as a gradually increasing flow that reaches its full speed at 1s for each AoA. A cosine profile was used to make sure that there were no accelerations at starting point and ending point. This prevented the structure from having sudden deflections (jerks) at the start of the simulation, which caused difficulties in convergence due to large deformation in the mesh. Both flow velocity vectors (V and W velocities) were given similar profiles. Eq. 6-2 specifies the cosine function used and Figure 6-22 illustrates an example velocity profile for $V_{max} = 1m/s$. Such a velocity profile greatly helped reduce convergence issues in the solution.

$$V = \begin{cases} \dfrac{1-\cos(\pi t)}{2} V_{max} & for\ t \le 1s \\ V_{max} & for\ t > 1s \end{cases} \qquad \textbf{Eq. 6-2}$$

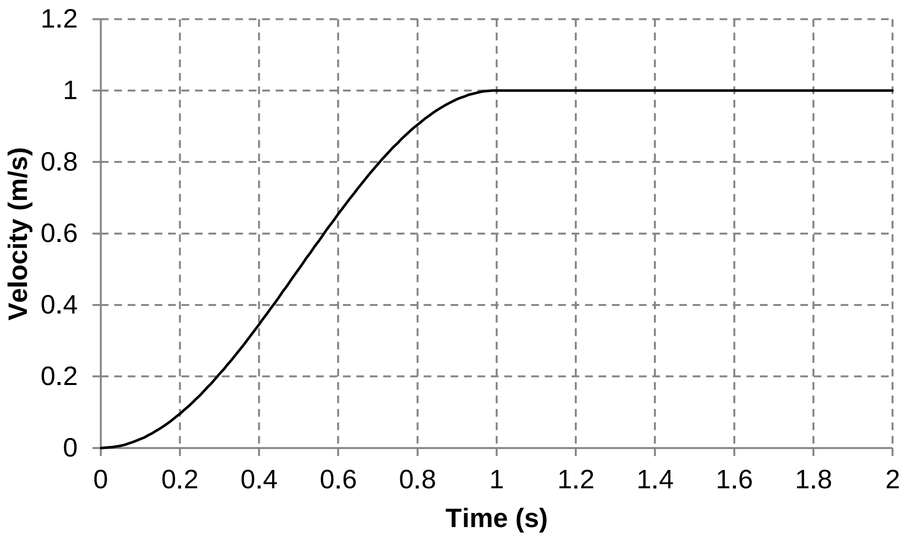

Figure 6-22: Velocity profile for $V_{max} = 1m/s$

As discussed in Chapter 5, the structural domain was constructed using the ANSYS Composite PrePost plugin using layered linear 3-dimensional solid elements. Composites in ANSYS can be modelled as several different ways in ANSYS, one being a full per-ply split model and the other being a one element thickness across the whole composite layup. The two models are presented in Figure 6-24. However, by applying simple structural loads it was identified that there is no considerable difference in these two methods of modelling. Thus, for FSI simulations the one element per laminate method was used. Per ply split modelling is important if it is intended to capture out of plane shear stresses, etc and when investigating failure of laminates. Care was taken to have a fine mesh at the leading edge of the hydrofoil as fluid pressure from the fluid domain acts as a sharp gradient close to the leading edge of the hydrofoil (Figure 6-23). Furthermore, during the experiments, it was identified that it is not accurate to consider that the hydrofoil clamp is at the end of the trapezoidal region of the hydrofoil. This is due to the fairing disk (Figure 6-4) used in the clamping assembly was made of very low stiffness resin material compared to the carbon fibre composite which the hydrofoil is constructed of. Therefore, in the FSI simulations the structural/hydrofoil domain was modified to be clamped 15mm from the trapezoidal hydrofoil region.

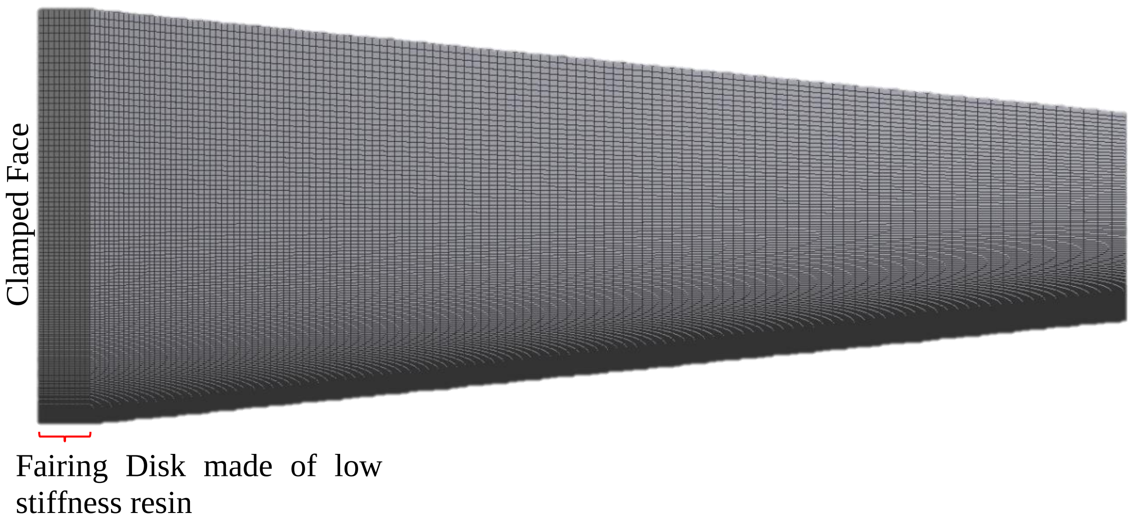

Figure 6-23: Top view of the hydrofoil mesh

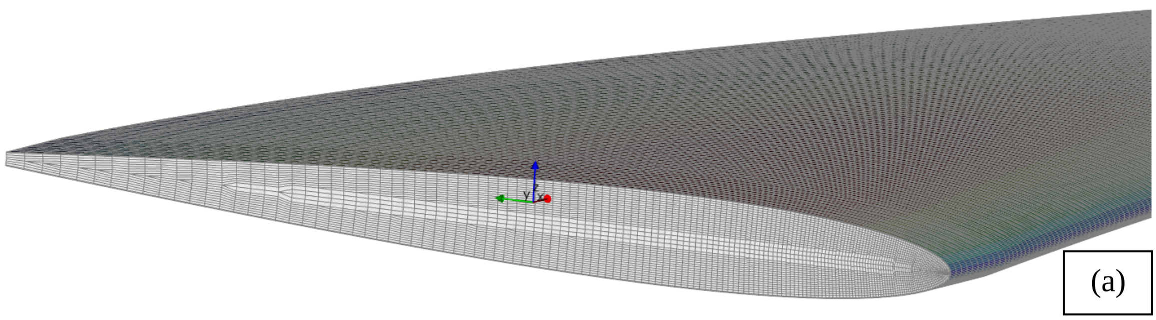

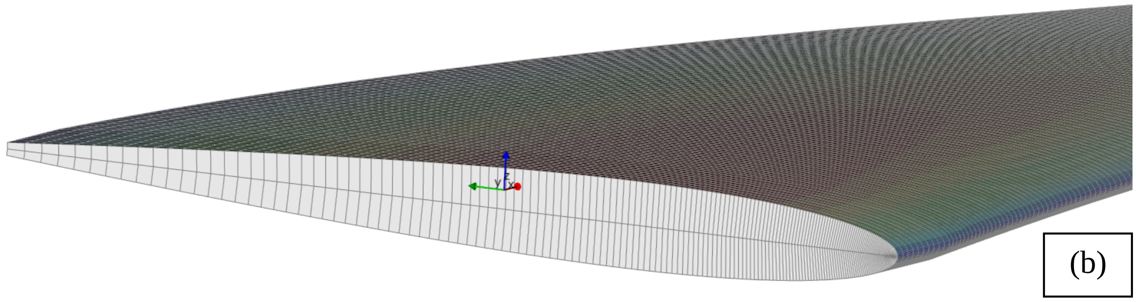

Figure 6-24: Composite mesh for the hydrofoil: (a) Ply wise modelling and (b) Single element (monolithic) modelling

6.6.2. Comparison against cavitation tunnel results

In order to validate the FSI results, they were first compared against hydrodynamic results obtained from tunnel testing. The lift-coefficient and drag-coefficient were used as comparison parameters and Figure 6-25 was construed to compare the results obtained from experiments and FSI. In this chapter only the $Re = 0.8 \times 10^6$ case is compared against experiments, although other FSI simulations also demonstrated to good agreement with experiments. In terms of hydrodynamic results, FSI simulations provided satisfactory results with percentage errors being less than 10% for all cases. Afterwards, the L/D curve was constructed based on FSI results and was compared against the experimental curve (Figure 6-26). Although, the L/D curve had a similar trend to the experimental curve, the L/D value seemed to be constantly underestimated. The error in L/D appears to have been amplified due to it being a ratio of two entities with error: L and D (or C_L and C_D).

Deflection and twist results obtained from FSI were then compared against experimental results. An overview of the deflection profile and the fluid flow is shown in Figure 6-27. The result shown in Figure 6-27 was created for $Re = 0.8 \times 10^6$ and the root incidence of 6°. This instance is meant to be the optimal operating condition the hydrofoil was designed for and is ideally meant to achieve a flat shape at this speed and incidence.

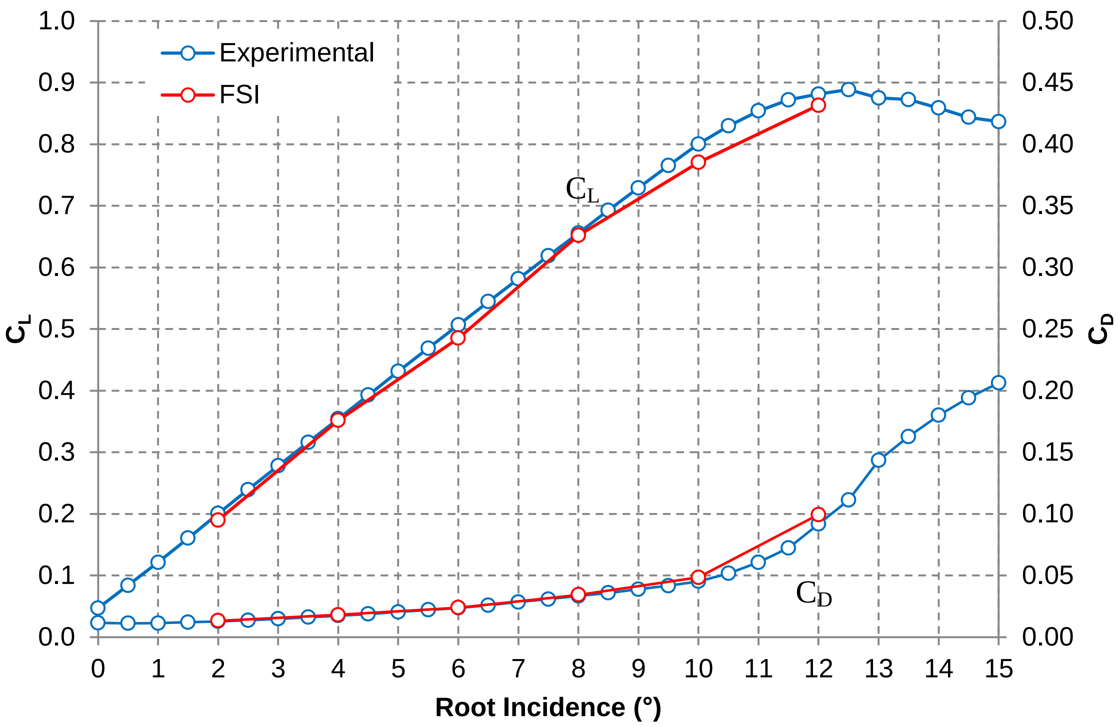

Figure 6-25: Comparison between hydrodynamic entities for experimental and FSI results

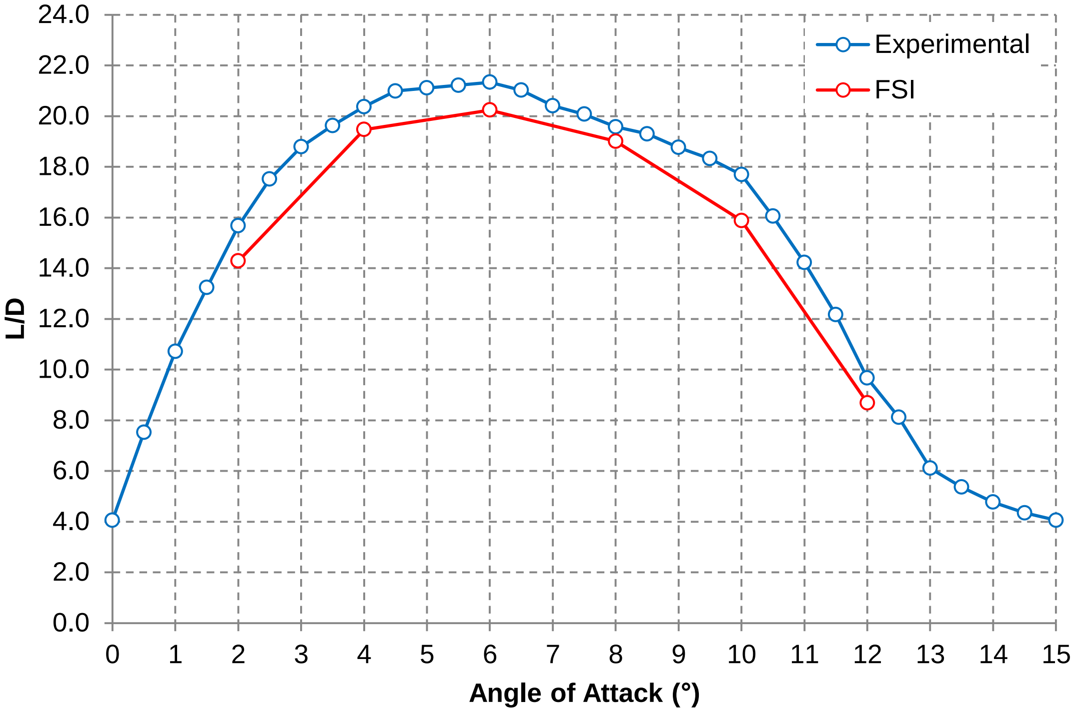

Figure 6-26: Comparison between L/D for experimental and FSI results

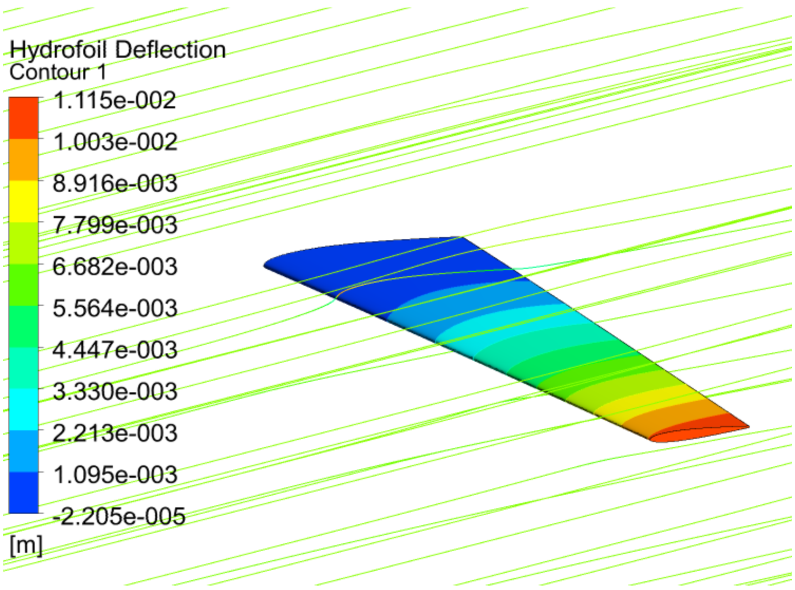

Figure 6-27: Deformation of the optimised hydrofoil at the operating point, i. e. - $Re = 0.8 \times 10^6$ and root incidence of 6°

Further structural results post-processing was performed in ANSYS APDL for better control and graphing capabilities. The comparison made between structural deformation in FSI simulations and experiments is given in Figure 6-28. Based on the comparison it was clear that the deflection curve approximated by FSI had good correlation to the deflections observed during experiments. The twist was also closely correlated. It must be noted here that FSI simulations demonstrated a considerable amount of vibrations, consequently, the average deflection is shown in the graph. The photogrammetry method used during experiments did not use such an averaging technique. The deflection measured by photogrammetry was simply the deflection at the instance the photo was taken, regardless of the vibrations of the structure. Figure 6-29 illustrates the vibrations that were observed in the LES based FSI simulation at $Re = 0.8 \times 10^6$ and root incidence of 6°. Such vibrations were very visible during experiments; however, there was no reliable way of accurately measuring them. The amplitude of such vibrations must be taken into account in deflection measurements as the uncertainty in FSI simulations. Furthermore, a much smaller time-step size is required to fully capture the vibration frequencies of the structure. The amplitude of vibrations were significantly increased for higher incidence angles. In fact, at root incidence 12°, there was considerable amount of difficulties in converging the FSI solution, thus was decided to not be given here. Note that the C_L and C_D values in Figure 6-25 were taken from the result of the time-step just before the solver failed to converge.

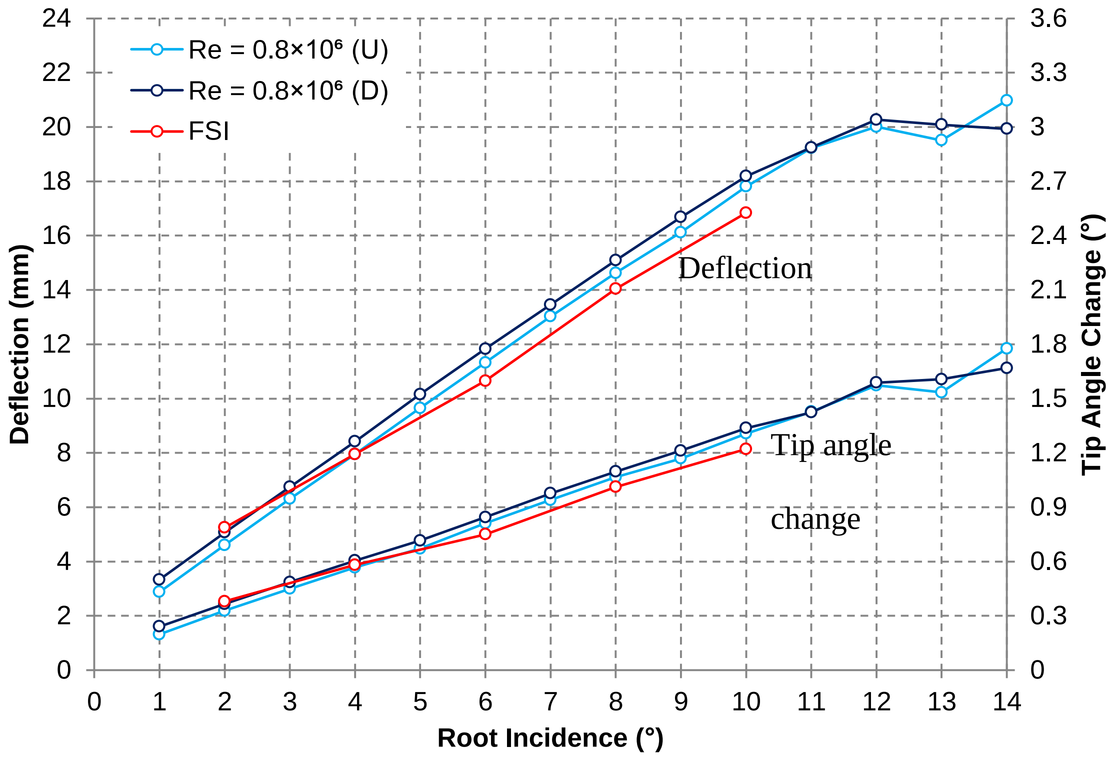

Figure 6-28: Comparison between structural deformations in the experiments and FSI simulations

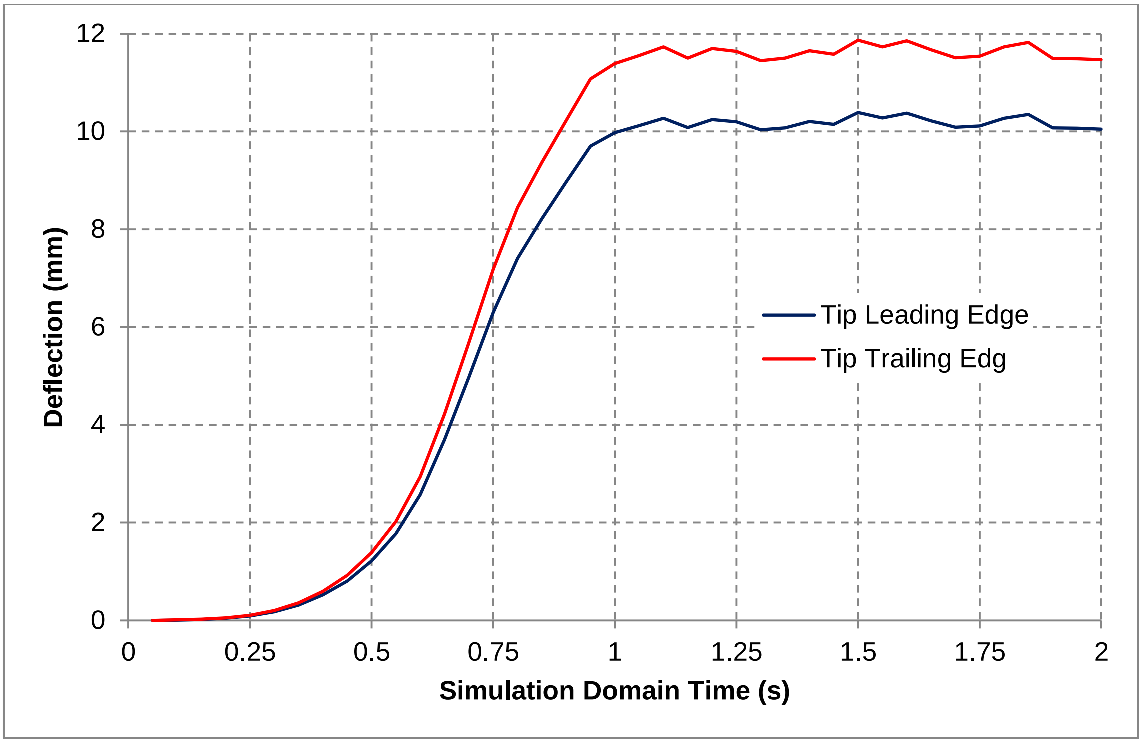

Figure 6-29: Vibrations observed in FSI simulations

6.6.3. Speed vs Reynold's Number effect

As explained in Chapter 6.3.2, the cavitation tunnel experiments were conducted at a different temperature to the experiments conducted by Zarruk et al. (2014). As a result, the flow velocity had to be run at a different speed compared to the speed previous experiments were conducted in order to maintain the same Reynold's Numbers. In other words, the flow speeds at which optimisation was conducted was different to the flow speeds that were used in the cavitation tunnel during experiments. The results showed a dependence of flow speed beyond the conventional idea of dependent on the Reynold's number. Traditionally, Reynold's number was used to categorise flows as non-dimensional fluid dynamic parameters for rigid hydrofoils predominantly depend on the Reynold's number of the flow. However, for flexible/shape-adaptive hydrofoils hydrodynamic entities also have a strong dependency on the actual flow speed due to different lift forces experienced by the deforming structure. Note that the focus here is on the absolute lift force which causes deflection in the structure rather than the coefficient of lift. This change in absolute lift values causes the deflection to change, which in turn changes the twist and other hydrodynamic characteristics of the deforming structures. Thus, it is argued here that for shape-adaptive structures, characterisation must be made based on both Reynold's number and actual flow speed. In order to test this argument, tests must be conducted with different flow speeds, but with same Reynold's numbers (conducting experiments at a different temperature and different flow viscosity). However, during the cavitation tunnel test schedule, such experiments were not conducted. Therefore, several FSI simulations were conducted to investigate this argument.

FSI simulations were conducted similar to the simulations explained in the preceding discussions. However, the viscosity observed in experiments explained in

Zarruk et al. (2014) was used and the FSI simulations were performed for a Reynold's Number of 0.8 Million. Table 6-2 summarises the flow conditions for the same Reynold's Number prevailed during the experiments conducted by Zarruk et al. (2014).

Entity	**Value**
Density	998.6 kg/m^3
Viscosity	0.001052 kg/m/s
Velocity	9.364715 m/s
Reynold's Number	0.8×10^6
Time Step	0.05s
End Time	2s

Table 6-2: Simulation parameters for the testing flow speed vs Reynold's Number

With the above settings, FSI simulations were performed on the same optimised hydrofoil structural model at 0.8 Million Reynold's Number. All other FEA related parameters such as mesh sizing, time-stepping, numerical accuracies of the solvers, turbulence model, etc. were kept the same as previous simulations. The deflection, lift and drag performance results were then obtained by these simulations and compared against previous simulations that were explained with flow physical properties of the latest cavitation tunnel tests performed at 24°C.

A comparison between the hydrofoil deflections for the two cases at 6° angle of attack is shown in Figure 6-30. It is clear that the deflection of the hydrofoil for the two cases is considerably different: trailing edge deflection of 14.99mm for the higher speed case versus 11.15mm for the lower speed case. As a result, the twist of the hydrofoils was also markedly different. The former flow conditions (higher speed) achieved a tip rotation (downwards) of 1.27° while the current flow conditions achieved a tip rotation (downwards) of 0.955°. Due to the difference in twist, the two cases produced different hydrodynamic measurements. Figure 6-31 summarises the lift coefficient and drag coefficient for the same Reynold's number with different speeds.

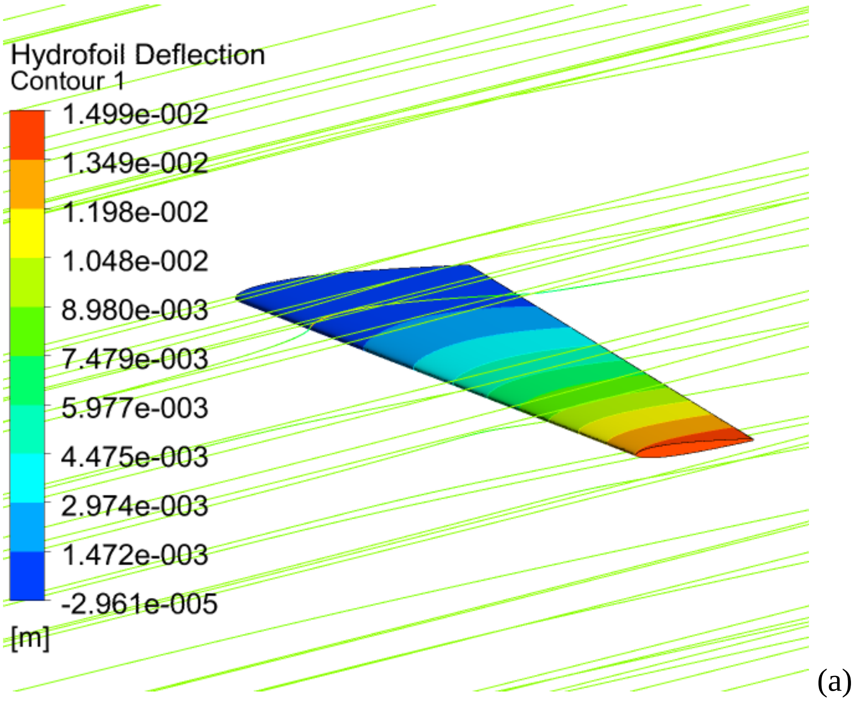

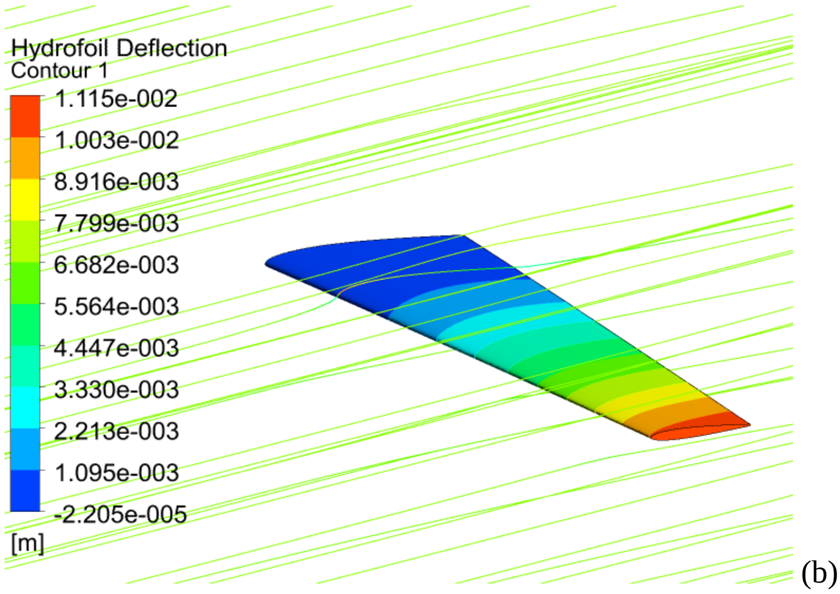

Figure 6-30: Hydrofoil deflection for different flow speeds with same Reynold's Number of 0.8×10^6: (a) Flow conditions in the experiment by Zarruk et al. (2014) & (b) Flow conditions in the latest experiments

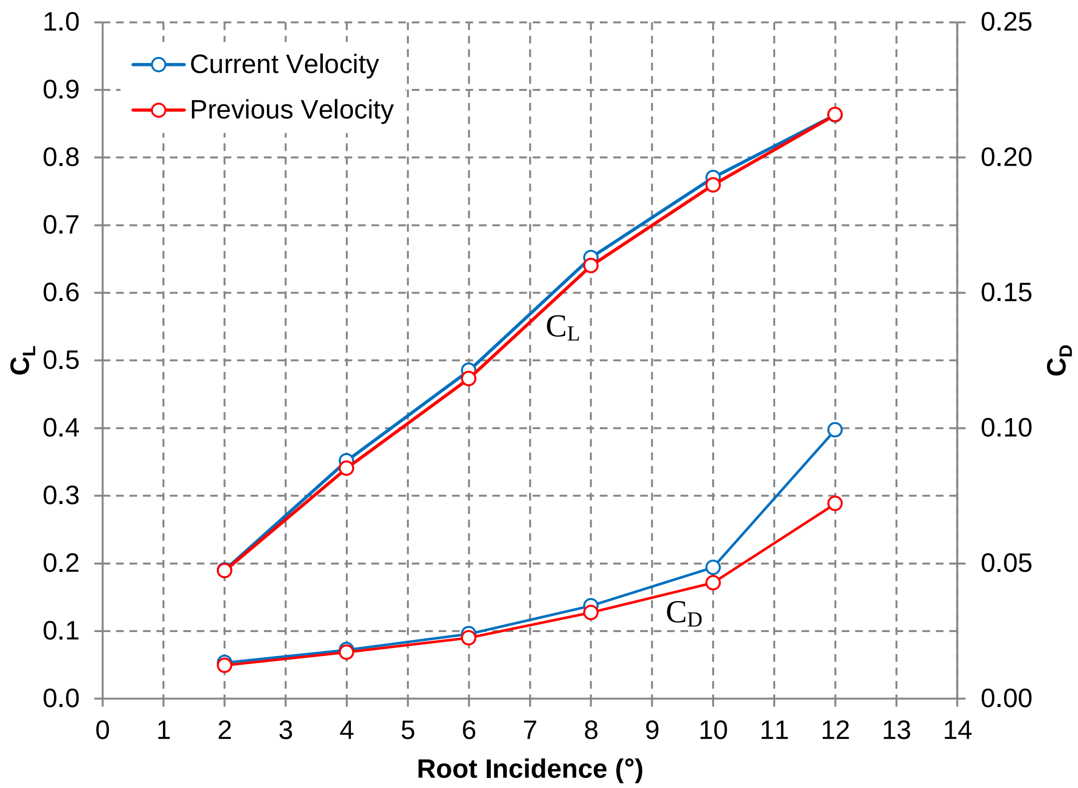

Figure 6-31: Comparison between non-dimensional hydrodynamic measurements for the same $Re = 0.8 \times 10^6$ with different velocities

Based on Figure 6-31, it was clear that the speed of the flow has a considerable influence beyond the traditional non-dimensional Reynold's Number. The higher speed of the previous experiments (Zarruk et al., 2014) caused the hydrofoil deflect more (regardless of the Reynold's Number), which caused more downward twist. This in-turn slightly reduced the non-dimensional lift parameter and more "flattening" of the hydrofoil from its original twisted shape caused the drag coefficient to decrease. The onset of stall seems to be further delayed for the higher velocity case as, at 12° angle of attack the trend of C_L being higher for the lower velocity flow seems to have reversed. Furthermore, the typical "drag bucket" of the higher velocity flow seems to be wider. These two observations prove that at 12° the lower velocity flow causes the onset of stall while the higher velocity flow has not reached stall at 12°. This is due to the higher velocity flow causing the hydrofoil to twist more and reduce the effective angle of attack at the tip. The difference between L/D values for the two flow cases were also investigated. The comparison between L/D values for the two cases is given in Figure 6-32.

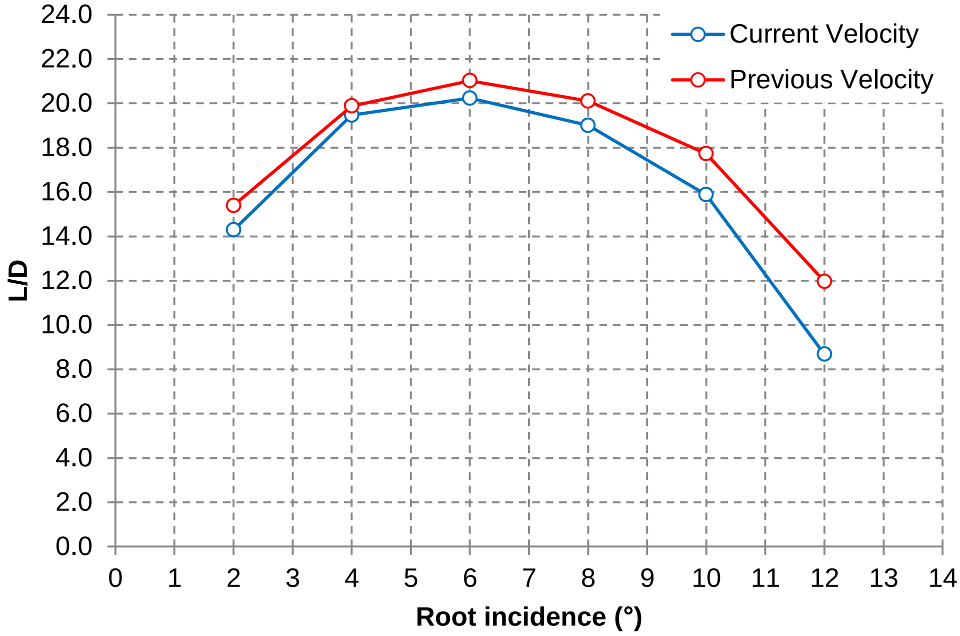

Figure 6-32: Comparison between L/D ratio for the same $Re = 0.8 \times 10^6$ with different velocities

The L/D curve for the higher velocity case was witnessed to have a higher peak value. This is due to the higher shape change/adaptivity that was prevalent in the higher velocity case. The higher downward twist from the original slightly upward twisted pre-deformed shape caused the higher velocity hydrofoil to act close to a flat NACA hydrofoil, which on principal has the lowest drag coefficient (in comparison to a twisted NACA hydrofoil). The reduction in drag resulted in a higher L/D ratio for the higher speed flow. Furthermore, the L/D envelope has clearly widened with the higher flow speed. This is again due to the higher effect of shape-adaptivity of the hydrofoil with the higher speed.

Thus, it was clear that in shape adaptive structures, the measurement of pure flow velocity (in conjunction with flow density) causes a considerable change in flow parameters. In other words, a shape adaptive structure must be optimised with a certain specific velocity set as the target, in addition to non-dimensional parameters such as Reynold's Number, advance ratio, etc. This justifies comparing the hydrodynamic entities, particularly the L/D ratio, of the optimised hydrofoil at Reynold's number 0.8×10^6 against L/D for the non-optimised hydrofoils (experiments performed by Zarruk et al. (2014)) at 0.6×10^6. The hydrofoil optimisation was performed based on the pressure maps and hydrodynamic flow parameters observed during the experiments performed by Zarruk et al. (2014). A comparison between flow velocities for the two different experiments schedules at the same Reynold's number is given in Table 6-3. Note that, as stated earlier, the difference in velocities is primarily due to the change in the viscosity of water at the two different ambient temperatures experiments were conducted at (approximately 24.06°C for the current experiment schedule vs. 18°C for the experiments conducted by Zarruk et al. (2014))

Flow property	**Current Experiments**	**Zarruk et al. (2014) experiments**
Temperature (°C)	24.06	18
Viscosity (kg/m/s)	0.00089952	0.001052
Density (kg/m^3)	997.275	998.6
Reynold's Number	0.6×10^6	
Flow Speed (m/s)	6.044	7.025
Reynold's Number	0.8×10^6	
Flow Speed (m/s)	8.018	9.365

Table 6-3: Comparison between flow properties for the two experiment schedules

Based on Table 6-3 it is clear that there is a difference between flow speeds the hydrofoil was optimised for and the flow speeds the experiments were conducted at. The optimisation was performed based on pressure distributions for the Reynold's number 0.6×10^6 case based on previous experiments. Therefore, in current experiments, the hydrofoil demonstrated more closer to its expected optimised performance at 0.8×10^6 due to having adequate flow velocity to cause the required shape-adaptive deformation. Thus, the current 0.8×10^6 Reynold's number case was compared against the former 0.6×10^6 case.

6.7. Conclusion

This chapter covered the Cavitation tunnel experiments that were conducted on the optimised hydrofoil and the positively bend-twist coupled hydrofoil. The optimised hydrofoil was a result of both layup and shape optimisation to maintain a higher L/D (efficiency) around its operating point compared to baseline hydrofoils that were tested in a previous test schedule. The optimised hydrofoil behaved as expected with the L/D attaining a wider envelope compared to the baseline hydrofoil. Furthermore, the offloading nature of the optimised hydrofoil was observed to delay stall by a considerable amount. Additionally, due to the stability at high incidences, the optimised hydrofoil was able to produce more lift than previously tested hydrofoils. Furthermore, Fluid-Structure Interaction simulations were performed using ANSYS to validate the results obtained by experiments. FSI simulations were observed to closely match the hydrodynamic results along with deflection and twist results.

The positive bend-twist coupled hydrofoil did behave as expected in terms of L/D ratio, but was interestingly observed to demonstrate considerable amount of hysteresis as magnitudes never been seen before or documented before for such hydrofoils. There is an explanation to this phenomenon still at its hypothesis stage, but needs to be further investigated for a concrete explanation. Due to the structural hysteresis, all hydrodynamic entities demonstrated considerable amount of hysteresis implying that there are two or more hydrodynamic solutions for one given flow state.

7. Summary and Conclusion

7.1. Summary

The investigation described in this thesis may be summarized as follows:

- This thesis presented a method for optimisation of composite marine propeller blades in order to improve their off-design propulsive efficiency. The improvement of off-design efficiency was due to the bend-twist coupling effects of composites. An optimisation technique was formulated using the Genetic Algorithm and Finite Element method. Two efficient finite element techniques were developed for the purpose and were coupled with the genetic algorithm. The first finite element approach was conceptually simpler and used a stable triangular element technique such that any complex geometry can be meshed with reasonable accuracy; while the second finite element approach used NURBS basis functions to represent the exact geometry of the structure with no mesh based defeaturing. Both techniques were numerically stable and accurate and were able to generate fast solutions required for a iterative optimisation algorithm such as the GA. The unloaded shape determination process was also formulated using an iterative inverse load approach.
- The developed optimisation scheme for propeller blades was then tested by using to optimise a simple hydrofoil structure. The optimisation was carried out using pressure measurements based on experimentally measured pressure readings from previous cavitation tunnel experiments. The optimisation technique provided both the layup angle configuration and the

unloaded shape. A mould was then designed for the manufacturing procedure of the hydrofoil based on the unloaded shape.

- The optimised hydrofoil was manufactured using primarily carbon fibre reinforced epoxy matrix using vacuum assisted resin transfer moulding. The specimens consistently had a very high quality. This was proven by the metrology scans performed on them. Manufactured specimens were subjected to modal testing and structural testing and were found to have an exceptionally high strength and consistency between specimens in terms of modal frequencies.
- Failed specimens were subjected to optical microscopy and neutron tomography to better understand their failure patterns. Neutron tomography is a potentially suitable technique to investigate internal of a carbon fibre composite in a non-destructive fashion. Detailed finite element models were created and validated against experimental results obtained from structural testing. The validation of finite element models provided confidence towards the accuracy of the structural domain of the fluid-structure interaction studies of the optimised hydrofoil.
- The optimised hydrofoil was subjected to cavitation tunnel experiments to study their hydrodynamic behaviour and structural response under fluid loadings. The optimised hydrofoil was indeed found to have a wider efficiency curve compared to baseline hydrofoils. However, it was also clear that the efficiency is also heavily influenced by the flow speed. In other words, advance ratio or the angle of attack is not adequate when explaining the hydrodynamic properties of a shape-adaptive blade, the absolute flow speed is also necessary. In addition to the better performance in efficiency,

the optimised hydrofoil was also witnessed to have a lower vibration induced changes in flow characteristics. In other words, the optimised hydrofoil was observed to be more stable at turbulent flow conditions. The cavitation tunnel results were then used to validate the FSI models. The FSI models were created using ANSYS and were found to predict the experimental results with a good accuracy.

7.2. Conclusions

Following conclusions are drawn based on the present investigation:

- Cell-Based Smoothed Finite Element method can be used as a viable finite element method to couple with the GA to optimise structures. The CS-FEM method is numerically stable, accurate and fast, making it ideal for iterative optimisation algorithms.
- The NURBS based FEM is an ideal solver for shapes such as propeller blades due to its capability to capture the exact geometry of the structure without any simplifications. The NURBS based FEM achieves fast mesh convergence and provides accurate solutions with a minimal amount of mesh density. Hygrothermal effects are considered for the first time in a NURBS based FEM together with GA based optimisation scheme for a complex geometry.
- Hygrothermal effects can change the response of the blade especially if non-symmetric laminate sequences are used.
- Unloaded shape calculation is a necessary component of the design process in order to achieve the same peak performance as the baseline propeller/hydrofoil.

- Complex shapes such as hydrofoils and propeller blades can be manufactured to a high quality using VARTM technique using a fully closed mould. The use of dry fabrics instead of pre-impregnated layers can considerably reduce the manufacturing cost.
- Hydrofoils constructed out of a predominantly carbon fibre using VARTM demonstrate excellent strength properties whilst retaining only a fraction of the mass of a metallic hydrofoil.
- Cavitation tunnel tests revealed that the non-dimensional hydrodynamic entities have a Reynold's number dependency. This was especially evident for the positively bend-twist coupled hydrofoil
- The lift to drag ratio curve of the optimised hydrofoil was wider than curve for the non-optimised baseline hydrofoil. In addition, the unloaded shape ensured that the L/D peak is achieved at a similar angle of attack as the baseline hydrofoil.
- The onset of stall was delayed in the optimised hydrofoil due to the reduction in angle of attack at the tip.
- The positively bend-twist coupled hydrofoil demonstrated a strong hysteresis effect.

7.3. Scope for future Research

Following are several research areas that may be performed in the future based the contents and work undertaken as a part of this thesis:

- Develop a three-way coupled optimisation scheme propeller blade. The optimisation scheme presented in this thesis employed ANSYS CFX to extract pressure maps at variation perturbations from the design point to optimise the layup. A three-way coupled solver (coupling GA, FEM and hydrodynamic solver) has the potential to improve the results. However, there may be a considerable increase in solver time for such an optimisation strategy. Thus, it is best to employ an efficient hydrodynamic solver specifically developed for propeller blades and hydrofoils in order to reduce the computational cost.
- Further understand the structural dynamics and, especially, vibration stability of optimised composite hydrofoils and compare them against standard metallic hydrofoils and non-optimised composite hydrofoils. It is important to perform underwater modal frequency studies for hydrofoil structures under a cantilevered boundary condition. It is important to understand the modal frequencies and mode shapes of metal and composite hydrofoil structures in order to understand and compare their differences in terms of structural dynamics and stability. A tap testing as demonstrated in this thesis (Chapter 5.3.1) may not be viable as it may be impractical to perform controlled tapping on an underwater structure without disturbing the fluid around the structure. Instead, it may be perform to attach accelerometers to the hydrofoil at various locations and perform one tap to construct the modal shapes using accelerometers.

- Further understand the load dependent performance behaviour of composite blades. This has been addressed and demonstrated both experimentally and using FSI simulations in Chapter 6.6.3. This load dependent performance variation of composite propeller blades is also demonstrated by Liu and Young (2009). However, it is necessary to further understand this phenomenon as it adds an extra degree of complexity into the design problem. The implication of this phenomenon is that although a ship maintains the appropriate ratio between advance and rotational speeds of its propeller blades, it may not be able to achieve its design efficiency unless the required speed is maintained. This can be a challenging design problem that needs to be addressed. Further investigations must be performed on this subject to investigate the possibility of improving the design strategy to include advance speed and rotation in the objective function.

  One possible strategy is to identify the possible advance speeds the vessel can have as a probability distribution and use these probabilities as weightages in the objective function presented in this thesis. The pressure distributions used for the optimisation will be for the different speeds considered in the layup optimisation rather than different advance ratios taken in this thesis.

- It is important to understand the reasons for hysteresis behaviour observed in the positively bend-twist coupled hydrofoil. As explained in Chapter 6.3.4, the hysteresis phenomenon of the positively coupled hydrofoil was clearly observed during cavitation tunnel experiments. This is an important phenomenon as this means that there could be two distinct operating points for the hydrofoil blade for the same flow condition depending on the history of prior flow condition. Although this is not a phenomenon that was not observed in the negatively bend-twist coupled hydrofoil, the importance of understanding this behaviour has great significance. It is argued here that the observed hysteresis/mismatch in curves is not due to a loss of stiffness of the blade as it was observed that the slope of C_L (Figure 6-14) remained the same for both Run 1 and 2. If the stiffness were affected, the slopes cannot be the same as there would be different deflections for the same angle of attack (same hydrodynamic load on the blade). It must also be investigated whether this was a mere transient effect of the structure and holding the blade at each angle of attack increment for a longer period of time may allow the structure to achieve the same deflections and hydrodynamic performance in both increasing and decreasing AoA sweeps.

- Fully understand the composite failure mechanisms involved in the failure of composite hydrofoils and propeller blades. These structures have complicated ply terminations, material interfaces, impurities, etc. that can led to various different failure types in composites. Repeated loading (fatigue) is also another important aspect that needs to be addressed. A good starting point could be to utilise an established interactive composite failure theory such as Tsai-Hill Failure Theory for composites. Based on the failure theory chosen for the blade, the objective function for optimisation can be reconstructed in the following way:

$$\min_{\boldsymbol{\theta}} f(\boldsymbol{\theta}) = 10^{1000|TH\times FOS-1|} \times \frac{\sum_{i=1}^{2} w_i \left|\Delta\phi_{Optimum}^{i}(\Delta P) - \Delta\phi_{GA}^{i}(\boldsymbol{\theta},\Delta P)\right|}{\sum_{i=1}^{n} w_i} \tag{7-1}$$

$$\left(\frac{\sigma_{11}}{\sigma_{TS1}}\right)^2 + \left(\frac{\sigma_{22}}{\sigma_{TS2}}\right)^2 - \frac{\sigma_{11}\sigma_{22}}{\sigma_{TS1}^2} + \left(\frac{\sigma_{12}}{\sigma_{SS}}\right)^2 = TH \quad (7\text{-}2)$$

Where σ_{11}, σ_{22} and σ_{12} are normal stress in fibre direction, normal stress lateral to fibres and in-plane shear stress. σ_{TS1}, $\sigma_{TS2}$and σ_{SS} are maximum allowable stress in fibre direction, lateral to fibres and in-plane shear stress In the modified optimisation objective function ((7-1), the penalty function takes into account the Tsai-Hill value (TH) calculated for the layup at the given pressure distribution on the blade. The FOS is the factor of safety specified for the application. In a similar way, other failure mechanisms can also be implemented into the objective function; such as the allowable maximum principal strain limit, commonly used in desing practice. Furthermore, multiple failure criteria can also be implemented into the objective function by a using the product of penalty functions.

However, one important step prior to implementing failure theories is an in-depth investigation into the accuracy of failure prediction by common composite failure theories for a composite blade structure. This has to be performed using experimentation and investigating crack propagation and the resulting failure mode of a composite blade. Fatigue life is also another important requirement that must be taken into account in the addressing failure of a composite blade. Fatigue in composites is, however, has much complexities to address compared to fatigue phenomena in traditional metals. Therefore, fatigue testing is also an important experimental step that must be performed in order to gain understanding into fatigue failure to incorporate into the objective function.

- Improve the Neutron tomography scan technique for carbon fibre composites. Several basic scans were attempted as a part of this research. However, there are many improvements to be made. This can potentially be extremely useful as a non-destructive damage detection technique for composites and manufacturing quality evaluation technique.

8. Bibliography

ATKINSON, P. & GLOVER, E. J. 1988. PROPELLER HYDROELASTIC EFFECTS. *S.N.A.M.E., Propellers '88 Symposium.* Virginia Beach, VA, USA: British Maritime Technology.

AUGIER, B., HAUVILLE, F., BOT, P., AUBIN, N. & DURAND, M. 2014. Numerical study of a flexible sail plan submitted to pitching: Hysteresis phenomenon and effect of rig adjustments. *Ocean Engineering,* 90**,** 119-128.

AWAD, Z. K., ARAVINTHAN, T., ZHUGE, Y. & GONZALEZ, F. 2012. A review of optimization techniques used in the design of fibre composite structures for civil engineering applications. *Materials and Design,* 33**,** 534-544.

BAKER, J. E. 1987. Reducing bias and inefficiency in the selection algorithm. *Proceedings of the Second International Conference on Genetic Algorithms on Genetic algorithms and their application.* Cambridge, Massachusetts, USA: L. Erlbaum Associates Inc.

BEIRÃO DA VEIGA, L., BUFFA, A., LOVADINA, C., MARTINELLI, M. & SANGALLI, G. 2012. An isogeometric method for the Reissner–Mindlin plate bending problem. *Computer Methods in Applied Mechanics and Engineering,* 209–212**,** 45-53.

BERTRAM, V. 2000. *Practical Ship Hydrodynamics*, Butterworth-Heinemann.

BLETZINGER, K.-U., BISCHOFF, M. & RAMM, E. 2000. A unified approach for shear-locking-free triangular and rectangular shell finite elements. *Computers & Structures,* 75**,** 321-334.

BORDAS, S. P. A. & NATARAJAN, S. 2010. On the approximation in the smoothed finite element method (SFEM). *International Journal for Numerical Methods in Engineering,* 81**,** 660-670.

BORDAS, S. P. A., NATARAJAN, S., KERFRIDEN, P., AUGARDE, C. E., MAHAPATRA, D. R., RABCZUK, T. & PONT, S. D. 2011. On the performance of strain smoothing for quadratic and enriched finite element approximations (XFEM/GFEM/PUFEM). *International Journal for Numerical Methods in Engineering,* 86**,** 637-666.

BRANDNER, P. A., LECOFFRE, Y. & WALKER, G. J. 2007. Design Considerations in the Development of a Modern Cavitation Tunnel *In:* JACOBS, P., MCINTYRE, T., CLEARY, M., BUTTSWORTH, D., DAVID MEE, CLEMENTS, R., MORGAN, R. & LEMCKERT, C. (eds.) *16th Australasian Fluid Mechanics Conference.* Brisbane, Australia School of Engineering, The University of Queensland

BRANDT, S. A. 2015. *Introduction to Aeronautics: A Design Perspective*, American Institute of Aeronautics and Astronautics, Inc., Reston, Virginia.

CARLTON, J. 2007. *Marine Propellers and Propulsion*, Elsevier Butterworth-Heinemann.

CAZES, F. & MESCHKE, G. 2012. An Edge-based Imbricate Finite Element Method (EI-FEM) with full and reduced integration. *Computers & Structures,* 106–107**,** 154-175.

CHEN, B. Y. H., NEELY, S. K., MICHAEL, T. J., GOWING, S., SZWERC, R. P., BUCHLER, D. & SCHULT, R. Design, fabrication and testing of pitch-adapting (Flexible) composite propellers. 2006.

CHEN, J.-S., WU, C.-T., YOON, S. & YOU, Y. 2001. A stabilized conforming nodal integration for Galerkin mesh-free methods. *International Journal for Numerical Methods in Engineering,* 50**,** 435-466.

COLCLOUGH, W. J. & RUSSELL, J. G. 1972. The development of a composite propeller blade with a carbon fibre reinforced plastics spar. *Aeronautical Journal,* 76**,** 53-57.

CORBETT, J. J. & KOEHLER, H. W. 2003. Updated emissions from ocean shipping. *J. Geophys. Res.,* 108**,** 4650.

COTTRELL, J. A., HUGHES, T. J. R. & BAZILEVS, Y. 2009. *Isogeometric Analysis: Toward Integration of CAD and FEA*, Wiley.

DAOUST, J. & HOA, S. V. 1989. Parameters affecting interlaminar stresses in tapered laminates under static loading conditions. *Polymer Composites,* 10**,** 374-383.

DAS, H. N. & KAPURIA, S. 2016. On the use of bend–twist coupling in full-scale composite marine propellers for improving hydrodynamic performance. *Journal of Fluids and Structures,* 61**,** 132-153.

DEEP, K., SINGH, K. P., KANSAL, M. L. & MOHAN, C. 2009. A real coded genetic algorithm for solving integer and mixed integer optimization problems. *Applied Mathematics and Computation,* 212**,** 505-518.

DEEP, K. & THAKUR, M. 2007. A new crossover operator for real coded genetic algorithms. *Applied Mathematics and Computation,* 188**,** 895-911.

DEFENCE, U. 2004. *Foreign Comparative Testing (FCT) Program – FY 2004: Summaries of New Start Projects* [Online]. United States. Available: http://www.defense.gov/news/Jan2004/ForeignCompTesting.pdf [Accessed July 2012.

DELAUNAY, B. 1934. Sur la sphere vide. A la memoire de George Voronoi. Izv. Acad. Nauk. SSSR.

DEPARTMENT OF DEFENSE, U. 2002. *COMPOSITE MATERIALS HANDBOOK: POLYMER MATRIX COMPOSITES MATERIALS PROPERTIES*

DUTTWEILER, M. E. & BRENNEN, C. E. 1999. Experimental Investigation of an Instability on a Cavitating Propeller. *FEDSM'99 3rd ASME/JSME Joint Fluids Engineering Conference.* San Francisco, CA, USA.

FANG, C. & SPRINGER, G. S. 1993. Design of Composite Laminates by a Monte Carlo Method. *Journal of Composite Materials,* 27**,** 721-753.

FELLI, M., DI FELICE, F., GUJ, G. & CAMUSSI, R. 2004. Analysis of the propeller wake by pressure and velocity correlation. *15th Australasian Fluid Mechanics Conference.* Sydney, Australia.

GOLDBERG, D. E. & DEB, K. 1991. A comparative analysis of selection schemes used in genetic algorithms. *Urbana,* 51**,** 61801-2996.

GOUPEE, A. J. & VEL, S. S. 2006. Two-dimensional optimization of material composition of functionally graded materials using meshless analyses and a genetic algorithm. *Computer Methods in Applied Mechanics and Engineering,* 195**,** 5926-5948.

GOWING, S., COFFIN, P. & DAI, C. Hydrofoil Cavitation Improvements with Elastically Coupled Composite Materials. 25th American Towing Tank Conference, 24-25 September 1998 Iowa, USA.

GRABOVAC, I., HUGHES, R. & MCGUCKIN, D. 2006. Composite Ship Propellers. DSTO.

HAMMER, V. B., BENDSØE, M. P., LIPTON, R. & PEDERSEN, P. 1997. Parametrization in laminate design for optimal compliance. *International Journal of Solids and Structures,* 34**,** 415-434.

HE, K., HOA, S. V. & GANESAN, R. 2000. The study of tapered laminated composite structures: a review. *Composites Science and Technology,* 60**,** 2643-2657.

HE, Z. C., CHENG, A. G., ZHANG, G. Y., ZHONG, Z. H. & LIU, G. R. 2011. Dispersion error reduction for acoustic problems using the edge-based smoothed finite element method (ES-FEM). *International Journal for Numerical Methods in Engineering,* 86**,** 1322-1338.

HER, S.-C. 2002. Stress analysis of ply drop-off in composite structures. *Composite Structures,* 57**,** 235-244.

HERRERA, F., LOZANO, M. & VERDEGAY, J. L. 1998. Tackling Real-Coded Genetic Algorithms: Operators and Tools for Behavioural Analysis. *Artificial Intelligence Review,* 12**,** 265-319.

HSIAO, C. T. & CHAHINE, G. L. 2001. Numerical Simulation of Bubble Dynamics in a Vortex Flow Using Navier-Stokes Computations and Moving Chimera Grid Scheme. *Fourth International Symposium on Cavitation.* Pasadena, CA USA.

HUANG, T. T., WANG, H. T., SANTELLI, N. & GROVES, N. C. 1976. Propeller/stern/boundary-layer Interaction on Axisymmetric Bodies: Theory and Experiment. BETHESDA MD: David W. Taylor Naval Ship Research and Development Center.

HUGHES, T. J. 2012. *The finite element method: linear static and dynamic finite element analysis,* Courier Corporation.

HUGHES, T. J. R., COTTRELL, J. A. & BAZILEVS, Y. 2005. Isogeometric analysis: CAD, finite elements, NURBS, exact geometry and mesh refinement. *Computer Methods in Applied Mechanics and Engineering,* 194**,** 4135-4195.

JESSUP, S. D. 1986. Further Measurements of Model Propeller Pressure Distributions Using a Novel Technique. Bethesda, MD 20084 USA: David Taylor Naval Ship R&D Center.

JONG, K. & SPEARS, W. 1991. An analysis of the interacting roles of population size and crossover in genetic algorithms. *In:* SCHWEFEL, H.-P. & MÄNNER, R. (eds.) *Parallel Problem Solving from Nature.* Springer Berlin Heidelberg.

KAM, T. Y. & SNYMAN, J. A. 1991. Optimal design of laminated composite plates using a global optimization technique. *Composite Structures,* 19**,** 351-370.

KAMEYAMA, M. & FUKUNAGA, H. 2007. Optimum design of composite plate wings for aeroelastic characteristics using lamination parameters. *Computers and Structures,* 85**,** 213-224.

KANT, T. & SWAMINATHAN, K. 2000. Estimation of transverse/interlaminar stresses in laminated composites – a selective review and survey of current developments. *Composite Structures,* 49**,** 65-75.

KHANDAN, R., NOROOZI, S., SEWELL, P. & VINNEY, J. 2012. The development of laminated composite plate theories: a review. *Journal of Materials Science,* 47**,** 5901-5910.

KIKUCHI, F. & ISHII, K. 1999. An improved 4-node quadrilateral plate bending element of the Reissner-Mindlin type. *Computational Mechanics,* 23**,** 240-249.

KIM, H.-B. & LEE, S.-J. 2002. Performance improvement of two-frame particle tracking velocimetry using a hybrid adaptive scheme. *Measurement Science and Technology,* 13**,** 573.

KUIPER, G. 1992. *The Wageningen Propeller Series,* The Netherlands, Maritime Research Institute Netherlands.

LEE, D. T. & SCHACHTER, B. J. 1980. Two algorithms for constructing a Delaunay triangulation. *International Journal of Computer & Information Sciences,* 9**,** 219-242.

LEE, S.-J., PAIK, B.-G. & LEE CHOUNG, M. 2005a. Phase-Averaged Particle Tracking Velocimetry Measurements of Propeller Wake. *Journal of Ship Research,* 49**,** 43-54.

LEE, S., PAIK, B., YOON, J. & LEE, C. 2004. Three-component velocity field measurements of propeller wake using a stereoscopic PIV technique. *Experiments in Fluids,* 36**,** 575-585.

LEE, Y.-J. & LIN, C.-C. 2004. Optimized Design of Composite Propeller. *Mechanics of Advanced Materials and Structures,* 11**,** 17-30.

LEE, Y. J., LIN, C. C., JI, J. C. & CHEN, J. S. 2005b. Optimization of a composite rotor blade using a genetic algorithm with local search. *Journal of Reinforced Plastics and Composites,* 24**,** 1759-1769.

LERBS, H. W. 1952. Moderately loaded propellers with a finite number of blades and an arbitrary distribution of circulation. *Transaction SNAME.*

LIN, C.-C. & LEE, Y.-J. 2004. Stacking sequence optimization of laminated composite structures using genetic algorithm with local improvement. *Composite Structures,* 63**,** 339-345.

LIN, C. C., LEE, Y. J. & HUNG, C. S. 2009. Optimization and experiment of composite marine propellers. *Composite Structures,* 89**,** 206-215.

LIU, G.-R. 2009. *Meshfree methods: moving beyond the finite element method,* Taylor & Francis.

LIU, G. R., DAI, K. Y. & NGUYEN, T. T. 2007. A Smoothed Finite Element Method for Mechanics Problems. *Computational Mechanics,* 39**,** 859-877.

LIU, G. R., NGUYEN-THOI, T. & LAM, K. Y. 2008. A novel alpha finite element method (αFEM) for exact solution to mechanics problems using triangular and tetrahedral elements. *Computer Methods in Applied Mechanics and Engineering,* 197**,** 3883-3897.

LIU, G. R., NGUYEN-THOI, T. & LAM, K. Y. 2009a. An edge-based smoothed finite element method (ES-FEM) for static, free and forced vibration analyses of solids. *Journal of Sound and Vibration,* 320**,** 1100-1130.

LIU, G. R., NGUYEN-THOI, T., NGUYEN-XUAN, H. & LAM, K. Y. 2009b. A node-based smoothed finite element method (NS-FEM) for upper bound solutions to solid mechanics problems. *Computers & Structures,* 87**,** 14-26.

LIU, Z. & YOUNG, Y. L. 2009. Utilization of bend–twist coupling for performance enhancement of composite marine propellers. *Journal of Fluids and Structures,* 25**,** 1102-1116.

MAAS, H. G., GRUEN, A. & PAPANTONIOU, D. 1993. Particle tracking velocimetry in three-dimensional flows. *Experiments in Fluids,* 15**,** 133-146.

MALLIKARJUNA & KANT, T. 1993. A critical review and some results of recently developed refined theories of fiber-reinforced laminated composites and sandwiches. *Composite Structures,* 23**,** 293-312.

MARINE 1993. Composites offer advantages for propellers. *Reinforced Plastics,* 37**,** 24-26.

MARKAIDE, N. 2005. Composite propeller for fishing vessels. *JEC Composites Magazine.* San Sebastián, Spain INASMET-TECNALIA.

MARSH, G. 2004. A new start for marine propellers? *Reinforced Plastics,* 48**,** 34-38.

MOTLEY, M. R., LIU, Z. & YOUNG, Y. L. 2009. Utilizing fluid–structure interactions to improve energy efficiency of composite marine propellers in spatially varying wake. *Composite Structures,* 90**,** 304-313.

MOTLEY, M. R., NELSON, M. & YOUNG, Y. L. 2012. Integrated probabilistic design of marine propulsors to minimize lifetime fuel consumption. *Ocean Engineering,* 45**,** 1-8.

MOTLEY, M. R. & YOUNG, Y. L. 2011a. Influence of uncertainties on the response and reliability of self-adaptive composite rotors. *Composite Structures,* 94**,** 114-120.

MOTLEY, M. R. & YOUNG, Y. L. 2011b. Performance-based design and analysis of flexible composite propulsors. *Journal of Fluids and Structures,* 27**,** 1310-1325.

MOURITZ, A. P., GELLERT, E., BURCHILL, P. & CHALLIS, K. 2001. Review of advanced composite structures for naval ships and submarines. *Composite Structures,* 53**,** 21-42.

MÜHLENBEIN, H. & SCHLIERKAMP-VOOSEN, D. 1993. Predictive Models for the Breeder Genetic Algorithm I. Continuous Parameter Optimization. *Evolutionary Computation,* 1**,** 25-49.

MUKHERJEE, A. & VARUGHESE, B. 1999. Development of a specialised finite element for the analysis of composite structures with ply drop-off. *Composite Structures,* 46**,** 1-16.

MUKHERJEE, A. & VARUGHESE, B. 2001. Design guidelines for ply drop-off in laminated composite structures. *Composites Part B: Engineering,* 32**,** 153-164.

MULCAHY, N. L., PRUSTY, B. G. & GARDINER, C. Flexible Composite Hydrofoils and Propeller Blades. PACIFIC2010 International Maritime Conference, Jan 27-29 2010a Sydney, Australia.

MULCAHY, N. L., PRUSTY, B. G. & GARDINER, C. 2010b. Hydroelastic design of composite components. *International Journal of Ship and Offshore Structures,* 5**,** 359-370.

MULCAHY, N. L., PRUSTY, B. G. & GARDINER, C. P. Optimisation of Composite Adaptive Response with Experimental Validation *In:* TOPPING, B. H. V. & PAPADRAKAKIS, M., eds. Ninth International Conference on Computational Structures Technology, , 2008 Athens, Greece. Civil-Comp Press, Stirlingshire, Scotland.

MULCAHY, N. L., PRUSTY, B. G. & GARDINER, C. P. 2011. Flexible composite hydrofoils and propeller blades. *Transactions of the Royal Institution of Naval Architects Part B: International Journal of Small Craft Technology,* 153**,** B39-B46.

NELKA, J. J. 1974. Experimental Evaluation of a Series of Skewed Propellers with Forward Rake: Open-Water Performance, Cavitation Performance, Field-Point Pressures, and Unsteady Propeller Loading. NAVAL SHIP RESEARCH AND DEVELOPMENT CENTER, BETHESDA MD.

NGUYEN-THANH, N., RABCZUK, T., NGUYEN-XUAN, H. & BORDAS, S. P. A. 2008. A smoothed finite element method for shell analysis. *Computer Methods in Applied Mechanics and Engineering,* 198**,** 165-177.

NGUYEN-THOI, T., LIU, G. R., LAM, K. Y. & ZHANG, G. Y. 2009. A face-based smoothed finite element method (FS-FEM) for 3D linear and geometrically non-linear solid mechanics problems using 4-node tetrahedral elements. *International Journal for Numerical Methods in Engineering,* 78**,** 324-353.

NGUYEN-THOI, T., PHUNG-VAN, P., NGUYEN-XUAN, H. & THAI-HOANG, C. 2012. A cell-based smoothed discrete shear gap method using triangular elements for static and free vibration analyses of Reissner–Mindlin plates. *International Journal for Numerical Methods in Engineering,* 91**,** 705-741.

NGUYEN-XUAN, H., BORDAS, S. & NGUYEN-DANG, H. 2008. Smooth finite element methods: Convergence, accuracy and properties. *International Journal for Numerical Methods in Engineering,* 74**,** 175-208.

NGUYEN-XUAN, H., LIU, G. R., BORDAS, S., NATARAJAN, S. & RABCZUK, T. 2013. An adaptive singular ES-FEM for mechanics problems with singular field of arbitrary order. *Computer Methods in Applied Mechanics and Engineering,* 253**,** 252-273.

NOOR, A. K. & BURTON, W. S. 1989. Assessment of Shear Deformation Theories for Multilayered Composite Plates. *Applied Mechanics Reviews,* 42**,** 1-13.

OHTAKE, T., NAKAE, Y. & MOTOHASHI, T. 2007. Nonlinearity of the Aerodynamic Characteristics of NACA0012 Aerofoil at Low Reynolds Numbers. *JOURNAL OF THE JAPAN SOCIETY FOR AERONAUTICAL AND SPACE SCIENCES,* 55**,** 439-445.

PLUCIŃSKI, M. M., YOUNG, Y. L. & LIU, Z. Optimization of a self-twisting composite marine propeller using genetic algorithms. 16th International Conference on Composite Materials, 2007 Kyoto, Japan.

POGUE, W. R. & VIZZINI, A. J. 1990. Structural Tailoring Techniques to Prevent Delamination in Composite Laminates. *Journal of the American Helicopter Society,* 35**,** 38-45.

RHEE, S. H. & JOSHI, S. 2003. CFD Validation for a Marine Propeller Using an Unstructured Mesh Based RANS Method. *ASME Conference Proceedings,* 2003**,** 1157-1163.

SCOTT, M. A., SIMPSON, R. N., EVANS, J. A., LIPTON, S., BORDAS, S. P. A., HUGHES, T. J. R. & SEDERBERG, T. W. 2013. Isogeometric boundary element analysis using unstructured T-splines. *Computer Methods in Applied Mechanics and Engineering,* 254**,** 197-221.

SELIG, M. S., GUGLIELMO, J. J., BROEREN, A. P. & GIGUERE, P. 1995. Summary of Low-Speed Airfoil Data. Virginia: SoarTech Publications.

SHOJAEE, S., IZADPANAH, E., VALIZADEH, N. & KIENDL, J. 2012. Free vibration analysis of thin plates by using a NURBS-based isogeometric approach. *Finite Elements in Analysis and Design,* 61**,** 23-34.

SOREMEKUN, G., GÜRDAL, Z., HAFTKA, R. T. & WATSON, L. T. 2001. Composite laminate design optimization by genetic algorithm with generalized elitist selection. *Computers and Structures,* 79**,** 131-143.

STRANG, G. & FIX, G. J. 1973. *An analysis of the finite element method,* Prentice-Hall Englewood Cliffs, NJ.

TAUCHERT, T. R. & ADIBHATLA, S. 1984. Design of Laminated Plates for Maximum Stiffness. *Journal of Composite Materials,* 18**,** 58-69.

THAI, C. H., NGUYEN-XUAN, H., NGUYEN-THANH, N., LE, T. H., NGUYEN-THOI, T. & RABCZUK, T. 2012. Static, free vibration, and buckling analysis of laminated composite Reissner–Mindlin plates using NURBS-based isogeometric approach. *International Journal for Numerical Methods in Engineering,* 91**,** 571-603.

TIAN, B., ZHONG, Y. & LI, R. 2011. Analytic bending solutions of rectangular cantilever thin plates. *Archives of Civil and Mechanical Engineering,* 11**,** 1043-1052.

TSAI, S. W. & PAGANO, N. J. 1968. Invariant Properties of Composite Materials. Air force materials lab Wright-Patterson AFB Ohio.

TUREK, S. & HRON, J. 2006. Proposal for Numerical Benchmarking of Fluid-Structure Interaction between an Elastic Object and Laminar Incompressible Flow

Fluid-Structure Interaction. *In:* BUNGARTZ, H.-J. & SCHÄFER, M. (eds.). Springer Berlin Heidelberg.

VALIZADEH, N., NATARAJAN, S., GONZALEZ-ESTRADA, O. A., RABCZUK, T., BUI, T. Q. & BORDAS, S. P. A. 2013. NURBS-based finite element analysis of functionally graded plates: Static bending, vibration, buckling and flutter. *Composite Structures,* 99**,** 309-326.

VIDYASHANKAR, B. R. & KRISHNA MURTY, A. V. 2001. Analysis of laminates with ply drops. *Composites Science and Technology,* 61**,** 749-758.

VOITH. 2004. *Contur Propeller the Intlligent Propulsion System* [Online]. Available: http://www.voithturbo.nl/sys/php/docdb_getfile.php?docnr=G2078&lang=en&pageid=553246 [Accessed July 2012.

VOLANTE. 2005. *Contur® - The intelligent propeller made of Carbon Fiber* [Online]. Available: http://www.compositecarbonfiberprop.com/contur_flexibility.htm [Accessed July 2012.

WOZNIAK, C. D. 2005. Analysis, Fabrication, and Testing of a Composite Bladed Propeller for a Naval Academy Yard Patrol (YP) Craft *Trident Scholar Report.* Annapolis, MD: US Naval Academy.

WU, C. M. L. 1987. Non-linear analysis of tapered (in steps) laminated plate under uniform inplane load. *Composite Structures,* 7**,** 205-223.

WU, C. M. L. & WEBBER, J. P. H. 1986. Analysis of tapered (in steps) laminated plates under uniform inplane load. *Composite Structures,* 5**,** 87-100.

WU, S. C., LIU, G. R., CUI, X. Y., NGUYEN, T. T. & ZHANG, G. Y. 2010. An edge-based smoothed point interpolation method (ES-PIM) for heat transfer analysis of rapid manufacturing system. *International Journal of Heat and Mass Transfer,* 53**,** 1938-1950.

YOUNG, Y. L. 2007a. Hydroelastic Behavior of Flexible Composite Propellers in Wake Inflow. *16th International Conference on Composite Materials* Kyoto, Japan.

YOUNG, Y. L. 2007b. Time-dependent hydroelastic analysis of cavitating propulsors. *Journal of Fluids and Structures,* 23**,** 269-295.

YOUNG, Y. L. 2008. Fluid–structure interaction analysis of flexible composite marine propellers. *Journal of Fluids and Structures,* 24**,** 799-818.

YOUNG, Y. L. 2010. Dynamic hydroelastic scaling of self-adaptive composite marine rotors. *Composite Structures,* 92**,** 97-106.

YOUNG, Y. L., BAKER, J. W. & MOTLEY, M. R. 2010. Reliability-based design and optimization of adaptive marine structures. *Composite Structures,* 92**,** 244-253.

ZARRUK, G. A., BRANDNER, P. A., PEARCE, B. W. & PHILLIPS, A. W. 2014. Experimental study of the steady fluid–structure interaction of flexible hydrofoils. *Journal of Fluids and Structures,* 51**,** 326-343.

ZIENKIEWICZ, O. C., TAYLOR, R. L., ZIENKIEWICZ, O. C. & TAYLOR, R. L. 1977. *The finite element method*, McGraw-hill London.

Appendix A: Technical Drawings of the Mould

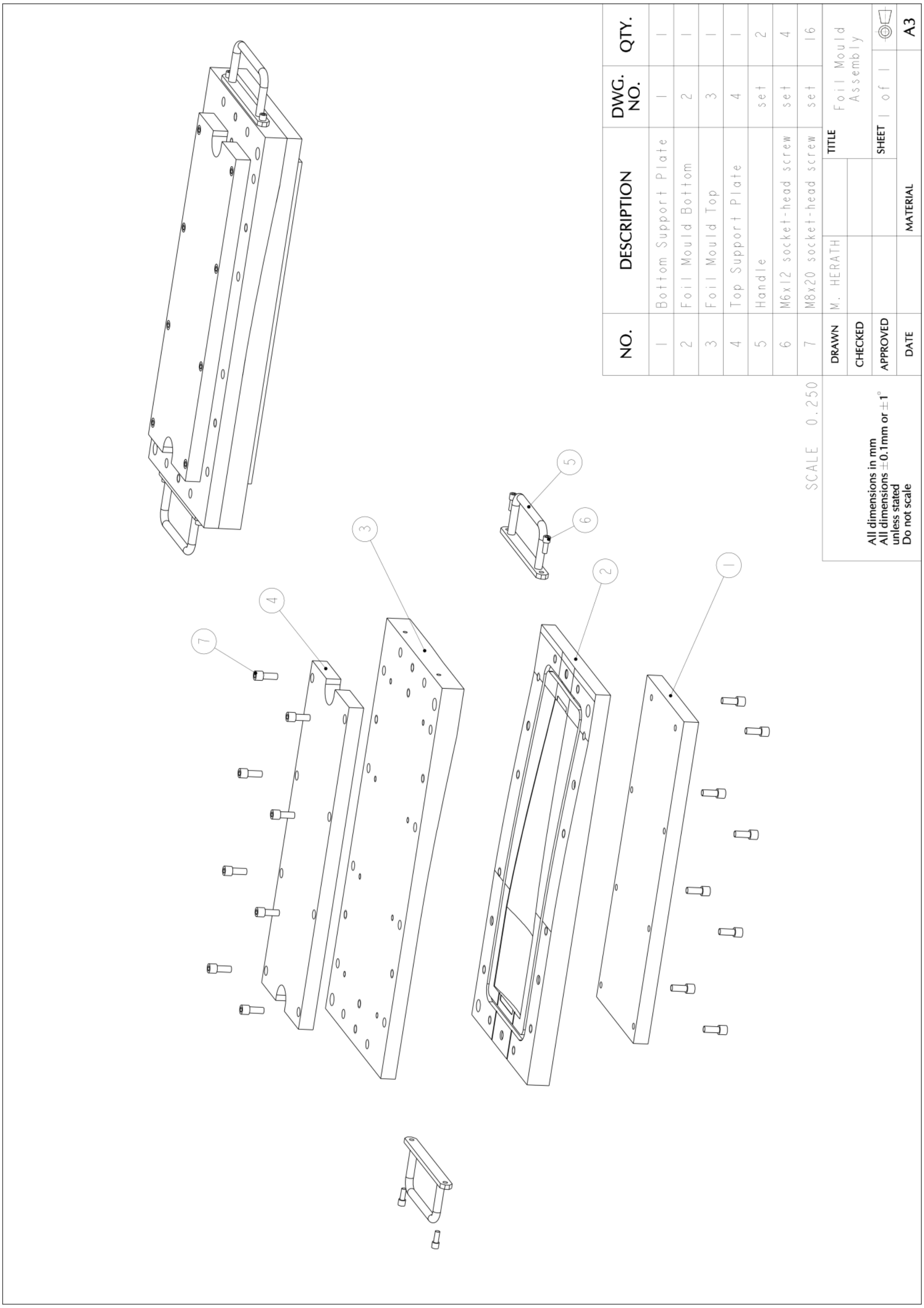

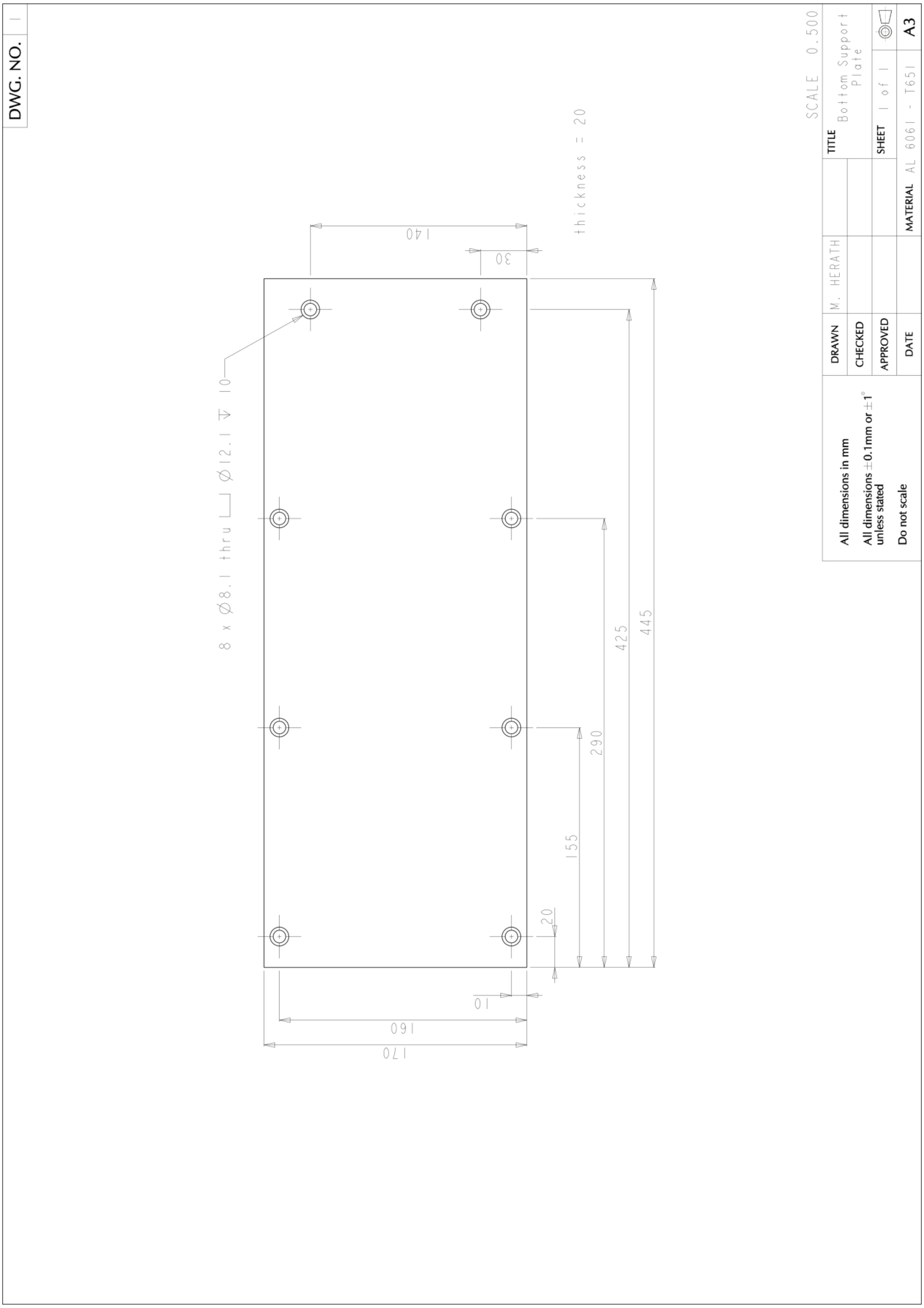
DWG. NO. 1
SCALE 0.500
TITLE Bottom Support Plate
SHEET 1 of 1
A3
MATERIAL AL 6061 - T651
DRAWN M. HERATH
CHECKED
APPROVED
DATE
All dimensions in mm
All dimensions ±0.1mm or ±1° unless stated
Do not scale
thickness = 20
8 x Ø8.1 thru ⌴ Ø12.1 ↧ 10
140
30
425
445
290
155
20
10
160
170

Appendix A: Technical Drawings of the Mould

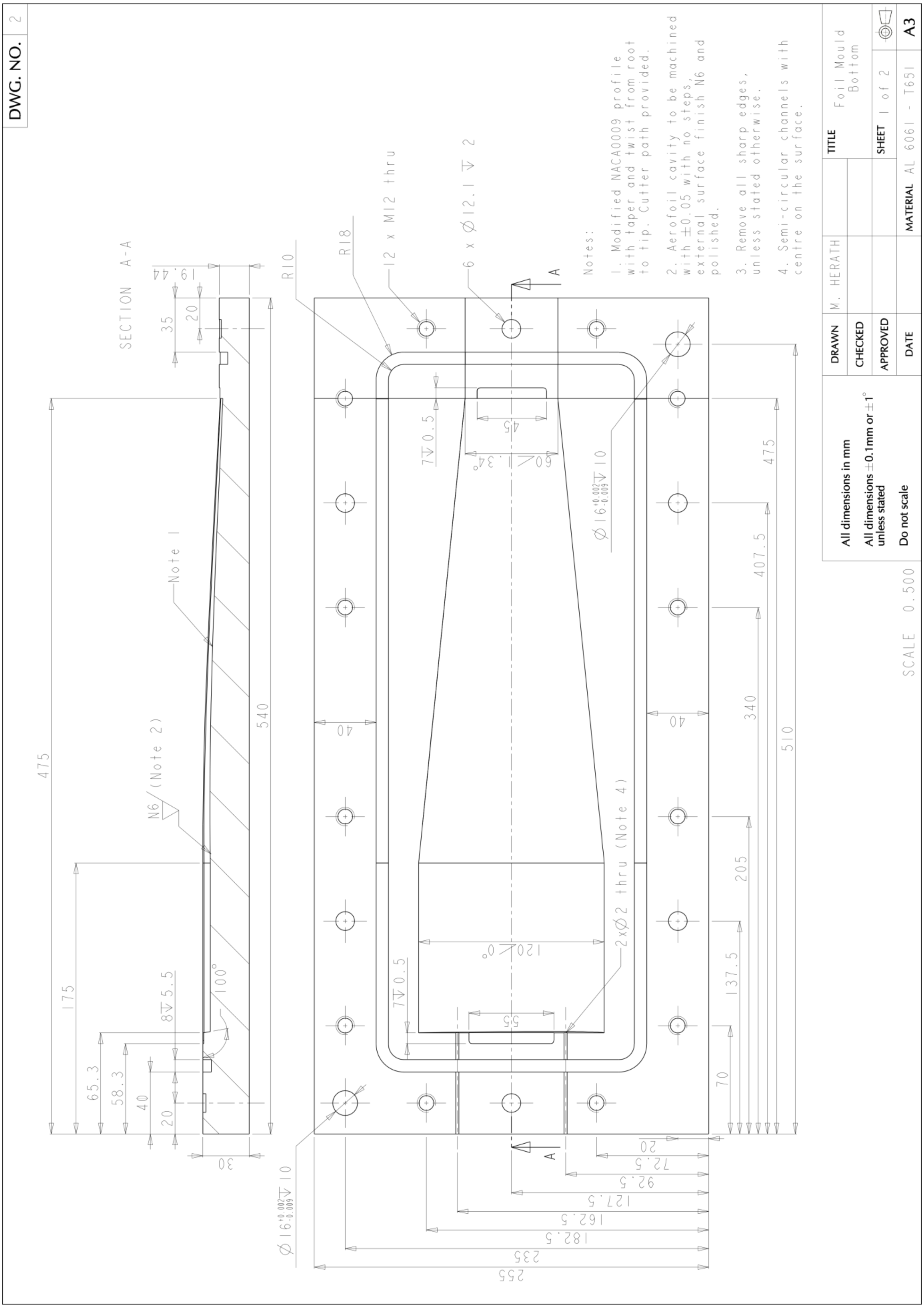

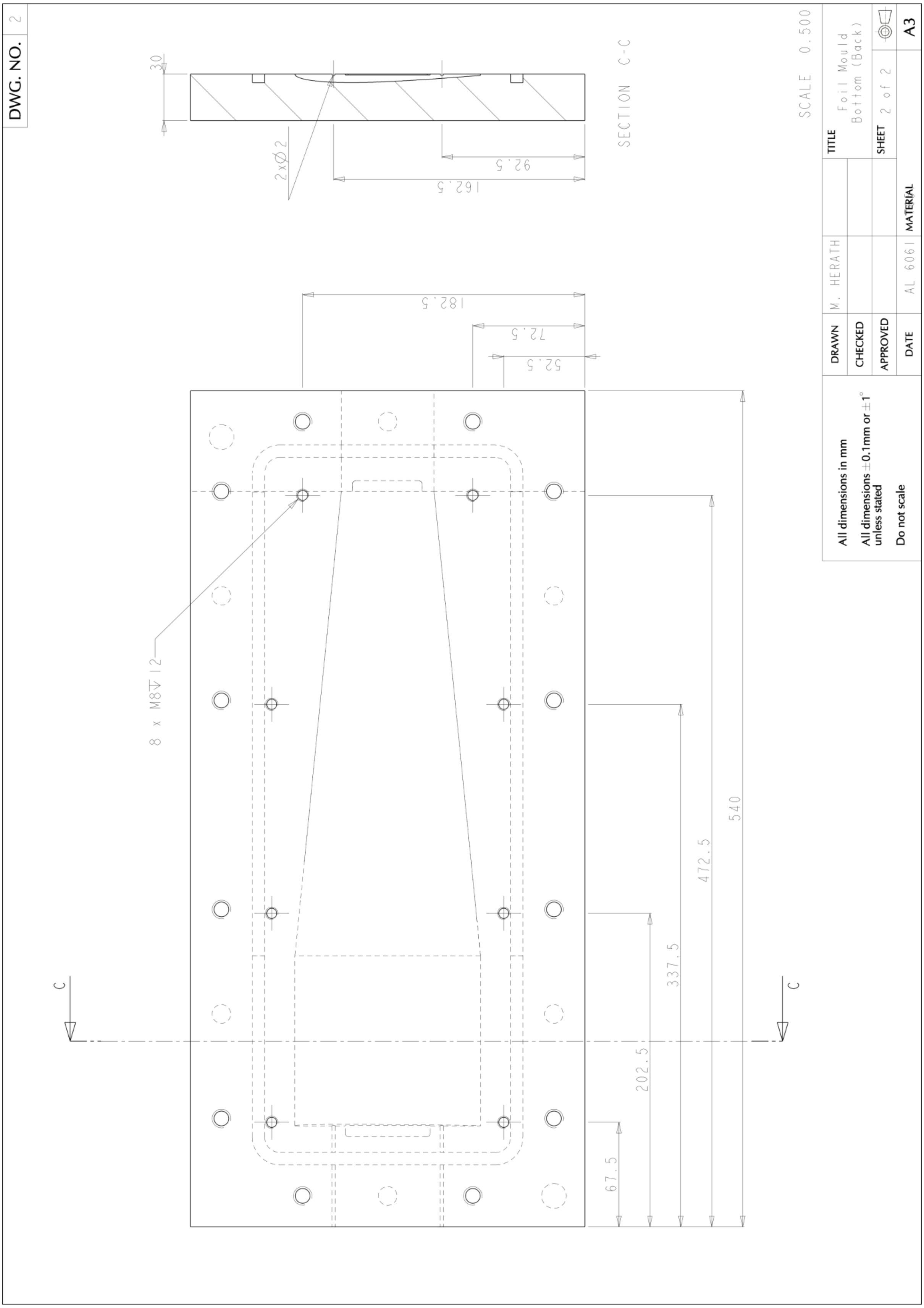
DWG. NO. 2
SECTION C-C
SCALE 0.500
30
2xØ2
92.5
162.5
182.5
72.5
52.5
8 x M8↧12
540
472.5
337.5
202.5
67.5
C
C
TITLE
Foil Mould Bottom (Back)
SHEET 2 of 2
A3
MATERIAL
AL 6061
DRAWN
M. HERATH
CHECKED
APPROVED
DATE
All dimensions in mm
All dimensions ±0.1mm or ±1° unless stated
Do not scale

Appendix A: Technical Drawings of the Mould

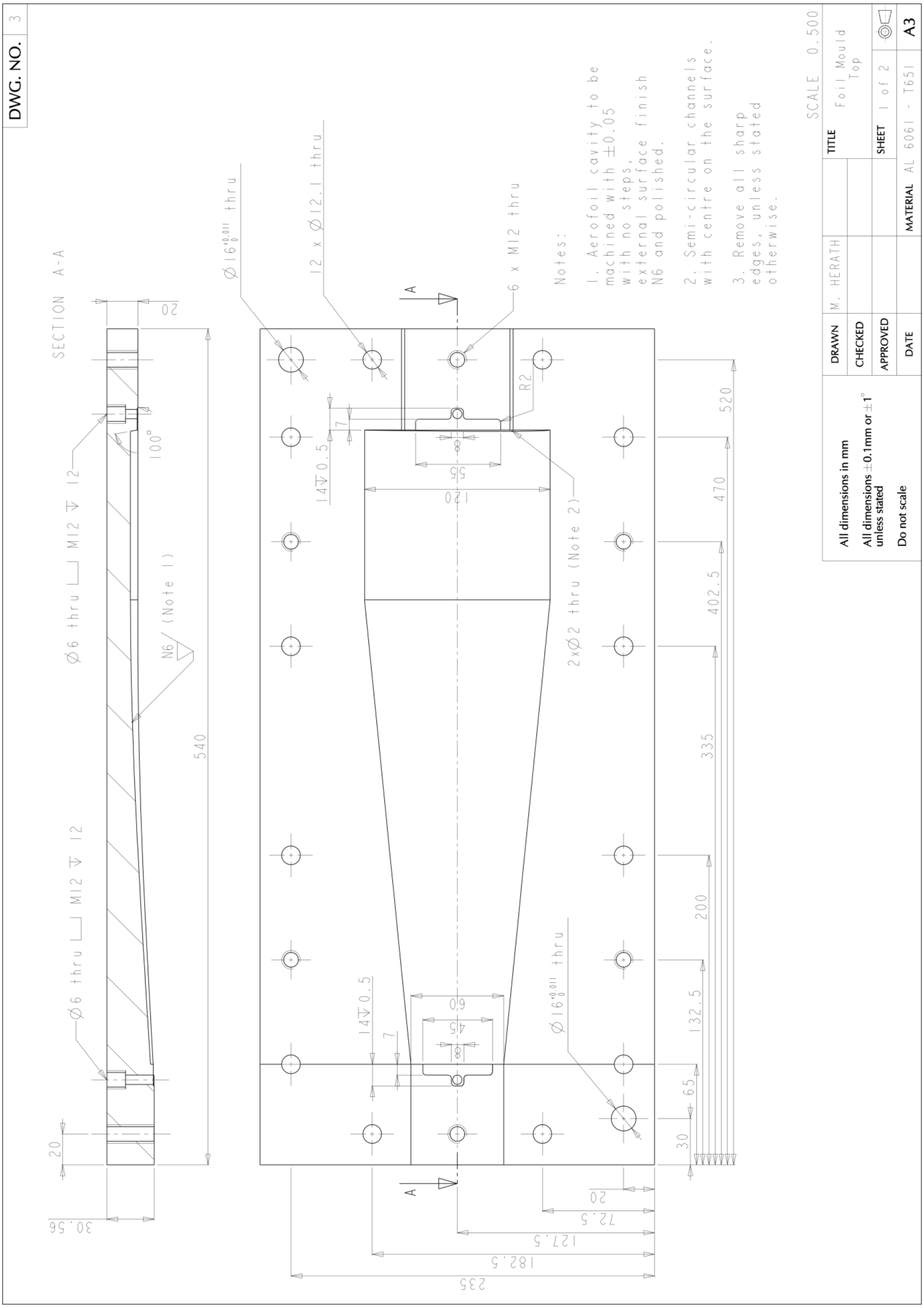

Appendix A: Technical Drawings of the Mould

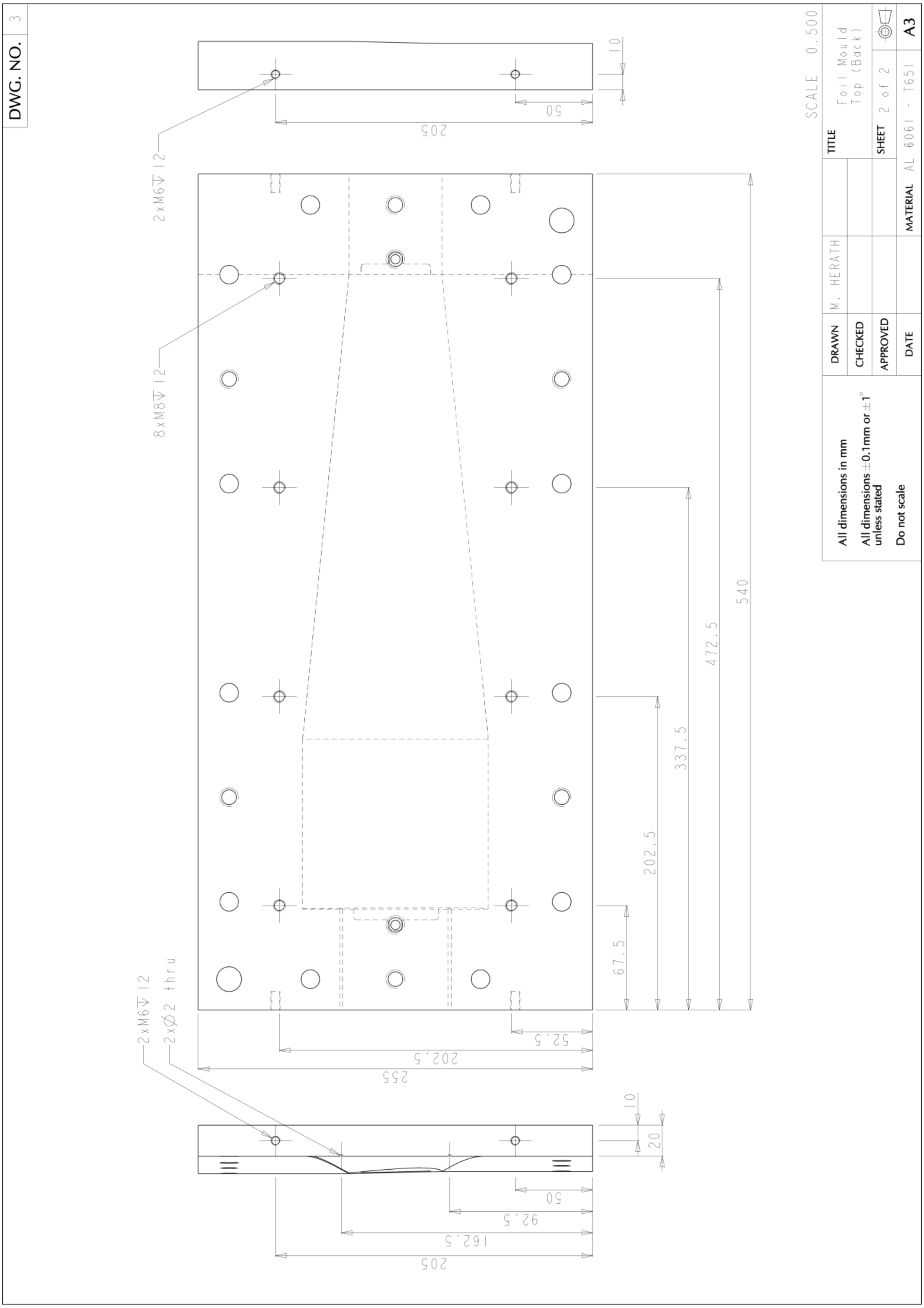

Appendix A: Technical Drawings of the Mould

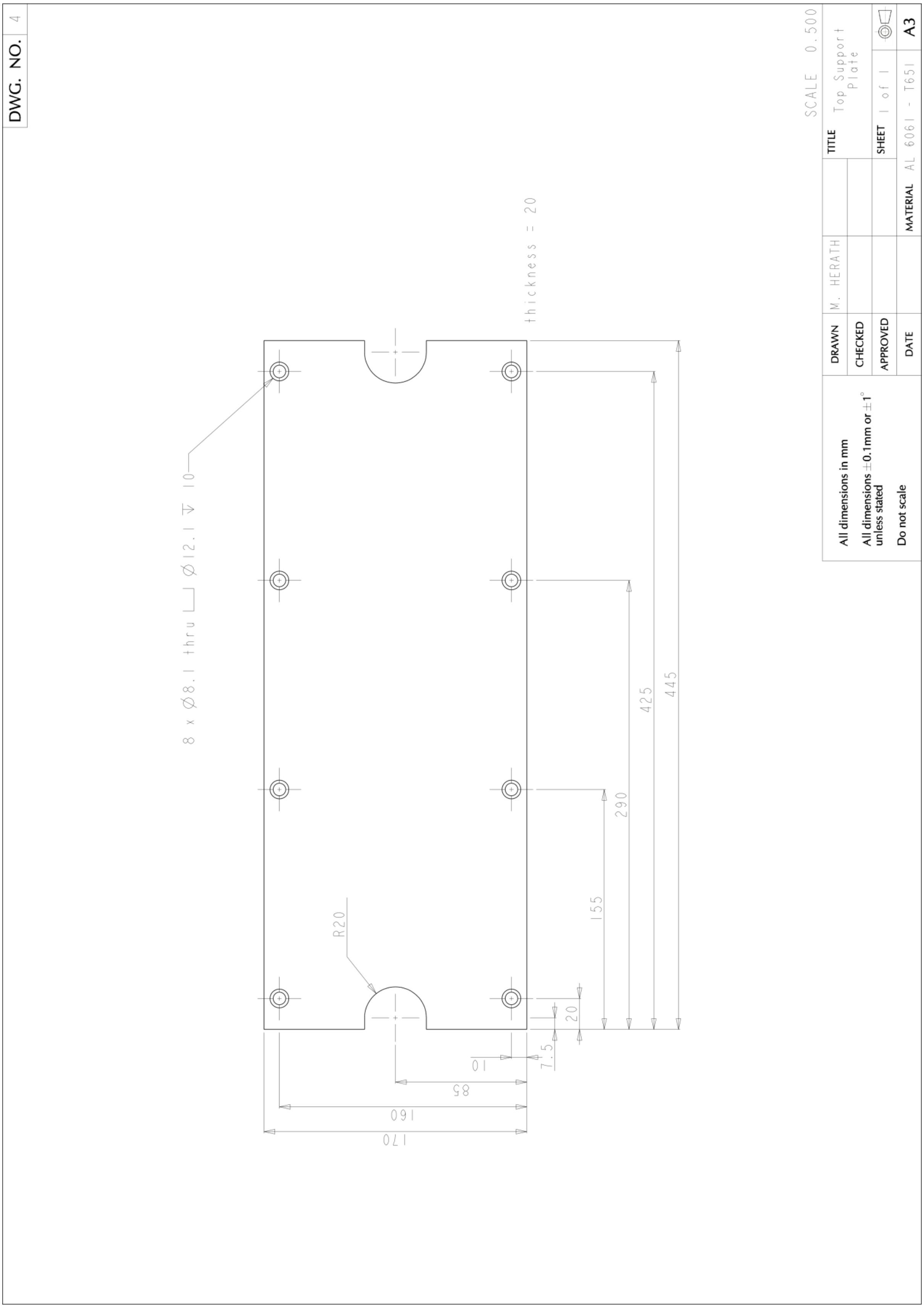

Appendix B: Metrology Scan Data

Point-1	X	Y	Z	3D
Actual	-103.134	59.807	0.036	GOOD
Nominal	-103.134	60.000	0.036	+/- 0.250
Deviation	0.000	-0.193	-0.000	-0.193
Point-2	X	Y	Z	3D
Actual	-44.541	59.920	-0.108	GOOD
Nominal	-44.541	60.000	-0.108	+/- 0.250
Deviation	0.000	-0.080	-0.000	-0.080
Point-3	X	Y	Z	3D
Actual	42.642	55.944	0.010	GOOD
Nominal	42.622	55.738	0.011	+/- 0.250
Deviation	0.021	0.206	-0.000	0.207
Point-4	X	Y	Z	3D
Actual	103.367	49.669	-2.110	GOOD
Nominal	103.366	49.659	-2.110	+/- 0.250
Deviation	0.001	0.010	-0.000	0.010
Point-5	X	Y	Z	3D
Actual	171.038	42.648	-4.514	GOOD
Nominal	171.063	42.892	-4.518	+/- 0.250
Deviation	-0.024	-0.244	0.004	-0.245
Point-6	X	Y	Z	3D
Actual	234.398	36.080	-7.509	OOT -0.228
Nominal	234.445	36.556	-7.518	+/- 0.250
Deviation	-0.047	-0.476	0.010	-0.478
Point-7	X	Y	Z	3D
Actual	294.093	29.873	-11.183	OOT -0.452
Nominal	294.162	30.571	-11.199	+/- 0.250
Deviation	-0.069	-0.698	0.016	-0.702
Point-8	X	Y	Z	3D
Actual	299.952	16.701	-10.647	GOOD
Nominal	300.000	16.701	-10.647	+/- 0.250
Deviation	-0.048	0.000	0.000	-0.048
Point-9	X	Y	Z	3D
Actual	299.959	-8.150	-10.103	GOOD
Nominal	300.000	-8.150	-10.103	+/- 0.250
Deviation	-0.041	-0.000	0.000	-0.041
Point-10	X	Y	Z	3D
Actual	299.890	-24.932	-10.021	GOOD
Nominal	300.000	-24.932	-10.021	+/- 0.250
Deviation	-0.110	0.000	-0.000	-0.110

Point-11	X	Y	Z	3D
Actual	-109.580	-52.640	1.014	GOOD
Nominal	-109.700	-52.640	1.014	+/- 0.250
Deviation	0.120	0.000	0.000	-0.120
Point-12	X	Y	Z	3D
Actual	-109.703	-23.108	-0.370	GOOD
Nominal	-109.700	-23.108	-0.370	+/- 0.250
Deviation	-0.003	0.000	0.000	0.003
Point-13	X	Y	Z	3D
Actual	-109.722	22.197	0.070	GOOD
Nominal	-109.700	22.197	0.070	+/- 0.250
Deviation	-0.022	0.000	0.000	0.022
Point-14	X	Y	Z	3D
Actual	-109.547	54.718	-0.153	GOOD
Nominal	-109.700	54.718	-0.153	+/- 0.250
Deviation	0.153	0.000	0.000	-0.153
Point-15	X	Y	Z	3D
Actual	-100.573	52.111	1.528	GOOD
Nominal	-100.573	52.103	1.430	+/- 0.250
Deviation	0.000	0.008	0.098	0.098
Point-16	X	Y	Z	3D
Actual	-39.892	54.755	1.332	GOOD
Nominal	-39.892	54.746	1.221	+/- 0.250
Deviation	0.000	0.009	0.112	0.112
Point-17	X	Y	Z	3D
Actual	29.639	50.818	1.402	GOOD
Nominal	29.636	50.804	1.227	+/- 0.250
Deviation	0.003	0.014	0.175	0.176
Point-18	X	Y	Z	3D
Actual	97.031	45.106	-0.118	OOT 0.006
Nominal	97.020	45.084	-0.373	+/- 0.250
Deviation	0.011	0.022	0.255	0.256
Point-19	X	Y	Z	3D
Actual	167.736	37.968	-3.006	OOT 0.051
Nominal	167.719	37.940	-3.305	+/- 0.250
Deviation	0.017	0.028	0.299	0.301
Point-20	X	Y	Z	3D
Actual	232.550	31.998	-6.428	OOT 0.027
Nominal	232.533	31.971	-6.703	+/- 0.250
Deviation	0.018	0.027	0.275	0.277
Point-21	X	Y	Z	3D
Actual	289.883	26.058	-9.511	OOT 0.042

Nominal	**289.864**	**26.029**	**-9.801**	**+/- 0.250**
Deviation	**0.019**	**0.029**	**0.290**	**0.292**
Point-22	**X**	**Y**	**Z**	**3D**
Actual	**-97.199**	**55.338**	**-1.188**	**GOOD**
Nominal	**-97.199**	**55.337**	**-1.173**	**+/- 0.250**
Deviation	**0.000**	**0.001**	**-0.015**	**0.015**
Point-23	**X**	**Y**	**Z**	**3D**
Actual	**-54.869**	**54.366**	**-1.385**	**GOOD**
Nominal	**-54.869**	**54.355**	**-1.252**	**+/- 0.250**
Deviation	**0.000**	**0.011**	**-0.133**	**0.133**
Point-24	**X**	**Y**	**Z**	**3D**
Actual	**-7.063**	**54.718**	**-1.427**	**GOOD**
Nominal	**-7.063**	**54.702**	**-1.224**	**+/- 0.250**
Deviation	**0.000**	**0.016**	**-0.202**	**0.203**
Point-25	**X**	**Y**	**Z**	**3D**
Actual	**47.993**	**51.244**	**-1.570**	**OOT 0.010**
Nominal	**47.995**	**51.224**	**-1.312**	**+/- 0.250**
Deviation	**-0.002**	**0.020**	**-0.259**	**0.260**
Point-26	**X**	**Y**	**Z**	**3D**
Actual	**92.866**	**45.088**	**-2.737**	**OOT 0.033**
Nominal	**92.872**	**45.067**	**-2.455**	**+/- 0.250**
Deviation	**-0.006**	**0.021**	**-0.282**	**0.283**
Point-27	**X**	**Y**	**Z**	**3D**
Actual	**145.409**	**37.407**	**-4.818**	**OOT 0.057**
Nominal	**145.419**	**37.387**	**-4.512**	**+/- 0.250**
Deviation	**-0.011**	**0.020**	**-0.306**	**0.307**
Point-28	**X**	**Y**	**Z**	**3D**
Actual	**205.480**	**32.928**	**-7.463**	**OOT 0.032**
Nominal	**205.493**	**32.911**	**-7.182**	**+/- 0.250**
Deviation	**-0.012**	**0.017**	**-0.281**	**0.282**
Point-29	**X**	**Y**	**Z**	**3D**
Actual	**256.137**	**29.466**	**-9.839**	**GOOD**
Nominal	**256.145**	**29.457**	**-9.673**	**+/- 0.250**
Deviation	**-0.008**	**0.009**	**-0.165**	**0.166**
Point-30	**X**	**Y**	**Z**	**3D**
Actual	**290.811**	**25.321**	**-11.490**	**GOOD**
Nominal	**290.810**	**25.322**	**-11.503**	**+/- 0.250**
Deviation	**0.001**	**-0.001**	**0.013**	**-0.013**
Point-31	**X**	**Y**	**Z**	**3D**
Actual	**-99.517**	**-2.622**	**4.925**	**GOOD**
Nominal	**-99.517**	**-2.622**	**4.919**	**+/- 0.250**
Deviation	**0.000**	**0.000**	**0.006**	**0.006**

Point-32	X	Y	Z	3D
Actual	-57.543	1.448	4.820	GOOD
Nominal	-57.543	1.444	4.742	+/- 0.250
Deviation	0.000	0.004	0.078	0.078
Point-33	X	Y	Z	3D
Actual	-11.475	0.947	4.874	GOOD
Nominal	-11.475	0.942	4.765	+/- 0.250
Deviation	0.000	0.005	0.110	0.110
Point-34	X	Y	Z	3D
Actual	28.449	0.448	4.714	GOOD
Nominal	28.447	0.441	4.559	+/- 0.250
Deviation	0.002	0.007	0.156	0.156
Point-35	X	Y	Z	3D
Actual	67.147	-0.323	4.012	GOOD
Nominal	67.142	-0.332	3.827	+/- 0.250
Deviation	0.005	0.009	0.185	0.185
Point-36	X	Y	Z	3D
Actual	115.310	1.238	2.321	GOOD
Nominal	115.302	1.226	2.113	+/- 0.250
Deviation	0.009	0.012	0.209	0.209
Point-37	X	Y	Z	3D
Actual	163.375	0.610	0.122	GOOD
Nominal	163.364	0.597	-0.088	+/- 0.250
Deviation	0.011	0.013	0.210	0.211
Point-38	X	Y	Z	3D
Actual	218.170	0.427	-2.956	GOOD
Nominal	218.158	0.415	-3.149	+/- 0.250
Deviation	0.011	0.012	0.192	0.193
Point-39	X	Y	Z	3D
Actual	259.683	-3.949	-5.274	GOOD
Nominal	259.674	-3.957	-5.412	+/- 0.250
Deviation	0.009	0.008	0.139	0.139
Point-40	X	Y	Z	3D
Actual	292.811	-5.684	-7.302	GOOD
Nominal	292.807	-5.688	-7.370	+/- 0.250
Deviation	0.004	0.003	0.069	0.069
Point-41	X	Y	Z	3D
Actual	289.718	-29.361	-8.130	GOOD
Nominal	289.722	-29.374	-8.090	+/- 0.250
Deviation	-0.004	0.013	-0.040	-0.042
Point-42	X	Y	Z	3D
Actual	255.444	-32.672	-6.172	GOOD

Nominal	**255.450**	**-32.695**	**-6.105**	**+/- 0.250**
Deviation	**-0.006**	**0.022**	**-0.067**	**-0.071**
Point-43	**X**	**Y**	**Z**	**3D**
Actual	**210.511**	**-37.158**	**-3.631**	**GOOD**
Nominal	**210.510**	**-37.154**	**-3.642**	**+/- 0.250**
Deviation	**0.001**	**-0.004**	**0.011**	**0.011**
Point-44	**X**	**Y**	**Z**	**3D**
Actual	**169.277**	**-40.021**	**-1.215**	**GOOD**
Nominal	**169.275**	**-40.013**	**-1.247**	**+/- 0.250**
Deviation	**0.002**	**-0.009**	**0.032**	**0.034**
Point-45	**X**	**Y**	**Z**	**3D**
Actual	**123.349**	**-44.438**	**0.567**	**GOOD**
Nominal	**123.351**	**-44.447**	**0.599**	**+/- 0.250**
Deviation	**-0.002**	**0.009**	**-0.032**	**-0.034**
Point-46	**X**	**Y**	**Z**	**3D**
Actual	**50.598**	**-50.856**	**2.396**	**GOOD**
Nominal	**50.601**	**-50.876**	**2.471**	**+/- 0.250**
Deviation	**-0.003**	**0.021**	**-0.075**	**-0.078**
Point-47	**X**	**Y**	**Z**	**3D**
Actual	**12.596**	**-53.841**	**2.870**	**GOOD**
Nominal	**12.598**	**-53.855**	**2.924**	**+/- 0.250**
Deviation	**-0.001**	**0.014**	**-0.054**	**-0.056**
Point-48	**X**	**Y**	**Z**	**3D**
Actual	**-28.197**	**-55.705**	**2.641**	**GOOD**
Nominal	**-28.197**	**-55.738**	**2.756**	**+/- 0.250**
Deviation	**0.000**	**0.033**	**-0.115**	**-0.120**
Point-49	**X**	**Y**	**Z**	**3D**
Actual	**-63.732**	**-56.311**	**2.404**	**GOOD**
Nominal	**-63.732**	**-56.363**	**2.568**	**+/- 0.250**
Deviation	**0.000**	**0.052**	**-0.163**	**-0.171**
Point-50	**X**	**Y**	**Z**	**3D**
Actual	**-99.219**	**-56.872**	**2.170**	**GOOD**
Nominal	**-99.219**	**-56.944**	**2.373**	**+/- 0.250**
Deviation	**0.000**	**0.072**	**-0.203**	**-0.216**
Point-51	**X**	**Y**	**Z**	**3D**
Actual	**-94.770**	**-1.121**	**-4.842**	**GOOD**
Nominal	**-94.770**	**-1.120**	**-4.856**	**+/- 0.250**
Deviation	**0.000**	**-0.001**	**0.014**	**-0.014**
Point-52	**X**	**Y**	**Z**	**3D**
Actual	**-49.498**	**-2.875**	**-4.995**	**GOOD**
Nominal	**-49.498**	**-2.878**	**-4.930**	**+/- 0.250**
Deviation	**0.000**	**0.003**	**-0.065**	**0.066**

Point-53	X	Y	Z	3D
Actual	4.923	-5.199	-5.102	GOOD
Nominal	4.921	-5.205	-4.962	+/- 0.250
Deviation	0.002	0.005	-0.140	0.140
Point-54	X	Y	Z	3D
Actual	44.370	-4.031	-4.920	GOOD
Nominal	44.370	-4.038	-4.740	+/- 0.250
Deviation	-0.000	0.007	-0.180	0.180
Point-55	X	Y	Z	3D
Actual	97.624	-3.810	-5.547	GOOD
Nominal	97.629	-3.817	-5.326	+/- 0.250
Deviation	-0.004	0.007	-0.221	0.221
Point-56	X	Y	Z	3D
Actual	136.441	-9.043	-6.629	GOOD
Nominal	136.448	-9.047	-6.392	+/- 0.250
Deviation	-0.007	0.004	-0.238	0.238
Point-57	X	Y	Z	3D
Actual	175.851	-8.384	-7.939	OOT 0.006
Nominal	175.861	-8.387	-7.684	+/- 0.250
Deviation	-0.009	0.003	-0.255	0.256
Point-58	X	Y	Z	3D
Actual	218.935	-4.823	-9.629	OOT 0.003
Nominal	218.946	-4.827	-9.376	+/- 0.250
Deviation	-0.011	0.004	-0.253	0.253
Point-59	X	Y	Z	3D
Actual	267.913	-4.193	-11.686	GOOD
Nominal	267.919	-4.194	-11.563	+/- 0.250
Deviation	-0.006	0.001	-0.122	0.122
Point-60	X	Y	Z	3D
Actual	289.799	-3.074	-12.563	GOOD
Nominal	289.800	-3.075	-12.551	+/- 0.250
Deviation	-0.001	0.000	-0.012	0.012
Point-61	X	Y	Z	3D
Actual	288.785	-26.564	-11.354	GOOD
Nominal	288.787	-26.555	-11.304	+/- 0.250
Deviation	-0.002	-0.010	-0.050	0.051
Point-62	X	Y	Z	3D
Actual	257.135	-30.736	-9.592	GOOD
Nominal	257.138	-30.706	-9.465	+/- 0.250
Deviation	-0.003	-0.030	-0.127	0.130
Point-63	X	Y	Z	3D
Actual	215.397	-35.138	-7.389	GOOD

Nominal	**215.398**	**-35.119**	**-7.321**	**+/- 0.250**
Deviation	**-0.001**	**-0.018**	**-0.068**	**0.071**
Point-64	**X**	**Y**	**Z**	**3D**
Actual	**176.614**	**-38.327**	**-5.813**	**GOOD**
Nominal	**176.615**	**-38.316**	**-5.768**	**+/- 0.250**
Deviation	**-0.001**	**-0.011**	**-0.045**	**0.047**
Point-65	**X**	**Y**	**Z**	**3D**
Actual	**123.311**	**-45.013**	**-3.506**	**GOOD**
Nominal	**123.311**	**-45.011**	**-3.501**	**+/- 0.250**
Deviation	**0.000**	**-0.002**	**-0.005**	**0.005**
Point-66	**X**	**Y**	**Z**	**3D**
Actual	**42.804**	**-48.162**	**-3.397**	**GOOD**
Nominal	**42.805**	**-48.166**	**-3.417**	**+/- 0.250**
Deviation	**-0.000**	**0.004**	**0.020**	**-0.020**
Point-67	**X**	**Y**	**Z**	**3D**
Actual	**0.106**	**-51.193**	**-3.677**	**GOOD**
Nominal	**0.107**	**-51.204**	**-3.743**	**+/- 0.250**
Deviation	**-0.002**	**0.011**	**0.066**	**-0.067**
Point-68	**X**	**Y**	**Z**	**3D**
Actual	**-44.499**	**-54.156**	**-2.988**	**GOOD**
Nominal	**-44.499**	**-54.195**	**-3.154**	**+/- 0.250**
Deviation	**0.000**	**0.039**	**0.166**	**-0.171**
Point-69	**X**	**Y**	**Z**	**3D**
Actual	**-76.785**	**-55.263**	**-2.649**	**GOOD**
Nominal	**-76.785**	**-55.323**	**-2.872**	**+/- 0.250**
Deviation	**0.000**	**0.060**	**0.223**	**-0.231**
Point-70	**X**	**Y**	**Z**	**3D**
Actual	**-99.931**	**-56.235**	**-2.286**	**OOT -0.057**
Nominal	**-99.931**	**-56.328**	**-2.579**	**+/- 0.250**
Deviation	**0.000**	**0.092**	**0.293**	**-0.307**
Point-71	**X**	**Y**	**Z**	**3D**
Actual	**-94.893**	**31.642**	**2.999**	**GOOD**
Nominal	**-94.893**	**31.638**	**2.947**	**+/- 0.250**
Deviation	**0.000**	**0.004**	**0.052**	**0.052**
Point-72	**X**	**Y**	**Z**	**3D**
Actual	**-25.072**	**33.190**	**2.957**	**GOOD**
Nominal	**-25.072**	**33.182**	**2.839**	**+/- 0.250**
Deviation	**0.000**	**0.008**	**0.118**	**0.118**
Point-73	**X**	**Y**	**Z**	**3D**
Actual	**57.305**	**26.501**	**2.668**	**GOOD**
Nominal	**57.299**	**26.486**	**2.451**	**+/- 0.250**
Deviation	**0.006**	**0.015**	**0.217**	**0.218**

Point-74	X	Y	Z	3D
Actual	135.302	20.388	0.191	OOT 0.016
Nominal	135.290	20.367	-0.074	+/- 0.250
Deviation	0.013	0.021	0.265	0.266
Point-75	X	Y	Z	3D
Actual	201.680	16.810	-3.158	GOOD
Nominal	201.665	16.789	-3.404	+/- 0.250
Deviation	0.015	0.021	0.245	0.247
Point-76	X	Y	Z	3D
Actual	270.161	12.812	-7.115	GOOD
Nominal	270.149	12.796	-7.300	+/- 0.250
Deviation	0.012	0.016	0.186	0.187
Point-77	X	Y	Z	3D
Actual	-75.753	30.956	-3.055	GOOD
Nominal	-75.753	30.952	-2.994	+/- 0.250
Deviation	0.000	0.004	-0.061	0.061
Point-78	X	Y	Z	3D
Actual	-28.702	28.009	-3.324	GOOD
Nominal	-28.702	28.000	-3.196	+/- 0.250
Deviation	0.000	0.009	-0.128	0.129
Point-79	X	Y	Z	3D
Actual	33.669	20.312	-3.673	GOOD
Nominal	33.669	20.299	-3.465	+/- 0.250
Deviation	0.000	0.013	-0.208	0.209
Point-80	X	Y	Z	3D
Actual	88.153	16.787	-4.442	GOOD
Nominal	88.157	16.773	-4.204	+/- 0.250
Deviation	-0.004	0.013	-0.238	0.238
Point-81	X	Y	Z	3D
Actual	142.123	13.285	-6.057	OOT 0.018
Nominal	142.132	13.272	-5.790	+/- 0.250
Deviation	-0.009	0.013	-0.267	0.268
Point-82	X	Y	Z	3D
Actual	195.213	8.427	-8.266	OOT 0.029
Nominal	195.224	8.416	-7.987	+/- 0.250
Deviation	-0.012	0.011	-0.279	0.279
Point-83	X	Y	Z	3D
Actual	244.271	6.094	-10.431	GOOD
Nominal	244.280	6.087	-10.228	+/- 0.250
Deviation	-0.009	0.007	-0.203	0.203
Point-84	X	Y	Z	3D
Actual	282.755	6.824	-12.048	GOOD

Nominal	**282.759**	**6.821**	**-11.975**	**+/- 0.250**
Deviation	**-0.003**	**0.003**	**-0.072**	**0.072**
Point-85	**X**	**Y**	**Z**	**3D**
Actual	**-64.760**	**-25.659**	**5.412**	**GOOD**
Nominal	**-64.760**	**-25.659**	**5.402**	**+/- 0.250**
Deviation	**0.000**	**-0.000**	**0.009**	**0.009**
Point-86	**X**	**Y**	**Z**	**3D**
Actual	**22.601**	**-24.245**	**5.330**	**GOOD**
Nominal	**22.599**	**-24.244**	**5.228**	**+/- 0.250**
Deviation	**0.001**	**-0.000**	**0.102**	**0.102**
Point-87	**X**	**Y**	**Z**	**3D**
Actual	**126.307**	**-24.004**	**2.508**	**GOOD**
Nominal	**126.302**	**-24.003**	**2.382**	**+/- 0.250**
Deviation	**0.005**	**-0.001**	**0.126**	**0.126**
Point-88	**X**	**Y**	**Z**	**3D**
Actual	**216.914**	**-18.539**	**-2.239**	**GOOD**
Nominal	**216.908**	**-18.539**	**-2.342**	**+/- 0.250**
Deviation	**0.006**	**0.000**	**0.103**	**0.103**
Point-89	**X**	**Y**	**Z**	**3D**
Actual	**281.861**	**-21.614**	**-6.407**	**GOOD**
Nominal	**281.855**	**-21.610**	**-6.500**	**+/- 0.250**
Deviation	**0.006**	**-0.004**	**0.092**	**0.093**
Point-90	**X**	**Y**	**Z**	**3D**
Actual	**-96.933**	**-25.929**	**-5.322**	**GOOD**
Nominal	**-96.933**	**-25.929**	**-5.401**	**+/- 0.250**
Deviation	**0.000**	**0.000**	**0.079**	**-0.079**
Point-91	**X**	**Y**	**Z**	**3D**
Actual	**-29.951**	**-33.342**	**-5.269**	**GOOD**
Nominal	**-29.951**	**-33.342**	**-5.265**	**+/- 0.250**
Deviation	**0.000**	**-0.000**	**-0.005**	**0.005**
Point-92	**X**	**Y**	**Z**	**3D**
Actual	**29.293**	**-28.828**	**-5.169**	**GOOD**
Nominal	**29.292**	**-28.826**	**-5.074**	**+/- 0.250**
Deviation	**0.001**	**-0.002**	**-0.095**	**0.095**
Point-93	**X**	**Y**	**Z**	**3D**
Actual	**116.805**	**-24.281**	**-6.020**	**GOOD**
Nominal	**116.809**	**-24.276**	**-5.840**	**+/- 0.250**
Deviation	**-0.004**	**-0.005**	**-0.180**	**0.180**
Point-94	**X**	**Y**	**Z**	**3D**
Actual	**183.477**	**-24.498**	**-7.889**	**GOOD**
Nominal	**183.485**	**-24.486**	**-7.680**	**+/- 0.250**
Deviation	**-0.007**	**-0.012**	**-0.209**	**0.210**

Point-95	X	Y	Z	3D
Actual	**269.410**	**-24.792**	**-10.974**	**GOOD**
Nominal	**269.414**	**-24.781**	**-10.882**	**+/- 0.250**
Deviation	**-0.004**	**-0.011**	**-0.092**	**0.093**

95 Total Points	DX	DY	DZ	3D
Maximum Deviation :	0.153	0.206	0.299	0.307
Minimum Deviation :	-0.110	-0.698	-0.306	-0.702
Deviation Range :	0.263	0.904	0.605	1.008
Average Deviation :	-0.000	-0.000	-0.000	0.066
RMS Deviation :	0.026	0.097	0.155	0.185
Standard Deviation:	0.026	0.097	0.156	0.173

Deviation Summary

Appendix C: Tap testing tapping points

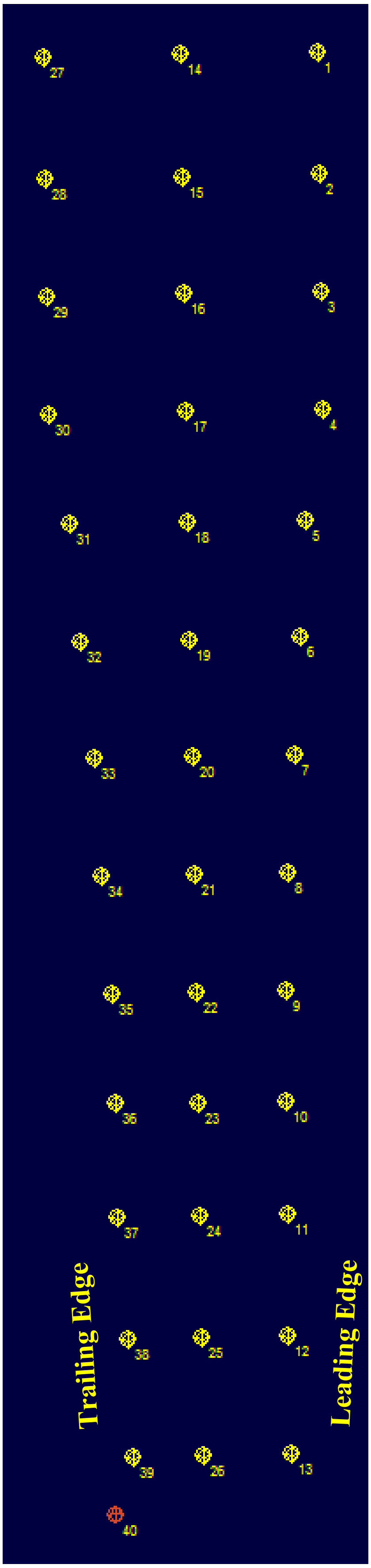

Tap Point No.	X (mm)	Y (mm)
1	9	25
2	40	25
3	70	25
4	100	25
5	128	30
6	158	32
7	188	34
8	218	36
9	248	37
10	276	38
11	305	38
12	336	38
13	366	38
14	9	60
15	40	60
16	70	60
17	100	60
18	128	60
19	158	60
20	188	60
21	218	60
22	248	60
23	276	60
24	305	60
25	336	60
26	366	60
27	9	95
28	40	95
29	70	95
30	100	95
31	128	90
32	158	88
33	188	85
34	218	84
35	248	82
36	276	81
37	305	81
38	336	79
39	366	78
40 (Accelerometer)	381	83